Active contraction in biological fiber networks

Pierre Ronceray

Numéro NNT : 2016SACLS154

THÈSE DE DOCTORAT
DE
L'UNIVERSITÉ PARIS-SACLAY
PRÉPARÉE À
L'UNIVERSITÉ PARIS-SUD

ECOLE DOCTORALE N° 564
« Physique en Île-de-France »

Spécialité de doctorat : Physique

Par

M. Pierre Ronceray

Contraction active de réseaux de fibres biologiques

Thèse présentée et soutenue à Orsay, le 31/05/2016.

Composition du Jury :

M. Jean-François Joanny, Professeur, Université Pierre-et-Marie-Curie, Président
M. Jean-Louis Barrat, Professeur, Université Grenoble Alpes, Rapporteur
M. Lev Truskinovsky, Directeur de Recherche, CNRS, Rapporteur
M. Abdul Barakat, Directeur de Recherche, CNRS, Examinateur
M. Chase Broedersz, Professeur, Ludwig-Maximilians-Universität München, Examinateur
M. Martin Lenz, Chargé de Recherche, CNRS, Directeur de thèse

Active Contraction in Biological Fiber Networks

par

Pierre Ronceray

Thèse de Doctorat
de l'Université Paris-Saclay
préparée à l'Université Paris-Sud

Laboratoire de Physique Théorique et Modèles Statistiques

École doctorale 564 : «Physique en Île-de-France»

Spécialité de doctorat : Physique

Directeur : Martin Lenz

À mes parents.

Contents

La cellule tire ses forces de son squelette

Ce résumé simplifié de mon travail est une adaptation de notre communiqué sur le site `actu.u-psud.fr`, à l'occasion de la publication de notre article dans PNAS.

Les propriétés mécaniques des fibres microscopiques structurant les cellules sont à l'origine des forces contractiles dans notre corps à grande échelle.

De nombreuses cellules de notre corps ont la faculté de se mouvoir et de se déformer de leur propre chef. Ces forces à l'œuvre pour des processus aussi divers que la division cellulaire, le façonnement de l'embryon ou encore la contraction musculaire ont toutes la même origine : elles sont produites par l'action simultanée d'une multitude de moteurs moléculaires contenus à l'intérieur de la cellule. Ces forces sont ensuite transmises pour passer de l'échelle nanométrique du moteur à celle de la cellule, mille fois plus grande, par un assemblage de fibres souples. Cet assemblage, véritable squelette de la cellule, lui confère sa structure et sa rigidité.

Cette thèse de physique porte sur la façon dont de tels réseaux de fibres transmettent les forces dans le vivant. Par des calculs théoriques et des simulations numériques, j'ai découvert que ces réseaux de fibres font bien plus que transmettre les forces : ils les réorganisent et les amplifient, générant ainsi des forces considérables aux grandes échelles. À l'origine de ce phénomène se trouve une propriété fondamentale inhérente aux fibres biologiques : de la même façon qu'une fine tige de plastique, ces fibres résistent si on les tire, tandis qu'en les comprimant elles vont avoir tendance à plier et se tordre.

En incluant cet effet, connu sous le nom de « flambage », dans les équations de transmission des forces, nous avons remarqué qu'un certain type de forces en ressortait amplifié. En effet, les forces contractiles, qui mettent le réseau sous tension, peuvent après transmission être vingt fois supérieures à ce qu'elles seraient sans flambage. Plus surprenant encore, ces forces contractiles émergent du seul fait des propriétés élastiques des filaments. Ainsi, les propriétés mécaniques de fibres microscopiques expliquent l'omniprésence des forces contractiles dans notre corps à grande échelle : non seulement sont-elles transmises très efficacement... Mais ce sont aussi les seules à être transmises ! Ceci explique peut-être pourquoi, de façon contre-intuitive, nous devons *contracter* nos muscles pour effectuer un mouvement d'*extension* – par exemple pour étendre les bras ou gonfler nos poumons : nos tissus musculaires génèrent des forces contractiles, et les os de notre squelette, par effet de levier, convertissent cette contraction en extension.

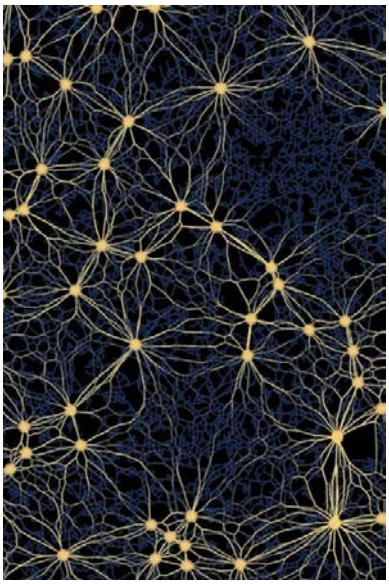

Figure 1: Simulation par ordinateur de la transmission de force dans un réseau de fibres biologiques. Les moteurs moléculaires (représentés par des cercles jaunes) réarrangent le réseau pour créer des motifs étoilés de fibres sous tension, responsables de l'amplification des forces contractiles.

Remerciements

Fini, c'est fini, ça va finir, ça va peut-être finir. Les grains s'ajoutent aux grains, un à un, et un jour, soudain, c'est un tas, un petit tas, l'impossible tas.

— Samuel Beckett, *Fin de partie.*

Cette thèse a été financée par l'Initiative Doctorale Interdisciplinaire 2013 de l'IDEX Paris-Saclay. J'ai aussi reçu le soutien de la Fondation des Treilles[1] *via* leur Prix Jeune Chercheur.

Je remercie Jean-Louis Barrat et Lev Truskinovsky pour leur lecture attentive de ce manuscrit et leurs commentaires constructifs, ainsi que l'ensemble des membres de mon jury pour avoir accepté d'assister à ma soutenance.

Mon goût pour les sciences m'a été pour bonne partie communiqué par les nombreux professeurs d'exception dont j'ai eu la chance d'être l'élève, et en particulier Jean Vassor, Mme Clapier, Mme Guilloux, Philippe Gallic, Jean-Pierre Foulon, Rémi Barbet-Massin, Emmanuel Trizac, Wendelin Werner, Bernard Derrida et Pawel Pieranski. À leur manière, ils façonné mes goûts et orienté mes choix en me transmettant leur passion, et je leur dois beaucoup. Je remercie aussi Bertrand Eynard pour ses enseignements, et pour ses conseils opportuns.

Je tiens à remercier tout particulièrement Emmanuel Trizac, qui depuis ma licence m'a servi tantôt de mentor avec des conseils amicaux et toujours avisés, tantôt d'ange gardien me tirant de quelque mauvais pas. C'est sur ses recommandations que j'ai choisi cette thèse, et c'est aussi lui qui m'a permis de trouver mon stage de Master 1 qui a débouché sur une collaboration de longue durée avec Peter Harrowell. Je suis aussi reconnaissant à Hubert Saleur pour ses précieuses suggestions.

Au cours de cette thèse, j'ai eu la chance d'effectuer plusieurs séjours aux États-Unis très enrichissants, et je remercie Tom Witten, Margaret Gardel et Chase Broedersz pour leur hospitalité.

[1] La Fondation des Treilles, créée par Anne Gruner Schlumberger, a notamment pour vocation d'ouvrir et de nourrir le dialogue entre les sciences et les arts afin de faire progresser la création et le recherche contemporaines. Elle accueille également des chercheurs dans le domaine des Treilles (Var). www.les-treilles.com

Mes travaux de thèse ont pour bonne partie été réalisés avec Chase Broedersz, en une collaboration fructueuse et plus qu'agréable – ce n'est que le début ! Je remercie aussi Peter Harrowell, avec qui j'ai continué de travailler en parallèle de ma thèse sur un projet toujours aussi passionnant et intriguant.

Je souhaite aussi remercier le Laboratoire de Physique Théorique et Modèles Statistiques dans son ensemble. C'est un lieu où il fait bon travailler, dans une ambiance toujours agréable, détendue et amicale où les échanges entre jeunes et moins jeunes sont naturels et spontanés. Merci à Claudine pour le fonctionnement impeccable.

Je remercie bien sûr Martin Lenz pour ces trois années de travail ensemble, qui furent fort agréables. Je ne regrette en rien mon choix de lui avoir fait confiance. Toujours disponible et curieux, prêt à discuter de nouveaux mystères, il a su me faire progresser par son exigeance bienveillante mais sans relâche, et m'a fait profiter sans compter de très nombreuses opportunités.

Il n'y a heureusement pas que la thèse dans la vie, et je tiens à remercier ma famille et mes amis, qui m'entourent et rendent la vie douce et rassurante. Mes parents, à qui je dois tant et auxquels je dédie cette thèse. Mes frères, cousins et amis de longue date, toujours là et tellement importants. La bande du Master avec qui la thèse a été une expérience collective, mes colocataires et Hanna, avec qui j'ai tant partagé ces dernières années. Mes collègues de laboratoire devenus des amis. Enfin, je remercie Chantal, mon meilleur public, et Guy, pour son soutien inconditionnel.

Foreword

Tomorrow, and tomorrow, and tomorrow,
Creeps in this petty pace from day to day,
To the last syllable of recorded time;
And all our yesterdays have lighted fools
The way to dusty death. Out, out, brief candle!
Life's but a walking shadow, a poor player
That struts and frets his hour upon the stage
And then is heard no more. It is a tale
Told by an idiot, full of sound and fury
Signifying nothing.

— William Shakespeare, *Macbeth*.

These are exciting times for a theoretical physicist to start a career. A few months ago, a new window on the universe was opened. Putting our ear to the ground, we heard the echo of an ancient cataclysm, as the ripples through the fabric of spacetime arrived to us a billion years later[2]. Four years before, the keystone to our description of the most intimate aspects of matter was finally set[3]; the theory stands, and physicists are now looking through the largest microscope in the world to find its flaws. In both cases, I was watching the webcast announcing the discovery, waiting eagerly for the news to break, and was elated when it did, as I felt I belonged to a community which was touching something absolute. Yet for some reason, I have decided that I prefer working on a much less absolute object of study – something a bit tepid, and somewhat slimy – *soft living matter*.

I haven't regretted this choice. This field is full of everyday surprises and hidden beauty, and because it is relatively new, there are many stones left unturned. Behind some of them, with a bit of luck and intuition, we can find what, as a theorist, I cherish the most: something novel, universal and, most of all, *simple.*

[2] LIGO Scientific Collaboration and Virgo Collaboration (2016). Observation of Gravitational Waves from a Binary Black Hole Merger. *Phys. Rev. Lett.*, 116(6):061102

[3] The ATLAS collaboration (2012). Observation of a new particle in the search for the Standard Model Higgs boson with the ATLAS detector at the LHC. *Physics Letters B*, 716(1):1–29

About this Thesis

This document presents my PhD work, performed under the supervision of Martin Lenz, at the Laboratoire de Physique Théorique et Modèles Statistiques, and, to a vast extent, in collaboration with Chase Broedersz. It tackles the questions of force transmission and active stress production in biological networks of fibrous polymers.

When I started my PhD with Martin in April 2013, the original subject was slightly more specific, and titled "Contraction of disordered actin networks". I didn't think it would keep me occupied for three years. Actually, six months later, I was convinced I had nailed the problem, and that it was time to write up and move on. Quite frustratingly, Martin disagreed, and told me that there was no hurry, and to keep digging. And I dug. Three years later, I'm still at it, and I hope to convince the reader that it was worth it.

During this PhD, I have published two research articles on this subject, which I fully detail in this Thesis. The first one was published in Soft Matter in early 2015[4], and presents our mathematical framework for quantifying contraction, as well as an exact solution to the stress production problem in linear elastic media. These results are presented in Chapter 4. A bit later, we started writing a second article, where we addressed the question of active stress production in linear and non-linear elastic fiber networks. This paper was published[5] in PNAS in early 2016 and, much to my pleasure, was featured on the cover (Figure 2). It condenses, in six pages, most of my PhD results, and this Thesis can be seen as an extended version of it. It culminates at the derivation of a comprehensive phase diagram for stress production summarizing our theoretical findings, which I present in Chapter 7. These theoretical results, in my opinion, solve the question posed by my PhD subject, as they explain *why* active fiber networks have a strong propensity to contract, and *how much* they do so.

This Thesis ends with a gallery of figures, where I present a selection of figures I made, chosen for their aesthetic value rather than their scientific content.

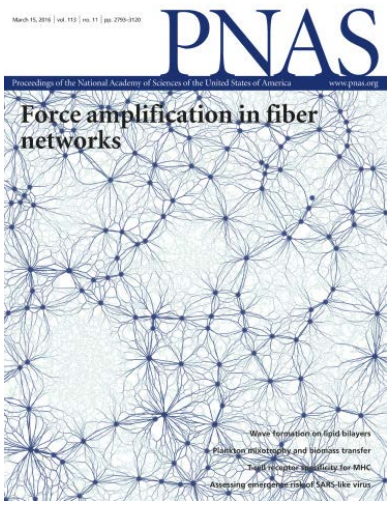

Figure 2: Cover illustration for our article (Ronceray et al., 2016).

[4] Ronceray, P. and Lenz, M. (2015). Connecting local active forces to macroscopic stress in elastic media. *Soft Matter*, 11(8):1597–1605

[5] Ronceray, P., Broedersz, C. P., and Lenz, M. (2016). Fiber networks amplify active stress. *Proc. Natl. Acad. Sci. U.S.A.*, 113(11):2827–2832

What this Thesis is not about

I have chosen not to present the integrality of my research work in this Thesis, but rather to focus on one consistent story. I have however worked on other scientific projects during my PhD, two of which I shortly present here.

Favoured Local Structures in supercooled liquids

One of the greatest open challenges in statistical physics is the nature of the glass transition: how a liquid of identical particles can undergo dynamical arrest on cooling, while remaining apparently amorphous. Two questions are intimately connected: why doesn't the supercooled liquid crystallize? Why does it slow down? Transient, stable local structures have been invoked as a reason for supercooled liquid (meta-)stability for more than 60 years. Their characterization has become classical, yet due to the descriptive nature of usual approaches, the causal links between the existence of such favoured local structures and the resulting crystallization (or lack thereof) has remained elusive.

During my first year of Master at École Normale Supérieure de Paris, I was lucky enough to go for a six-months research internship in Sydney, Australia. I started a project there with Peter Harrowell, at the School of Chemistry of the University of Sydney. The (*a posteriori*) aim was to investigate the role of stable local structures in stabilizing supercooled liquids, through the study of a novel two-dimensional lattice model allowing direct selection of a favoured local structure among a small pool of discrete geometries. This model turned out to be very rich, and I carried on analyzing it on the side since then. By the time I started my PhD, we had published three articles about this *Favoured Local Structures model*[6], and it was only the beginning. In these articles, we used our model to unravel the deep, surprisingly non-universal influence of local geometry on the ordering properties of condensed phases. By demonstrating analytically the importance of symmetry and overlap properties of the local structures in the loss of configurational entropy on cooling, we provided hints as to what kind of structures will best stabilize a liquid.

In the first year of my PhD, I completed our study of this two-dimensional model by a thorough study of an intriguing specific case, where a low-symmetry stable structure stabilizes the supercooled liquid to the point of dynamical arrest[7] (Figure 3). We related this apparent glassiness to the frustrated, structurally degenerate nature of the ground state of this system, and the presence of a liquid-liquid phase transition.

I then started extending these results to three dimensions. The adapted model was challenging to study, as the number of possible favoured local structures jumped from 9 in 2D to 144 in 3D. I simulated and characterized the ordering properties of each of them (Figure 4), developing *en passant* new tools to identify the ground state of lattice spin models. Using the statistical power of this large data set, we demonstrated counter-intuitive connections between the dense tiling properties of local structures and their symmetry properties[8]. However, rather disappointingly, almost all of these systems crystallized easily,

[6] Ronceray, P. and Harrowell, P. (2011). The variety of ordering transitions in liquids characterized by a locally favoured structure. *EPL (Europhysics Letters)*, 96(3):36005
Ronceray, P. and Harrowell, P. (2012). Geometry and the entropic cost of locally favoured structures in a liquid. *The Journal of chemical physics*, 136(13):134504
Ronceray, P. and Harrowell, P. (2013). Influence of liquid structure on the thermodynamics of freezing. *Physical Review E*, 87(5):052313

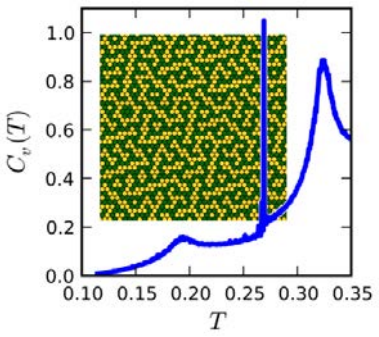

Figure 3: Heat capacity curve of a liquid with low-symmetry stable local structure, revealing multiple phase transitions. Inset: snapshot of a dynamically arrested amorphous state in the Favoured Local Structures lattice model.

[7] Ronceray, P. and Harrowell, P. (2014). Multiple ordering transitions in a liquid stabilized by low symmetry structures. *Physical review letters*, 112(1):017801

[8] Ronceray, P. and Harrowell, P. (2015a). Favoured local structures in liquids and solids: a 3d lattice model. *Soft matter*, 11(17):3322–3331

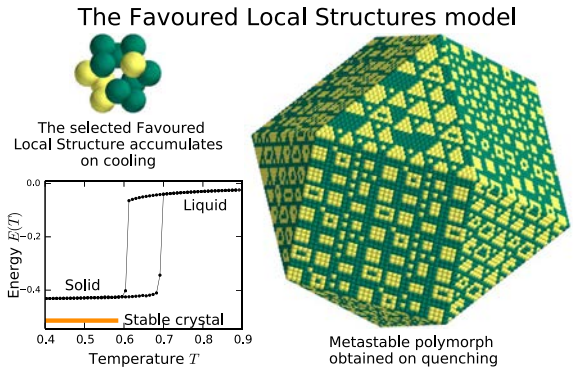

Figure 4: The three-dimensional Favoured Local Structures model. Graphical abstract of (Ronceray and Harrowell, 2015a).

which prevented us from addressing deeper questions about the glass transition and the conditions to observe low-temperature amorphous states.

In this project, we had focused so far on the implications of a single stable local structures. In molecular supercooled liquids however, the connection between local configuration and energy density can be complex, with, *e.g.*, many stable local structures. This lead us to new questions: how do distinct favoured local structures interact within a supercooled liquid? What influence do they have on its stability? Recently, we started to tackle this more complex problem by adapting our model to the case of multiple favoured local structures. The number of possibilities here is daunting, and there would be no point in a comprehensive study of the ways to combine even only two stable local structures (Figure 5). However, using our knowledge from the single favoured local structure model, we found that when combining two low-symmetry, ill-packing local structures, the resulting system often arrests into a glassy state, while for other pairs of structures it crystallizes easily (Figure 6). In order to understand how local geometrical properties can have such a dramatic influence on the thermodynamic properties of the system, I developed a new type of exact, high-temperature approach for calculating the configurational entropy in such systems[9]. Using this framework, we introduced a new quantity to measure the geometrical affinity between different structures, namely the *structural covariance*[10], which we have shown to correlate with glass-forming ability: geometrically compatible structures tend to crystallize well, while ill-fitting structures compete for ordering as they mutually exclude each other, hindering crystallization. We suggest that the presence of such competing stable structures in supercooled liquid can provide a way to stabilize it against crystallization down to low temperature – a prerequisite for the system to undergo a glass transition[11].

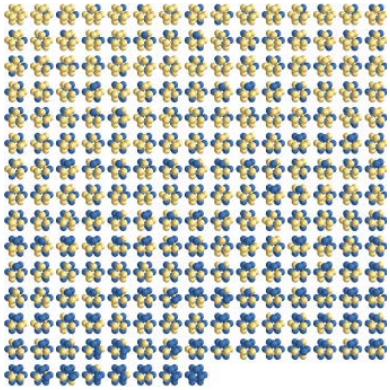

Figure 5: The 218 possible favoured local structures in the three-dimensional model.

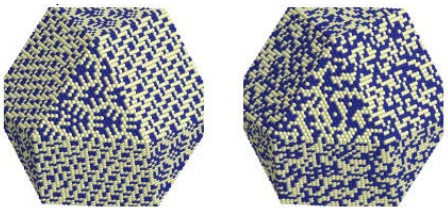

Figure 6: Low-temperature states of similar systems with two ill-packing favoured local structures. Left: a crystal; right: an amorphous arrested state. What microscopic parameter controls this dramatic difference?

[9] Ronceray, P. and Harrowell, P. (2015b). The free energy of a liquid when viewed as a population of overlapping clusters. *accepted for publication in Mol. Simul.*, (arXiv:1510.03073)

[10] Ronceray, P. and Harrowell, P. (2016a). From Liquid Structure to Configurational Entropy: Introducing Structural Covariance. *submitted to the Journal of Statistical Mechanics: Theory and Experiment*

[11] Ronceray, P. and Harrowell, P. (2016b). Suppression of crystalline order by competing liquid structures. *in preparation*

Self-assembly of proteins and colloids

The aggregation of dilute, identical particles with irregular shapes can lead to a surprising variety of morphologies. This generic problem is perhaps best illustrated by the well-known phase diagram of surfactants, which exhibits a rich variety of micellar structures in very similar systems. However, the more general question of the morphology of self-assembled aggregates of particles with attractive, directional short-range interactions remains essentially uncharted. For instance, globular proteins often tend to aggregate into one-dimensional fibers, which are involved in a number of pathologies, ranging from sickle cell anemia to neurodegenerative diseases such as Parkinson's or Alzheimer's, to type II diabetes. Recently, model systems such as patchy colloids have focused a lot of experimental efforts. From the theoretical side however, the aggregation of spherically symmetric particles already represents a challenging problem. To tackle this problem in systems of particles interacting with high specificity and directionality requires the development of new tools and techniques.

I have started studying this problem early in my PhD, as a side project also with Martin Lenz. Making use of the discrete geometries defined in favoured local structures model (Figure 5), I have introduced a new lattice model adapted to this study. Its originality lies in the selection of the geometry of irregular particles among this large yet finite pool. Preliminary results show that depending on this geometry, a wide variety of such morphologies can be obtained on annealing (Figure 8). We now aim at finding out which local quantities control the macroscopic shape of an aggregate, and in first place its dimensionality. Geometrical frustration – reflecting the specificity and geometrical incompatibility of interactions – will serve as a guide to define such local quantities.

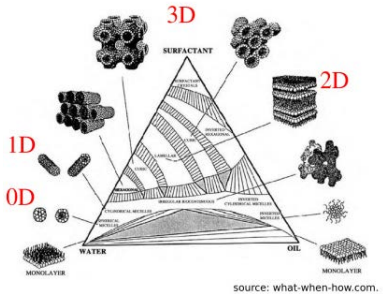

Figure 7: The phase diagram of surfactants reveals a variety of self-assembled structures of all possible dimensionalities.

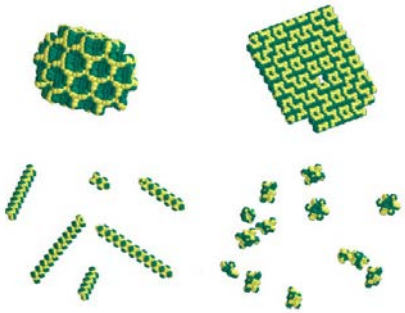

Figure 8: Low temperature dilute states of a lattice model for self-assembly with different particle geometries. What determines the dimensionality of the final aggregate?

Methods

Numerical simulations take a central place in my research, as will be apparent in this Thesis. I am proud to say that I conduct my research using only free, open-source software, which I cite here. My operating system is GNU/Linux, with a Linux Mint distribution. My text editor is GNU Emacs. I program in C++ 2014 using gcc, the GNU Scientific Library[12], and Eigen. I also extensively use Python, including the IPython[13] console, and the SciPy[14] libraries. I use Matplotlib[15] for data visualization and plotting, and Mayavi[16] for 3D imaging. I also use Inkscape[17] for figures. Movies are assembled using avconv[18]. This Thesis was written in LaTeX using the Tufte-LaTeX[19] class.

[12] M. Galassi et al, GNU Scientific Library Reference Manual (3rd Ed.), ISBN 09546120

[13] Perez, F. and Granger, B. E. (2007). IPython: A System for Interactive Scientific Computing. *Computing in Science & Engineering*, 9(3):21–29

[14] Oliphant, T. E. (2007). Python for Scientific Computing. *Computing in Science & Engineering*, 9(3):10–20

[15] Hunter, J. D. (2007). Matplotlib: A 2d graphics environment. *Comput. Sci. Eng.*, 9(3):90–95

[16] Ramachandran, P. and Varoquaux, G. (2011). Mayavi: 3d Visualization of Scientific Data. *Computing in Science Engineering*, 13(2):40–51

[17] `www.inkscape.org`

[18] `https://libav.org/`

[19] `https://tufte-latex.github.io/tufte-latex/`

1
Introduction

Muchos años después, frente al pelotón de fusilamiento, el coronel Aureliano Buendía había de recordar aquella tarde remota en que su padre lo llevó a conocer el hielo.

— Gabriel García Márquez, *Cien años de soledad*.

Living systems constantly convert biochemical energy into forces and motion. In cells, forces are largely generated internally at the nanometer scale by molecular motors acting on the cytoskeleton, a scaffold of fibrous biopolymers (Figure 1.1**a**). Forces from multiple motors are propagated along this fiber network, driving numerous processes such as mitosis, cell motility[1] and adhesion[2], and allowing the cell as a whole to exert stresses on its surroundings. At the larger scale of connective tissue, many such stress-exerting cells act on another type of fiber network known as the extracellular matrix (Figure 1.1**b**). This network propagates cellular forces to the scale of the whole tissue, powering processes such as wound healing[3] and morphogenesis. Despite important differences in molecular details and length scales, a

[1] Blanchoin, L., Boujemaa-Paterski, R., Sykes, C., and Plastino, J. (2014). Actin Dynamics, Architecture, and Mechanics in Cell Motility. *Physiol. Rev.*, 94:235–263

[2] Alberts, B., Johnson, A., Lewis, J., Raff, M., Roberts, K., and Walter, P. (2002). *Molecular Biology of the Cell*. Garland Science, 4th edition

[3] Ehrlich, H. P. (1988). Wound closure: evidence of cooperation between fibroblasts and collagen matrix. *Eye*, 2:149–157

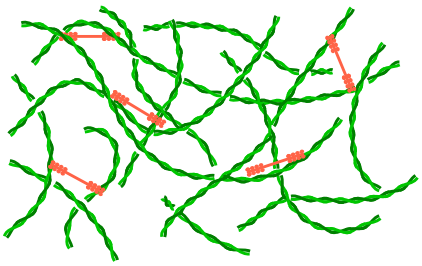

a. Actomyosin cortex

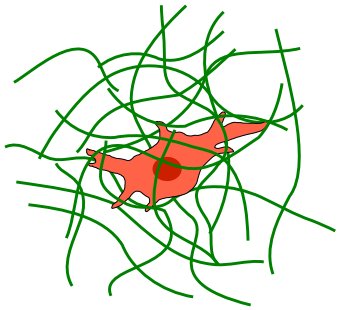

b. Contractile cell in ECM

Figure 1.1: Biological fiber networks (green) transmit forces generated by localized active units (red). **a:** Myosin molecular motors consume ATP to move processively along the polar filaments of the actin cytoskeleton, and exert forces on it. **b:** Contractile cells exert forces on the extracellular matrix. The goal of this Thesis is to investigate the generic problem of the transmission of these active forces through semiflexible fiber networks.

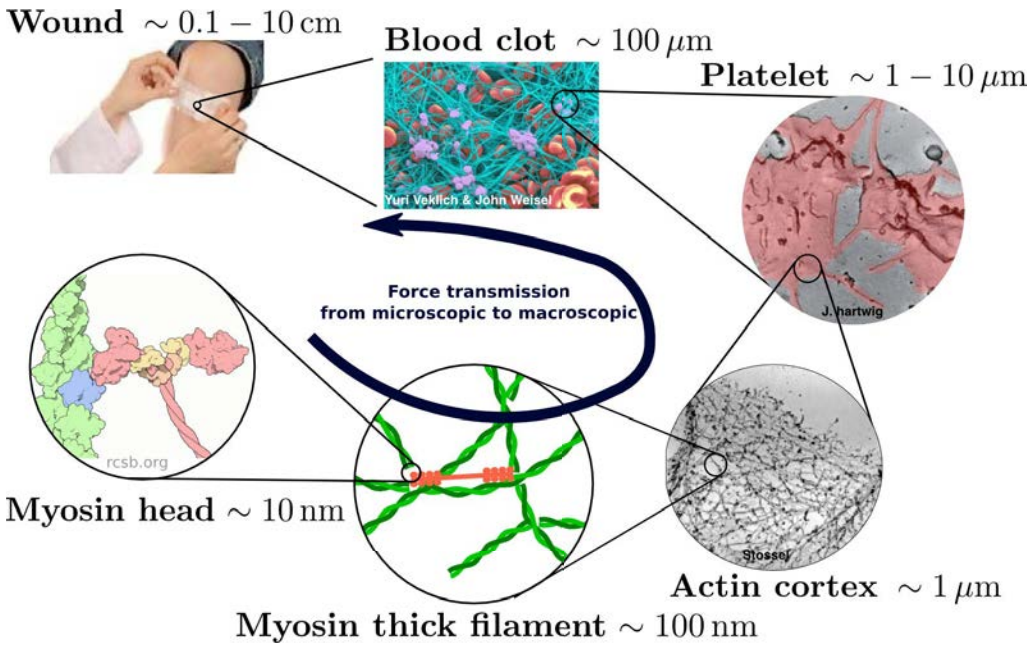

Figure 1.2: Wound healing involves transmission of forces by fiber networks at multiple scales. When skin is damaged, a blood clot forms, constituted of a matrix of fibrin polymers. This clot contracts and stiffens under the forces exerted by platelets, which helps close the wound. The contractile forces generated by platelets originate at the intracellular scale from the cytoskeleton, where myosin molecular motors exert active forces on the actin cortex. The microscopic origin of these forces are the *power strokes* that individual myosin heads exert on actin, using the energy released by the hydrolysis of a single ATP molecule to perform elementary steps along the polar actin filaments. Sources: (Lam et al., 2011; Jen and McIntire, 1982; Ehrlich, 1988), `en.wikipedia.org/wiki/wound_healing`.

common physical principle thus governs stress generation in biological matter: internal forces from multiple localized "active units"—motors or cells—are propagated by a fiber network to generate large-scale stresses (Figure 1.2). However, a theoretical framework relating microscopic internal active forces to macroscopic stresses in these networks is lacking. The aim of this Thesis is to propose such a framework:

How do elastic fiber networks transmit microscopic active forces, and what is their resulting macroscopic stress?

We investigate this question from a theoretical physics point of view. While molecular motors are traditionally regarded as the defining elements of biological force generation, we will show here that the surrounding network also plays a central role in this process. Indeed, rather than merely propagating forces like a simple elastic medium, fiber networks can produce emergent, dramatically amplified stresses, and can go so far as reversing small-scale extensile forces into large-scale contraction. The theory we develop quantitatively accounts for

experimental measurements of contraction, and suggests mechanisms for the physiological regulation of biological active stresses.

This Thesis is organized as follows. In Chapter 2, we present a theoretical model for these networks, and study their passive mechanical properties in the absence of active units in Chapter 3. Chapter 4 then presents our mathematical framework for studying force transmission. We show that in the linear, small-force regime, this problem admits an exact, simple solution that we term *dipole conservation*. Importantly however, this relationship is not applicable to most biological systems, since typical active forces are amply sufficient to probe the nonlinear properties of their constitutive fibers, which stiffen under tension and buckle under compression[4]. Indeed, recent experiments on reconstituted biopolymer gels have shown that individual active units induce widespread buckling and stiffening[5]. In Chapter 5 we show that non-linearities at the scale of the network's mesh size, such as filament buckling, result in an emergent contractility of the system, with dramatic deviations to dipole conservation. In Chapter 6, we study the role of filament buckling in large-scale force transmission, showing that it dramatically increases the range of propagation of contractile stresses. Finally, Chapter 7 deals with collective stress production by many active units. We present a comprehensive theory in the form of a scaling phase diagram, which elucidates the origins and magnitude of stress amplification observed in experiments on reconstituted tissues and actomyosin networks. We thus provide a new conceptual framework allowing for quantitative predictions for stress generation in biological fiber networks.

[4] Broedersz, C. P. and MacKintosh, F. C. (2014). Modeling semiflexible polymer networks. *Rev. Mod. Phys.*, 86:995

[5] Lam, W. A., Chaudhuri, O., Crow, A., Webster, K. D., Li, T.-D., Kita, A., Huang, J., and Fletcher, D. A. (2011). Mechanics and contraction dynamics of single platelets and implications for clot stiffening. *Nat. Mater.*, 10:61–66
Murrell, M. and Gardel, M. L. (2012). F-actin Buckling Coordinates Contractility and Severing in a Biomimetic Actomyosin Cortex. *Proc. Natl. Acad. Sci. U.S.A.*, 109(51):20820–20825

2
Modelling fiber networks

— Morris and Goscinny, *L'héritage de Rantanplan.*

In this Chapter, we present the theoretical model that we use throughout this Thesis. We start by describing in Section 2.1 the physical ingredients that we include in our model for elastic fiber networks. We give its mathematical definition in Section 2.2. In Section 2.3, we then present a (non-exhaustive) discussion of the physical effects neglected in this Thesis. In Section 2.4, we discuss the dimension of the parameters of our model, and give orders of magnitude corresponding to realistic biological situations. We conclude this Chapter by a short discussion of other possible theoretical models for biopolymer networks.

2.1 Physical ingredients

Semiflexible fibers. Semiflexible biopolymers are ubiquitous in living systems, both inside and outside cells. In contrast with most artificial polymers which form thermal coils, they tend to be quite stiff, and resist bending. When subjected to thermal fluctuations, the length below which they remain approximately straight – the *persistence length* ℓ_p – is much larger than the monomer scale; for instance, $\ell_p \approx 10\,\mu\text{m}$ in

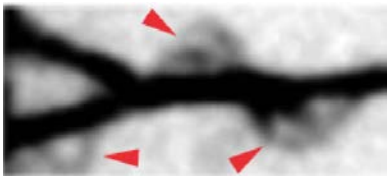

Figure 2.1: Buckling in nonsarcomeric contractile actomyosin bundles: time-lapse images of fluorescent actin (inverted contrast) show F-actin buckling (arrowheads) following the addition of 1 mM ATP. Scale bar, $5\mu m$. Source: (Lenz et al., 2012b)).

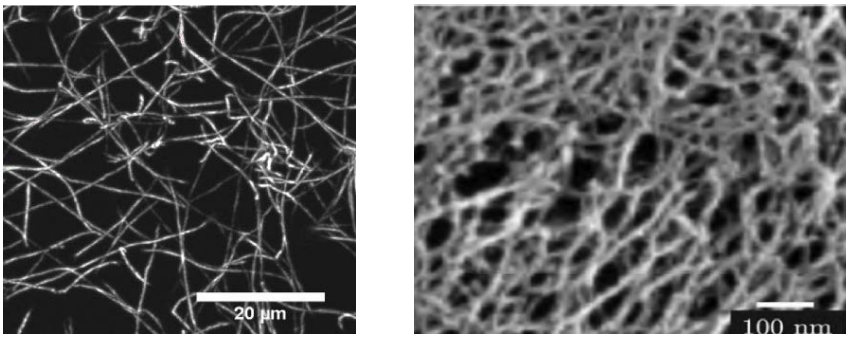

Figure 2.2: *Left:* Confocal microscopy image of a fluorescently labeled collagen network. Source: (Broedersz and MacKintosh, 2014). *Right:* Electron micrograph of a F-actin network crosslinked with filamin proteins. Source: (Kasza et al., 2009).

filamentous actin, a key component of the cell cytoskeleton. While the curvature due to thermal fluctuations remains therefore small at the cell scale, these transverse deformation modes are nonetheless important for the mechanical properties of these filaments: indeed, stretching or compressing them respectively decreases or increases this thermal curvature, as it is much easier than changing the filament's arc length. When compressed, these filaments tend to soften and eventually buckle (Figure 2.1), while stretching them *pulls out* the thermal curvature, which effectively stiffens the filaments. Because physiological filaments are generally shorter than their persistence length, it is much easier to bend them than to stretch them.

Biopolymer networks. In many physiological situations, these semi-flexible fibers form networks, as the filaments entangle, branch or are bound together by specific cross-linking proteins (Figure 2.2). These networks typically behave as soft elastic media on short enough time scales, which we consider here; at longer times they tend to remodel and flow as biological processes such as polymer turnover and cross-link detachment take place.

Active units. The mechanical forces involved in processes as diverse as intracellular transport, cell mitosis and migration, blood clot stiffening, muscular contraction and animal locomotion all have the same microscopic origin: the power strokes exerted by motor proteins. These molecular machines harness the chemical free energy released by the hydrolysis of ATP in order to perform mechanical work. In contrast with macroscopic human-made combustion engines, motor proteins convert directly chemical energy into mechanical work without the intermediate of thermal energy.

Skeletal myosin II motors, for instance, forms polymers of hundreds of heads which are responsible for muscular contraction. Each of these heads is bound about 2% of the time to another kind of cytoskeletal

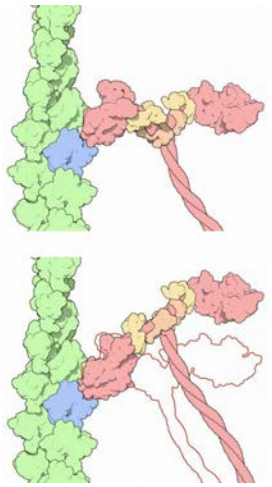

Figure 2.3: Power stroke of a myosin motor on an actin filament: pre-power stroke state (top) and rigor state (bottom). Source: `http://pdb101.rcsb.org/motm/18`.

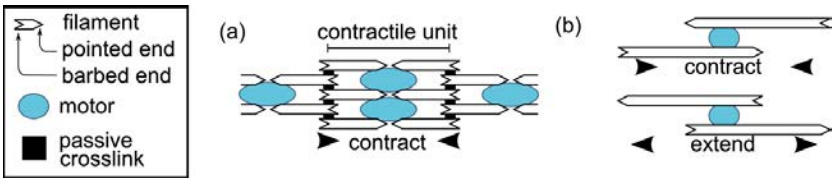

Figure 2.4: Myosin motors bound to actin filaments slide toward their "barbed ends". (a) In striated muscle, motors are localized close to the filaments' pointed ends. When activated, every motor pulls in the neighboring filaments and thus induces local contraction. (b) If filament polarities are not carefully selected, striated muscle-like locally contractile configurations (top) are just as likely as extensile ones (bottom), and the overall behavior of the actomyosin assembly is unclear. Adapted from (Lenz, 2014).

filament known as *actin*, and exerts a force of approximately 4 pN during this power stroke (Figure 2.3). Muscular actomyosin is organized in regular structures known as *sarcomeres* (Figure 2.4**a.**), which harness these forces to shorten, resulting in contraction[1]. In the cell cytoskeleton however, there is no such sarcomeric organization, and it has been argued that myosin motors have no intrinsic propensity to contract in such disordered networks[2].

In this Thesis, we will not explicitly describe the structure of such active units, but simply model them as distributions of point forces. In particular, we will not always assume that they are contractile; instead, we focus on the generic response of fiber networks to localized forces – which can model cytoskeletal motor proteins as well as contractile cells, on a much larger scale. Since these active units are physically embedded in the network, and isolated from the rest of the universe, we only consider force distribution with zero total force and torque. Note that in the literature, the term "active" generally refers to systems out of thermodynamic equilibrium. In this Thesis however, this out-of-equilibrium nature of active units is hidden in the internal parameters of the the units, and the problem we consider here of the equilibrium mechanical response of networks to localized forces is not intrinsically out-of-equilibrium.

[1] Quoting (Alberts et al., 2002), "each head cycles about five times per second in the course of a rapid contraction—sliding the myosin and actin filaments past one another at rates of up to $15\,\mu m\,s^{-1}$ and enabling the sarcomere to shorten by 10% of its length in less than 1/50th of a second. The rapid synchronized shortening of the thousands of sarcomeres lying end-to-end in each myofibril gives skeletal muscle the ability to contract rapidly enough for running and flying, and even for playing the piano."

[2] Lenz, M. (2014). Geometrical Origins of Contractility in Disordered Actomyosin Networks. *Phys. Rev. X*, 4(4):041002

2.2 The lattice fiber network model

We now introduce the model we employ throughout this Thesis. This model was originally introduced by Broedersz *et al.*[3], and consists in identical fiber segments arranged on a regular lattice. Straight fibers are connected at each lattice vertex by crosslinks that do not constrain their relative angles. Each lattice edge represents a "bond" made of two straight segments and can thus stretch, bend, or buckle, as pictured in Figure 2.5. The position of the lattice vertices, along with that of the mid-edge nodes, are the degrees of freedom of this model.

[3] Broedersz, C. P., Mao, X., Lubensky, T. C., and MacKintosh, F. C. (2011). Criticality and isostaticity in fibre networks. *Nat Phys*, 7(12):983–988

Segments behave as Hookean springs with a stretching rigidity μ and a rest length equal to one, implying a stretching energy

$$E_{\text{stretch}}(\ell) = \frac{\mu}{2}(\ell - 1)^2 \tag{2.1}$$

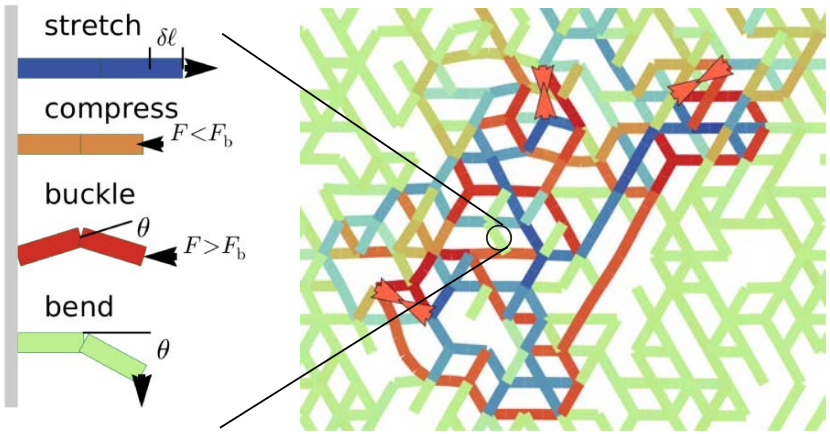

Figure 2.5: Our model for elastic fiber networks consists in identical bonds, comprising two hinged fiber segments with stretching rigidity μ and unit bending rigidity (left). These bonds are arranged on a regular lattice, which is bond depleted: each bond is present with a probability p. Here (right) we take a 2D triangular network with $p = 0.6$. We consider the mechanical equilibrium response of such networks to local active forces (red arrows), which induce deformations of the network. The color of the bonds indicate the stress: red for compression, blue for tension. Unstressed bonds are in green.

per segment of length ℓ. The fiber bending rigidity is set to unity[4] by penalizing angular deflections θ between two consecutive fiber segments through a bending energy

$$E_{\text{bend}}(\theta) = 2\sin^2\frac{\theta}{2} \tag{2.2}$$

This specific form was chosen because of its simplicity and regularity[5]; it is maximal as $\theta = \pi$ (corresponding to a fully folded filament) and its first-order term at small angles is simply $E_{\text{bend}}(\theta) \sim \theta^2/2$. Consequently, individual bonds buckle under a critical force $F_b = 1$. We consider nearly inextensible fibers by assuming $\mu \gg 1$.

Network disorder is introduced through bond depletion, *i.e.*, by randomly decimating the lattice so that two neighboring vertices are connected by a bond with probability p. This probability controls the network's connectivity, the average fiber length, and the amount of disorder. The regular lattice case simply corresponds to $p = 1$.

In this Thesis, we investigate the response to localized active forces, with an energy of the form $-\mathbf{F}_i \cdot \mathbf{R}_i$ where $\mathbf{R}_i$ is the position of vertex i of the network, as illustrated in Figure 2.6. In Chapters 4 and 5, we will consider simple force distributions in the form of two-point force dipoles, like the red arrowheads in Figure 2.5. In Chapter 6 we will introduce another, slightly more complicated model to study the large force case.

Summing the associated elastic energy with all fiber stretching and bending contributions, our total Hamiltonian reads:

$$\mathcal{H} = -\sum_{\text{forces } i} \mathbf{F}_i \cdot \mathbf{R}_i + \sum_{\text{segments } (i,j)} \mu\frac{(\ell_{ij}-1)^2}{2} + \sum_{\text{hinges } (i,j,k)} 2\sin^2\frac{\theta_{ijk}}{2} \tag{2.3}$$

where ℓ_{ij} is the length of the segment (i,j) linking vertices i and j, θ_{ijk} is the angle formed between two consecutive segments (i,j) and (j,k).

[4] In the literature – for instance in (Broedersz et al., 2011) – the convention is usually to set $\mu = 1$ and to have the bending rigidity κ as a parameter. In this Thesis, our focus on buckling makes our convention more convenient, as it implies a unit buckling force.

[5] A note on non-linearities in our Hamiltonian: the sine form for the bending energy involves non-linear terms in θ. This cannot be avoided, as any reasonable expression for this energy should be 2π-periodic in θ to remain relevant at large deformations. Besides, the degrees of freedom of the model are the coordinates of the nodes, and so even the stretching energy $\delta\ell^2/2$ is non-linear in these variables, as $\delta\ell_{ij} = \sqrt{x_{ij}^2 + y_{ij}^2} - 1$. All in all, it is impossible to design a Hamiltonian which would be linear in its degrees of freedom and physically reasonable at large deformations.

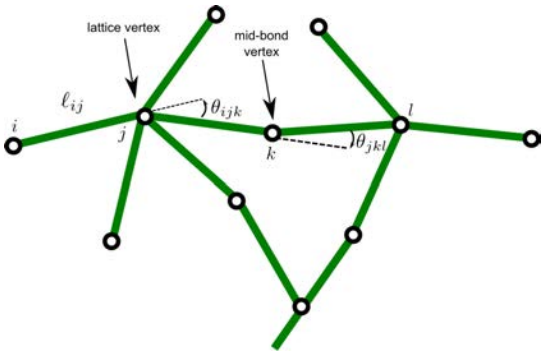

Figure 2.6: Schematic representation of the lattice model. The mid-bond vertices allow buckling of individual bonds.

In depleted networks, only segments which have not been removed contribute to these sums. We consider only the athermal equilibrium response of the system, which is obtained by numerically minimizing the total Hamiltonian. Details on the numerical implementation of this model are presented in Section 2.A.

2.3 Neglected phenomena

When modeling a physical system – and in particular a biophysical one – we need to decide which physical ingredients we decide to take in, and think about those we leave out. There is a bit of arbitrariness here, and the hope is to keep those which are truly important in the situations we're interested in (and only those). In this Thesis, our choices are motivated by simplicity: the model introduced in the previous Section aims at giving a minimalist description of semiflexible fiber networks in the elastic regime. There are therefore many phenomena we do *not* include in our description of these networks. We propose here a short list of them, which to us as the most important ones. We shall come back to this list in the last Chapter of this Thesis, and briefly question how they would modify our results if taken into account.

- *fiber stiffening*. We have seen in Section 2.1 that semiflexible fibers buckle under compression, and stiffen under tension. While we take the former effect into account, we chose not to implement the latter in our model.

- *fiber and segment length*. In our model, fiber length is not an explicit parameter of our model; it depends on the segment length and the depletion parameter. Similarly, the distance between two cross-links along a given fiber is also set by the mesh size, and cannot be much larger than the average distance between fibers. We do not consider any dispersion in the distance between cross-links either.

- *non-penetration.* Two filaments cannot cross each other in real networks. In our model, they can, as we do not implement their impenetrability and excluded volume.

- *topology changes.* Many phenomena lead to a reorganization of the network, and possibly change its topology: attachment/detachment of crosslink proteins, filament rupture or severing, turnover and polymerization/depolymerization... We do not consider any of these.

- *dynamics and viscoelastic response.* In connection with the previous point, we only consider the elastic response of the network at mechanical equilibrium: we do not describe how this equilibrium is

reached (short times), nor how the network will flow irreversibly at long time scales.

- *thermal fluctuations*. While we do not explicitly consider thermal agitation in our model, the parameters we use for the stretching and bending rigidities are effective values that take into account thermal modes of deformation of individual filaments, as discussed in Section 2.1.

- *prestress.* In our model, there is a reference, undeformed state in which all fibers are unstressed. This state may not exist, in particular when there is filament entanglement and excluded volume.

- *internal dynamics of active units.* In this Thesis, we will not give an explicit description of the active units, nor take into account their internal properties. Instead, we focus on the generic response of the network to localized forces.

2.4 Dimensions and orders of magnitude

The model we study in this Thesis is dimensionless. In this Section we discuss the give a dictionary to put back dimensions, and give an estimate of relevant values for the dimensionless parameters of the model, in the example of the cell cytoskeleton. We discuss here only mechanical properties; the structural ones – which are encoded in our model as the average connectivity z – have deep implications on the network's mechanical properties, and will be discussed in the next Chapter.

Worm-like chain model. Semiflexible cytoskeletal filaments are well described by the *worm-like chain* (WLC) model[6]. In this model, fibers are inextensible, and owe their finite stretching rigidity to thermal bending modes. They are characterized by their persistence length ℓ_p.

Considering a fiber segment of length ξ between two crosslinks, bent with uniform curvature radius R, its bending energy within the WLC model is:

$$E_{\text{bend}} = \frac{kT\ell_p\xi}{2R^2} \tag{2.4}$$

where kT is the thermal energy. Its stretching energy is:

$$E_{\text{stretch}} = \frac{90kT\ell_p^2}{\xi^4}\frac{(\delta\ell)^2}{2} \tag{2.5}$$

for an elongation of $\delta\ell$. The surprisingly large numerical factor 90 originates from the thermal integration of all bending modes of the filament.

[6] Broedersz, C. P. and MacKintosh, F. C. (2014). Modeling semiflexible polymer networks. *Rev. Mod. Phys.*, 86:995

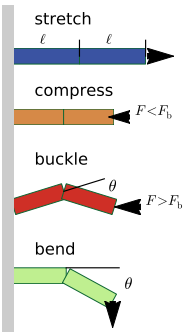

Figure 2.7: Fiber segments in our model.

Hamiltonian with dimensions. We now translate these formulas into our model parameters. The elementary constituents of our model are fiber half-segments (Figure 2.7), which are hinged Hookean springs. The stretching energy of such a half-segment, with length ℓ and rest length $\ell_0 = \xi/2$, is therefore

$$E_{\text{stretch}} = \frac{180kT\ell_p^2}{\xi^4}\frac{(\ell-\ell_0)^2}{2} = \frac{45kT\ell_p^2}{\xi^2} \times \frac{1}{2}\left(\frac{\ell}{\ell_0}-1\right)^2 \tag{2.6}$$

To each vertex and mid-edge corresponds a hinge. We can therefore assume that the curvature corresponding to the angle θ between two consecutive segments is localized in a region of length ℓ_0 around this hinge[7], and thus the curvature radius is $R = \ell_0/(2\sin(\theta/2))$. The bending energy for such a hinge is thus

$$E_{\text{bend}} = \frac{2kT\ell_p}{\xi} \times 2\sin^2\frac{\theta}{2} \tag{2.7}$$

[7] In depleted networks, there are filaments with free ends, where the curvature can thus spread on the full segment. We neglect this effect here, and thus slightly overestimate the bending energy.

We can therefore rewrite the passive part of our Hamiltonian (Equation 2.3), now including the dimensions:

$$\mathcal{H} = \frac{2kT\ell_p}{\xi}\left[\frac{45\ell_p}{2\xi}\sum_{\text{segments }(i,j)}\frac{1}{2}\left(\frac{\ell_{ij}}{\ell_0}-1\right)^2 + \sum_{\text{hinges }(i,j,k)} 2\sin^2\frac{\theta_{ijk}}{2}\right] \tag{2.8}$$

Our dimensionless model is obtained by setting the energy scale as $2kT\ell_p/\xi = 1$ and the length scale $\ell_0 = \xi/2 = 1$. The buckling force[8] for a single filament is:

$$F_b = \frac{2kT\ell_p}{\xi^2} \tag{2.9}$$

[8] A more precise calculation of the buckling force within the WLC model yields a slightly larger value, $F_b = \pi^2 kT\ell_p/\xi^2$.

The stretching-to-bending rigidity ratio of our model is thus, within the WLC model:

$$\mu = \frac{45\ell_p}{2\xi} \tag{2.10}$$

These formulas apply for cytoskeletal filaments which are well described by the WLC model.

Orders of magnitude. We now give estimate for these parameters. We have seen that cytoskeletal actin filaments have a persistence length $l_p \sim 10\,\mu\text{m}$. The mesh size ξ can vary much depending on the context; reasonable values are in the range $\xi \sim 0.1\,\mu\text{m}$ to $1\,\mu\text{m}$. We have $kT \approx 4.10^{-21}\,J$. Typical values for the buckling force are therefore $F_b \sim$0.4 pN to 40 pN, while the dimensionless stretching rigidity takes values in the range

$$\mu \sim 200 \text{ to } 2000.$$

We will use these values as a guide to throughout this Thesis, and often use $\mu = 10^3$.

Active forces. We have seen in Section 2.1 that the force a cytoskeletal myosin II motors exerts during a power stroke is about 4 pN. Myosin thick filaments can consist in several hundreds of heads, each being attached only a small fraction of the time, and can thus exert significantly larger forces. In units of the buckling force, this therefore gives a wide range of active forces:

$$F \sim 0.1 \text{ to } 10$$

Buckling of individual filaments is thus relevant in a wide range of parameters.

2.5 Variants and alternative models

The simple lattice model used here is one of many models and variants employed in the literature. As most lattice models, it has the advantage to be relatively easy to implement and study numerically. Besides, its mechanical properties have already been extensively studied, such as its linear and nonlinear elastic moduli, which we will discuss in the next sections. We mention here a few other approaches to modelling biopolymer networks, which have been reviewed in (Broedersz and MacKintosh, 2014)[9].

Variants. In the original version of our model, only the linear response of the network was investigated, and a linearized version of the Hamiltonian presented here (Equation 2.3) was used. These early versions also did not include the possibility to have single bond buckling. Since we are interested in large, nonlinear deformations of the network, we adapted the model consequently.

Phantom networks. As mentioned in Section 2.1, in our model the segment length – *i.e.*, the distance between two cross-links along a given fiber – and the typical distance between two fibers are both comparable to the lattice mesh size. This is due to the presence of cross-links at each lattice node: fibers that intersect at a lattice node are constrained to move together. A popular way to relax this constraint in such lattice models, termed *phantom networks*, is to duplicate some of the nodes, such that two fibers crossing at a lattice node can either be cross-linked and bound together, or allowed to move independently without interaction at that node. This introduces a new parameter – the probability that two intersecting fibers are cross-linked – that permits to tune fiber length and network connectivity independently. This model allowed for fruitful characterization of the deformation modes of networks in the limit of long fibers[10].

[9] Broedersz, C. P. and MacKintosh, F. C. (2014). Modeling semiflexible polymer networks. *Rev. Mod. Phys.*, 86:995

[10] Broedersz, C. P., Sheinman, M., and MacKintosh, F. C. (2012). Filament-Length-Controlled Elasticity in 3d Fiber Networks. *Phys. Rev. Lett.*, 108(7):078102

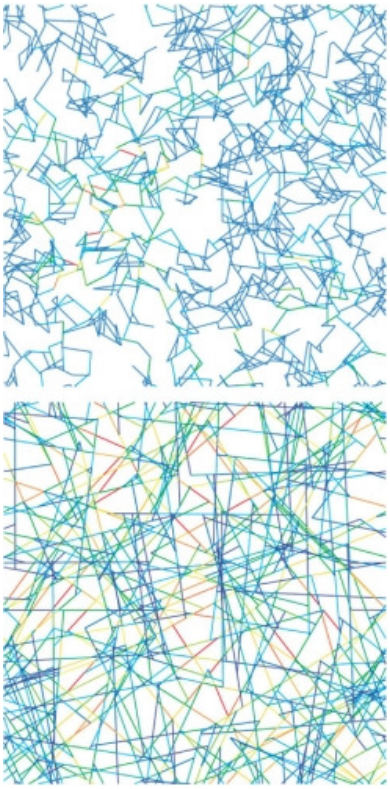

Figure 2.8: 2D Mikado networks at low and high density under a small shear. The colors indicate distribution of tensions on a filament. Source: (Broedersz and MacKintosh, 2014).

Mikado networks. The models we have discussed so far are all lattice-based, while biological fiber networks have no such underlying regularity[11]. An appealingly simple way to model two-dimensional fiber networks without the artifice of an underlying lattice, termed *mikado model*, has received a lot of attention in the literature. The idea is to "throw" fibers with monodisperse length, isotropically and uniformly, on a 2D system, and add freely hinging cross-links at all intersections (Figure 2.8). The positions of these cross-links are the degrees of freedom of the model, and the Hamiltonian contains stretching and bending contributions as in our lattice model. The main flaws of this elegant model are the difficulty to extend it to three dimensions, and the presence of very short fiber segments (when two interactions are close) which are thus very rigid, and impede the numerical convergence of energy minimization schemes. In contrast, in lattice models the lattice mesh size provides a cut-off length at small scales, which regularizes the energy.

As we will see, most results presented in this Thesis are remarkably robust, and we do not expect that they would be strongly affected by such changes of model (provided that fiber buckling, a key ingredient for our results, is permitted). However, a few subtle phenomena presented here appear to be sensitive to the precise properties of the network, and could be affected by such a change of model, as we will discuss in the last Chapter.

[11] With the exception of spectrin networks, which can form beautiful triangular patterns in the cytoskeleton of red blood cells.

2.A Numerical Implementation of the Model

In this Appendix, we discuss the methods employed to simulate numerically our model. Figure 2.9 presents our simulation scheme, which consists in a large, object-oriented program written in C++. This program takes as input an `instruction` file (see Sample File 2.1), which is a script written in a custom mini-language. This file points towards a `lattice` file which contains the geometrical information about the lattice (see Sample File 2.2). The program contains a parser that translates these instructions into a list of commands, and creates an instance of the `System` class which encodes the whole physical properties of the system. The outer layer of the program then controls this system and performs measurements on it. It finally outputs data files which can then be analyzed externally using Python scripts.

2.A.1 Lattice

The system we simulate is contained in a box of dimensions `height` $\times$ `width` $\times$ `depth` in lattice coordinates. Our numerical implementation is always three-dimensional, with the third degree of freedom frozen when considering 2D systems. At each triplet of integer coordinates (i, j, k) lies a unit cell, which can consist in several vertices.

The geometry of the lattice is encoded in the lattice file (as in Sample File 2.2) as:

- Its space dimension d.
- A matrix $\mathcal{P}$ encoding the change of basis between lattice coordinates and cartesian coordinates. A site at lattice coordinates $\mathbf{R}$ will be associated to cartesian coordinates $\vec{r} = \mathcal{P}\mathbf{R}$ in the undeformed state of the lattice. This matrix is such that the length of all undeformed edges is 1.

  For the triangular lattice,

$$\mathcal{P} = \begin{pmatrix} 1 & 1/2 & 0 \\ 0 & \sqrt{3}/2 & 0 \\ 0 & 0 & 1 \end{pmatrix}$$

- Its number of vertices in a unit cell, and their relative positions. For Bravais lattice, there's only one vertex, but we will also consider more complex network. An example we shall use in this Thesis is presented in Sample File 2.3.
- A list $\mathcal{V}$ of neighbouring links between sites, both inside the unit cell and between a cell and its neighbours.

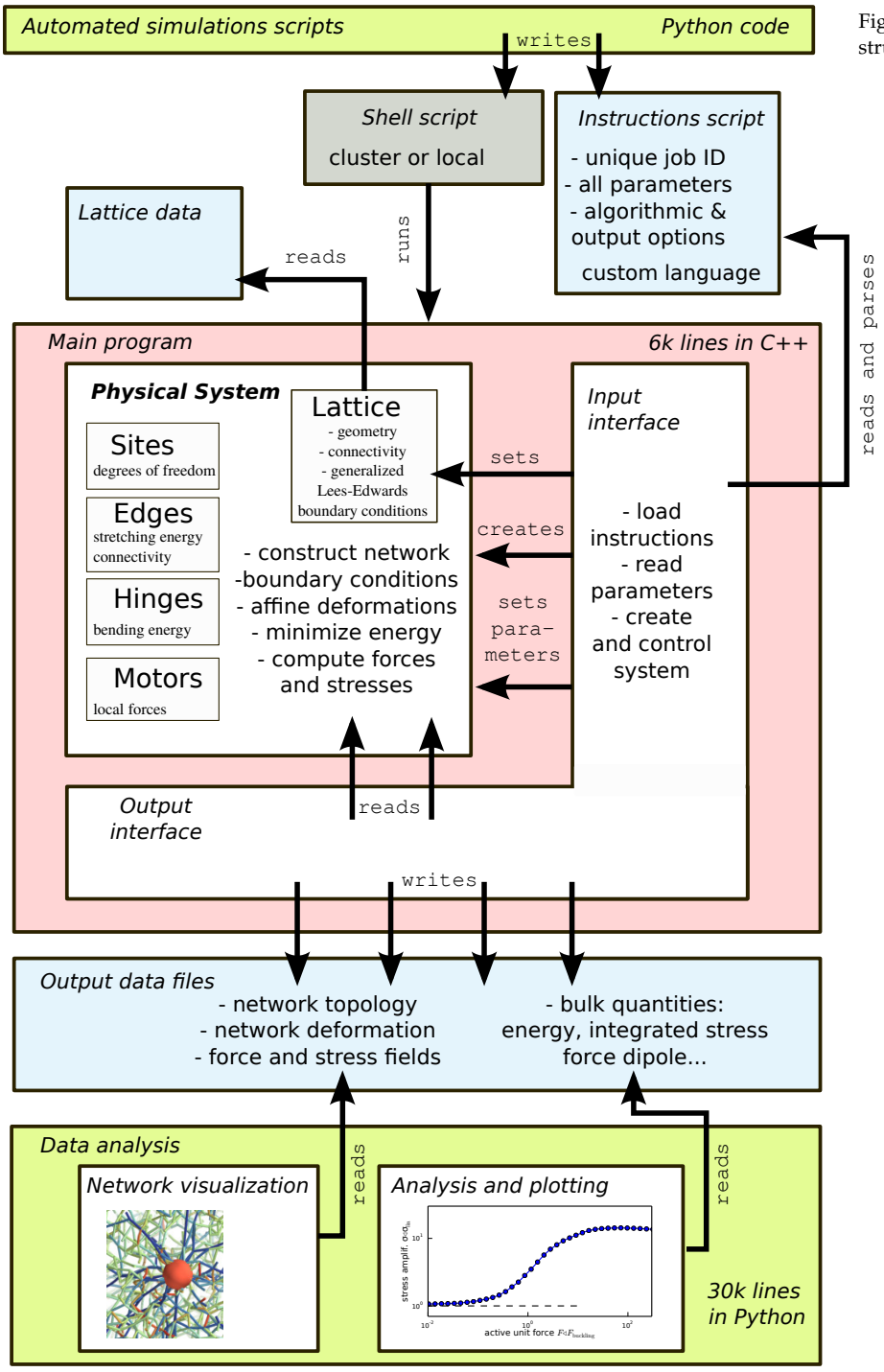

Figure 2.9: Schematic of the program structure.

```
PROGRAM v4.2 - Elastic moduli - Poisson ratio run #

DIR=   ../RESULTS/
REPEAT= 1

INSTRUCTIONS=

CREATE
           LATTICE= FCC
           SHAPE= 30 30 30
           BOUNDARY_CONDITIONS= PERIODIC
           PERCOLATION_p= 0.3
           LAMBDA= 1.
       SPRING_CONSTANT_mu= 100000.0
       SPRING_CONSTANT_sigma= 0.
       FORCE_EXTENSION_RELATION= Hooke
       MID_EDGE_NODE= yes
       kappa= 1.
           CIRCULAR_DOMAIN= no
&

SaveNetworkFile &

RUN
    gamma= 1e-100  PureDilation
    Fs= 0.
    FrozenRadius  no
    CG ALGO= BFGS Maxiter= 2000000 GradientTol= 0. LineTol= 0.1 InitialStep= 0.1
    RecordConfig= no
    RecordForces= no
    ResetPositionsAfter= yes
    &

RUN
    gamma= 1e-100  SimpleShear
    Fs= 0.
    FrozenRadius  no
    CG ALGO= BFGS Maxiter= 2000000 GradientTol= 0. LineTol= 0.1 InitialStep= 0.1
    RecordConfig= no
    RecordForces= no
    ResetPositionsAfter= yes
    &
```

Listing 2.1: Sample `instruction` file used to compute the Poisson ratio of a depleted FCC network (Figure 3.11). It consists in the following sequence of instructions: CREATE the system with given arguments, SAVE it, then RUN energy minimization under dilation and shear.

```
  2D triangular network - lattice file for ActinNetworks-v4.2

Space dimension : #
2

Projection matrix to cartesian coordinates : #
1. 0.5 0.
0. 0.8660254037844386 0.
0. 0. 1.

Number of sites ("atoms") per unit cell : #
1

Relative positions of the atoms inside the cell with respect to the cell origin : #
0. 0. 0.

Number of edge vectors : #
3

Connections between the sites :
lattice coordinates of target cell    -     atom index of 1st site (in *this cell)     -   atom
     index of 2nd site (in target cell)  #
1  0 0          0   0
0 -1 0          0   0
1 -1 0          0   0

That's it ! Hinges are added automatically by detecting alignments. #
```

Listing 2.2: Sample `lattice` file: two-dimensional triangular network.

```
2D regular bending-dominated network lattice file for ActinNetworks-v4.2
''Martin's Amazing Network''

Space dimension : #
2

Projection matrix to cartesian coordinates : #
3.0 3.0 0
-1.73205080757 1.73205080757 0
0.0 0.0 1.0

Number of sites ("atoms") per unit cell : #
6

Relative positions of the atoms inside the cell with respect to the cell origin : #
0.0 0.0 0
1.0 0.0 0
2.0 0.0 0
3.0 0.0 0
0.5 -0.866025403784 0
2.5 -0.866025403784 0

Number of edge vectors in cell: #
9

Connections between the sites: Format:
lattice coordinates of target cell    -     atom index of 1st site (in *this cell)     -   atom
    index of 2nd site (in target cell)  #
0 0 0   0 1
0 0 0   1 2
0 0 0   2 3
0 0 0   5 3
0 1 0   3 4
0 0 0   4 1
0 0 0   2 5
1 0 0   5 0
0 0 0   0 4

That's it ! Hinges are added automatically by detecting alignments. #
```

Listing 2.3: Sample `lattice` file: the MAN network (Figure 3.34), a lattice with several vertices per unit cell.

2.A.2 Geometry and boundary conditions

We consider two types of boundary conditions in this Thesis: periodic and fixed. As usual in numerical physics, we employ periodic boundary conditions when considering the macroscopic properties of a system, as in Chapter 3 and Chapter 7. Indeed, this choice of boundary conditions is the closest approximation of an infinite system. In contrast, when considering the effects of a single active unit, as in Chapter 5 and Chapter 6, we choose to employ *fixed* boundary conditions, where the network's vertices are held fixed to zero displacement at a given distance R of the active unit. Indeed, periodic boundary conditions would in this case lead to inconvenient self-interaction of the unit with its periodic copies.

Fixed boundary conditions are straightforward. As for periodic ones, we employ a trick to simplify our program. To each edge (A, B) we attach the associated vector $\mathbf{R}_{(A,B)} \in \mathcal{V}$ (making no difference between edges going through the boundaries and in the bulk). The cartesian end-to-end vector of the edge is then $\vec{r}_{(A,B)} = \mathcal{P}\mathbf{R}_{(A,B)}$. As all physical quantities depend only on $\vec{r}_{(A,B)}$, it is not necessary in the following to distinguish between the boundaries and the bulk.

Affine deformations. In Chapter 3, we consider the elastic moduli of our networks. In order measure them, we apply a uniform strain to the network, and measure the response. We use generalized Lees-Edwards boundary conditions to implement such a strain with periodic boundary conditions. This strain is characterized by the displacement gradient tensor $\mathbf{T}$, such that the action of the deformation is :

$$\vec{r} \mapsto \vec{r} + \mathbf{T}\vec{r} \tag{2.11}$$

The most simple forms for the displacement gradient tensor $\mathbf{T}$ are :

- Simple shear : $\mathbf{T} = \begin{pmatrix} 0 & \gamma & 0 \\ 0 & 0 & 0 \\ 0 & 0 & 0 \end{pmatrix}$
- Pure dilation : $\mathbf{T} = \begin{pmatrix} \epsilon & 0 & 0 \\ 0 & \epsilon & 0 \\ 0 & 0 & \epsilon \end{pmatrix}$

Under such a bulk deformation, both the orientation and the length of the edges will change : the edge vector will be written $\vec{u} = \vec{r} + \vec{v}$, where $\vec{r}$ is the reference vector and $\vec{v}$ is the *displacement vector*. We distinguish between affine and non-affine components of the displacement vector, respectively $\vec{v}^{(\text{aff})}$ and $\vec{v}^{(\text{nonaff})}$.

The affine displacement of a site A is denoted as

$$\vec{v}_A^{(\text{aff})} = \mathbf{T}\vec{r}_A$$

and it's the same for the deformation of an edge (A, B) :

$$\vec{v}^{(\mathrm{aff})}_{(A,B)} = \mathbf{T}\vec{r}_{(A,B)}$$

This displacement is a fixed quantity depending only on the reference vector $\vec{r}$ and on the displacement gradient tensor. There again there is nothing special with the boundaries – the boundary conditions are fully contained in the computation of $\vec{r}_{(A,B)}$ at the initialization of the system. Lees-Edwards boundary conditions, which correspond to the case of simple shear, are implemented automatically with this method.

Non-affine response Each `Site` of the system is assigned a non-affine displacement vector $\vec{v}^{(\mathrm{nonaff})}_A$ which corresponds to the *degrees of freedom of the system*. In the equilibrium position (at zero temperature) these variables minimize the total energy of the system.

Eventually the Cartesian coordinates of the site in the deformed state are given by the vector $\vec{u_A} = \vec{r}_A + \vec{v}^{(\mathrm{aff})}_A + \vec{v}^{(\mathrm{nonaff})}_A$, and similarly the vector representing the real-space embedding of an edge is given by :

$$\vec{u}_{(A,B)} = \vec{r}_{(A,B)} + \vec{v}^{(\mathrm{aff})}_{(A,B)} + \underbrace{\vec{v}^{(\mathrm{nonaff})}_B - \vec{v}^{(\mathrm{nonaff})}_A}_{\text{degrees of freedom}} \tag{2.12}$$

2.A.3 Energetics

In this Section we present the formulas we use in our implementation of the model.

Stretching energy The deformation of the edges of the network leads to an increase of the free energy of the system. The length of an undeformed edge is $\ell_0 = 1$ (which sets the length scale). The stretching of an edge to a length ℓ costs an energy :

$$E_s = \frac{\mu}{2}(\ell - 1)^2 \tag{2.13}$$

Let $\vec{u}$ be the end-to-end vector associated to the edge in the *deformed* state. Then :

$$E_s = \frac{\mu}{2}(|\vec{u}| - 1)^2 \tag{2.14}$$

And we deduce easily the gradient with respect to the deformation:

$$\frac{\partial E_s}{\partial u^\mu} = \mu u^\mu \left(1 - \frac{1}{|\vec{u}|}\right) \tag{2.15}$$

Bending energy Any sequence of two consecutives edges constitute a `Hinge`. In order to model the stiffness of the fibres, we associate a

bending energy to each such bend. Let θ be the angle between these two edges. The associated bending energy is chosen to be :

$$E_b = 2\sin^2\frac{\theta}{2} \tag{2.16}$$

Let $\vec{u_1}, \vec{u_2}$ be the end-to-end vectors for the two consecutive edges. Then a computationally tractable form for E_b is:

$$E_b = \left(1 - \frac{\vec{u_1}.\vec{u_2}}{|\vec{u_1}||\vec{u_2}|}\right) \tag{2.17}$$

Its gradient is :

$$\frac{\partial E_b}{\partial u_1^\mu} = \frac{1}{|\vec{u_1}|^3|\vec{u_2}|}\left((\vec{u_1}.\vec{u_2})u_1^\mu - |\vec{u_1}|^2 u_2^\mu\right) \tag{2.18}$$

2.A.4 Numerically precise formulas

Equations 2.14-2.18 are exact, but prone to generate large numerical errors due to compensating terms of order one. Indeed, when writing $\vec{u} = \vec{r} + \vec{v}$, the reference vector has norm $|\vec{r}| = 1$ while in the small displacement limit $|\vec{v}| \ll 1$. In this section we derive equivalent forms for these formulas that are less elegant, but avoid this problem.

In the case of the stretching energy :

$$E_s = \frac{\mu}{2}\left(\frac{\vec{v}.(2\vec{r}+\vec{v})}{|\vec{u}|+1}\right)^2 \tag{2.19}$$

$$\frac{\partial E_s}{\partial u^\mu} = \mu\frac{u^\mu}{|\vec{u}|}\left(\frac{\vec{v}.(2\vec{r}+\vec{v})}{|\vec{u}|+1}\right) \tag{2.20}$$

The solution is more painful in the case of the bending energy. At the end of the day we find :

$$E_b = \frac{1}{|\vec{u_1}|\ |\vec{u_2}|}\ \frac{|(\vec{v}_1-\vec{v}_2)\times\vec{r}+\vec{v}_1\times\vec{v}_2|^2}{\vec{u_1}\cdot\vec{u_2}+|\vec{u_1}|\ |\vec{u_2}|} \tag{2.21}$$

And :

$$\frac{\partial E_b}{\partial u_1^\mu} = \frac{1}{|\vec{u_1}|\ |\vec{u_2}|}\left[\frac{r^\mu(\vec{v}_2-\vec{v}_1)\cdot\vec{u_1}+v_1^\mu(\vec{u_1}.\vec{u_2})}{\vec{u_1}^2} - v_2^\mu\right] \tag{2.22}$$

Using these formulas, we can study the linear response of the system by using arbitrarily small deformations. In all the linear response part we take 10^{-100} as a typical value for the strain.

2.A.5 Numerical minimization of the energy

We consider in this Thesis only the mechanical equilibrium response, in which the total energy is minimal. The numerical resolution of this

problem is done using the GNU Scientific Library (GSL) implementation of the Broyden-Fletcher-Goldfarb-Shanno (BFGS) algorithm.

When performing such a minimization, the program spends most of its time implementing Equations 2.19 to 2.22. More precisely, on a typical run it spends:

- 35% of the run time computing the gradient of the bending energy (Equation 2.22);
- 20% of the run time computing the bending energy itself (Equation 2.21);
- 16% of the run time computing the gradient of the stretching energy (Equation 2.20);
- 12% of the run time computing the gradient of the bending energy (Equation 2.19).

Most of our optimization work was done on these four formulas, which still represent 83% of the run time. This bottleneck effect makes our implementation near optimal. The remaining 17% are essentially distributed between the active unit forces, copying values to interface between the GSL and our classes, and in internal operation within the BFGS minimizer.

3
The mechanics of elastic fiber networks

La Nature est un temple où de vivants piliers
Laissent parfois sortir de confuses paroles;
L'homme y passe à travers des forêts de symboles
Qui l'observent avec des regards familiers.

— Charles Baudelaire, *Correspondances*.

In this Chapter, we present a theoretical discussion of the passive mechanical properties of elastic fiber networks, in the absence of active units exerting forces. This subject has been abundantly discussed in the literature in the past decades[1], and here we review the main physical features that will be useful in our discussion of the active contraction of fiber networks.

In Section 3.1, we start by discussing the elastic properties of spring networks, and show that they undergo a *rigidity percolation* transition when depleted. We then turn to the more complex case of lattice fiber networks. We show in Section 3.2 that they are characterized by *two* rigidity transitions, delimiting three elastic regimes: floppy, bending-dominated and stretching dominated. Section 3.3.3 then presents a short discussion of the linear and non-linear elastic properties of these networks. Finally, in Section 3.4 we discuss the biological relevance of these results. As an Appendix to this Chapter, we present in Section 3.A our study to design custom bending-dominated regular lattices.

[1] Broedersz, C. P. and MacKintosh, F. C. (2014). Modeling semiflexible polymer networks. *Rev. Mod. Phys.*, 86:995

3.1 The rigidity of spring networks

Before studying the elastic properties of fiber networks, it is instructive to start with the simpler case of networks of Hookean springs, in the absence of bending rigidity.

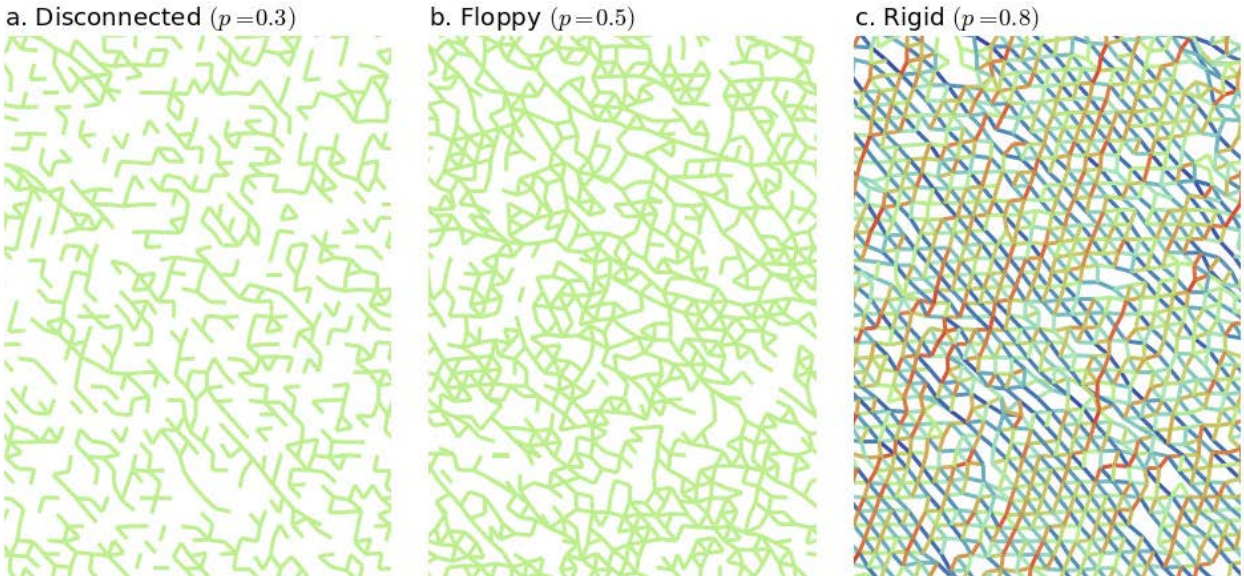

Figure 3.1: The response of a spring network to a shear $\gamma = 0.3$ depends on its connectivity. A disconnected (a) or floppy (b) network can be sheared at zero energy cost (the energy density of these configurations is $\sim 10^{-16}$ for a strain of order one). In contrast, a rigid, highly connected network (c) under the same shear is stressed. The color of the bonds indicate the stress: red for compression, blue for tension. Unstressed bonds are in green.

3.1.1 Rigidity percolation

Here we consider depleted lattices, starting with a regular triangular lattice of Hookean springs with unit spring constant, and severing bonds independently with probability $1 - p$. The physics of such spring networks has been extensively considered in the literature, as they provide a minimal model for studying the influence of connectivity on the network's rigidity.

In Figure 3.2, we plot the bulk modulus of such a depleted network as a function of the depletion parameter p. Starting from a finite value at $p = 1$, the modulus steadily decreases and the network becomes softer and softer as it is depleted. At a given value $p_c \approx 0.65$, the linear elastic moduli of the network vanish exactly, and below this threshold the network is *floppy*. We note that this *rigidity percolation point* occurs at a much higher value than the usual connectivity percolation point[2] $p_p = 2\sin(\pi/18) \approx 0.347$, where the network becomes disconnected.

Indeed, connectedness is not sufficient to ensure mechanical rigidity: for instance, two springs hinged together can rotate freely, and do not transmit any force. Only sufficiently connected regions of the network are rigid, and the emergence of a macroscopic non-zero modulus occurs when these regions percolate[3]. This rigidity percolation transition is continuous, with non-trivial exponents for the elastic moduli around the critical point, and has focused a lot of attention in the literature.

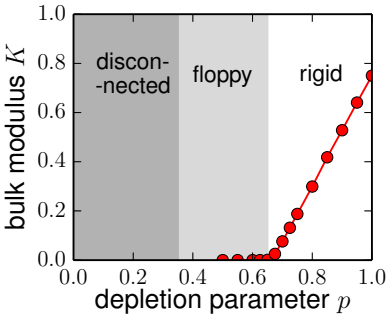

Figure 3.2: The linear bulk modulus of a depleted triangular spring network as a function of the depletion parameter. In the gray areas, the modulus vanishes up to the numerical precision ($K < 10^{-14}$). Parameters: system size 100^2 with periodic boundary conditions, under an infinitesimal isotropic bulk strain $\gamma = 10^{-100}$.

[2] Sykes, M. F. and Essam, J. W. (1964). Exact Critical Percolation Probabilities for Site and Bond Problems in Two Dimensions. *Journal of Mathematical Physics*, 5(8):1117–1127

[3] Feng, S., Thorpe, M. F., and Garboczi, E. (1985). Effective-medium theory of percolation on central-force elastic networks. *Phys. Rev. B*, 31(1):276–280

For a three-dimensional face-centered cubic network, a similar phenomenology is observed (Figure 3.3), with a central-force critical point $p_c \approx 0.49$, again well above the connectivity percolation point $p_p \approx 0.12$.

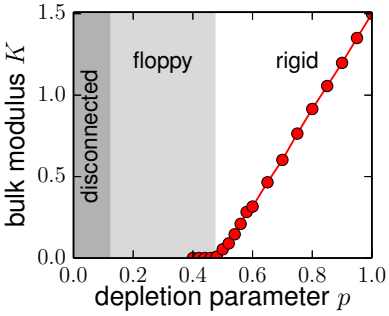

Figure 3.3: The linear bulk modulus of a depleted FCC spring network as a function of the depletion parameter. Parameters: system size 20^3 with periodic boundary conditions.

3.1.2 Maxwell's constraint counting argument.

A simple argument can provide a good intuition on the nature of rigidity percolation. The question of the rigidity of structures was pioneered by Maxwell[4] in 1864, where he considered a d-dimensional[5] object made of an ensemble of N vertices connected by E rigid edges. He noticed that the edges each provide a mechanical equation which determine their internal state of stress, while the position of each vertex provides d degrees of freedom. There are $d(d+1)/2$ bulk translational and rotational degrees of freedom, and therefore $Nd - d(d+1)/2$ internal degrees of freedom in the system that characterize its mechanical state. The numbers of equations constraining the system therefore equates the number degrees of freedom when:

$$E = Nd - \frac{d(d+1)}{2} \tag{3.1}$$

In such a case, the system is said to be *isostatic*: the constraints exactly compensate the degrees of freedom, and thus the tensions in the edges are uniquely determined by the positions of the vertices, and conversely. For $E < Nd - d(d+1)/2$, the system is floppy and mechanically unstable, or *hypostatic*: the edges do not constrain it enough to set the positions of the vertices, and it can deform at no energy cost: there are *soft modes* (or *zero modes*) of deformations. On the other hand, for $E > Nd - d(d+1)/2$, the system is overconstrained, or *hyperstatic*, and the forces through the edges are not fully determined by the deformation of the system: there are *states of self-stress*. These cases are illustrated in Figure 3.4.

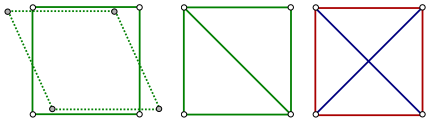

Figure 3.4: Mechanical stability of a system of $N = 4$ vertices in two dimensions. There are two bulk translational and one bulk rotational degrees of freedom, and thus 5 remaining internal parameters. Left: with $E = 4$ edges, the system is underconstrained, and can be deformed at zero cost. Center: with $E = 5$, the system is isostatic, and mechanically stable. Right: with $E = 6$, there exists a state of self-stress, in which edges are stressed while the system is not deformed: for instance, the blue edges can be tensed, and the red edges compressed.

We can apply constraint counting to depleted spring networks. Consider a macroscopic network of N vertices connected by $E = zN/2$ springs, where z is the average connectivity of the network. The isostatic connectivity is:

$$z_c = 2d \tag{3.2}$$

where we consider $N \gg 1$, making bulk rotations and translations negligible. For $z > z_c$, the system is therefore hyperstatic, while $z < z_c$ leads to hypostatic networks. Since the connectivity in our depleted networks is $z = pz_{\text{lattice}}$, this translates into an isostatic depletion parameter:

$$p_c = \frac{2d}{z_{\text{lattice}}} \tag{3.3}$$

This threshold is also called the *central-force critical point*. For a two-dimensional triangular network, $z_{\text{lattice}} = 6$, and hence this argument

[4] Maxwell, J. C. (1864). On the calculation of the equilibrium and stiffness of frames. *Philosophical Magazine Series 4*, 27(182):294–299

[5] In Maxwell's original article, $d = 3$; here it is convenient to consider the general case.

predicts $p_c = 2/3$, in excellent agreement with numerical data shown in Figure 3.2, where we find $p_c \approx 0.651$. Similarly, for a three-dimensional face-centered cubic lattice, $z_{\text{lattice}} = 12$ and constraint counting thus predicts $p_c = 1/2$, again in good agreement with the numerical value $p_c \approx 0.473$ as in Figure 3.3.

3.1.3 Soft modes and states of self-stress

This simple constraints counting argument was later shown to be incomplete[6]. Indeed, states of self-stress and soft modes can coexist in such systems, as the constraints can be distributed heterogeneously, as in Figure 3.5. Denoting by N_0 the number of internal soft modes, and N_{ss} the number of states of self-stress, we have the exact relation at linear order:

$$N_0 - N_{ss} = Nd - E - \frac{d(d+1)}{2} \tag{3.4}$$

This result can be expressed in terms of an *index theorem* for the dynamical matrix of the system, which connects forces to displacements. The topological properties of soft modes and states of self-stress have focused a lot of attention in the past years, with notable analogies between mechanical systems and topological insulators[7]. However, in a reasonably homogeneous structure, Maxwell's argument already gives a good idea of whether a system will be mechanically stable or not, and we will neglect the heterogeneities leading to compensating soft modes and states of self-stress.

The connectivity of a spring network thus has a dramatic influence on its elastic properties. Indeed, in a hyperstatic material – where there are no soft modes[8] – the response to a bulk strain is energetically costly. In contrast, in hypostatic networks, the existence of extended soft modes allows for the system to adapt to a deformation of its boundaries at zero energetic cost: hypostatic spring networks are *floppy*, with vanishing linear elastic moduli.

3.2 Rigidity transitions in fiber networks

We now move to the study of the elastic properties of our model elastic fiber networks, and first consider their mechanical rigidity. These networks are more complex than spring networks, as their constituents are characterized by two distinct types of rigidities: stretching and bending.

Stretching constraints between two connected vertices are simple central-force constraints, equivalent to stiff Hookean springs. In contrast, bending constraints are much softer three-body, angular interactions, and can stabilize the network when stretching constraints are

[6] Calladine, C. R. (1978). Buckminster Fuller's "Tensegrity" structures and Clerk Maxwell's rules for the construction of stiff frames. *International Journal of Solids and Structures*, 14(2):161–172

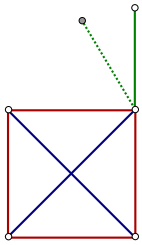

Figure 3.5: A system with $N = 5$ points connected by $E = 7$ edges. Constraint counting (Equation 3.1) predicts that it should be isostatic. However, it actually has a soft mode (the top dangling edge) and a state of self-stress as in Figure 3.4.

[7] Kane, C. L. and Lubensky, T. C. (2014). Topological boundary modes in isostatic lattices. *Nat Phys*, 10(1):39–45

[8] There can be soft modes in disordered hyperstatic networks as an effect of randomness, but they are localized, and have little effect on the macroscopic response.

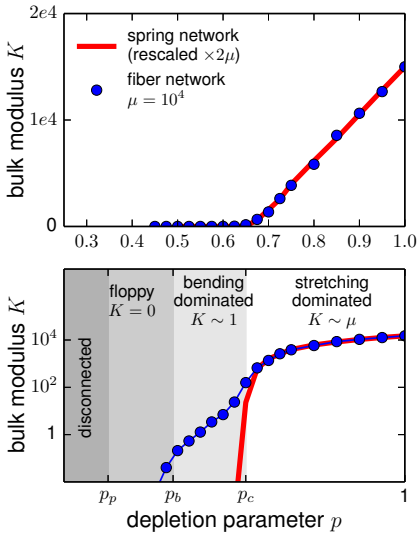

Figure 3.6: The linear bulk modulus of our model fiber network on a depleted triangular lattice, as a function of the depletion parameter. Top: in linear scale, and bottom: in semi-log scale. The red line shows the rescaled modulus of a depleted spring network, as in Figure 3.2. Parameters: $\mu = 10^4$, system size 200^2 with periodic boundary conditions under an infinitesimal dilation.

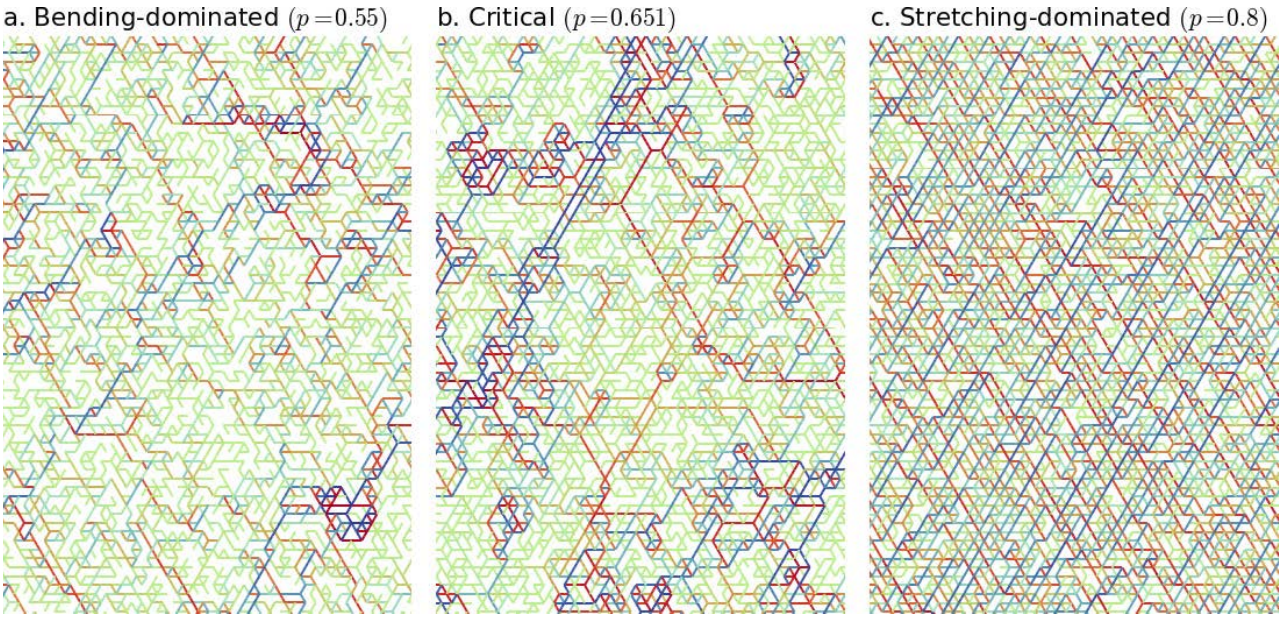

Figure 3.7: Linear response of depleted fiber networks to an infinitesimal shear. **a.** a bending-dominated network ($p = 0.55$), **b.** at the central-force critical point, and **c.** a stretching-dominated network ($p = 0.8$). Parameters: system size 150×150 with periodic boundary conditions, $\mu = 10^4$, strain $\gamma = 10^{-100}$. The color of the bonds indicate the stress: red for compression, blue for tension, unstressed bonds are in green. The stress color scale is magnified $\times 10$ in the panel **b.** and $\times 1000$ in panel **a.**, compared to **c.**

not sufficient to ensure mechanical rigidity. Figure 3.6 shows the linear bulk elastic modulus of a depleted triangular fiber network. In comparison with spring networks (red line), an intermediate, softer regime appears, in which the elasticity is *bending-dominated*. In this Section, we discuss each of the elastic regimes, then adapt to fiber networks the constraint-counting arguments developed for spring networks.

3.2.1 Stretching-dominated regime

The stretching constraints in our model form a network of central-force springs which is identical (to a scale factor) to the depleted spring networks studied in Section 3.1. Because these constraints are orders of magnitude stiffer than bending constraints, as discussed in Section 2.4, for $p > p_c$ the latter are negligible, and the system is therefore indistinguishable from a depleted spring network, as evident in the top panel of Figure 3.6. In densely connected fiber networks, the stretching properties of the filaments thus prevail in the linear elastic response, and the elastic moduli are proportional to the stretching rigidity μ of the fibers (red squares in Figure 3.8). We qualify such networks as *stretching-dominated*. The linear response of depleted, stretching-dominated networks to a bulk strain is quite homogeneous,

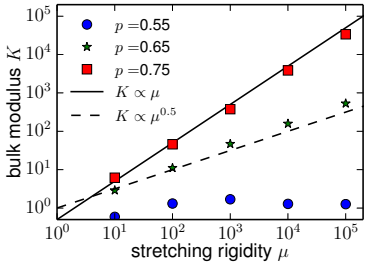

Figure 3.8: The bulk modulus of fiber networks on a 2D triangular network as a function of the stretching rigidity, below, at and above the central-force rigidity threshold. At $p = p_c$ the modulus exhibits a mixed regime $K \sim \mu^x$, with $\mu \approx 0.5$ (dashed line).

as illustrated in Figure 3.7**c**.

3.2.2 Bending-dominated regime

For $p < p_c$, stretching constraints are not sufficient to ensure the network's mechanical rigidity. While a spring network with only central force constraints would then be floppy, in fiber network the bending constraints, however weak, can help stabilize the network and maintain a finite modulus. This is apparent in the lower panel of Figure 3.6, where we observe an intermediate regime: for $p_b < p < p_c$, the network has a small yet finite elastic modulus. We qualify such intermediate systems, where stretching constraints alone are not sufficient to induce a macroscopic rigidity, as *bending-dominated*. In contrast with stretching-dominated networks, the linear response of such depleted, bending-dominated networks to a bulk strain is heterogeneous, with pronounced stress lines between large unstressed regions, as illustrated in Figure 3.7**a**.

Further depletion of the network leads to a rarefaction of bending constraints too, and below some lower value p_b – the *bending rigidity threshold* – these constraints are too sparse to ensure rigidity of the network, which then becomes floppy.

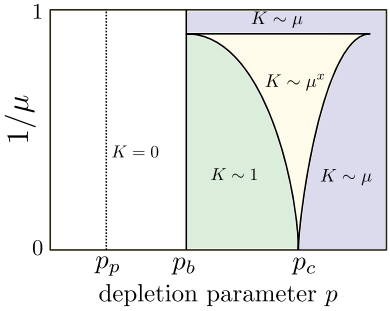

Figure 3.9: Schematic scaling diagram for the linear elastic modulus, as discussed in the text. We show the stretching-dominated regime (blue), the bending-dominated regime (green) and the intermediate, mixed regime around p_c (yellow). Floppy networks have vanishing modulus (white). For better legibility, the y-axis is the inverse of the stretching rigidity μ.

3.2.3 Critical regimes

In spring networks without bending constraints, the central-force percolation threshold is a critical point, analog to a second-order phase transition: the elastic moduli vanish continuously, with non-trivial critical exponents and diverging correlation lengths, such as the characteristic size of soft modes. In fiber networks, due to the bending rigidity, this critical point is avoided, and depleting the system leads to a smooth crossover between stretching- and bending-dominated regimes. However, for large μ and near p_c, bending constraints are weak and the system is close to a critical point. This affects the bulk modulus, and results in a mixed regime $K \sim \mu^x$, resulting from the non-trivial interplay of bending and stretching[9], as shown in Figure 3.8. This critical region is narrow at large μ, and becomes wider when μ is close to the bending rigidity, as schematized in Figure 3.9. This behaviour is very similar to that of an Ising ferromagnet under a weak magnetic field, close to the critical temperature. In this mixed regime, large stretching-dominated regions are present, leading to a highly heterogeneous response of the network, as pictured in Figure 3.7**b**

Finally, similarly to spring networks near p_c, fiber networks undergo a critical transition when $p \to p_b$, as they continuously lose their rigidity.

[9] Broedersz, C. P., Mao, X., Lubensky, T. C., and MacKintosh, F. C. (2011). Criticality and isostaticity in fibre networks. *Nat Phys*, 7(12):983–988

3.2.4 Counting bending constraints

Maxwell's constraint counting method can help us estimate p_b too. In the reasoning presented here we neglect mid-edge nodes allowing for buckling: indeed, they become relevant only if the stress of the bond exceeds the buckling threshold.

We have seen in Section 3.1 that in a depleted lattice network with N vertices there are

$$N_{\text{stretch}} = \frac{z}{2}N = \frac{pz_{\text{lattice}}}{2}N \tag{3.5}$$

stretching constraints.

To these we should add the bending constraints, which are associated to hinges, *i.e.* pairs of consecutive, aligned fiber segments. For simplicity we assume here that the original regular lattice is centrally symmetric at any vertex: each bond has a symmetric, and together they form a hinge. There are thus $z_{\text{lattice}}N/2$ hinges in a regular network. In a depleted network, each bond is present with a probability p. A hinge requires that both bonds are present to be effective, and thus any hinge has a probability p^2 to be present in a depleted network. Each hinge constrains the $(d-1)$ angles between the two segments, resulting in

$$N_{\text{bend}} = \frac{(d-1)p^2 z_{\text{lattice}}}{2}N \tag{3.6}$$

bending constraints. These angular constraints are not redundant with the central-force constraints due to stretching, and we can therefore add them up to determine the rigidity threshold p_b, at which the number of degrees of freedom Nd equates the total number of constraints $N_{\text{stretch}} + N_{\text{bend}}$. This constraint counting argument therefore predicts the following value for p_b:

$$p_b = \frac{\sqrt{1 + \frac{8d(d-1)}{z_{\text{lattice}}}} - 1}{2(d-1)} \tag{3.7}$$

For triangular networks, this formula predicts $p_b = (\sqrt{11/3} - 1)/2 \approx 0.457$, in close agreement with the numerical value $p_b \approx 0.445$. Similarly, for FCC networks the prediction is $p_b = (\sqrt{5} - 1)/4 \approx 0.309$, to compare with the numerical value $p_b \approx 0.268$. These values are summarized in Table 3.1.

3.3 Bulk elastic properties

In this Section, we study the passive mechanical properties of our lattice fiber network model. In Section 3.3.1, we complement our discussion of linear elastic moduli. In Section 3.3.2, we discuss the mesoscopic heterogeneities of deformation known as *non-affine* displacements, and their

Lattice	Connectivity	Bending	Central-force
Triangular $d = 2, z_{\text{lattice}} = 6$	$p_p = 0.35$	$p_b = 0.45$	$p_c = 0.65$
FCC $d = 3, z_{\text{lattice}} = 12$	$p_p = 0.12$	$p_b = 0.27$	$p_c = 0.47$

Table 3.1: The percolation thresholds in our model fiber networks for our most used lattices. Numerical values from (Broedersz et al., 2011).

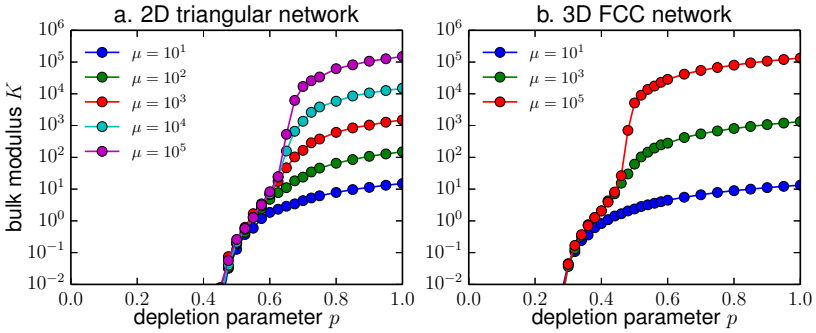

Figure 3.10: The linear bulk modulus of our model networks in 2D (a) and 3D (b), as a function of the depletion parameter and for several values of μ. Parameters: system size 200^2 (30^3) with periodic boundary conditions.

consequences on the energetics of the system. Finally, in Section 3.3.3, we study the nonlinear response of these networks at finite strain.

3.3.1 Linear elastic moduli

The macroscopic elastic properties of an isotropic material are, at linear order, characterized by only two positive parameters: its shear modulus G and bulk modulus K. These two parameters can be combined as a scale parameter K and a dimensionless number, namely the Poisson ratio ν:

$$\nu = \frac{dK - 2G}{d(d-1)K - 2G} \tag{3.8}$$

This number ranges between -1 (for $K/G = 0$, *i.e.* an *auxetic* material that resists shear but not compression) and $1/(d-1)$ (for $K/G = \infty$, *i.e.* an incompressible material).

Lattice materials are anisotropic; however, two-dimensional lattices – such as the triangular lattice – can possess a sufficiently high degree of symmetry such that their linear elastic response is also fully characterized by these two parameters. In the case of three-dimensional networks such as the FCC lattice, a third parameter would be needed to describe their anisotropy. We neglect this anisotropy in the following. We plot in Figure 3.10 the bulk elastic modulus of two- and three-dimensional depleted networks. We have seen in Section 3.2 that there are three regimes of elasticity in these networks: for $p > p_c$, the system is rigid and similar to a spring network, and its bulk elastic modulus is proportional to μ. For $p_b < p < p_c$, the system is much softer, as it owes

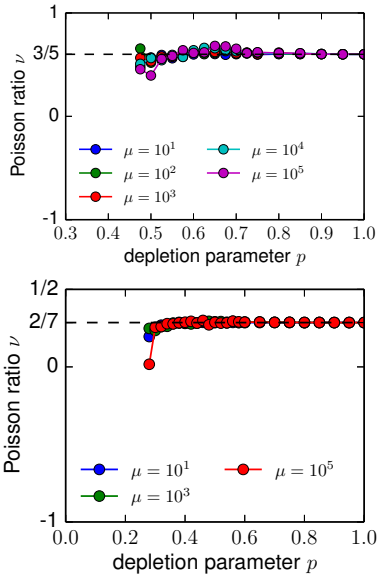

Figure 3.11: The Poisson ratio of our lattice fiber network is approximately independent of p and μ. Top: in a 2D triangular network, and bottom: in a 3D FCC network. Parameters: system size 200^2 (30^3) with periodic boundary conditions.

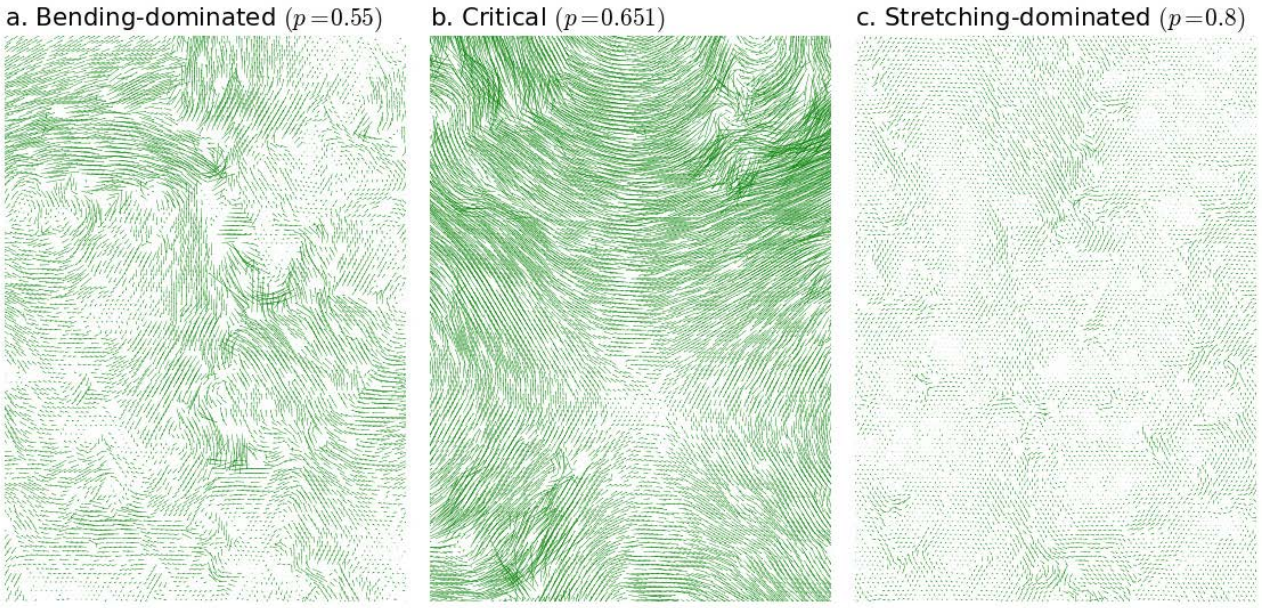

Figure 3.12: Vector fields showing non-affine displacements in the linear response of depleted fiber networks to an infinitesimal shear, showing large non-affine deformations at the central-force critical point. The networks are the same as in Figure 3.7, with an infinitesimal shear of $\gamma = 10^{-100}$. The non-affine displacement vectors are amplified $\times 2.10^{99}$ for better legibility.

its rigidity to filament bending, and the bulk modulus is independent of μ. Note however that it exhibits a strong dependence on p in this regime, varying steadily over several orders of magnitude. Finally for $p < p_b$ the system is floppy and its linear elastic moduli vanish.

The linear shear modulus exhibits quantitatively similar behaviour. Indeed, using Equation 3.8, we measure the material's Poisson ratio, and find that it is essentially independent of p, as shown in Figure 3.11. We can calculate these values exactly in the case of regular networks; we find $\nu = 3/5 = 0.6$ in 2D and $\nu = 2/7 \approx 0.2857$ in 3D[10].

[10] Amusingly, this is precisely the value reported for the Poisson ratio of soil in (Huang et al., 1999).

3.3.2 Non-affine deformations

In macroscopic elasticity, materials characterized by spatially homogeneous elastic moduli undergo *affine* distortions when their boundaries are strained: the local displacements coincide with the linear interpolation of boundary displacements. More precisely, denoting $\mathbf{T}$ the displacement gradient tensor of the boundaries, the affine displacement at position $\mathbf{R}$ is:

$$u_\mu^{(\text{affine})}(\mathbf{R}) = T_{\mu\nu} R_\nu \tag{3.9}$$

However, many materials have elastic moduli that vary randomly with position, and they necessarily undergo nonaffine distortions in response

to external stress – *i.e.*, their displacement field deviates from Equation 3.9. We can therefore define the *non-affine* displacement field as:

$$u_\mu^{(\text{non-affine})}(\mathbf{R}) = u_\mu(\mathbf{R}) - u_\mu^{(\text{affine})}(\mathbf{R}) \tag{3.10}$$

These non-affine displacements are a fingerprint of the heterogeneous nature of the elastic material. They are the degrees of freedom of our model network, and straightforwardly available in our simulations. In Figure 3.12, we plot the non-affine displacement fields of the infinitesimally sheared networks of Figure 3.7.

A common mistake is to confuse non-affinity with non-linear effects, while non-affine displacements actually exist at linear order. We can quantify this by defining a linear *non-affine parameter* Γ as[11]:

$$\Gamma = \frac{1}{\gamma^2 V} \sum_{\text{vertices } i} \left|\left| \mathbf{u}^{(\text{non-affine})} \right|\right|^2 \tag{3.11}$$

where γ is the infinitesimal strain, and V the volume of the system. This is a good quantity to characterize 3D materials; however, in 2D disordered materials (no matter how small the disorder is), it diverges[12] as $\log(V)$. This is one of many oddities that 2D elasticity exhibits when considering large scale effects; in this Thesis we will carefully avoid situations where this is a problem.

In Figure 3.13, we plot Γ as a function of the depletion parameter, for several values of the stretching rigidity μ. Qualitatively, we observe that stretching-dominated networks, away from the central-force percolation point p_c, are close to affine. The proximity to the critical point is characterized by a bump in the non-affine parameter, which diverges at p_c in the $\mu \to \infty$ limit as the correlation length of non-affine displacements diverges. These large correlation domains are apparent in Figure 3.12b. In the bending-dominated regime, the non-affinity is large yet finite, and it apparently diverges again when rigidity is lost at $p = p_b$.

Bending and stretching energy In our model, non-affine deformations have a close connection with the energetic properties of the system. Indeed, as the reference, unstressed state consists in straight, unbent fibers, any *affinely* deformed state also has zero bending energy (note that this would no longer be true if the filaments were initially bent).

In an infinitesimally deformed network, consider the ratio between the amount of energy E_{bend} stored in bending modes to that E_{stretch} stored in filament stretching. In Figure 3.14, we plot this ratio as a function of μ for several values of p. We observe different scaling, depending on the elastic regime set by the network's connectivity:

- For $p > p_c$, we have $E_{\text{bend}}/E_{\text{stretch}} \sim \mu^{-1}$.
- For $p = p_c$, we have $E_{\text{bend}}/E_{\text{stretch}} \sim 1$.

[11] Broedersz, C. P., Mao, X., Lubensky, T. C., and MacKintosh, F. C. (2011). Criticality and isostaticity in fibre networks. *Nat Phys*, 7(12):983–988

[12] DiDonna, B. A. and Lubensky, T. C. (2005). Nonaffine correlations in random elastic media. *Phys. Rev. E*, 72(6):066619

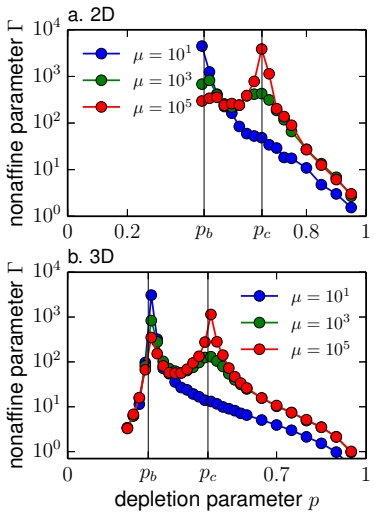

Figure 3.13: The non-affine parameter Γ in (a) 2D and (b) 3D depleted networks. Note that all quantities plotted in (a) diverge logarithmically with the system size. Parameters: system size 200^2 (30^3) with periodic boundary conditions.

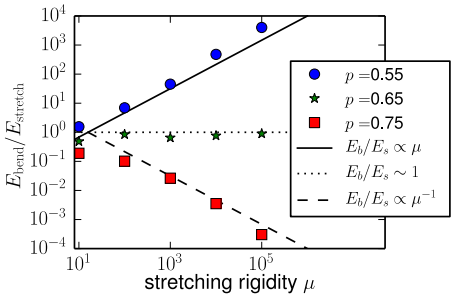

Figure 3.14: The ratio between bending energy and stretching energy against bending rigidity κ, for values of p above, at and below the central-force critical point.

- For $p < p_c$, we have $E_{\text{bend}}/E_{\text{stretch}} \sim \mu$.

We can explain this striking behaviour with an analogy with a simple mechanical toy model. There are two ways, or "channels", by which the network can deform: affine and non-affine. The resulting deformation is a combination of the response of these two channels to the external stress. We can therefore model these different channels as springs in series, with a load that is the analog to the external stress.

- *Affine channel:* affine deformations which involve no bending. Thus the stiffness associated with this channel is of order μ.
- *Non-affine channe:l* the system can alternatively deform in a non-affine way, involving bending.
  - if $p > p_c$ the system is rigid even in the absence of bending: the non-affine stiffness is thus composed of both bending and stretching rigidity. We model this by two springs in parallel, one with stiffness μ and the other with unit stiffness (see Figure 3.15.)
  - on the other hand for $p < p_c$ the system is floppy in the absence of bending rigidity, and so there are non-affine deformations that involve no stretching, which we model as a spring of unit stiffness (see Figure 3.16).

Within this simple model, we find the following distribution of the energy between bending and stretching:

$$\frac{E_{\text{bend}}}{E_{\text{stretch}}} = \mu \quad , \quad p < p_c \tag{3.12}$$

$$\frac{E_{\text{bend}}}{E_{\text{stretch}}} = \frac{\mu}{\mu^2 + (\mu+1)^2} \sim \mu^{-1} \quad , \quad p > p_c \tag{3.13}$$

This simple model therefore accounts for the scaling of the distribution of the energy between bending and stretching modes. This picture also provides predictions for the limit $\mu \ll 1$, in which case both stretching- and bending-dominated regimes have $\frac{E_{\text{bend}}}{E_{\text{stretch}}} \sim \mu$. This is validated by our simulations; however this regime is not relevant for biological fiber networks.

We have therefore shown that the stretching-dominated regime is characterized by deformations which are close to affine, and the energy is stored in stretching modes, while the bending-dominated is elastically heterogeneous, which translates into large non-affine deformations, and has its energy stored into bending modes.

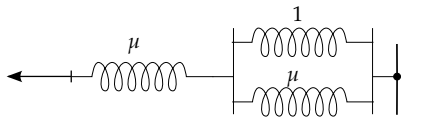

Figure 3.15: Schematics of the repartition of the response in the $p > p_c$ regime : the system can either deform affinely, which involves only stretching, or according to non-affine modes that involve both bending and stretching.

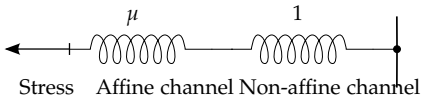

Figure 3.16: Schematics of the repartition of the response in the $p < p_c$ regime : the system can either deform affinely, which involves only stretching, or according to non-affine modes that involve only bending.

3.3.3 Non-linear response

We finally discuss the response of our networks to finite strains. This subject is vast and complex, and still in development – for instance, it

was recently argued[13] that the elastic response of amorphous solids is defined only in the infinitesimal strain limit, as non-affine deformations lead to a divergence of all non-linear elastic coefficients. We first discuss the origins of non-linearity in our networks. Rather than attempting a full description of this difficult problem, we then choose here to give a qualitative description of the bulk non-linear behaviour of our networks, for each elastic regime. We finally discuss the critical stress for the onset of non-linearity.

Origins of non-linearity. We can distinguish two main sources of non-linear behaviour in elastic materials:

- constituent non-linearity: the macroscopic response of the medium will reflect the non-linearities in the intrinsic force-extension relation of the objects.
- geometrical non-linearity: it may not be obvious, but even a material whose constituents are purely linear will generically exhibit a non-linear response at finite strain, as illustrated in Figure 3.17. This is amplified when non-affine deformations are large, as the threshold for geometrical non-linearity is lowered.

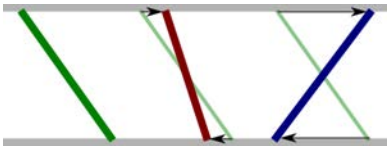

Figure 3.17: A simple example of geometric non-linearity: consider the spring on the left in its rest state, attached to horizontal boundaries, and shear it. It will first be under compression, and thus exert pushing forces on the vertical axis. At large strain its stress reverses and becomes tensile, and the spring pulls on the vertical axis. A linear mechanical element can therefore respond non-linearly to deformation,for geometrical reasons.

In our model, buckling is our main constituent non-linearity. Note that when fibers are bent with an angle of order one, the bending forces are also non-linear.

Stretching-dominated networks. In Figure 3.18, we show the energetic response of a depleted stretching-dominated 2D network to isotropic and shear strain, along with typical network configurations in each case. Regular networks (Figure 3.27) exhibit similar behaviour. Qualitatively, the network yields under compression, softens slightly then stiffens again slightly under tension, and softens under shear.

Shear and tension softening are due to buckling: regions of the network which are under compression will yield under large enough force, resulting in a softening of the network. We regard this effect as rather unphysical: indeed, it occurs because of our omission of fiber stiffening under tension.

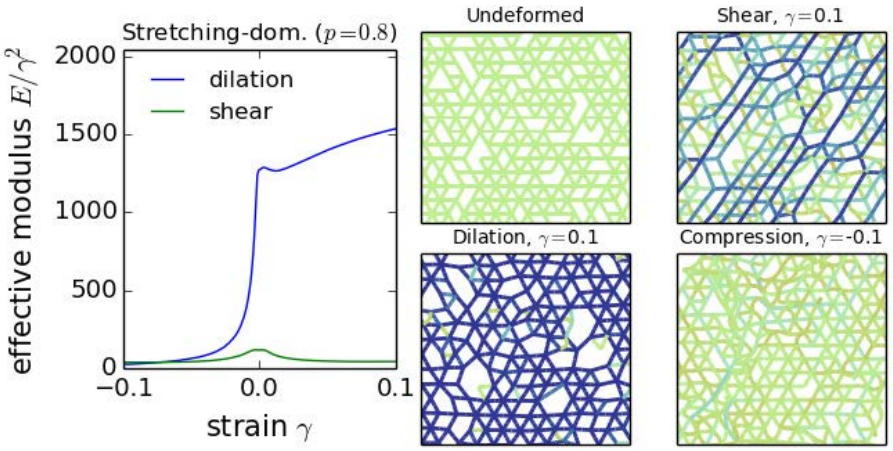

Figure 3.18: Response of a stretching-dominated network to shear, compression and dilation. Parameters: system size 20^2, stretching rigidity $\mu = 10^3$. Because our data is noisy, we plot here an effective elastic modulus E/γ^2 rather than the more usual differential modulus $\mathrm{d}^2E/d\gamma^2$ as in Section 3.A.

The response of our networks to compression is more complex. Indeed, indeed, under a small compression, it is advantageous for a large system to buckle and "fold" along a line (as in Figure 3.19) rather than spreading the strain homogeneously. Indeed, such a fold can accommodate arbitrarily large deformations at a sub-extensive energetic cost[14], in a similar way to failure lines in an atomic material under tension.

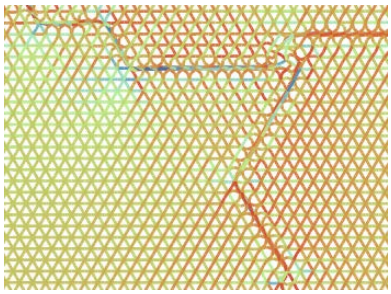

Figure 3.19: Buckling "fold" in a regular network under small compression. Parameters: strain $\gamma = -0.02$, system size 50^2, $\mu = 10^3$.

[14] In the absence of any hard-core repulsion, a spring network can also fold, but the energy barrier is much higher than in a bucklable fiber network.

Bending-dominated networks. We now turn to the non-linear response of bending-dominated networks, as presented in Figure 3.21. We observe that the network softens under compression, and stiffens dramatically under tension. At large shear, a similar stiffening would be observed as the filaments align with the shear direction. This behaviour is qualitatively identical to that of our regular, bending-dominated networks, such as in Figure 3.34.

Buckling under compression leads to a softening of the network, similarly to the stretching-dominated case. More interestingly, under large tension or shear, the network's effective modulus increases dramatically, to the point that it becomes stretching-dominated, *i.e.* proportional to the stretching rigidity μ. Qualitatively, this is due to the system having its soft, bending modes "pulled out". Indeed, bending deformations involve a variation of angles; once these angles become of order unity, filaments align and can no longer bend. Further pulling on the network induces stretching deformations. In the $\mu \to \infty$ limit, this becomes an actual transition: there exists a finite strain $\tilde{\gamma}$ (which depends on the type of deformation) such that the elastic energy is of order unity for $\gamma < \tilde{\gamma}$, and $\sim \mu$ for $\gamma > \tilde{\gamma}$. A new length scale, the pore size separating tensed fibers, seems to emerge in this regime, as apparent in Figure 3.20.

a. 2D bending-dominated network ($p = 0.55$) under dilation ($\gamma = 0.1$).

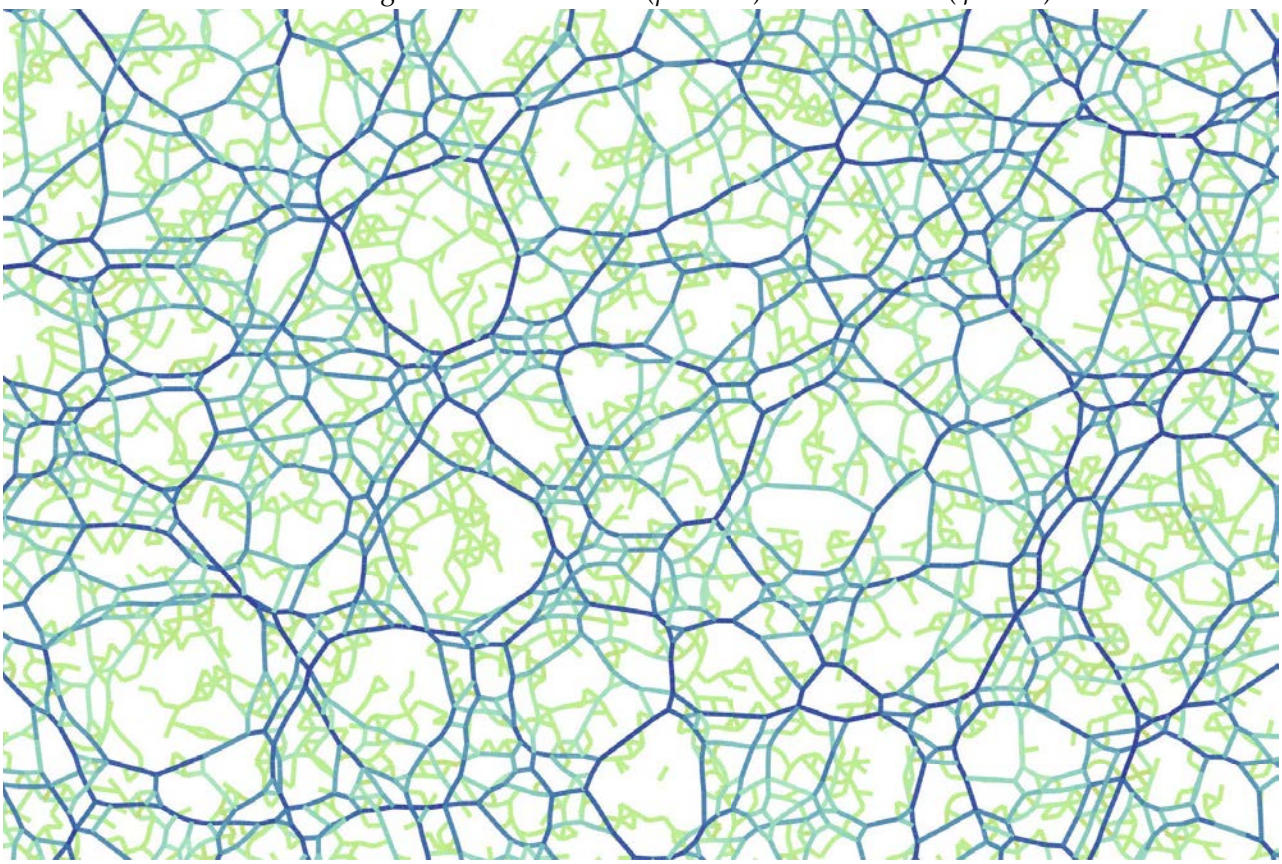

b. 3D bending-dominated network ($p = 0.35$) under dilation ($\gamma = 0.3$).

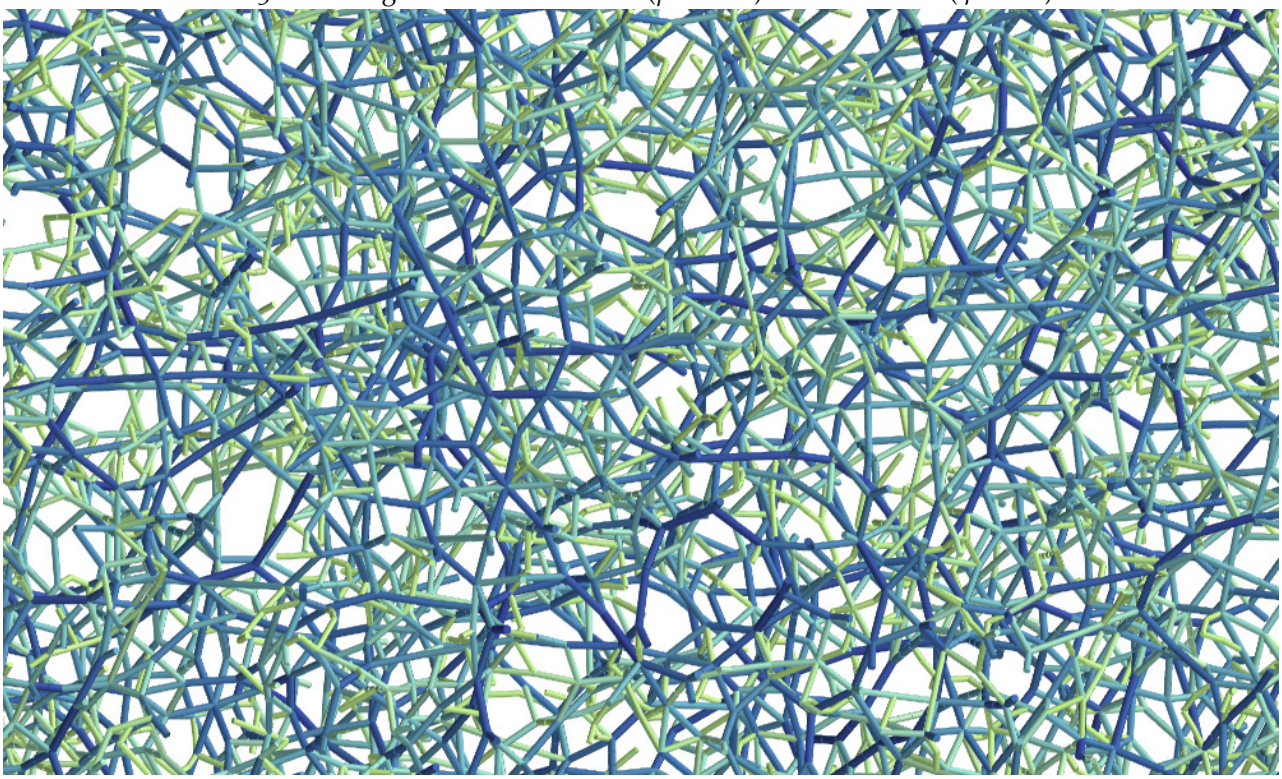

Figure 3.20: Under a large dilation, the response of a bending-dominated network becomes stretching-dominated, as soft bending modes are "pulled out".

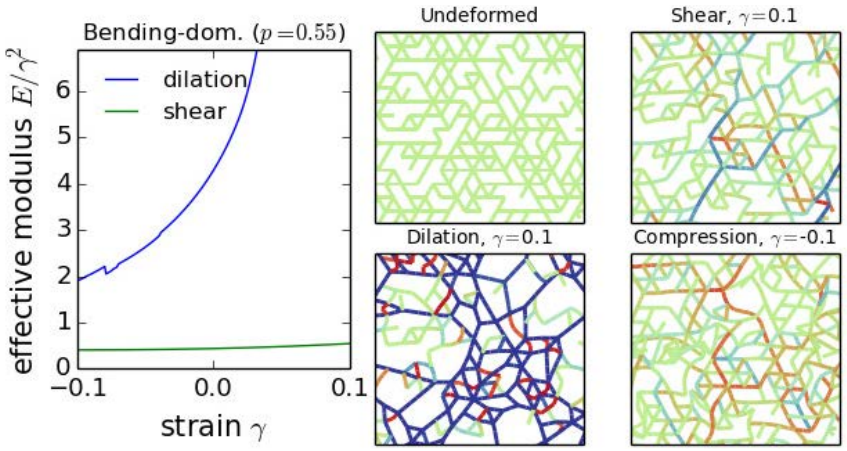

Figure 3.21: Response of a bending-dominated network to shear, compression and dilation. Parameters: system size 20^2, stretching rigidity $\mu = 10^3$. The stress scale is $\times 10$ compared to Figure 3.18.

Floppy networks. Floppy networks, which are connected but have zero linear elastic moduli, also have interesting non-linear properties, as shown in Figure 3.22. Their modulus is exactly zero for all compression and in a range of dilation and shear. However, above some critical strain value, some rigidity appears under shear or strain.

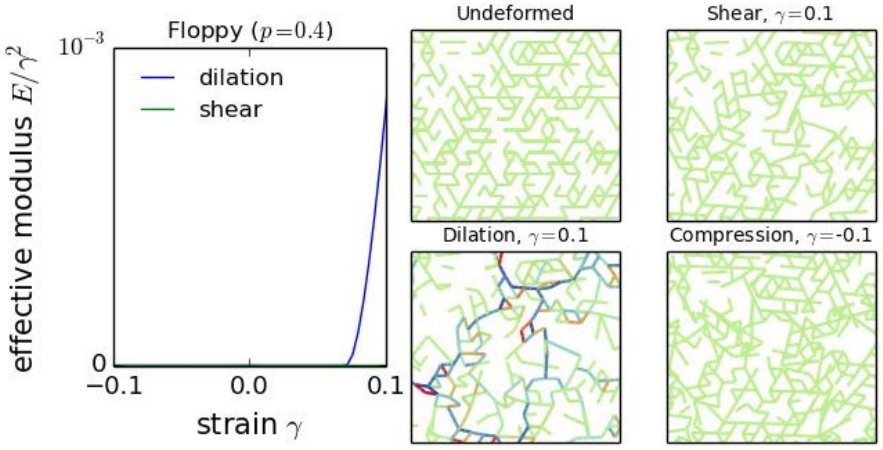

Figure 3.22: Response of a floppy network to shear, compression and dilation. The energy is zero, apart from the dilated case. Parameters: system size 20^2, stretching rigidity $\mu = 10^3$. The stress scale is $\times 150$ compared to Figure 3.18.

There are three kinds of deformation modes in floppy fiber networks: zero modes, which are completely soft; bending modes with rigidity ~ 1; and stretching modes with rigidity $\sim \mu$. When dilated or sheared, the network's zero modes are solicited first. At some first threshold strain $\hat{\gamma}$, the system runs out of zero modes as they are all pulled out, and bending modes enter the response, resulting in an elastic energy ~ 1. At a second, larger critical strain $\tilde{\gamma}$, these bending modes are also exhausted, and the system's response becomes stretching-dominated. This scenario is summarized on our schematic scaling

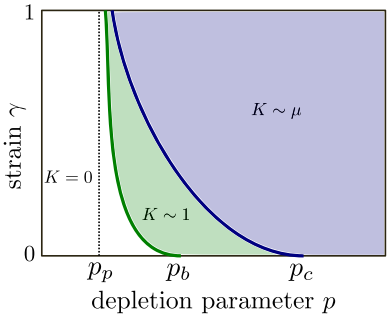

Figure 3.23: Schematic scaling diagram for the elastic energy in the response of a network to a finite dilation. In the stretching-dominated regime or at strain larger than $\tilde{\gamma}$ (blue line), the response is stretching-dominated (blue region). In the bending-dominated regime, and in the floppy regime for strain larger than $\hat{\gamma}$ (green line), the response is controlled by the bending rigidity (green region). Finally, disconnected networks or floppy networks under small shear have zero elastic energy.

diagram (Figure 3.23).

Critical strain and stress for geometrical non-linearity. Finally, we give an estimate of the typical strain and stress at which the network's geometrical non-linear response becomes important. In order to isolate the geometrical effects from the constituent non-linearity, here we will prevent buckling – at least at the single segment scale – by removing the mid-segment vertices in our model.

Even in the absence of buckling, the response of the network to isotropic strain is singular, due to folding effects under compression. For this reason, we consider the response to a shear strain γ. The elastic energy takes the form:

$$E(\gamma) = G\frac{\gamma^2}{2} + G_3\frac{\gamma^3}{3} + G_4\frac{\gamma^4}{4} + O(\gamma^5) \tag{3.14}$$

By reflection symmetry, all odd coefficients should vanish in the thermodynamic limit, and the first non-linear coefficient is G_4 (or would be, if it existed[15]). However, for a given realization of the disorder in a finite system, there will be a non-zero cubic coefficient G_3, which is a random centered variable. In order to estimate G_4, we measure the elastic energy E for three values of the strain: an infinitesimal value $\epsilon = 10^{-100}$ to compute G, and two finite, opposite values $\gamma = \pm 0.01$ to eliminate the cubic term. Our estimator for G_4 is thus:

$$G4 \approx 2\frac{\frac{E(\gamma)+E(-\gamma)}{\gamma^2} - 2\frac{E(\epsilon)}{\epsilon^2}}{\gamma^2} \tag{3.15}$$

This coefficient defines a typical strain γ^* at which the stress becomes dominated by the nonlinear effect:

$$\gamma^* = \sqrt{\frac{G}{|G_4|}} \tag{3.16}$$

Note the absolute value: indeed, in some – but not all – stretching-dominated networks, G_4 can be negative, corresponding to a shear softening material. We plot γ^* as a function of the depletion parameter in Figure 3.24. Aside from taking very small values at $p = p_c$ in the $\mu \to \infty$ limit, this curve is relatively unimpressive, as γ^* takes moderately small values $\approx 10^{-2} - 10^{-1}$ in the whole bending-dominated range and most of the depleted, stretching-dominated regime. More interesting is the typical *stress* σ^* at which this strain is reached, which is

$$\sigma^* = G\sqrt{\frac{G}{|G_4|}} \tag{3.17}$$

We plot σ^* in Figure 3.25. In the whole stretching-dominated regime, we have $\sigma^* > 1$: the typical stress for the onset of geometrical non-linearity

[15] Hentschel, H. G. E., Karmakar, S., Lerner, E., and Procaccia, I. (2011). Do athermal amorphous solids exist? *Phys. Rev. E*, 83(6):061101

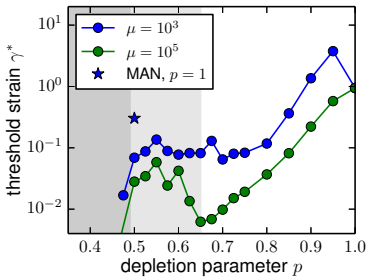

Figure 3.24: The typical strain γ^* for non-linear effects in depleted 2D networks, without the mid-segment nodes allowing buckling. The white, light gray and dark gray regions indicate stretching-dominated, bending-dominated and floppy regimes, respectively. The blue star corresponds to a regular, bending dominated MAN network. Parameters: system size 200^2.

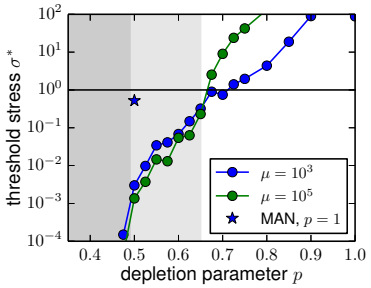

Figure 3.25: The typical stress σ^* for geometrically non-linear response. The buckling stress $\sigma_b = 1$ is indicated as a comparison (black line).

is larger than the buckling stress. Such geometrical non-linearities can therefore be neglected, as the constituent non-linearity will take over first: *non-linear effects in stretching-dominated networks mostly reflect the non-linearity of their constituents.*

In contrast, because bending-dominated networks are much softer than stretching-dominated ones, the associated σ^* can be much smaller than the buckling stress, being typically in the range $\sigma^* \sim 10^{-3} - 10^{-1}$. This geometrical non-linear response is intimately connected to the network's disorder: indeed, $\sigma^* \approx 0.5$ in a regular bending-dominated MAN network (star symbol in Figure 3.25), to be compared to the value $\sigma^* \sim 10^{-3}$ in depleted networks with similar connectivity.

Therefore, *in disordered bending-dominated networks, geometrical non-linearities will start taking over before constituent non-linearity dominates*, and are thus relevant to our study. In regular bending-dominated networks, this is not the case.

3.4 Discussion

In this Chapter, we have studied the passive elastic properties of our model fiber networks. We have shown that the network's connectivity – controlled by the depletion parameter and the choice of lattice – has a dramatic influence on the elastic properties of the network, which delimits three elastic regimes, and we have studied their linear response and non-linear properties.

For connectivities $z > z_c \approx 2d$ – the *central-force rigidity percolation threshold* – the network is *stretching-dominated*, and its linear properties are similar to those of a dense spring networks. It deforms affinely, and its non-linear response is controlled by that of its elementary constituents.

At lower connectivities $z_b < z < z_c$, the network is *bending-dominated*, and much softer, as it owes its rigidity to the bending deformation modes. Its non-affine response is large, and it exhibits significant geometrical non-linearity at stresses well below the buckling threshold. It tends to stiffen under tension and soften under compression. We have designed a non-depleted bending-dominated network, which exhibits similar properties.

Finally, at low connectivities $z < z_b$, the network is floppy, and does not have a linear elastic response. However, when tensed, it acquires a non-linear rigidity.

Close to z_b and z_c, the network exhibits near-critical behaviour, characterized by large correlated domains of non-affine displacements and high non-linear susceptibility.

Biologically relevant networks. Which of these regimes correspond to physiological situations? Cross-linking proteins generally connect filaments by pairs, which corresponds to $z = 4$, while in branching network there are $z = 3$ filaments at a branch point. These arguments are often employed to argue that biological fiber networks are bending-dominated – in particular in three dimensions, where constraint counting predicts $z_c \approx 6$.

However, constraints counting does not tell the whole story. A simple way to notice this is to remark that when counting constraints in our model in Section 3.2.4, we have discreetly omitted the degrees of freedom associated to the mid-segment vertices that allow buckling. Had we included them, we would have predicted that the network is always stretching-dominated. More generally, it has been shown recently[16] that in the limit of long filaments, networks become stretching-dominated, even when constraint counting would predict that they are not connected enough for this. This limit may be physiologically relevant, as, for instance, cytoskeletal filaments may be much longer than the network's mesh size.

[16] Broedersz, C. P., Sheinman, M., and MacKintosh, F. C. (2012). Filament-Length-Controlled Elasticity in 3d Fiber Networks. *Phys. Rev. Lett.*, 108(7):078102

Practical choices. Consequently, we choose not to exclude stretching-dominated networks from our study. An additional good reason for that is that they are simpler than bending-dominated ones: they essentially deform affinely, and their non-linear properties simply reflect that of individual fibers.

In practice, we will also avoid working with near-critical networks in this Thesis. Indeed, our goal is to study the generic response of fiber networks, not the specific case of those with finely tuned connectivity. This choice is also convenient, as critical slowing-down impedes the convergence of our numerical simulations near p_c and p_b, leading to computation times orders of magnitude larger than away from these points. Note that it has been argued recently[17] that *in vitro* cytoskeletal networks can self-organize to a critical point of connectivity; however to the best of our knowledge the central-force critical point was not observed experimentally.

[17] Alvarado, J., Sheinman, M., Sharma, A., MacKintosh, F. C., and Koenderink, G. H. (2013). Molecular motors robustly drive active gels to a critically connected state. *Nat. Phys.*, 9:591

3.A A study of fiber networks on regular lattices

In this Thesis, we often make a distinction between stretching- and bending-dominated networks, as presented in Section 3.2. We will most often consider depleted networks whose regular counterpart is stretching-dominated – such as the triangular and FCC networks. However, in such networks, it is hard to disentangle the effects of disorder from those of the elastic regime of the network: indeed, bending-dominated depleted networks are highly disordered in those cases. It is therefore useful to come with a model of ordered, bending-dominated network.

2D networks. Here we present a study of such attempts to design a regular bending-dominated network in two dimensions. For each network, we show in Figures 3.27-3.36 its depictions in undeformed, dilated, compressed and sheared states. Its elastic properties are evaluated by simulating a shear and compression of a single unit cell, with periodic boundary conditions ($\mu = 10^3$). In both cases, we plot the associate differential modulus characterizing the non-linear elastic response.

We start by noticing that no Bravais lattice is suitable: the triangular lattice (Figure 3.27) is stretching-dominated. The square lattice (Figure 3.28) is singular, as its linear shear modulus vanishes even when there are bending interactions. The honeycomb lattice (Figure 3.29) has no alignment of bonds, and therefore is not adapted to our network, as bending interactions cannot stabilize it.

A popular lattice to study isostatic systems is the Kagome network (Figure 3.30), as it stands just at the threshold with $z_{\text{lattice}} = 4$. However, the infinite alignments of bonds make its response to bulk strains stretching-dominated, while rotation modes of the triangular units result in complex, pathological soft modes.

Our program allows us to simulate more complex lattices, with several vertices per unit cell, and we investigated several possibilities. Figures 3.30-3.36 present our study of candidates for regular bending-dominated networks. Although we found several suitable options, we retain only the simplest and least singular one, namely the "MAN" network presented in Figure 3.34.

Figure 3.26: Large-scale zero modes of a BCC lattice under isotropic compression with $\epsilon = -0.01$. For legibility, we show the lattice vertices instead of the bonds here.

3D networks. In three dimensions, we only consider the FCC lattice in this Thesis. The body-centered cubic (BCC) might seem a good alternate candidate, as it is much closer to the central-force critical point, having $z_{\text{lattice}} = 8$. However, in spite of being stretching-dominated from a constraint counting point of view, it is highly singular, and exhibits

large-scale zero modes of deformation under compression, due to its particular geometry: it can be "folded". Indeed there is no linear elastic response to an infinitesimal strain of the form :

$$\mathbf{T} = \begin{pmatrix} \epsilon_1 & 0 & 0 \\ 0 & \epsilon_2 & 0 \\ 0 & 0 & \epsilon_3 \end{pmatrix}$$

with the eigenvectors being the direction of the cubic geometry, and $\epsilon_1 + \epsilon_2 + \epsilon_3 = 0$. This results in large-scale undulations when the system is compressed, as shown in Figure 3.26.

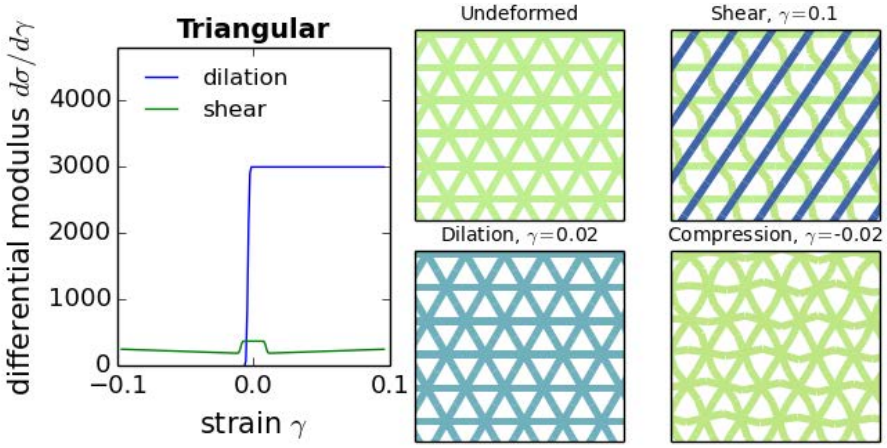

Figure 3.27: The triangular lattice is a Bravais lattice with $z_{\text{lattice}} = 6$, which is well suited for the study of stretching-dominated networks. It softens under shear and compression, as individual bonds buckle.

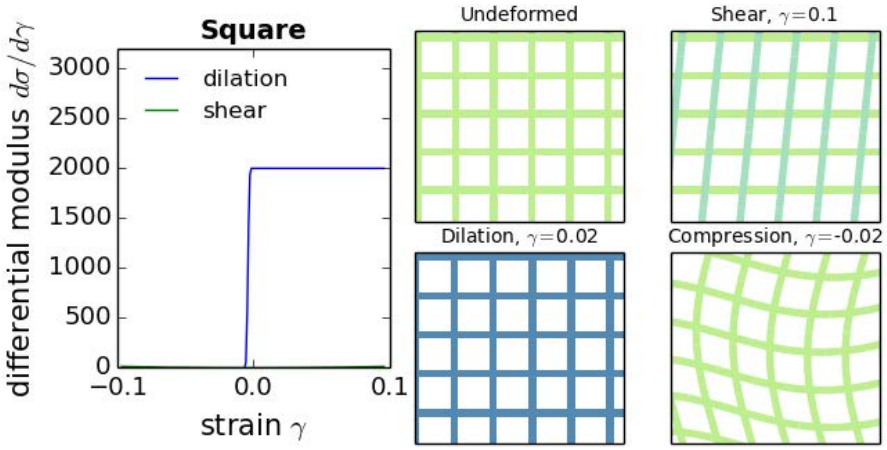

Figure 3.28: The square lattice is a Bravais lattice with $z_{\text{lattice}} = 4$. It stands just at the central-force threshold; however due to its particular geometry it has zero shear modulus, and is thus quite singular. We exclude it from our study for this reason.

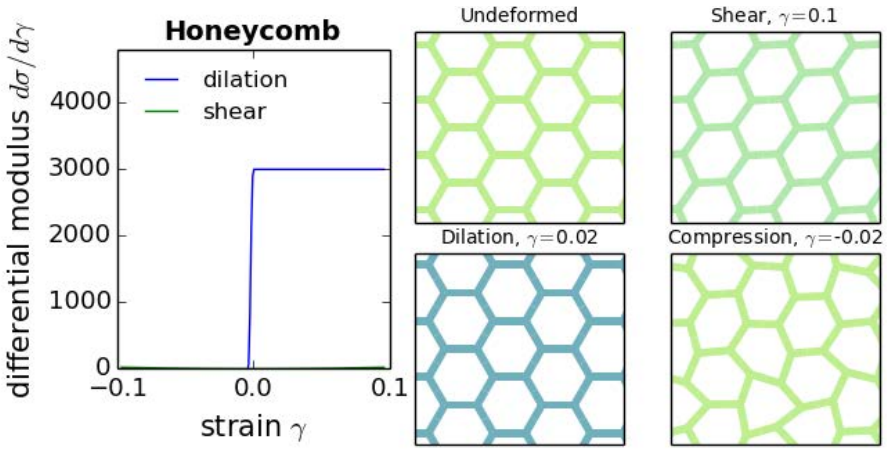

Figure 3.29: The honeycomb lattice is a Bravais lattice with $z_{\text{lattice}} = 3$. It stands below the central-force threshold, and is not stabilized by bending as it lacks hinges. We exclude it from our study for this reason.

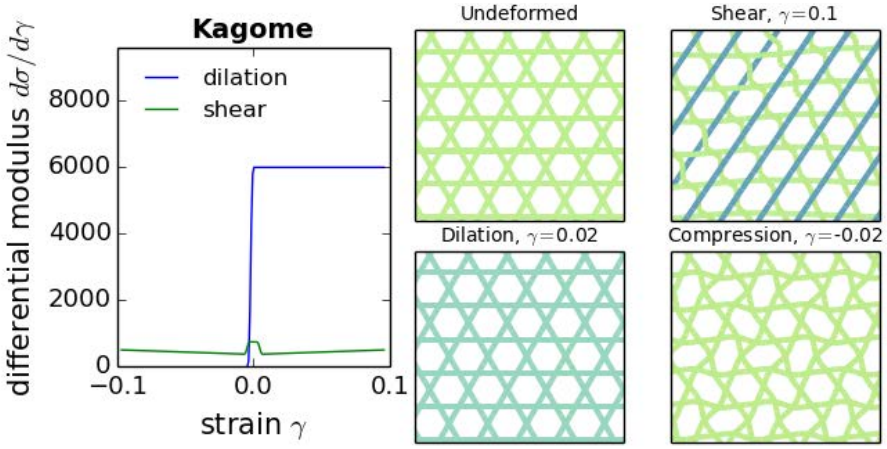

Figure 3.30: The Kagome lattice is a uniform lattice (with one type of vertices) and with $z_{\text{lattice}} = 4$. It stands at the central-force threshold. However its mechanical properties are quite singular due to soft rotation modes and infinite alignments of bonds. We exclude it from our study for this reason.

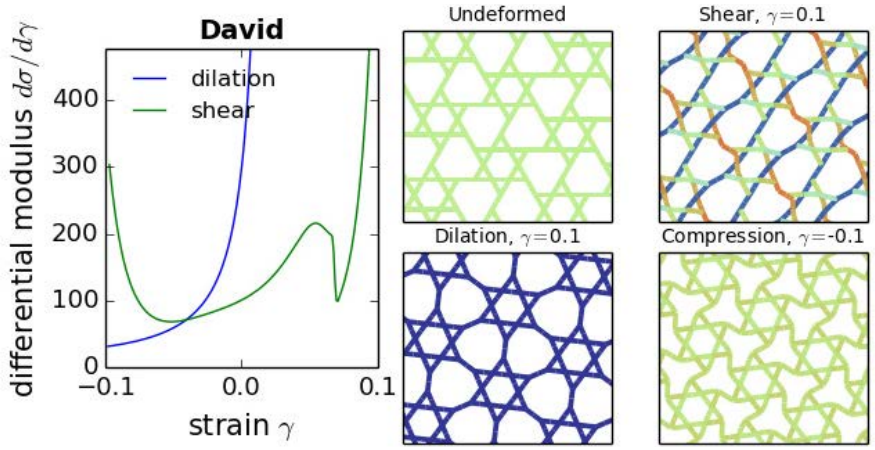

Figure 3.31: The "David" lattice is a custom lattice introduced here. It is chiral and has two distinct types of vertices, and with $z_{\text{lattice}} = 7/2$ it is bending-dominated. Its elastic properties are regular at small strain; however it stiffens strongly and becomes stretching-dominated under a finite dilation. Its chirality is reflected by the asymmetry in the shear curve.

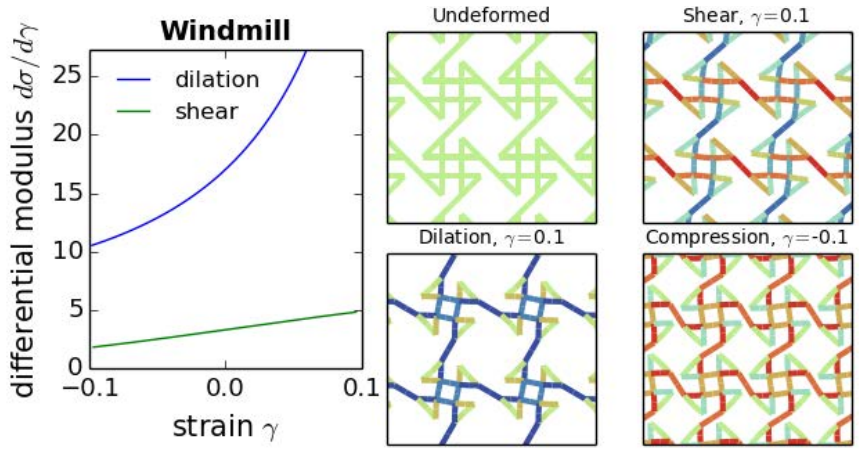

Figure 3.32: The "Windmill" lattice is a custom lattice introduced here. It is chiral and has three distinct types of vertices, and with $z_{\text{lattice}} = 3$ it is bending-dominated. Its elastic properties are regular; the helices of the "windmill" patterns rotate when it is stretched or compressed. It has four-fold rotational symmetry, which does not guarantee that its bulk linear properties are described by only two coefficients.

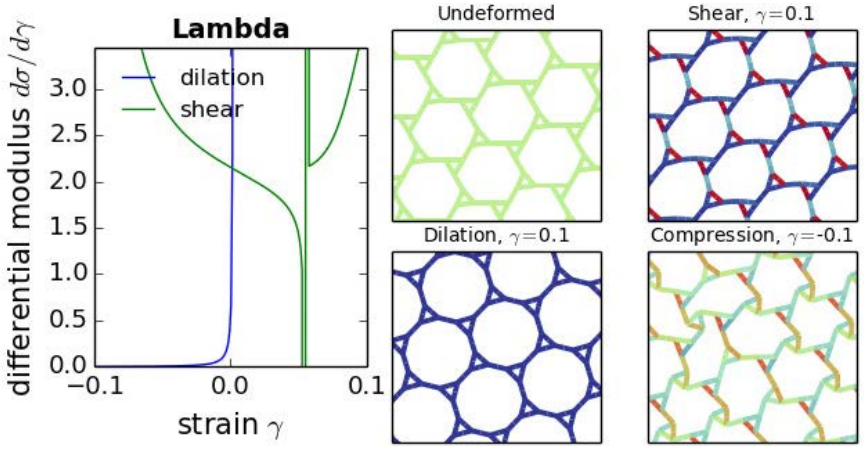

Figure 3.33: The "Lambda" lattice is a custom lattice introduced here. It is chiral and has a single type of vertices. With $z_{\text{lattice}} = 3$ it is bending-dominated. Its elastic properties are surprising, as it appears to be multistable and can exhibit hysteresis under shear or compression. It also stiffens at very small dilation.

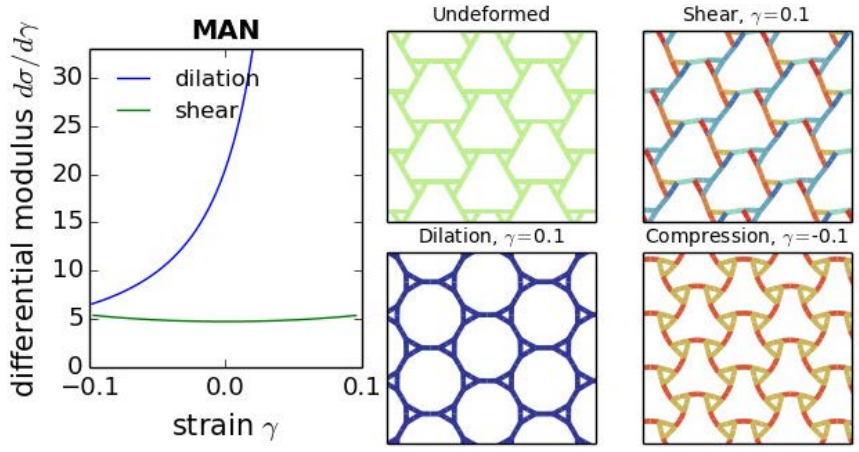

Figure 3.34: The "M.A.N." lattice (standing for "Martin's Amazing Network") is a custom lattice introduced here. It is the achiral counterpart of the Lambda lattice. It has a single type of vertices, and with $z_{\text{lattice}} = 3$ it is bending-dominated. Its elastic properties are regular and robust, making it our top choice for regular bending-dominated networks.

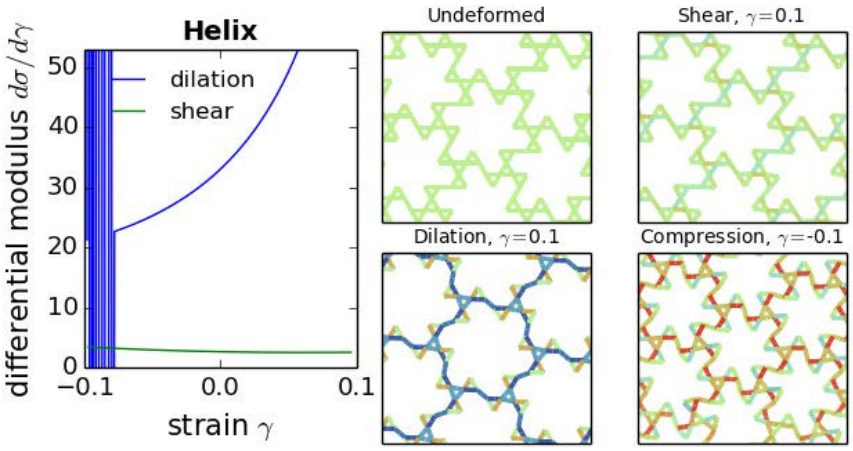

Figure 3.35: The "Helix" lattice is a custom lattice introduced here. It has three types of vertices, and with $z_{\text{lattice}} = 3$ it is bending-dominated. Its elastic properties are regular, however we discard it due to its complexity.

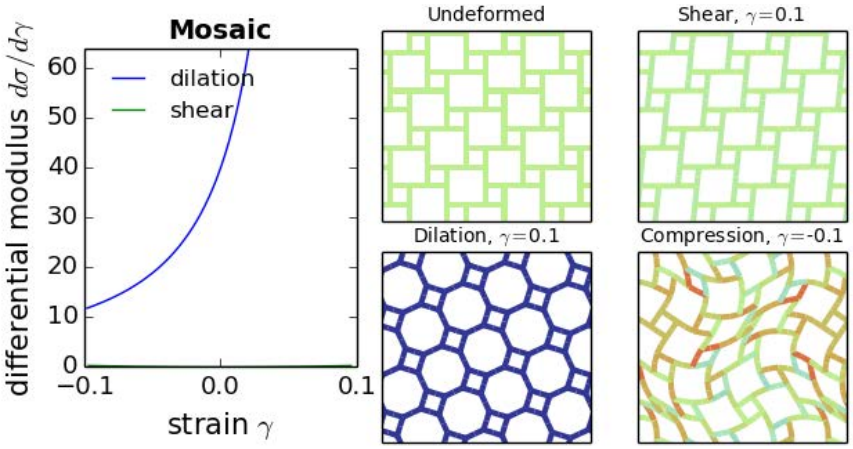

Figure 3.36: The "Mosaic" lattice is a custom lattice introduced here. Because it is a sublattice of the square lattice, it inherits its singularities; we present it here for aesthetic reasons.

4
Linear stress production

Le hasard ne favorise que les esprits préparés.

— Louis Pasteur , *discours prononcé à Douai.*

In this Chapter, we start our study of the transmission of localized forces exerted by active units in elastic fiber networks. Here we consider the case of the *linear* response of these networks, corresponding to the limit of very small active forces. We do not restrict this discussion to our model network, but rather address the more general question:

How are forces transmitted in linear elastic media?

We show that in this linear case – when deformations are proportional to forces – force transmission obeys a simple and universal law, where the far-field stress distribution is strongly constrained by the geometry of active units. We introduce a direct relation – termed "dipole conservation" – between the macroscopic active stress and the force dipole tensor, a local quantity describing the individual force-exerting elements, as illustrated in Figure 4.1. We show that this relation applies in both continuum (Section 4.1) and discrete (Section 4.2) homogeneous, linear elastic media, irrespective of the shape of the system and of the spatial distribution of the active forces. To understand the biologically relevant influence of heterogeneities, we investigate the linear response of random spring networks and our model of depleted lattice fiber networks in Section 4.3. We show that force transmission is unreliable in individual realizations of the network, as we further discuss in Section 4.4. However, dipole conservation still holds in an average sense provided the disorder is the same everywhere. The relation we derive is therefore widely applicable, and gives an exact prediction for the active stress in linear elastic media, as we show in Section 4.5.

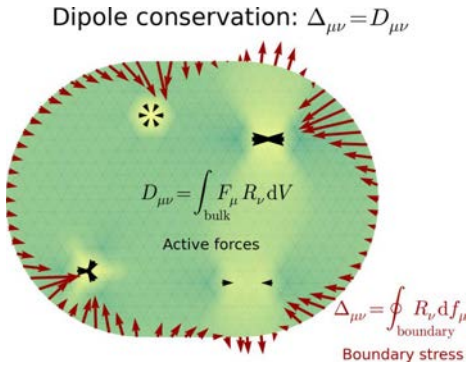

Figure 4.1: Dipole conservation relates local active forces to the resulting far-field stresses in linear elastic media.

4.1 Dipole conservation in continuum elastic media

The transmission of localized active forces to the outer boundary of a continuum elastic body is a geometrically complex problem, and the distribution of transmitted forces strongly depend on the body's shape and material properties. Nevertheless, here we show that strong nonlocal constraints exist between body and boundary forces. In Sec. 4.1.1 we introduce the boundary dipole tensor, a quantity characterizing the boundary forces that is directly related to the stress tensor. Using general conditions of mechanical equilibrium, we relate this boundary dipole to the spatial distribution of body forces in Sec. 4.1.2. Specializing our result to homogeneous linear media, we then show in Sec. 4.1.3 that the boundary dipole is exactly equal to the dipolar moment of the body force distribution, which we refer to as "dipole conservation".

4.1.1 Boundary dipole tensor

Let us consider a general d-dimensional piece of elastic material at mechanical equilibrium, filling a domain Ω of space with boundary $\partial\Omega$ and volume V. We model the active elements embedded in the elastic body as a distribution of body forces $F_\mu(\mathbf{R})$. To quantify the macroscopic consequences of these active forces, we consider the response of the total system composed of the elastic medium and the embedded elements to an infinitesimal, affine deformation characterized by a strain tensor $\gamma_{\mu\nu}$. Under this transformation, a point belonging to the boundary $\partial\Omega$ of the elastic body with position $\mathbf{R}$ in the resting state is displaced by a quantity $\delta R_\mu(\mathbf{R}) = \gamma_{\mu\nu} R_\nu$ (summation over repeated Greek indices is implied here). Denoting the elastic stress tensor by $\sigma_{\lambda\mu}(\mathbf{R})$ and considering a surface element $\mathrm{d}s_\lambda$ lying on the boundary $\partial\Omega$, the force exerted by the outside world on the surface element reads $-\sigma_{\lambda\mu}(\mathbf{R})\ \mathrm{d}s_\lambda$. As the surface element gets displaced by an infinitesimal δR_μ, the work performed by this force is $[-\sigma_{\lambda\mu}(\mathbf{R})\ \mathrm{d}s_\lambda] \times \delta R_\mu$. The change in energy of the total system is given by the work performed over the whole boundary:

Throughout this Chapter, the positions $\mathbf{R}$ can be chosen to refer to either the undeformed or deformed state, provided that the correct form of the stress (nominal *vs.* Cauchy) is used. The mean-stress theorem holds for arbitrary deformations in both cases.

$$\begin{aligned} \delta E &= \oint_{\partial\Omega} [-\sigma_{\lambda\mu}(\mathbf{R})\ \mathrm{d}s_\lambda] \times \delta R_\mu \\ &= -\gamma_{\mu\nu} \times \oint_{\partial\Omega} \sigma_{\lambda\mu}(\mathbf{R}) R_\nu\ \mathrm{d}s_\lambda. \end{aligned} \tag{4.1}$$

Noting that the integral in the right-hand side of Equation 4.1 is the dipolar moment of the boundary forces, we refer to this quantity as the "boundary dipole tensor" and denote it as

$$\mathcal{D}^{\mathrm{far}}_{\mu\nu} = \oint_{\partial\Omega} \sigma_{\lambda\mu}(\mathbf{R}) R_\nu\ \mathrm{d}s_\lambda. \tag{4.2}$$

The meaning of this new quantity becomes clear if we note that according to Equation 4.1, $\mathcal{D}^{\text{far}}_{\mu\nu}$ is the derivative of the energy of the total system with respect to the boundary strain $\gamma_{\mu\nu}$. This is reminiscent of the definition of the stress tensor $\sigma_{\mu\nu}$ as the derivative of the energy density e with respect to the local strain tensor $\gamma_{\mu\nu}(\mathbf{R}$. Considering a coarse-grained approximation of the total system with a uniform bulk deformation $\gamma_{\mu\nu}$ and uniform stress $\tilde{\sigma}_{\mu\nu}$, we have $E = Ve$ with e a uniform elastic energy density and the boundary dipole tensor is directly related to the coarse-grained stress tensor:

$$\mathcal{D}^{\text{far}}_{\mu\nu} = \frac{\partial(Ve)}{\partial\gamma_{\mu\nu}} = -V\tilde{\sigma}_{\mu\nu}. \tag{4.3}$$

Thus $-\mathcal{D}^{\text{far}}_{\mu\nu}/V$ is the medium's coarse-grained stress tensor and $\mathcal{D}^{\text{far}}/(Vd) = \mathcal{D}^{\text{far}}_{\mu\mu}/(Vd)$ is the analog of a hydrostatic pressure. In an active medium language, $\mathcal{D}^{\text{far}} < 0$ thus characterizes a contractile medium while $\mathcal{D}^{\text{far}} > 0$ is associated with extensility.

Note that in a system with periodic boundary condition, the boundary dipole tensor can be defined through the relation $\mathcal{D}^{\text{far}}_{\mu\nu} = -\partial E/\partial(\gamma_{\mu\nu})$, where the affine deformation can be imposed through Lees-Edwards boundary conditions. Unless explicitly stated, all the continuum and discrete results presented in this manuscript can be rederived under periodic boundary conditions with only minimal modifications to their proofs.

4.1.2 Mean-stress theorem

As a first step towards establishing dipole conservation, here we rederive a result known as the mean-stress theorem[1]. We introduce the dipolar moment of the active forces $F_\mu(\mathbf{R})$ as

$$\mathcal{D}^{\text{loc}}_{\mu\nu} = \int_\Omega F_\mu(\mathbf{R}) R_\nu \, \mathrm{d}V. \tag{4.4}$$

Note that $\mathcal{D}^{\text{loc}}_{\mu\nu}$ is independent of the origin of the coordinates if the body forces sum to zero as expected for active elements embedded in an elastic medium, and that the total force dipole exerted by several active elements is equal to the sum of the individual force dipoles.

Inserting the force balance equation $\partial_\nu\sigma_{\mu\nu} = -F_\mu$ into Equation 4.4 and integrating by part yields the mean stress theorem

$$\mathcal{D}^{\text{loc}}_{\mu\nu} = \oint_{\partial\Omega} \sigma_{\lambda\mu}(\mathbf{R}) R_\nu \, \mathrm{d}s_\lambda + \int_\Omega \sigma_{\mu\nu}(\mathbf{R}) \, \mathrm{d}V. \tag{4.5}$$

Defining the integrated stress tensor $\Sigma_{\mu\nu} = \int_\Omega \sigma_{\mu\nu} \, \mathrm{d}V$ and using the definition of the boundary dipole Equation 4.2, Equation 4.5 can be cast into a compact form:

$$\mathcal{D}^{\text{far}}_{\mu\nu} = \mathcal{D}^{\text{loc}}_{\mu\nu} - \Sigma_{\mu\nu}. \tag{4.6}$$

[1] Eshelby, J. D. (1956). The Continuum Theory of Lattice Defects. *Solid State Phys.*, 3:79–144
Gurtin, M. E. (1973). The Linear Theory of Elasticity. In Truesdell, P. D. C., editor, *Linear Theories of Elasticity and Thermoelasticity*, pages 1–295. Springer Berlin Heidelberg. DOI: 10.1007/978-3-662-39776-3_1
Carlsson, A. E. (2006). Contractile stress generation by actomyosin gels. *Phys. Rev. E*, 74(5 Pt 1):051912

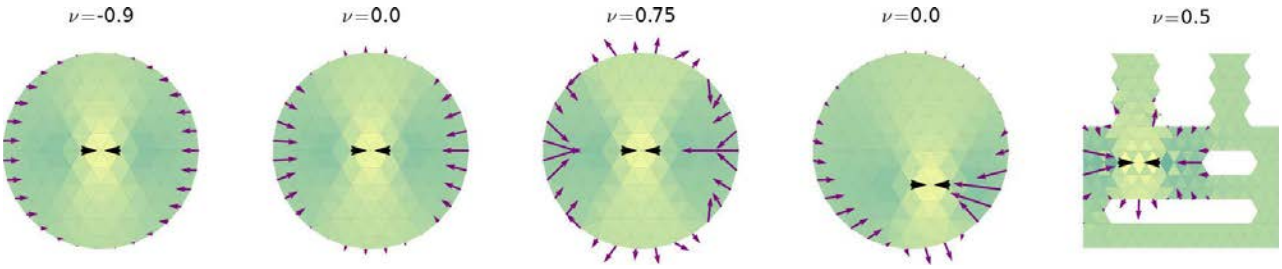

Figure 4.2: Boundary forces (*purple arrows*) transmitted by a two-dimensional homogeneous linear elastic medium under the influence of a localized force dipole (*black arrowheads*) computed using finite elements. The boundary force distribution is strongly influenced by both the medium's material properties (ν denotes the Poisson ratio) and the geometry of the problem. Nevertheless, in all cases the boundary dipole tensor is equal to the body forces' dipolar moment.

This result holds irrespective of the medium's material properties, including homogeneity and linearity.

4.1.3 Dipole conservation

Despite its universality, in the general case the result of Equation 4.6 involves a complicated unknown object $\Sigma_{\mu\nu}$ and is thus of limited practical use. Here we show that this limitation is lifted when considering a linear homogeneous elastic medium with fixed boundaries.

In a linear homogeneous elastic medium, stress is related to strain through a position-independent stiffness tensor: $\sigma_{\mu\nu}(\mathbf{R}) = C_{\mu\nu\alpha\beta}\gamma_{\alpha\beta}(\mathbf{R})$. Integrating this relation over space, we get

$$\Sigma_{\mu\nu} = C_{\mu\nu\alpha\beta}\Gamma_{\alpha\beta} \quad \text{with} \quad \Gamma_{\alpha\beta} = \int_\Omega \gamma_{\alpha\beta}(\mathbf{R}) \; \mathrm{d}V, \tag{4.7}$$

with $\Gamma_{\alpha\beta}$ the integrated strain. Assuming small displacements, we use the linear strain $\gamma_{\alpha\beta}(\mathbf{R}) = [\partial_\alpha u_\beta(\mathbf{R}) + \partial_\beta u_\alpha(\mathbf{R})]/2$ with $u_\alpha(\mathbf{R})$ the medium's displacement vector. Integration of Equation 4.7) then yields a boundary integral

$$\Gamma_{\alpha\beta} = \oint_{\partial\Omega} \left[\frac{u_\beta(\mathbf{R})}{2} \, \mathrm{d}s_\alpha + \frac{u_\alpha(\mathbf{R})}{2} \, \mathrm{d}s_\beta \right]. \tag{4.8}$$

Equation 4.6 thus provides a decomposition of the boundary stress as a sum of a bulk term $\mathcal{D}^{\mathrm{loc}}_{\mu\nu}$ involving active forces and a boundary term $\Sigma_{\mu\nu} = C_{\mu\nu\alpha\beta}\Gamma_{\alpha\beta}$ related to the system deformation. Note that the latter depends on the system's elastic properties through the stiffness tensor $C_{\alpha\beta\mu\nu}$, while the former does not. Now introducing the assumption of fixed boundary conditions, we find that the boundary displacements in the right-hand side of Equation 4.8 vanish, implying that the whole integral vanishes[2]. Using Equation 4.7, we thus find that $\Sigma_{\mu\nu} = 0$, and thus Equation 4.6 can be rewritten as the dipole conservation relation:

$$\mathcal{D}^{\mathrm{far}}_{\mu\nu} = \mathcal{D}^{\mathrm{loc}}_{\mu\nu} \tag{4.9}$$

[2] Gurtin, M. E. (1973). The Linear Theory of Elasticity. In Truesdell, P. D. C., editor, *Linear Theories of Elasticity and Thermoelasticity*, pages 1–295. Springer Berlin Heidelberg. DOI: 10.1007/978-3-662-39776-3_1

which relates bulk and boundary forces. To understand the meaning of this equation, we decompose it into the equality of the traces, symmetric traceless parts and antisymmetric parts of the two tensors. The equality of the traces, $\mathcal{D}^{\text{far}} = \mathcal{D}^{\text{loc}}_{\mu\mu} = \mathcal{D}^{\text{loc}}$, is of particular interest for biological systems as it relates the "hydrostatic pressure" $\mathcal{D}^{\text{far}}$ of the medium to the local force dipole $\mathcal{D}^{\text{loc}}$, a quantity routinely interpreted as the amount of contractility of the active elements[3]. Next, the symmetric traceless part of each of the two dipole tensors $[(\mathcal{D}^{\text{far}}_{\mu\nu} + \mathcal{D}^{\text{far}}_{\nu\mu})/2$ and $(\mathcal{D}^{\text{loc}}_{\mu\nu} + \mathcal{D}^{\text{loc}}_{\nu\mu})/2]$ is analogous to a nematic order parameter characterizing the anisotropy of the corresponding forces, and thus their equality means that the anisotropy of the contractile forces is also conserved across scales. Finally, the equality $\mathcal{D}^{\text{far}}_{\mu\nu} - \mathcal{D}^{\text{far}}_{\nu\mu} = \mathcal{D}^{\text{loc}}_{\mu\nu} - \mathcal{D}^{\text{loc}}_{\nu\mu}$ of the antisymmetric parts is equivalent to torque balance in the elastic medium; since embedded active elements exert a vanishing total torque on the elastic medium, it simply reduces to $\mathcal{D}^{\text{far}}_{\mu\nu} - \mathcal{D}^{\text{far}}_{\nu\mu} = 0$, and thus expresses torque balance on the total system.

For systems without fixed boundaries, Equation 4.9 takes the more general form

$$\mathcal{D}^{\text{far}}_{\mu\nu} = \mathcal{D}^{\text{loc}}_{\mu\nu} - C_{\mu\nu\alpha\beta}\Gamma_{\alpha\beta}, \tag{4.10}$$

meaning that the total coarse-grained stress $-\mathcal{D}^{\text{far}}_{\mu\nu}/V$ is the sum of an active contribution and of the elastic stress $C_{\mu\nu\alpha\beta}\Gamma_{\alpha\beta}$. This relation has previously been derived in an isotropic geometry[4].

Note that Equation 4.9, as well as the other dipole conservation relations presented in this Chapter, assume a homogeneous (or statistically homogeneous in Sec. 4.3) elastic medium. In cases where a piece of elastic material is removed to make space for an embedded active element with different elastic properties, no generic relation holds, and the far-field dipole will depend, for instance, on the system size.

[3] Lenz, M. (2014). Geometrical Origins of Contractility in Disordered Actomyosin Networks. *Phys. Rev. X*, 4(4):041002
Dasanayake, N. L., Michalski, P. J., and Carlsson, A. E. (2011). General Mechanism of Actomyosin Contractility. *Phys. Rev. Lett.*, 107(11):118101
Carlsson, A. E. (2006). Contractile stress generation by actomyosin gels. *Phys. Rev. E*, 74(5 Pt 1):051912
Broedersz, C. P. and MacKintosh, F. C. (2011). Molecular motors stiffen nonaffine semiflexible polymer networks. *Soft Matter*, 7:3186–3191
Head, D. A., Levine, A. J., and MacKintosh, F. C. (2005). Mechanical response of semiflexible networks to localized perturbations. *Phys. Rev. E*, 72(6 Pt 1):061914

[4] Eshelby, J. D. (1956). The Continuum Theory of Lattice Defects. *Solid State Phys.*, 3:79–144

4.2 Dipole conservation in discrete elastic media

We now prove dipole conservation in discrete media, with similar implications as in the continuum case of Sec. 4.1. Although more technically involved, this new derivation parallels the one of the previous section and its results have a similar physical interpretation. We introduce the active force dipole tensor and the boundary dipole tensor in Sec. 4.2.1 and show that it satisfies a discrete mean-stress theorem in Sec. 4.2.2. Dipole conservation is then derived in Sec. 4.2.3 under the assumptions of linearity and local point reflection symmetry, a variant of the homogeneity assumption used above.

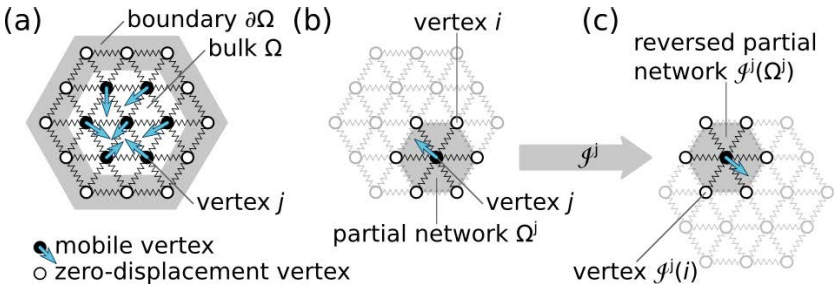

Figure 4.3: Parametrization and point reflection invariance in a discrete elastic system (a) Mobile bulk vertices (*solid circles*) comprised in the bulk Ω of the network are connected to each other and to zero-displacement boundary vertices belonging to the boundary $\partial\Omega$ (*open circles*). *Blue arrows* represent their displacements. (b) The partial network Ω^j is obtained by setting all displacements to zero except that of vertex j. (c) The partial network Ω^j is invariant under point reflection about vertex j even though the total network Ω (*in grey*) is not. The displacement of vertex j is reversed under this transformation.

4.2.1 Active force and boundary dipole tensors

We consider a d-dimensional system Ω comprised of interacting vertices i located at positions $\mathbf{R}^{(i)}$ in the reference configuration, and at $\mathbf{R}^{(i)} + \mathbf{u}^{(i)}$ in the deformed configuration characterized by the displacements $\mathbf{u}^{(i)}$. The system's boundary $\partial\Omega$ consists in a set of additional vertices whose displacements are set to zero [see Figure 4.3(a)]. The active force dipole tensor and the boundary dipole tensor are thus respectively defined as

$$\mathcal{D}^{\text{loc}}_{\mu\nu} = \sum_{i\in\Omega} F^{(i)}_{\mu}\, R^{(i)}_{\nu}, \tag{4.11a}$$

$$\mathcal{D}^{\text{far}}_{\mu\nu} = \sum_{l\in\partial\Omega} f^{(i)}_{\mu}\, R^{(i)}_{\nu} \tag{4.11b}$$

where $F^{(i)}_{\mu}$ is the body force applied on the elastic network at vertex i and $f^{(i)}_{\mu}$ is the force exerted by the system on boundary vertex i.

4.2.2 Discrete stress definition and mean-stress theorem

Bulk and boundary forces are unambiguous mechanical quantities, both in continuum and discrete systems. On the other hand, the stress is an intrinsically continuous quantity. In order to be uniquely defined, it requires the interactions to be purely local (*i.e.* to have zero range) and thus to be mediated by a continuum. The standard definitions of the stress tensor (globally as the force across a surface "cut" in the material, or locally as the derivative of the energy with respect to the local strain) are then equivalent. For a discrete system, these definitions fail to provide a unique definition of the stress tensor: the local strain is not defined, while the notion of force through a "surface cut" is made ambiguous due to the finite range of the interactions. Furthermore, let us remark that any definition of a discrete stress would depend not only on the forces applied to a point, but also on the direction from which this force originates.

To illustrate this ambiguity, let us consider a system of point particles, knowing only its total Hamiltonian $\mathcal{H}$. This information is sufficient to

determine all observable quantities about this system, and in particular its energetics and dynamics. In continuous materials, the hypothesis of zero-range interactions ensures that the Hamiltonian is sufficient to define the stress as

$$\sigma_{\mu\nu}(\mathbf{R}) = \frac{\delta \mathcal{H}}{\delta \gamma_{\mu\nu}(\mathbf{R})}$$

On the other hand, in a discrete system, the sole data of the N-bodies Hamiltonian does not provide enough information to specify local stress. Actually, the simple notion of *interaction* between two material points is ambiguous, and not explicitly contained in the Hamiltoniant. To realize that, let us consider the following trivial example: a set of three points $(x_1 < x_2 < x_3)$ on a line, such that the system's Hamiltonian vanishes:

$$\mathcal{H}(x_1, x_2, x_3) = 0 \tag{4.12}$$

The stress obviously vanishes in this system. We can however also write:

$$\mathcal{H}(x_1, x_2, x_3) = -f.(x_2 - x_1) - f.(x_3 - x_2) - f.(x_1 - x_3) \tag{4.13}$$

In this second, equivalent expression, though, the point x_2 receives a force $\mathbf{f}$ from the left, and a force $-\mathbf{f}$ from the right: for positive f, we would then say that it is subject to compressive stress. This is a simple example of a state of self-stress in a discrete system. In general, the data of the N-bodies Hamiltonian gives no prescription on the interaction forces between points, leaving the notion of stress ambiguous. We thus argue that the explicit data of *interaction forces* is a necessary preliminary to any definition of stress.

We can use the mean-stress theorem connecting $\mathcal{D}^{\text{far}}$ and $\mathcal{D}^{\text{loc}}$, which we derived in the continuous case, as a guide to define stress in discrete systems. Again, we rely only on force balance. We consider only forces between pairs of vertices, as many-body interactions can always be decomposed into sums of pair interactions[5]. We assume these interactions to have finite range. Denoting by $f_\mu^{(ij)}$ the force exerted by vertex i on vertex j, the force balance condition reads

$$F_\mu^{(i)} = \sum_{j \sim i} f_\mu^{(ij)} \tag{4.14a}$$

$$f_\mu^{(i)} = \sum_{j \sim i} f_\mu^{(ij)} \tag{4.14b}$$

for bulk and boundary vertices, respectively. Here $\sum_{j\sim i}$ denotes a sum over the vertices j that interact with i.

Inserting Equation 4.14a into Equation 4.11a, we obtain a double sum over vertices of the form $\sum_{i\in\Omega}\sum_{j\sim i}$. Reorganizing it into a sum

[5] For instance, bending forces associated to hinges (i, j, k) in our lattice fiber model are three-body interactions, but can easily be decomposed into two interaction forces $\mathbf{f}_{ij}(\mathbf{R}_i, \mathbf{R}_j, \mathbf{R}_k)$ and $\mathbf{f}_{jk}(\mathbf{R}_i, \mathbf{R}_j, \mathbf{R}_k)$.

over pairs of neighboring vertices and splitting the resulting expression into two sums, one over bulk pairs and the other over pairs straddling the boundary, we use Newton's third law $f_\mu^{(ij)} = -f_\mu^{(ji)}$ to find

$$\mathcal{D}_{\mu\nu}^{\text{far}} = \mathcal{D}_{\mu\nu}^{\text{loc}} + \sum_{(ij)} f_\mu^{(ij)} \left[R_\nu^{(j)} - R_\nu^{(i)} \right] \tag{4.15}$$

where the sum runs over all pairs of interacting vertices, including boundary vertices. This expression yields a natural definition for the discrete stress associated with a pair of interacting vertices as

$$\sigma_{\mu\nu}^{(ij)} = -f_\mu^{(ij)} \left[R_\nu^{(j)} - R_\nu^{(i)} \right] \tag{4.16}$$

Note that several different conventions can be chosen to generalize the stress tensor to discrete systems. However, most expressions employed in the literature, termed "atomic-level stresses"[6], distribute the stress on a local volume around each vertex in a rather arbitrary way, which is incompatible with any expression of the mean-stress theorem. Here, in contrast, we chose to localize the stress on the bonds of the network[7], yielding a mean-stress theorem with a concise expression:

$$\mathcal{D}_{\mu\nu}^{\text{far}} = \mathcal{D}_{\mu\nu}^{\text{loc}} - \Sigma_{\mu\nu} \quad \text{with} \quad \Sigma_{\mu\nu} = \sum_{(ij)} \sigma_{\mu\nu}^{(ij)}, \tag{4.17}$$

which constitutes the discrete mean-stress theorem. This equation relating boundary forces to the integrated stress in discrete particle systems parallels previous works using the virial theorem for stress computations in molecular systems[8].

[6] Liu, B. and Qiu, X. (2009). How to Compute the Atomic Stress Objectively? *Journal of Computational and Theoretical Nanoscience*, 6(5):1081–1089
Zimmerman, J. A., WebbIII, E. B., Hoyt, J. J., Jones, R. E., Klein, P. A., and Bammann, D. J. (2004). Calculation of stress in atomistic simulation. *Modelling Simul. Mater. Sci. Eng.*, 12(4):S319
Egami, T. (2011). Atomic level stresses. *Progress in Materials Science*, 56(6):637–653

[7] Note that our discrete stress definition has the dimension of a force dipole, rather than a continuous stress – just like forces (density) change dimension whether they are discrete or continuous.

[8] Tsai, D. H. (1979). The virial theorem and stress calculation in molecular dynamics. *The Journal of Chemical Physics*, 70(3):1375–1382

4.2.3 Dipole conservation

As in the continuum case, here we assume linear elasticity to demonstrate $\Sigma_{\mu\nu} = 0$, implying dipole conservation. Linearity implies that $\Sigma_{\mu\nu}$ is a linear function of the set $\left\{ u_\lambda^{(i)} \right\}_{i\in\Omega}$ of equilibrium vertex displacements, which are themselves unspecified functions of the active forces. Therefore, the integrated stress in the network can be decomposed into a sum over fictitious partial networks Ω_j where all displacements but that of vertex j are set to zero [Figure 4.3(a-b)]:

$$\Sigma_{\mu\nu} \left(\left\{ u_\lambda^{(i)} \right\}_{i\in\Omega} \right) = \sum_{j\in\Omega} \Sigma_{\mu\nu}^{\Omega_j} \left(u_\lambda^{(j)} \right), \tag{4.18}$$

where $\Sigma_{\mu\nu}^{\Omega_j}$ is the integrated stress in partial network Ω_j.

To demonstrate dipole conservation, we show that the partial integrated stress $\Sigma_{\mu\nu}^{\Omega_j}$ vanishes for all j in networks invariant under local point reflection. Considering a specific partial network Ω_j, we first

note that reversing the vertex displacement also reverses the integrated stress by linearity:

$$\Sigma_{\mu\nu}^{\Omega_j}\left(-u_\lambda^{(j)}\right) = -\Sigma_{\mu\nu}^{\Omega_j}\left(u_\lambda^{(j)}\right). \tag{4.19}$$

We next introduce the assumption that each partial network Ω_j is invariant under local point reflection about vertex j. The result of this transformation is illustrated in Figure 4.3(c), and we denote the symmetric of vertex i by $\mathcal{I}^j(i)$. Since stresses are proper tensors, the integrated stress is unchanged under this transformation:

$$\Sigma_{\mu\nu}^{\mathcal{I}^j(\Omega_j)}\left(\mathcal{I}^j\left(u_\lambda^{\mathcal{I}^j(j)}\right)\right) = \Sigma_{\mu\nu}^{\Omega_j}\left(u_\lambda^{(j)}\right), \tag{4.20}$$

meaning that the point-reversed image of a system under, *e.g.*, overall compression is a system under the same amount of overall compression. Since vertex j is its own image under this transformation, its displacement is reversed:

$$\mathcal{I}^j\left(u_\lambda^{\mathcal{I}^j(j)}\right) = \mathcal{I}^j\left(u_\lambda^{(j)}\right) = -u_\lambda^{(j)}. \tag{4.21}$$

Noting that local point reflection means that the partial network Ω_j is invariant under $\mathcal{I}^j$, *i.e.*, $\mathcal{I}^j(\Omega^j) = \Omega^j$, Equation 4.20 becomes

$$\Sigma_{\mu\nu}^{\Omega_j}\left(-u_\lambda^{(j)}\right) = \Sigma_{\mu\nu}^{\Omega_j}\left(u_\lambda^{(j)}\right). \tag{4.22}$$

Combining Equations 4.19 and 4.22, we find that $\Sigma_{\mu\nu}^{\Omega_j} = 0$ for any j, which we insert into Equations 4.17 and 4.18 to prove dipole conservation in the original, full network Ω:

$$\mathcal{D}_{\mu\nu}^{\text{far}} = \mathcal{D}_{\mu\nu}^{\text{loc}} \tag{4.23}$$

Although superficially different from the translational invariance used in Sec. 4.1, our local point reflection symmetry has a similar physical meaning. Indeed, it states that from any point of observation, the elastic medium looks the same to two observers looking in opposite directions. It is however more restrictive than translational symmetry, as it does not apply to, *e.g.*, the honeycomb and diamond lattices, or to more complex cases such as the MAN lattice introduced in Section 3.A. In such case, local heterogeneities will lead to violations to dipole conservation, depending on the position and orientation of the applied forces. Local point reflection symmetry is nevertheless fulfilled by most usual lattices, including the triangular, square, simple-, face-centered- and body-centered-cubic lattices, and thus the discrete dipole conservation relation Equation 4.23 remains of wide practical interest. Furthermore, in a regular lattice with periodic boundary conditions translational invariance is sufficient to prove dipole conservation (with a proof similar to that presented in Sec. 4.3.1).

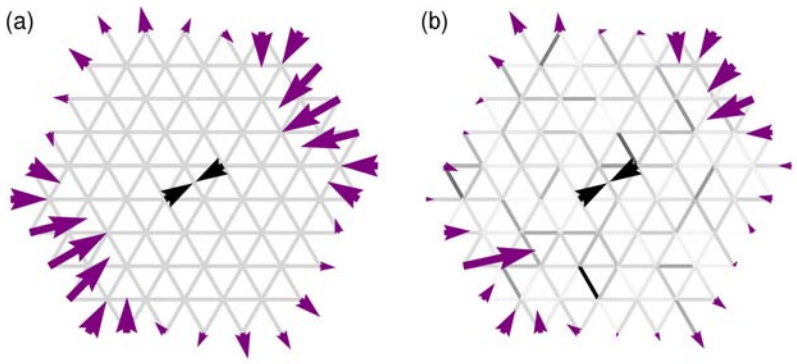

Figure 4.4: Force transmission in a linear spring network is strongly affected by elastic inhomogeneities. Here the opacity of a bond is proportional to its stiffness, and black arrowheads (purple arrows) represent body (boundary) forces. (a) In a homogeneous network, dipole conservation $\mathcal{D}^{\text{far}} = \mathcal{D}^{\text{loc}}$ is satisfied to the numerical precision. (b) In a random spring network, dipole conservation is typically violated; in this specific example, $\mathcal{D}^{\text{far}}/\mathcal{D}^{\text{loc}} \approx 0.60$. Here the spring constants are drawn from a lognormal law with standard deviation $\delta\alpha = 0.8$.

4.3 Linear force transmission in random elastic media

We now investigate how relaxing the assumption of homogeneity affects dipole conservation. As shown in Figure 4.4, inhomogeneous elastic properties significantly affect dipole transmission in a spring network. Nevertheless, we show here that in generic disordered elastic media, linear dipole conservation is is preserved in an average sense. We start by deriving this exact result in the case of periodic boundary conditions (Section 4.3.1). Sec. 4.3.2 then shows numerically that fixed boundary conditions in 2- and 3-dimensional systems spoil this result, although deviations from it are small and go to zero for large-size systems. A complementary proof of average dipole conservation, within a popular mean-field treatment of disordered termed "effective medium theories", is presented in Appendix 4.A.

4.3.1 Average dipole conservation in periodic geometry

Consider the linear response of a regular lattice of independent, identically distributed random springs with periodic boundary conditions subjected to a distribution of body forces $F_\mu^{(i)}$ of zero sum (*i.e.*, $\sum_i F_\mu^{(i)} = 0$ as expected for active elements embedded in an elastic medium). Let $G_{\mu\nu\alpha}^{(i)}$ be the sample-dependent linear response function relating the body force at site i to the integrated stress:

$$\Sigma_{\mu\nu} = \sum_i G_{\mu\nu\alpha}^{(i)} F_\alpha^{(i)}. \tag{4.24}$$

Denoting averages over lattice disorder by a bar, this equation implies

$$\overline{\Sigma}_{\mu\nu} = \sum_i \overline{G_{\mu\nu\alpha}^{(i)}} F_\alpha^{(i)} = \overline{G_{\mu\nu\alpha}} \sum_i F_\alpha^{(i)}, \tag{4.25}$$

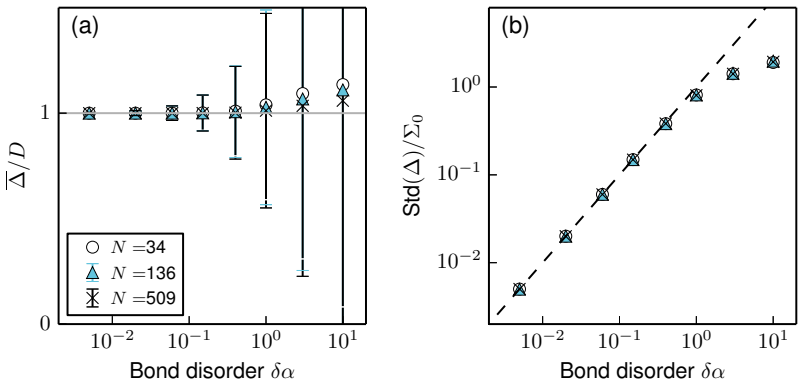

Figure 4.5: Deviations from average dipole conservation and sample-to-sample fluctuations in random spring networks. (a) The average dipole conservation condition $\overline{\mathcal{D}^{\text{far}}}/\mathcal{D}^{\text{loc}} = 1$ (*grey line*) is well respected for systems with large enough number of mobile vertices N. *Bars* represent the standard deviation of this ratio, thus indicating the magnitude of sample-to-sample fluctuations. Each point in this figure represents data averaged over $\mathcal{O}(10^5)$ samples, ensuring that the plotted deviations in the average $\overline{\mathcal{D}^{\text{far}}}$ are statistically significant. (b) Standard deviation of the boundary force dipole, $\mathcal{D}^{\text{far}}$ [proportional to the length of the bars in panel (a)] normalized by the second moment of the effective medium stress Σ_0 (see Appendix 4.A) as a function of disorder. We find good agreement with the small-disorder effective medium theory prediction Equation 4.28 (*dashed line*) up to $\delta\alpha \simeq 1$.

where the second equality stems from the statistical equivalence of all sites in the network, implying that the average response function $\overline{G^{(i)}_{\mu\nu\alpha}}$ is independent of i. Finally, inserting our assumption of vanishing sum of the body forces into Equation 4.25 yields $\overline{\Sigma}_{\mu\nu} = 0$, and thus through Equation 4.17 the force dipole is conserved on average:

$$\overline{\mathcal{D}^{\text{far}}}_{\mu\nu} = \mathcal{D}^{\text{loc}}{}_{\mu\nu}. \tag{4.26}$$

This result is valid in any system where all vertices are equivalent, and thus also holds in infinite lattices.

4.3.2 Violations of average dipole conservation in the presence of fixed boundaries

To investigate the influence of finite domain size on the average dipole conservation Equation 4.26, we numerically study the linear response to a force dipole of a finite hexagonal system with fixed boundary conditions, as pictured in Figure 4.4(b). The network is a two-dimensional triangular lattice of independent identically distributed random hookean springs of unit rest length. The spring constant of the bond joining two neighboring sites i and j is denoted $\alpha^{(ij)}$ and drawn from a distribution $\mathrm{d}P(\alpha)$ with average $\overline{\alpha} = 1$ and variance $\mathrm{Var}(\alpha) = \delta\alpha^2$.

Assuming a lognormal form for $\mathrm{d}P(\alpha)$, we minimize the elastic energy of systems of different sizes using a conjugate gradient algorithm. Our procedure uses displacements of order 10^{-100} times the lattice constant, for which we checked that nonlinear effects are absent. Figure 4.5(a) shows that average dipole conservation is violated for small systems, but that these violations vanish for larger system sizes.

4.4 Stress randomization in disordered networks

While we have shown in the previous Section that in large enough systems the boundary dipole becomes equal to the local force dipole *on average*, Figure 4.5(a) suggests that significant fluctuations *around* this average subsist even in infinite systems. Physically, this stems from the fact that the configuration of the immediate surroundings of the force-exerting active element can strongly amplify or attenuate the local force dipole. These near-field distortions are then faithfully propagated to long distances by the more distant regions of the network, which tend to transmit forces in a more dipole-conserving way. Therefore, due to their local origin these distortions are not cured by increasing the system size. The resulting boundary dipole fluctuations have a clear practical significance, as they represent an intrinsic limitation on the reliability of force transmission through disordered elastic networks and thus represent a challenge for biological systems.

We now study these sample-to-sample variations in the amount of transmitted force dipole. We first describe empirically the decorrelation of the local and far-field forces in random fiber networks. We then use an effective medium (*i.e.*, mean-field) approach to quantify more precisely this "stress randomization" effect in random spring networks.

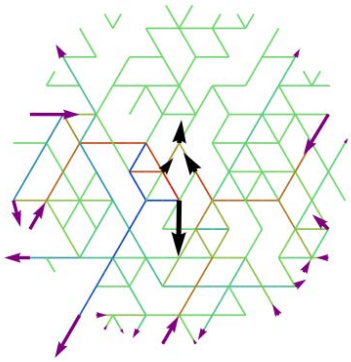

Figure 4.6: A random quadrupole in a depleted 2D network with $p = 0.6$.

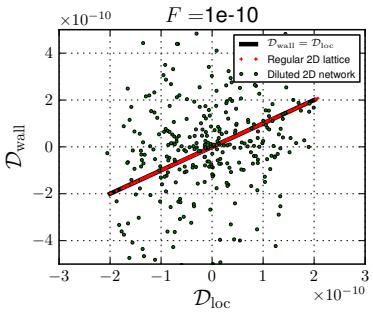

Figure 4.7: Scatter plot of $\mathcal{D}^{\mathrm{far}}$ versus $\mathcal{D}^{\mathrm{loc}}$ for 100 realizations of random force quadrupole, in the case of a regular network (red crosses) and diluted network ($p = 0.61$, green circles), with stretching rigidity $\mu = 10^3$.

4.4.1 Decorrelation between local and far-field stresses

In this Section, we consider force transmission in our model depleted lattice fiber networks. We investigate the correlation between the local force dipole $\mathcal{D}_{\mathrm{loc}}$ and the wall dipole $\mathcal{D}_{\mathrm{wall}}$ by studying the response to a *random quadrupole* of force. This object is obtained as the sum of random radial interactions between the four sites that are closest to the center of the system (see Figure 4.6), with random prefactors (obtained with a centered normal distribution), and such that the sum of force norms is equal to F. Note that this force distribution shares some similarity with that of a myosin motor anchored on two actin filaments [9]. However our main reason for studying this force distribution is that it allows us to separate the effect of the total force norm and that of the source dipole.

The study of the linear response of diluted networks to such a random quadrupole is plotted in Figure 4.7, for both regular and bending-dominated depleted networks. In the case of the regular network we recover the linear elasticity result $\mathcal{D}_{\mathrm{wall}} = \mathcal{D}_{\mathrm{loc}}$ for all realizations of the system. However, in the case of disordered, bending-dominated networks, these two quantities are seemingly independent.

To quantify this effect, we plot in Figure 4.8 the linear correlation factor r between $\mathcal{D}^{\mathrm{far}}$ and $\mathcal{D}^{\mathrm{loc}}$, defined as the quotient of the covariance

[9] Lenz, M. (2014). Geometrical Origins of Contractility in Disordered Actomyosin Networks. *Phys. Rev. X*, 4(4):041002

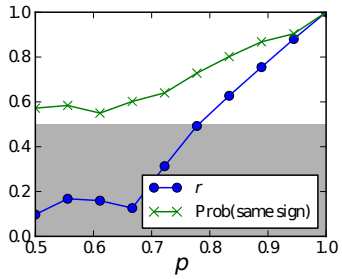

Figure 4.8: The correlation factor r between source dipole and wall dipole *versus* the dilution parameter p of the network, for random forces located in an area of radius $R_{\mathrm{forces}} = 2.5$ in the linear regime ($F = 10^{-10}$). This measure is complemented by that of the probability that $\mathcal{D}^{\mathrm{far}}$ and $\mathcal{D}^{\mathrm{loc}}$ share the same sign, which goes to 1/2 as the correlation decreases.

to the product of standard deviations:

$$r = \frac{\mathrm{Cov}(\mathcal{D}^{\mathrm{far}}, \mathcal{D}^{\mathrm{loc}})}{\sqrt{\mathrm{Var}(\mathcal{D}^{\mathrm{far}})\mathrm{Var}(\mathcal{D}^{\mathrm{loc}})}}$$

as a function of the dilution parameter p of the network. This plot is strikingly similar to that of the bulk elastic modulus in such systems. Starting with a complete correlation in regular networks $r(p = 1) = 1$, the correlation steadily decreases with decreasing p in the stretching-dominated network, and is statistically negligible in the whole bending-dominated network ($p < 0.67$). The effect of the disordered geometry of the fiber network around the source of forces is therefore to randomize the distribution of these forces, such that the far-field dipole depends little on the local one.

4.4.2 Influence of network disorder on the reliability of force transmission

To better understand the magnitude of this randomization effect in relation to the amount of network disorder, we compute a mean-field-type approximation of the boundary dipole fluctuations through an effective medium theory[10]. As detailed in Appendix 4.A, effective medium theories assimilate the effect of bond disorder in a fully random network to that of a single random bond with spring constant α immersed in an effective regular network. The spring constant α_m associated with this effective network is chosen so that the average of the displacement v of the random bond in the regular network is equal to the elongation v_m of the non-random bonds, *i.e.*, $\overline{v} = v_m$. This formalism allows us to calculate an approximation of the tension of each random bond, allowing us to compute the integrated stress Σ. We find that the tension of the random bond is equal to the bond tension in a fully regular medium plus a quantity proportional to $v - v_m$. Since the integrated stress in the ordered medium vanishes [Equation 4.23], our approximate system has $\Sigma \propto v - v_m$. Now averaging this relation and using $\overline{v} - v_m = 0$, we find

$$\overline{\Sigma} = \mathcal{D}^{\mathrm{loc}} - \overline{\mathcal{D}^{\mathrm{far}}} = 0, \tag{4.27}$$

i.e., the effective medium theory predicts average dipole conservation irrespective of boundary conditions. Going beyond this vanishing average stress, we further compute the variance $\overline{\Sigma^2}$ of the integrated stress, which is proportional to $\overline{(v - v_m)^2}$. For small disorder, the typical mismatch $v - v_m$ between the random bond and its deterministic neighbors is moreover proportional to the mismatch $\alpha - \alpha_m$ of their spring constants, and thus to the amplitude $\delta\alpha$ of the disorder. This finally yields

$$\mathrm{Std}(\Sigma) = \mathrm{Std}(\mathcal{D}^{\mathrm{far}}) = \Sigma_0 \delta\alpha, \tag{4.28}$$

[10] Feng, S., Thorpe, M. F., and Garboczi, E. (1985). Effective-medium theory of percolation on central-force elastic networks. *Phys. Rev. B*, 31(1):276–280

where the geometry-dependent prefactor Σ_0 in the right-hand side is given in Appendix 4.A. Comparing this effective medium prediction with the numerical data of Sec. 4.3.2, we find an excellent agreement up to a bond disorder $\delta\alpha \simeq 1$, following which our small-disorder expansion breaks down [Figure 4.5(b)]. The deviation at large $\delta\alpha$ can be imputed to elastic interactions between spring constant fluctuations between distinct bonds, which are neglected in the effective medium theory approach.

This proportionality of dipole fluctuations $\delta\Sigma$ to the network disorder $\delta\alpha$ suggests that reliable dipole transmission is only possible in well-ordered media. However, due to the linearity of the elastic medium, the fluctuations stemming from many small contractile elements scattered through space average out to zero. This scattered geometry is reminiscent of the structure of force-generating cytoskeletal networks.

4.5 Discussion

In this Chapter, we have considered the response of general elastic media to localized active forces, in the small-force limit where the medium responds linearly. We have shown that a simple, geometry-independent law governs force transmission in homogeneous linear elastic media, whereby the force dipole is an invariant of linear elasticity. More specifically, the force dipole tensor exerted by the medium on its boundaries is equal to the sum of the microscopic force dipoles exerted on it by embedded active elements. This dipole conservation relation is valid both for continuum media and for discrete media with unspecified finite range interactions. It also holds true in anisotropic media.

In disordered media, we have seen that there are fluctuations in the far-field response to an individual active unit. This is particularly striking in bending-dominated lattice fiber networks, which exhibit a decorrelation of local and far-field forces. However, we have proved that dipole conservation still holds on average in these systems, which thus applies to the depleted lattice fiber network model on triangular and face-centered cubic lattices studied in this Thesis.

In linear active media, this relation bridges the gap between microscopic forces and macroscopic stress. Indeed, consider a mesoscopic region of volume V in a large active medium, and write $\tilde{\gamma}_{\mu\nu}$ the strain at the boundaries of this region (with respect to the undeformed reference state) and $\tilde{\sigma}_{\mu\nu}$ its stress. We have seen with Equation 4.3 that the mesoscopic region exerts at its boundaries a force dipole tensor $\mathcal{D}^{\text{far}}_{\mu\nu} = -V\tilde{\sigma}_{\mu\nu}$ on the outside world, where $\tilde{\sigma}_{\mu\nu}$ is the coarse-grained stress of this region in a macroscopic description of the active medium.

Assuming linearity of force transmission, we can combine this with the mean-stress theorem inside the mesoscopic region (Equation 4.10) to obtain:

$$\tilde{\sigma}_{\mu\nu} = C_{\mu\nu\alpha\beta}\tilde{\gamma}_{\alpha\beta} - \frac{\mathcal{D}^{\text{loc}}_{\mu\nu}}{V} \tag{4.29}$$

where $\mathcal{D}^{\text{loc}}_{\mu\nu}$ is the total force dipole exerted locally by active units inside the mesoscopic region, and C is the material's stiffness matrix. If the medium is disordered, this relation is only exact on average; however assuming that the mesoscopic region is large enough to contain many active units, fluctuations average out and can be neglected. Assuming there are on average N active units in the region, we can write $\rho = N/V$ the active unit density, and $d_{\mu\nu} = \mathcal{D}^{\text{loc}}_{\mu\nu}/N$ the average force dipole that active units exert locally. If the orientation of the active units are distributed isotropically, $d_{\mu\nu}$ is entirely characterized by its trace.

The two terms in right-hand side of Equation 4.29 can be straightforwardly interpreted as a *passive elastic* term $\tilde{\sigma}^{(\text{elastic})}_{\mu\nu} = C_{\mu\nu\alpha\beta}\tilde{\gamma}_{\alpha\beta}$ which corresponds to Hooke's law, and an *active stress* $\tilde{\sigma}^{(\text{active})}_{\mu\nu} = -\rho d_{\mu\nu}$. The stress in the macroscopic linear active medium is therefore the superposition of a passive elastic stress and an active stress,

$$\tilde{\sigma}_{\mu\nu} = \tilde{\sigma}^{(\text{elastic})}_{\mu\nu} + \tilde{\sigma}^{(\text{active})}_{\mu\nu} \tag{4.30}$$

This decomposition is explicitly used in popular hydrodynamic approaches termed *active gels*[11], where the active stress $\tilde{\sigma}^{(\text{active})}_{\mu\nu}$ is a parameter of the model. In this Chapter, we have demonstrated the microscopic foundation of this decomposition, and provided an exact formula for the active stress in terms of properties of the active unit population:

$$\tilde{\sigma}^{(\text{active})}_{\mu\nu} = -\rho d_{\mu\nu} \tag{4.31}$$

This remarkably simple relation shows the importance of the geometry of the active units, through the local force dipole $d_{\mu\nu} = \sum F_\mu R_\nu$ each unit exerts on the network. This equation contains no adjustable parameter, and can be tested experimentally, as we will discuss in Chapter 7. Interestingly, the active stress does *not* depend on the mechanical properties of the medium, and in particular on its stiffness: *in a linear medium, the active stress depends only on the density, force and geometry of the active units.*

For this relation to hold, however, force transmission must be linear at all scales, from the vicinity of the active unit to the macroscopic scale at which the active gel is expressed. In biological media, this condition is often violated; the next Chapters of this Thesis will discuss the role of non-linearities in force transmission, and show how to adapt Equation 4.31 to these more complex situations.

[11] Jülicher, F., Kruse, K., Prost, J., and Joanny, J.-F. (2007). Active behavior of the Cytoskeleton. *Phys. Rep.-Rev. Sec. Phys. Lett.*, 449(1–3):3–28
Joanny, J.-F. and Prost, J. (2009). Active gels as a description of the actin-myosin cytoskeleton. *HFSP J.*, 3(2):94–104
Marchetti, M. C., Joanny, J. F., Ramaswamy, S., Liverpool, T. B., Prost, J., Rao, M., and Simha, R. A. (2013). Hydrodynamics of soft active matter. *Rev. Mod. Phys.*, 85:1143
Prost, J., Julicher, F., and Joanny, J.-F. (2015). Active gel physics. *Nat Phys*, 11(2):111–117

4.A Effective medium theory for disordered spring networks

Here we derive the results of Sec. 4.4.2 by developing an effective medium theory, following Ref.[12]. In this approach the disordered network described in Sec. 4.3 is approximated by an effective homogeneous network where every bond has a spring constant α_m. When subjected to the same body forces and boundary conditions as the original network, the effective network deforms so that the bond joining adjacent vertices i and j has elongation $v_m^{(ij)}$ with respect to its rest length. To determine the value of α_m, we introduce a third system obtained by replacing bond (ij) by a random spring with constant α drawn with probability law $\mathrm{d}P(\alpha)$. This induces a change in the deformation field, and the elongation of the considered bond in the single-random-bond system is denoted $v^{(ij)} = v_m^{(ij)} + \delta v^{(ij)}$. Mechanical equilibrium then imposes

$$\delta v^{(ij)} = v_m^{(ij)} \frac{\alpha_m - \alpha}{q\alpha_m + \alpha} \tag{4.32}$$

where $q = z/2d - 1$ with z the network connectivity and d the spatial dimension. The effective spring constant α_m is fixed by imposing

$$\overline{\delta v^{(ij)}} = v_m^{(ij)} \int \frac{\alpha_m - \alpha}{q\alpha_m + \alpha} \,\mathrm{d}P(\alpha) = 0, \tag{4.33}$$

where the average is taken over the distribution of α.

To compute the integrated stress Σ, we note that displacements in our single random bond system are the same as in a homogeneous lattice of α_m springs with an active force dipole of amplitude $(\alpha - \alpha_m)v^{(ij)}$ applied along bond (ij). We further note that the integrated stress in this homogeneous, linear system vanishes according to Equation 4.23. Since stresses in this system are identical to those in our single-random-bond system except at bond (ij), the integrated stress in the latter is equal to the integrated stress in the former (*i.e.*, zero) plus the contribution of bond (ij):

$$\Sigma = 0 + (\alpha - \alpha_m)v^{(ij)} = \frac{z\alpha_m}{2d}\delta v^{(ij)} \tag{4.34}$$

where Equation 4.32 was used. Inserting Equation 4.33 into Equation 4.34, we obtain $\overline{\Sigma} = 0$, *i.e.*, the average dipole conservation equation Equation 4.27.

Denoting $\sigma_m^{(ij)} = \alpha_m v_m^{(ij)}$ and $\delta\sigma^{(ij)} = \sigma_m^{(ij)} + \delta\sigma^{(ij)}$, we plug Equation 4.32 into Equation 4.34 and compute $\overline{\left[\delta\sigma^{(ij)}\right]^2} = C\left[\sigma_m^{(ij)}\right]^2$, where

$$C = \int \left[\frac{\alpha_m - \alpha}{(1 - 2d/z)\alpha_m + 2d\alpha/z}\right]^2 \mathrm{d}P(\alpha). \tag{4.35}$$

In the spirit of the effective medium theory, we approximate the fully random lattice as a superposition of single random bond lattices and

[12] Feng, S., Thorpe, M. F., and Garboczi, E. (1985). Effective-medium theory of percolation on central-force elastic networks. *Phys. Rev. B*, 31(1):276–280

sum the bond stresses $\sigma^{(ij)}$ as independent identically distributed variables:

$$\overline{\Sigma^2} = \sum_{(ij)} \overline{\left[\delta\sigma^{(ij)}\right]^2} = C\Sigma_0^2, \tag{4.36}$$

where $\Sigma_0^2 = \sum_{(ij)} \left[\sigma_m^{(ij)}\right]^2$ can be computed from the stress field in the homogeneous system with appropriate boundary conditions and active body forces. This procedure is used to obtain the normalization factor of Figure 4.5(b). Note that C takes a simple form in the weak disorder limit $\mathrm{Var}(\alpha) = \delta\alpha^2 \ll \overline{\alpha}^2$. Indeed, setting $\overline{\alpha} = 1$ Equation 4.33 yields

$$\alpha_m = 1 - \frac{2d}{z}(\delta\alpha)^2 + \mathcal{O}\left[(\delta\alpha)^3\right], \tag{4.37}$$

and the numerical factor becomes $C = \delta\alpha^2 + \mathcal{O}\left[(\delta\alpha)^3\right]$, yielding Equation 4.28.

5
Local nonlinearities in fiber networks

> The most exciting phrase to hear in science, the one that heralds new discoveries, is not "Eureka!" (I found it!) but rather, "hmm.... that's funny..."
>
> — Isaac Asimov.

In the previous Chapter, we have solved the question of stress production by active units embedded in linear elastic media, by showing that it obeys a simple law (Equation 4.31) that is independent from the network's mechanical properties. This is a consequence of the conservation of the force dipole, which in turn results from the symmetry between compressive and tensile stresses in linear media.

However, biological fiber networks do not always respond linearly to active forces. For instance, we have seen in Chapter 2 that the active forces exerted by molecular can exceed the buckling threshold for individual filaments, which results in a non-linear response of the network. In the remainder of this Thesis, we will discuss how these non-linearity modify force transmission. In this Chapter, we first focus on the scale of the network's mesh size:

How do nonlinear properties of single filaments, at the scale of the fiber network's mesh size, affect active stress generation?

We show here that non-linear effects can modify dramatically force distributions as they are transmitted through fiber networks. At large forces, the network *rectifies* all active forces into contraction, as illustrated in Figure 5.1: in this Figure, any local force distribution considered – either contractile or extensile, isotropic or anisotropic – results in far-field stresses that are strongly contractile and close to isotropic stress.

Contraction thus *emerges* in fiber networks subjected to large local forces. This comes in stark contrast with linear materials, in which far-

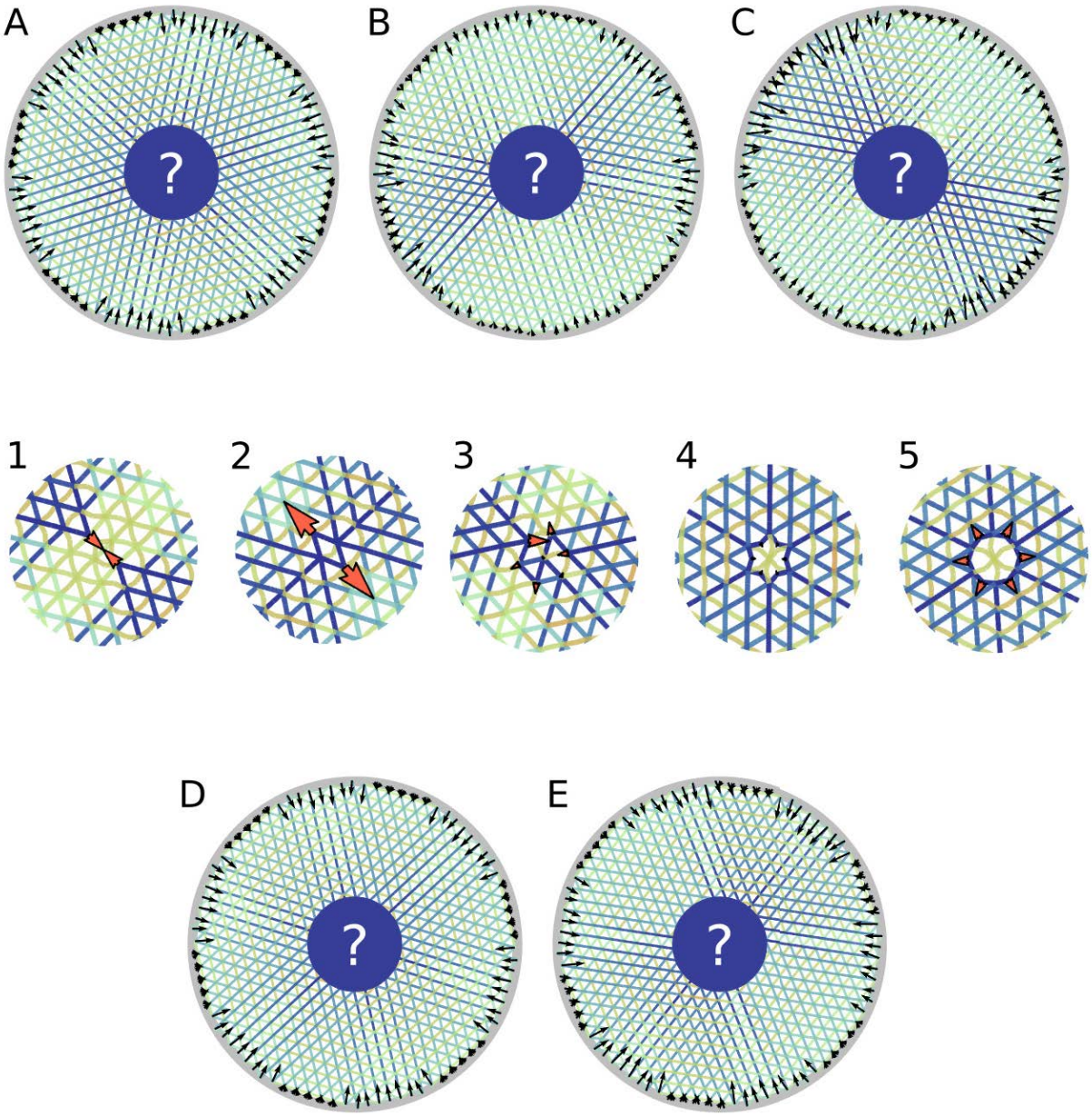

Figure 5.1: Illustration of the non-linear emergence of contractility in fiber networks. Applied local forces (red arrowheads) are transmitted through the network to result in boundary forces (black arrows) at the fixed boundary. The color patterns indicate stress in the network: red for compression, blue for tension, unstressed bonds in green.

Which local force distribution (1-5) results in which far-field stresses (A-E)?

Local forces, network stresses and boundary forces are to scale between each figure. Note that the rotation varies between the middle row and the networks. Parameters: regular triangular lattice with fixed boundaries and radius $R = 25$, $\mu = 10^4$. The force in (1) is $F = 250$, other forces are to scale. Answer: $_{\text{D-A-3-B-2-C-1.}}$

field stresses are completely determined by the geometry of active force distributions, regardless of the material's properties. The mechanical properties of the network will thus be of importance here, and in particular the distinction we have made in Chapter 3 between stiff, highly connected stretching-dominated networks, and softer, loosely connected bending-dominated fiber networks. In this Chapter, we study the local effects that result in this striking emergence of contractility. We identify two elementary mechanisms that bias the network's response towards contraction, which we study in turn:

1. *Plucking* (Section 5.1): a filament will tense when subjected to a transverse force, and exert effectively contractile forces on the surrounding network (Figure 5.2). This purely local effect can result in a strong stress amplification, which can occur at forces well below the buckling threshold, although only in stretching-dominated fiber networks.

2. *Buckling:* (Section 5.2): a filament will yield and buckle when compressed. This results in a robust rectification of forces larger than the buckling threshold towards contraction. This rectification effect occurs at the local scale, irrespective of the nature of the network. At large forces, buckling also result in a stress *amplification* and *isotropization*, and significantly affects force transmission on large scales, as we will show in Chapter 6.

Figure 5.2: Filament plucking.

Figure 5.3: Filament buckling.

In both cases, we study the regime of parameters in which the effect occurs, and assess their relative importance in the network's far-field response. We will make use of the framework introduced in Chapter 4: the effect of the nonlinearity on stress generation will be assessed in terms of the deviation from force dipole conservation, *i.e.* the difference between the local force dipole $\mathcal{D}^{\text{loc}}$ and the resulting far-field dipole $\mathcal{D}^{\text{far}}$.

Unless explicitly specified, in this Chapter – as in the remainder of this Thesis – we will not consider the tensorial nature of the force dipole, and focus on its trace.

5.1 Plucking

In this Section, we consider the response of fiber networks to local active forces applied transversely on a filament, similarly to a plucked guitar string. We will show in Section 5.1.1 that this effect can lead to dramatic stress amplification in stretching-dominated networks, while it remains moderate in bending-dominated networks. To elucidate the origins of this amplification, we consider in Section 5.1.2 the deformation of an individual semiflexible filament in response to transverse forces. We discuss in Section 5.1.3 the forces that are then transmitted to the networks, establishing scaling relations for this effect. We show in Section 5.1.4 how this results in an amplification of the far-field forces,

and confirm these predictions within our lattice fiber network. We conclude on the importance of this phenomenon by studying how it in Section 5.1.5.

5.1.1 The relative importance of plucking

The effect of fiber *plucking* studied here occurs when active forces are exerted transversely of a fiber segment, rather than at a network vertex where several fibers intersect. To assess the magnitude of plucking-induced stress, we can thus compare the far-field response of the network to forces of similar magnitude exerted as a "plucked circle" with forces exerted at mid-segments to a comparable geometry where the forces are exerted on the fiber intersections, as in Figure 5.4.

Starting with the case of a stretching-dominated regular network (Figure 5.4**a**), we plot in Figure 5.5 (white circles) the ratio between far-field dipoles in plucked and non-plucked cases. At very small forces, force transmission is linear, and this ratio is equal to unity. However, at a force $F \approx 10^{-3}$, well below the buckling threshold $F_b = 1$, linear force transmission breaks down, and the response of the plucked system becomes amplified at larger forces. This effect plateaus at $F \approx 0.2$, where this amplification is $\mathcal{D}^{\text{far}}_{(pluck)}/\mathcal{D}^{\text{far}}_{(non\text{-}pluck)} \approx 17$: in this range of forces, the far-field effects of plucking can completely dominate the response, and overwhelm the dipole resulting from linear transmission of applied forces, as evident in Figure 5.6. In particular, the far-field dipole is strongly contractile, regardless of the applied force dipole: strikingly, the stress pattern for contractile (Figure 5.6**b**) or extensile (Figure 5.6**c**) local forces are qualitatively similar, and quantitatively very close. In this regime, plucking thus *rectifies* active forces into contractile stress, which is *amplified* with respect to the linear prediction. At larger forces, this amplification starts decreasing slightly, up to the buckling threshold F_b where new phenomena appear, as the response to non-plucking forces becomes non-linear too. In this Section, we will focus on the case of forces smaller than F_b, where plucking is the only relevant non-linear phenomenon.

Consider now the case of a regular, bending-dominated network as introduced in Section 3.A. We can also distinguish situations where forces are applied so as to pluck filaments from cases where plucking is prevented, as shown in Figure 5.4**b**. However, plotting the ratio between far-field dipoles in these two cases (Figure 5.5, blue circles) shows only a very modest amplification due to plucking, culminating at $F = F_b$ with $\mathcal{D}^{\text{far}}_{(pluck)}/\mathcal{D}^{\text{far}}_{(non\text{-}pluck)} \approx 1.15$.

Plucking can therefore lead to a dramatic amplification of far-field forces in stretching-dominated networks, while it remains limited in bending-dominated networks.

a. Stretching-dominated network.

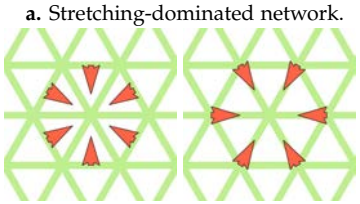

b. Bending-dominated network.

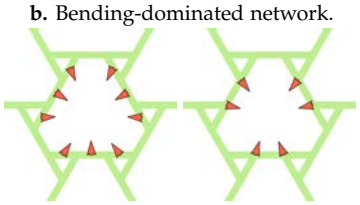

Figure 5.4: Circular forces applied in geometries with (left) and without (right) plucking.

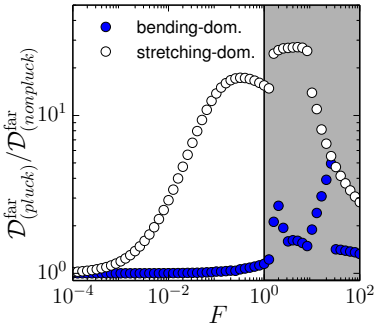

Figure 5.5: Contribution of the plucking effect to the far-field contraction, assessed by measuring the ratio of $\mathcal{D}^{\text{far}}$ for a plucked circle to that in a similar system, without plucking (*i.e.,* with forces applied at lattice nodes rather than mid-segments), as in Figure 5.4. White: triangular lattice, blue: bending-dominated regular network ("MAN"). In the gray area, buckling occurs, resulting in large displacements and complicated response of the network. Parameters: $\mu = 10^4$, far-field dipole measured at a fixed boundary at distance $R = 20$ of the active forces.

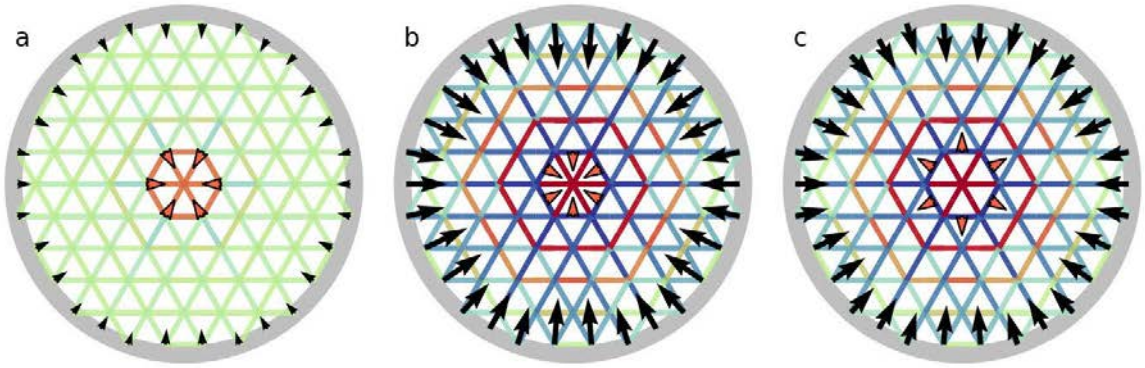

Figure 5.6: Nonlinear plucking effect in a regular, stretching-dominated network at maximal amplification. **a.** In the absence of plucking, force transmission is linear as the applied force is smaller than F_b. **b.** When forces of equal magnitude are applied such that they pluck filaments, the far-field dipole is dramatically amplified, being $17\times$ larger than in **a.** **c.** The response to a local extensile force dipole is quantitatively very close to a locally contractile one (**b.**), and the stress pattern is strikingly similar. Plucking thus dominates completely the response in this regime, and *rectifies all forces into amplified contraction*. Active force and stress scale are the same in the three panels; boundary forces are magnified $\times 5$ in panel **a.** for legibility. Parameters: $F = \pm 0.2$, $\mu = 10^4$.

5.1.2 Deformation of a single filament in response to transverse forces

We now propose a theoretical framework to explain the surprising results of the previous Section. We first set up the problem mathematically, then solve it in the case of small and large deformations. We will discuss the magnitude of the resulting stress transmitted to the network in the next Section.

Setup. Consider a semiflexible fiber with a transverse force applied at its middle-point, and bound to the network at its ends, as schematized in Figure 5.7. As we have discussed in Chapter 2, two effects oppose the deformation of the filament: its resistance to bending and to stretching. The resistance to bending is characterized by a bending energy $E_{\text{bend}}(\theta) = 2\sin^2(\theta/2)$, while the resistance to elongation is associated to a stretching energy $E_{\text{stretch}} = \mu(\delta\ell)^2/2$. The stretching-to-bending rigidity ratio $\mu \gg 1$ characterizes the relative importance of the two terms.

We have seen in the previous Section that the elastic properties of the network as a whole, and not only of the plucked filament, are important in this problem: indeed, bending- and stretching-dominated networks respond very differently to plucking. These networks mainly differ by their elastic modulus G, which is ~ 1 in soft, bending-dominated networks and $\sim \mu$ in stiff, stretching-dominated networks.

In the case of our plucked filament, the endpoints of the segment which are anchored to the rest of the network. Displacing them thus results in a deformation of the network, and a response that depends on the network's rigidity. A minimal way of including this response is to model the anchoring of the filament to the network by Hookean springs attached to fixed points. The deformation of these springs thus reflects the deformation of the network, and their spring constant k models the local rigidity of the network. A minimal model gathering all these physical ingredients is presented in Figure 5.7. The associated energy reads:

$$E = \underbrace{-F(x_0+X)}_{\text{plucking force}} + \underbrace{\left(\mu(\delta\ell)^2 + 2\sin^2\frac{\theta}{2}\right)}_{\text{filament deformation}} + \underbrace{k(x_0^2+y_0^2)}_{\text{network response}} \tag{5.1}$$

where $\delta\ell$ is the elongation of a filament, which is equal to:

$$\delta\ell = \sqrt{(1-y_0)^2+X^2} - 1 \tag{5.2}$$

As always in this Thesis, distances are normalized by setting $\ell_0 = 1$ and forces by setting the buckling force to unity. There are three free variables X, y_0 and x_0 in the configuration of the filament, whose values are set by minimizing the energy in Equation 5.1. The variable x_0 corresponds to a bulk translation of the filament with respect to the network, and is decoupled from the two other parameters, as evident by rewriting:

$$E = \left(-Fx_0 + kx_0^2\right) + \left(-FX + \mu(\delta\ell)^2 + 2\sin^2\frac{\theta}{2} + ky_0^2\right) \tag{5.3}$$

We can therefore set the value of x_0 by minimizing the first part, $-Fx_0 + kx_0^2$, of the energy, which simply corresponds to force balance in the x direction: the force monopole applied in the x direction is transmitted to the rest of the network without modification, and we will omit it in the following.

We will only consider cases where the elongation of the filament is small, *i.e.* when $\delta\ell \ll 1$. Indeed, typical values of the active forces do not result in significant elongation of biopolymers, as we have discussed Section 2.4. Besides, our model of filaments as hinged Hookean springs is inadequate for large extension of the fibers, as it does not include fiber stiffening. We now discuss solutions to the minimization of the energy in Equation 5.3.

Small displacements. We first consider the case where the response of the system to the active force has a small amplitude, *i.e.* when both $X \ll 1$ and $y_0 \ll 1$. In this regime we have

$$\delta\ell \approx \frac{X^2}{2} - y_0 \qquad \text{and} \qquad \sin\frac{\theta}{2} \approx X \tag{5.4}$$

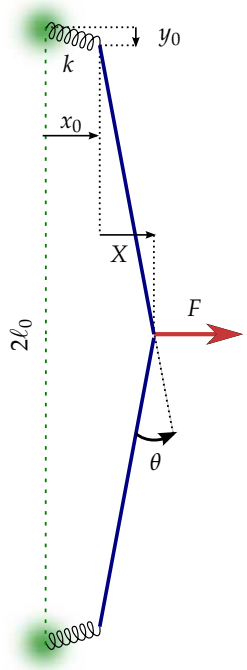

Figure 5.7: Schematics of the plucking scenario: a filament is anchored to the network (green clouds) by two springs of stiffness k and zero rest length that represent the network's propensity to deformate. Under the active force F (red arrow) exerted perpendicularly to the filament, it deforms and transmits forces to the network.

We rewrite the energy, omitting the translation term involving x_0:

$$E = \underbrace{-FX}_{\text{applied force}} + \underbrace{\mu\left(\frac{X^2}{2} - y_0\right)^2}_{\text{filament stretching}} + \underbrace{2X^2}_{\substack{\text{filament}\\\text{bending}}} + \underbrace{ky_0^2}_{\substack{\text{network's}\\\text{response}}} \tag{5.5}$$

Minimizing this energy yields:

$$F = \mu X(X^2 - 2y_0) + 4X \tag{5.6}$$
$$0 = -\mu(X^2 - 2y_0) + 2ky_0 \tag{5.7}$$

We can simplify this problem by replacing y_0 by its value

$$y_0 = \frac{\mu X^2}{2\mu + 2k} \tag{5.8}$$

which yields the following equation for the value of X:

$$F = \frac{\mu k}{\mu + k} X^3 + 4X \tag{5.9}$$

Importantly, the role of the filament's stretching modulus and the network's stiffness are combined in a single parameter

$$g = \frac{\mu k}{\mu + k} \sim \min(k, \mu) \tag{5.10}$$

which corresponds to an *effective stiffness* of the system. This dimensionless parameter controls the response of the filament to the plucking force: indeed, its deflection X is governed by

$$F = gX^3 + 4X \tag{5.11}$$

Physically, there are two ways the end-to-end distance of the filament can vary: either by stretching the filament, or by deforming the surrounding network. The response of the system is controlled by the softest of these two deformation modes, encoded by the effective stiffness g. The solution of this equation is thus determined by the interplay between the plucking force F and the effective stiffness g. We can distinguish two scaling regimes for the solution of Equation 5.11:

- $F \ll \min\left(8/\sqrt{g}, 1\right)$: the bending term dominates the energy, and thus:

  $$X \sim \frac{F}{4} \tag{5.12}$$

  and (using Equation 5.8)

  $$y_0 \sim \frac{gF^2}{32k} \tag{5.13}$$

Although from a strict scaling point of view we could omit the numerical prefactors factor 8, 1/4, *etc.*, they significantly affects the order of magnitude of the effect and the crossover values from one regime to another. For realistic values of μ in the $10^3 - 10^4$ range, $8/\sqrt{g}$ is very different from $1/\sqrt{g}$. For this reason, numerical prefactors are included in scaling relations in this section.

- $8/\sqrt{g} \ll F \ll g$: the stretching term dominates, hence

$$X \sim \left(\frac{F}{g}\right)^{1/3} \tag{5.14}$$

and

$$y_0 \sim \frac{g^{1/3}F^{2/3}}{2k} \tag{5.15}$$

Note that this regime only exists if $g \gg 1$, *i.e.* if both the network's and the filament's stretching rigidities are much larger than the filament's bending rigidity.

The upper bounds of these scaling regimes are set by physical consistency of our reasoning, which requires that displacements are small, *i.e.* $X \ll 1$ and $y_0 \ll 1$, for the simplification in Equation 5.4 to apply.

Large deformations. At large deformations, this simplification no longer applies, and minimizing the energy is mathematically difficult. We now briefly consider this case, where X and y_0 (as defined on Figure 5.7) are of order one, while $\delta\ell$ should remain small as discussed earlier.

This requires to have $k \ll \mu$ to remain in the physical regime where stretching remains small; in this situation the springs and fiber segments align, as depicted in Figure 5.8. Even in this asymptotic regime, the solution is quite complicated, and here we simply mention its asymptotic solution when $k \ll F \ll \mu$ (and $F \gg 1$ so that the deformation is large), in which case we have:

$$y_0 \approx 1 - \sqrt{\frac{k}{F}} + O(k/F) \tag{5.16}$$

In this regime, we thus have $y_0 \sim 1$ and $X \sim 1$.

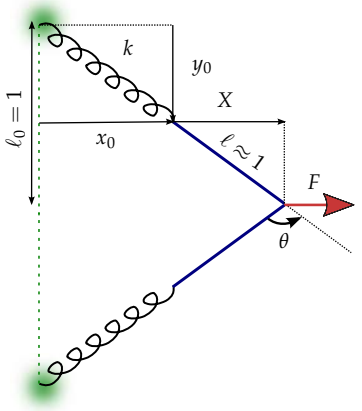

Figure 5.8: Plucking in the $k \ll F \ll \mu$ limit.

5.1.3 Scaling regimes for the plucking dipole

Equations 5.12 to 5.16 describe quantitatively the deformation of a plucked filament bound to a deformable network. We now discuss the forces that this filament exerts on the surrounding network. They can be decomposed in two components: a monopole of force F transmitted in the x direction, and an additional force dipole $\Delta = -2F_y = -2ky_0$ in the tangent direction. This *plucking dipole* is the relevant quantity to assess the non-linear effects of plucking: indeed the network is equivalent to a non-plucked network with a force F distributed at the two anchor points of the filament, plus this additional dipole Δ between these two points. There are three scaling regimes for Δ, corresponding to the three regimes for y_0 (Equations 5.13, 5.13 and 5.16). In Figure 5.9, we draw a scaling diagram for the value of Δ, as a function of the applied force F and the effective stiffness g.

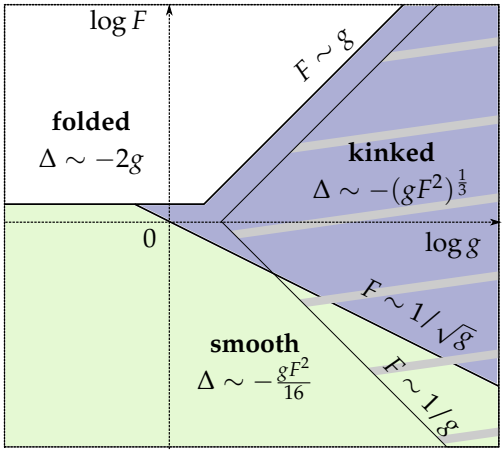

Figure 5.9: Phase diagram for the scaling regimes of the plucking dipole Δ as a function of applied force F and effective stiffness g. The filled areas are the scaling regions; the hatched area represents the domain of parameters where the filament's tangential force F_y is larger than the applied force F, and thus non-linear contraction dominates linear dipole transmission.

- smooth plucking: $(F \ll \min(1, 8/\sqrt{g})$

$$\Delta \sim -gF^2/16 \tag{5.17}$$

  In this regime, the filament curves smoothly, with a curvature radius larger than the filament length. Its response is dominated by its bending rigidity. The tangent force F_y is smaller than the buckling force, but can be much larger than the applied force F.

- kinked plucking: $(8/\sqrt{g} \ll F \ll g)$

$$\Delta \sim -g^{1/3}F^{2/3} \tag{5.18}$$

  Here the tangent force F_y is larger than both the buckling force and the applied force F, while the stretching rigidity and the network's rigidity keep the deformation of the filament small. The curvature is localized around the applied force, while the rest of the filament is straight. This regime only exists if $g \gg 1$.

- folded plucking: $(\max(g, 1) \ll F \ll \mu)$

$$\Delta \sim -2g \tag{5.19}$$

  In this last regime, the filament forms a cusp and folds around the point where the force is applied, and the network undergoes large deformations.

In all cases, the plucking dipole is contractile. Its magnitude depends strongly on the stiffness of the network k through the effective stiffness $g \sim \min(\mu, k)$. In Figure 5.11, we plot this plucking dipole for in the case of a stretching- and a bending-dominated network.

A pertinent point of comparison for Δ is the force dipole that an active unit would exert on a filament if the same force F were exerted tangentially on the filament: the typical force dipole is then $\Delta_{\text{ref}} = -2F$,

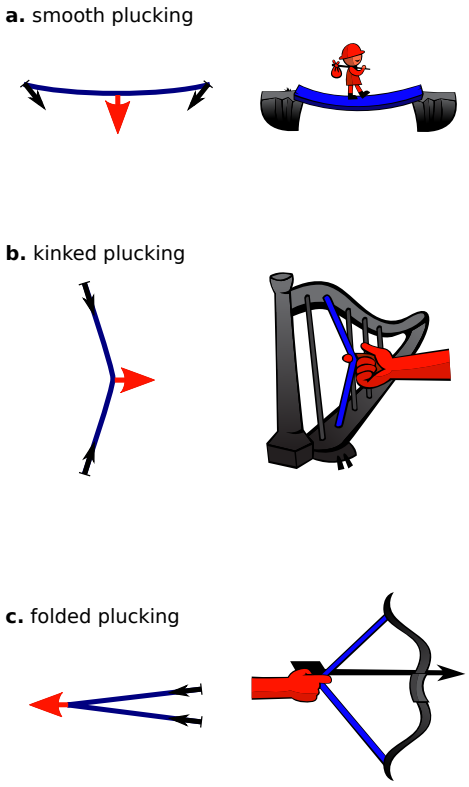

Figure 5.10: The three regimes for filament plucking, with everyday life analogs. Schematics courtesy of Dominika Šulcová.

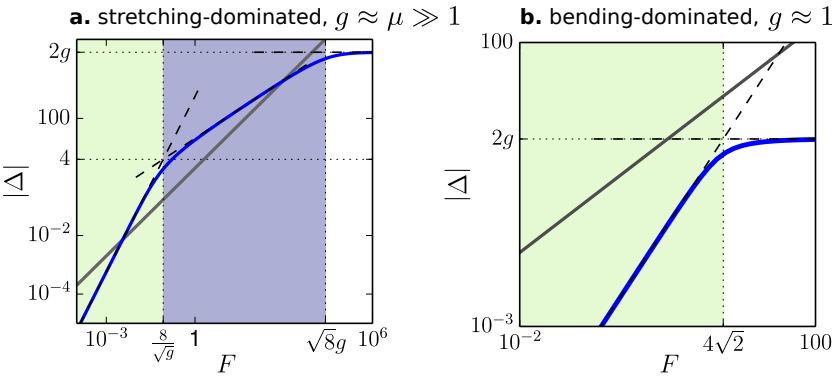

Figure 5.11: Force dipole exerted by a plucked filament at its attachment points, in the case of **a.** a stiff, stretching-dominated network ($k = \mu$), and **b.** a soft, bending-dominated network ($k = 1$). The blue line indicates the dipole Δ predicted by the numerical minimization of the energy in Equation 5.3). The dashed lines are the scaling regimes described in Equations 5.17 to 5.19, which are indicated as colored areas in the background: smooth (green), kinked (blue) and folded (white). The reference dipole $\Delta_{\text{ref}} = -2F$ is also shown as a gray line. Force dipole exerted by a plucked filament at its attachment points, in the case of a soft, bending-dominated network $k = \kappa = 1$, with $\mu = 10^4$.

which is plotted as gray lines in Figure 5.11. In other words, we compare the tangent force F_y the filament exerts on the surrounding network to the applied force F. In a large region of the phase diagram, as materialized by the hatched area of Figure 5.9 (a part of the smooth regime, and in particular in most of the "kinked" regime), the plucking dipole's magnitude is actually larger than Δ_{ref}. This means that for these parameters, contractility due to plucking is likely to dominate the network's response to local forces. Note however that this effect only occurs when $g \gg 1$, *i.e.* when the network's elastic modulus is much larger than the filament's bending rigidity. As a consequence, this dominance of the plucking dipole can occur in stiff stretching-dominated networks, but not in soft bending-dominated ones.

5.1.4 Force rectification and amplification in plucked networks

We have seen in Section 5.1.1 that plucking can result in a dramatic amplification of the far-field dipole and, in the case of locally extensile forces, stress rectification towards contraction. We now show that the formulas we have derived in Section 5.1.3 in the case of a single filament account for these effects.

We consider the system depicted in Figure 5.12, where as in Section 5.1.1 forces are applied perpendicularly to a circle of radius R_0, at approximately πR_0 mid-segment points (the rest length of a segment being 2). The applied force dipole is thus:

$$\mathcal{D}^{\text{loc}} = \pi R_0 \times F \times R_0 = \pi R_0^2 F \tag{5.20}$$

Each plucked filament responds non-linearly to the applied force, and exerts a plucking dipole Δ in the orthoradial direction. These non-linear contributions add up, resulting in an additional force dipole:

$$\mathcal{D}^{\text{pluck}} = \pi R_0 \Delta \tag{5.21}$$

Figure 5.12: Plucking forces applied as a circular dipole of radius R_0. The force F is counted positive if going outwards (*i.e.*, an extensile dipole) and negative for a contractile dipole, as depicted here.

When $F < 1$, force transmission beyond the individual filament level is then linear, and dipole conservation thus avails. The far-field force dipole is then:

$$\mathcal{D}^{\text{far}} \approx \mathcal{D}^{\text{loc}} + \mathcal{D}^{\text{pluck}} = \pi R_0 \left(R_0 F + \Delta\right) \tag{5.22}$$

Dipole amplification The contribution of plucking to the far-field dipole can be quantified by the *dipole amplification*[1] A with respect to the linear theory, which thus reads:

$$A = \frac{\mathcal{D}^{\text{far}}}{\mathcal{D}^{\text{loc}}} \approx 1 + \frac{\Delta}{F R_0} \tag{5.23}$$

The three scaling regimes for Δ discussed in Section 5.1.3 thus imply the following scaling regimes for the dipole amplification:

$$A \approx \begin{cases} 1 - \frac{gF}{16 R_0} & \text{smooth regime,} \quad F \ll \min(1, 8g^{-1/2}) \\ 1 - \frac{g^{1/3}}{F^{1/3} R_0} & \text{kinked regime,} \quad 8g^{-1/2} \ll F \ll g \\ 1 - \frac{2g}{F R_0} & \text{folded regime,} \quad \max(g, 1) \ll F \ll \mu \end{cases} \tag{5.24}$$

In the smooth regime, the amplification increases with increasing F, while it decreases in the kinked and folded regimes. It thus exhibits a maximum close to the crossover value.

Stretching-dominated networks. In stiff networks, the plucking dipole becomes of the same order of magnitude as the linear dipole within the smooth plucking regime, for a force $F \approx 16 R_0 / g$. At forces larger than this value, if the applied force dipole is extensile, the far-field dipole is *reversed* and becomes contractile: the network *rectifies* extensile forces towards contraction, as illustrated in Figure 5.14.

The maximal value of the amplification is attained at the crossover between smooth and kinked regimes, for $F \approx 8g^{-1/2}$ (Figure 5.9), where it culminates at

$$A_{\max} \approx 1 + \frac{\sqrt{g}}{2R_0} \tag{5.25}$$

As g can be very large in this regime, so can the amplification. For instance, for $R_0 = 2$ and $\mu = 10^4$, as in Figures 5.5 and 5.6, and taking $k = \mu$ as the network is stretching-dominated, we thus predict $A_{\max} \approx 18.7$. This single-filament prediction is in excellent agreement with data presented in Figure 5.5, where we find $A_{\max} = 17.3$. More generally, we find that the predictions from Equation 5.24 are quantitative in the whole range of values $F < 1$ where there is no buckling, as shown in Figure 5.13. Our theory thus quantitatively accounts for the dramatic stress amplification due to plucking in stretching-dominated networks.

[1] Read "capital alpha".

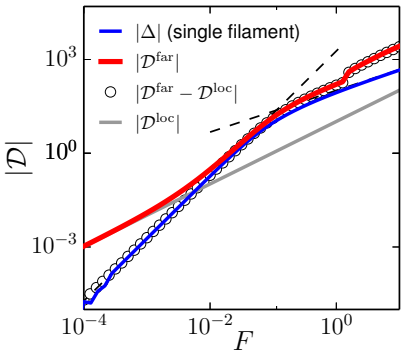

Figure 5.13: Force dipole for circular contractile plucking forces, as in Figure 5.14. The theoretical prediction from the minimization of Equation 5.1 (blue line as in Figure 5.11**a.**) was obtained by taking a network stiffness $k = \mu$. The agreement between network simulations and single filament plucking prediction is quantitative for $F < 1$; at larger forces, buckling occurs, which complicates the network's response. Parameters: $\mu = 10^4$, system radius $R = 9$. As force transmission is linear beyond the plucked circle, the size of the system is unimportant.

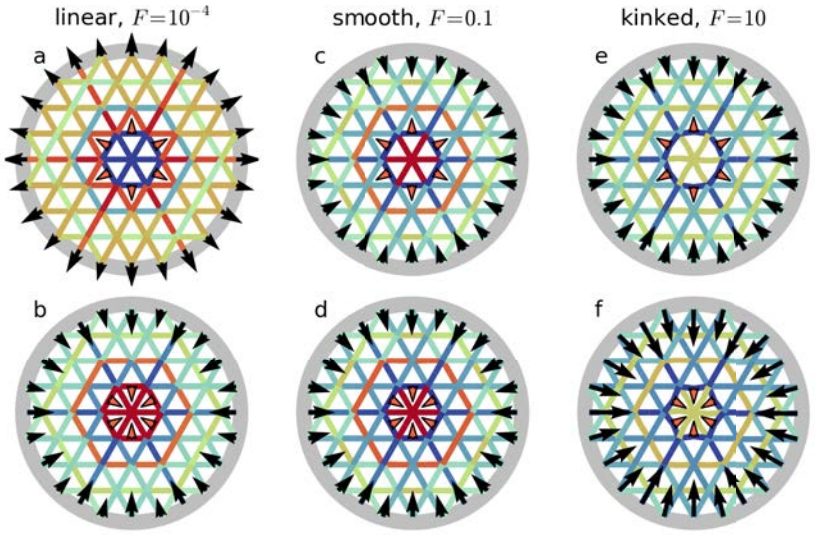

Figure 5.14: Linear response of a regular network to a circle of plucking forces. Unstressed, tensed and compressed filaments are respectively depicted in green, blue and red. Red arrow represent the plucking forces. The system is circular, with fixed boundary conditions at the gray circle; forces exerted by the system at this boundary are shown as black arrows. Parameters: $\mu = 10^4$, $F = 10^{-4}$.

Bending-dominated networks. In contrast, when $g \sim 1$, the amplification is maximal at $F \approx 4\sqrt{2}$ regardless of the value of g. This maximal amplification is

$$A_{\max} \approx 1 + \frac{g}{2\sqrt{2}R_0} \tag{5.26}$$

which remains close to one in this regime of parameters. For instance, consider the case of a regular, bending-dominated network subjected to circular plucking forces at a radius $R_0 = 3.2$, as in Figure 5.15. Taking a network rigidity $k = 1$, corresponding to a response dominated by the bending rigidity, we predict using Equation 5.26 a maximal amplification $A_{\max} \approx 1.11$, in very good agreement with our the data in Figure 5.5, where we have $A_{\max} \approx 1.15$. Our local theory thus also successfully captures the fact that the magnitude of the plucking effect is negligible in bending-dominated networks. Indeed, in such networks plucking is typically unable to reverse an extensile force dipole, as shown in Figure 5.15**b**.

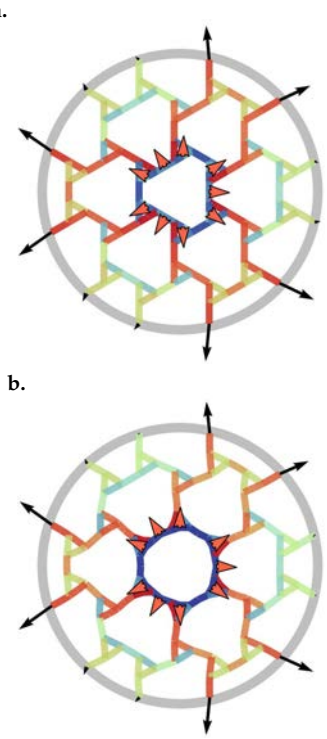

Figure 5.15: Plucking in a bending-dominated network. **a.** in the linear regime ($F = 10^{-4}$), and **b.** at the buckling threshold, $F = 1$. Parameters: $\mu = 10^3$.

5.1.5 Discussion

In this Section, we have shown that exerting transverse forces on a semi-flexible fiber segment, between its attachment points to the network, results in an effective force dipole that contains a non-linear contractile term, which we dub *plucking dipole*. We have proposed a simple theory for this effect, which considers only the deformation of a single filament, modeling the surrounding network as springs. The scaling regimes we predict quantitatively account for far-field stress measurements in simulated networks. We find that in soft, bending-dominated networks,

this effect is essentially negligible. On the contrary, in stiff, stretching-dominated networks, the plucking dipole completely dominates the far-field response in a wide range of parameters. This results in a dramatic amplification of the far-field dipole and, in the case of locally extensile forces, in their rectification into effective contraction.

These effects of amplification and rectification are robust, and do not depend on the network's geometry or dimensionality, provided that it is stretching-dominated. For instance, Figure 5.16 presents rectification of a spherical extensile force dipole in a three-dimensional face-centered cubic network. Indeed, the formulas derived in Section 5.1.3 are dimensionality-independent.

Plucking was previously discussed by Lenz in the context of actomyosin contractility[2], where he theoretically considers the force dipole that a complex of a myosin motor bound to two actin filaments transmits to the surrounding network. Actin semiflexible filaments are modeled as worm-like chains, while myosin is modeled as a "zipper" that processively moves along the polar filaments. Lenz then finds that filament plucking dominates this response and can lead to large force dipoles transmitted to the network; however he considers only rigid anchor points for the actin filaments, which fails to capture the key importance of the network's rigidity on the amplitude of the plucking dipole. Including network deformations in this kind of more realistic models would be, we suggest, an interesting direction for future research.

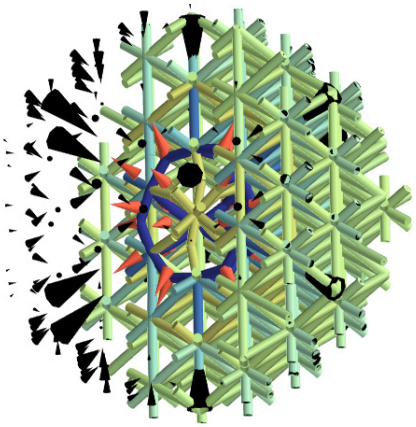

Figure 5.16: Dipole reversal in a plucked 3D stretching-dominated network, in the kinked regime. The extensile dipole applied at a spherical geometry (red cones) are rectified into contractile forces at the fixed boundary (black cones). For legibility, only half of the networks is shown. Parameters: FCC network with $F = 50$ and $\mu = 10^3$.

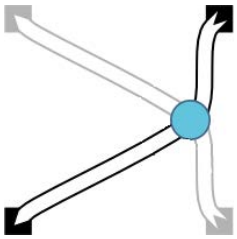

Figure 5.17: A myosin motor (blue) can bind to a pair of actin filaments, and will move towards their barbed end (right) until it stalls. The force it transmit to each filament includes a tangential component, which results in plucking-induced contraction at the binding points of the filaments to the network (black squares). Adapted from (Lenz, 2014).

[2] Lenz, M. (2014). Geometrical Origins of Contractility in Disordered Actomyosin Networks. *Phys. Rev. X*, 4(4):041002

5.2 Buckling

The second kind of local non-linearity in fiber networks we consider in this Chapter is the buckling instability. Buckling occurs when a filament is subjected to compressive, tangential forces. If the compressive stress is larger than the *buckling threshold*, the filament yields and bends, and is unable to withstand further stress. This results in a truncation of compressive stresses along a fiber, which cannot exceed the buckling threshold. Tensile stresses, on the other hand, are not bounded, and can propagate. In this Chapter, we investigate the consequences of this constitutive asymmetry between tension and compression on the local response of fiber networks to active forces.

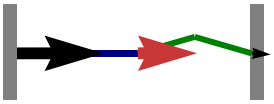

Figure 5.18: Buckling of a filament prevents it from transmitting compressive stress, leading to a local dominance of tensile stresses that results in far-field contraction.

The fact that fibers cannot bear compressive stresses above the buckling threshold leads to a shift of the average stress towards tension, which can propagate. We have seen in Section 4.1.2 that the mean-stress theorem[3] connects local to far-field forces through the *integrated stress* $\Sigma = \int \sigma \, \mathrm{d}V$. At linear order, symmetry between compression and tension in the response to point forces makes this quantity vanish. When there is buckling however, compressed elements yield, leading to a dominance of tensile stresses, for which $\sigma > 0$. As a result, $\Sigma > 0$, which leads to far-field stresses that are more contractile (or less extensile) than in the linear regime. We illustrate this effect with Figure 5.1, where large local forces result in uniform far-field contraction, regardless of their local geometry. In the specific case where forces are applied transversely to a filament in a stiff, stretching-dominated network, we have shown in the previous Section how plucking accounts for this far-field contraction. In this Section, we show how buckling, more generically, can account for the rectification of all local forces towards uniform, amplified contractility in both stretching-dominated and bending-dominated elastic fiber network.

We start this Section by considering the case of regular, two-dimensional stretching-dominated networks. In Section 5.2.1 we show how buckling there results in such a rectification of local forces into uniform and strongly contractile stress. In Section 5.2.2, we then show how these results extend to soft, disordered bending-dominated networks. We conclude on the generality of these effects in Section 5.2.3 by demonstrating that they apply independently of the dimensionality of the network and the distribution of local active forces. Finally, using a specific model, we demonstrate in Section 5.2.4 that buckling of individual filaments is indeed responsible for force rectification and amplification in fiber networks.

[3] We recall the mean-stress theorem:

$$\mathcal{D}^{\mathrm{far}} = \mathcal{D}^{\mathrm{loc}} - \Sigma$$

5.2.1 Stress rectification and isotropization

We now show that in two-dimensional, stretching-dominated networks, local forces larger than the buckling threshold are rectified into strong isotropic contraction. Consider local forces applied in a simple, regular triangular lattice, as in Figure 5.19. We choose forces applied in the form of a two-points force dipole, exerted at the nodes of the network to avoid plucking of the filaments. For emphasis of the effect, we consider locally extensile forces. The linear response results in a simple transmission of these pushing forces to the boundary, as depicted in Figure 5.19. Note the presence of slightly contractile forces in the direction normal to the dipole, which result from the fact that the network's Poisson ratio is positive.

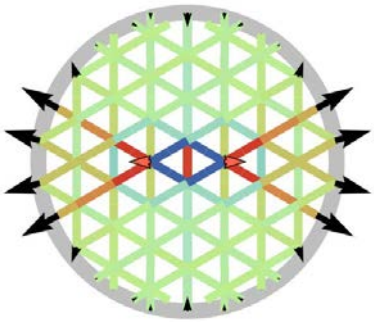

Figure 5.19: Linear response to an extensile force dipole.

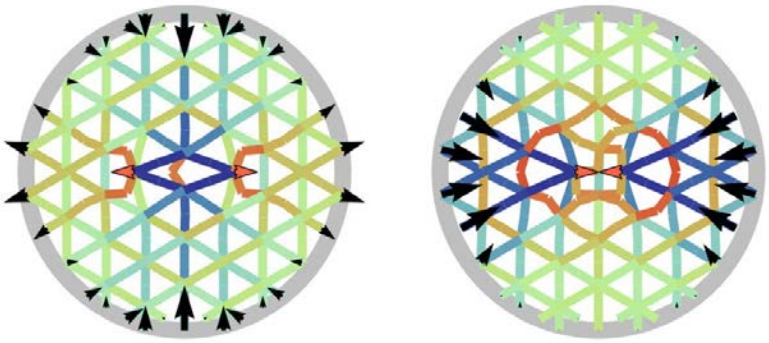

Figure 5.20: Response of the network to forces larger than F_b, respectively extensile (left) and contractile (right). The amplification of far-field forces is $A = -0.55$ and $A = 3.6$, respectively. For better rendering of the deformation, the following parameters were chosen: $\mu = 10^2$, $F = 40$.

Rectification and amplification. The situation is dramatically different in the large force regime ($F \gg F_b$), where fibers buckle and induce nonlinear network response. This is illustrated in Figure 5.20, where in response to a strong extensile force dipole, the far-field forces are contractile. The amplification ratio $A = \mathcal{D}^{\text{far}}/\mathcal{D}^{\text{loc}}$ is thus negative. Extensile local forces are thus *rectified towards contraction*. In response to contractile local forces, on the other hand, the far-field stresses remain contractile and become *amplified*, with $A > 1$. We will study this amplification ratio more thoroughly in the next Chapter, however let us note here that it can become significantly larger than one, as in shown in Figure 5.22.

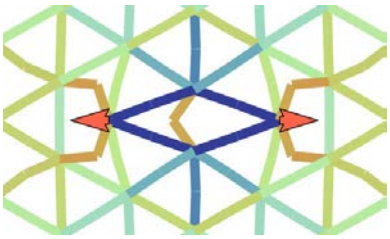

Figure 5.21: Close-up on the network around the strong extensile dipole in Figure 5.20.

These three regimes – linear for $|F| < F_b$, amplification for $F < -F_b$ and rectification for $F > F_b$ – are visible in Figure 5.22, where we plot $\mathcal{D}^{\text{far}}$ as a function of $\mathcal{D}^{\text{loc}}$. The breakdown of the linear relation $\mathcal{D}^{\text{far}} = \mathcal{D}^{\text{loc}}$ is concomitant with the onset of buckling in the vicinity of the points of application of the forces. The origin of these behaviors is apparent from the spatial arrangement of the forces around the applied

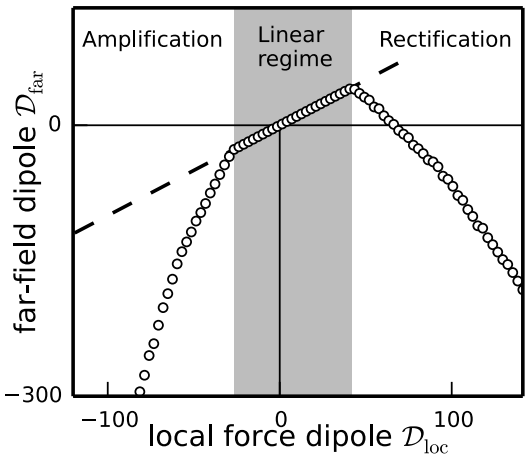

Figure 5.22: Amplification, linear and rectification regimes for $\mathcal{D}^{\text{far}}$ in a regular triangular network, as a function of the local dipole $\mathcal{D}^{\text{loc}}$. The dashed line indicates the linear relation $\mathcal{D}^{\text{far}} = \mathcal{D}^{\text{loc}}$. Parameters: $\mu = 2.10^3$, system radius $R = 11$.

forces, as shown in Figure 5.21. While contractile and extensile active units both induce a combination of compressive and tensile stresses in their immediate surroundings, the buckling of the individual bonds prevents the long-range propagation of the former. This results in enhanced tensile stresses in the far-field, and thus in strongly contractile far-field dipoles.

Note that in this Section, we apply force dipoles on next-to-nearest neighbors rather than nearest neighbors, such that the two point forces are exerted on distinct fibers. The rationale for this choice is both physical and practical. Physically, cells embedded in extracellular matrix, as well as myosin motors pulling on actin, typically exert forces on different filaments (a myosin thick filament will, for instance, anchor to a pair of actin filaments). Practically, force dipoles applied on nearest neighbor vertices result in a stress response that is dominated by the very stiff stretching response of the bond joining the two vertices. In such a situation, the response of the system will be dominated by local effects even in the bending-dominated regime, which is both unrealistic and trivial. An alternative option would have been to systematically remove the bond joining the two vertices. However, this biases the network to be locally softer than average, while applying the forces on next-to-nearest neighbors does not introduce such a bias.

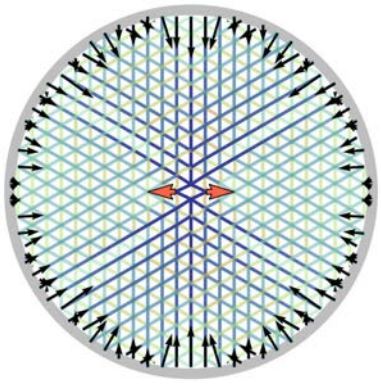

Figure 5.23: At large local forces, far-field stresses become isotropically contractile regardless of the local anisotropy of the active force distribution. Parameters: $\mu = 10^4$, $R = 25$, $F = 250$.

Stress isotropization. In Chapter 4, we have seen that linear force transmission preserves not only the trace of the force dipole, but also all of its tensorial components: the local force anisotropies (up to the dipolar order) are transmitted to the far-field. This comes in sharp contrast to force transmission in the presence of buckling: on top of rectifying all forces into contraction, buckling leads to a loss of information about

the geometry of local forces in the far-field. At relatively large forces, this far-field stress distribution becomes close to isotropic contractility, regardless of the geometry of the active local forces. This phenomenon is well illustrated by Figure 5.1, where various local force distributions – contractile (1) and extensile (2, and Figure 5.23) dipoles, and a random set of forces with zero sum and torque (3) – all lead to very similar far-field stresses.

We can quantify this effect of *isotropization* using an anisotropy parameter for force dipoles, which we define as the squared norm of its non-isotropic component, divided by its total squared norm:

$$\alpha(\mathbf{D}) = \frac{\left\| \mathbf{D} - \frac{1}{d}\mathrm{Tr}(\mathbf{D})\mathbf{I}_d \right\|^2}{\|\mathbf{D}\|^2} = 1 - \frac{\left(\sum_\mu \mathcal{D}_{\mu\mu}\right)^2}{d\sum_{\mu,\nu}\mathcal{D}_{\mu\nu}\mathcal{D}_{\nu\mu}} \tag{5.27}$$

where d is the space dimension, $\mathbf{D}$ is a force dipole tensor, and $\mathbf{I}_d$ is the d-dimensional identity matrix. Defining $\alpha^{\mathrm{loc}} = \alpha(\mathbf{D}^{\mathrm{loc}})$ and $\alpha^{\mathrm{far}} = \alpha(\mathbf{D}^{\mathrm{far}})$, the conservation of the force dipole tensor in linear elastic media imply that $\alpha^{\mathrm{far}} = \alpha^{\mathrm{loc}}$.

We plot α^{far} as a function of the local force dipole in Figure 5.24. In the linear regime, for $|F| < F_b$, the anisotropy of the applied forces $\alpha^{\mathrm{loc}} = 0.5$ is indeed transmitted to the far-field, as indicated by the dashed line. In contrast, this anisotropy parameter indeed becomes very small for large local dipoles of either sign: the force distribution is "isotropized" through non-linear force transmission.

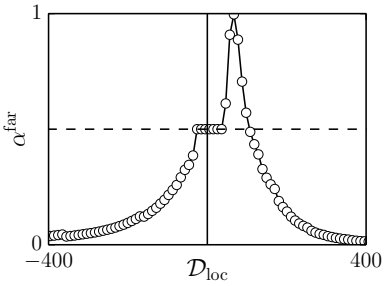

Figure 5.24: Anisotropy parameter as a function of the local dipole, in a regular triangular network. Parameters: $\mu = 10^4$, $R = 25$.

More precisely, α^{far} appears to go to zero in the triple limit of infinite system size $R \to \infty$, infinite force $F \to \infty$ and infinite stretching modulus $\mu \to \infty$. Indeed, as shown in Figure 5.25, α^{far} exhibit an apparently exponential decay with F, which saturates at a plateau that depends on R and μ. It seems that when these two quantities are large, the plateau value decreases, down to very small values of α^{far} – which can be as small as 10^{-6} in our simulations – where the far-field stress is almost isotropic. While a large system size seems to be necessary to attain the fully isotropic limit, we note that $\alpha^{\mathrm{far}} \approx 0.05$ is attainable with a system of only two mesh sizes of radius: most of the isotropization happens locally.

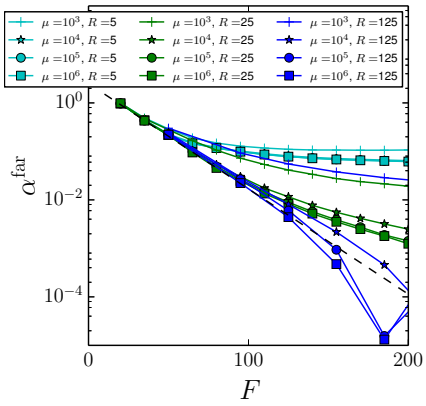

Figure 5.25: Decay of the anisotropy parameter at large local forces (extensile dipole), for various values of the system size R and stretching modulus μ. The dashed line is a tentative exponential decay fit, which works reasonably well over three decades of α^{far}.

We have thus shown in this Section that in regular, stretching-dominated lattice fiber networks, local force dipoles which exceed the filament buckling threshold are rectified into large contraction, which is close to isotropic at large force.

5.2.2 Disordered, bending-dominated networks

We now extend these results to the case of soft, bending-dominated depleted networks. In contrast with the plucking effect introduced in Section 5.1, which is relevant only in stiff, stretching-dominated

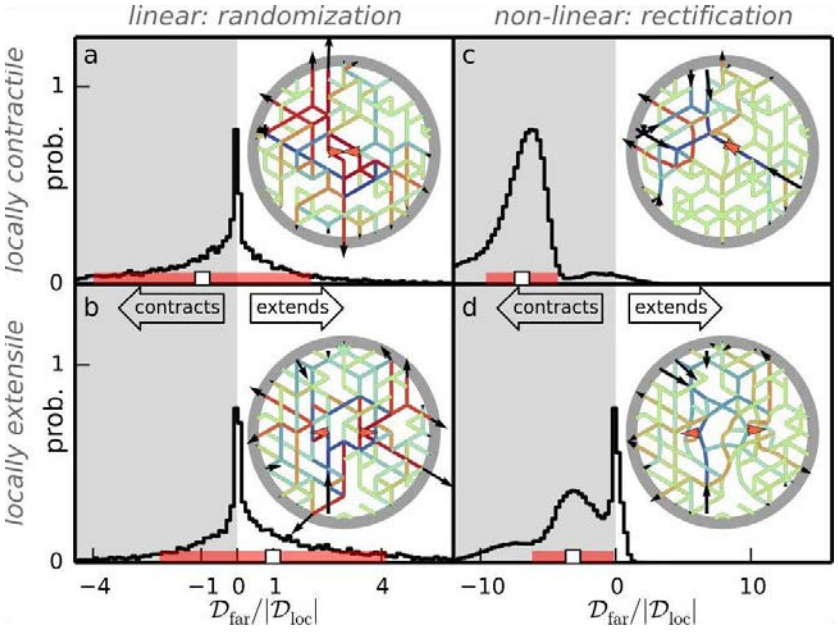

Figure 5.26: **(a-b):** In the linear response regime, the far-field dipole $\mathcal{D}_{far}$ exhibits a broad distribution with average $\mathcal{D}_{loc}$ and signal-to-noise ratio $= 0.3$. (histogram; the gray and white areas correspond to contractile and extensile systems, respectively). The square and red bar indicate the mean and standard deviation of the distribution. Insets: contractile and extensile active forces (red arrowheads) propagate along a complex network of force lines (blue=tension, red=compression), resulting in randomized force distributions at a fixed boundary (black arrows). **c-d:** At larger forces, both contractile and extensile dipoles typically result in contractile forces at the boundary ($\mathcal{D}_{far} < 0$). The corresponding distributions of amplifications are narrower than in the linear case (signal-to-noise ratio $= 2.6$ and 1.1, respectively). Parameters: $p = 0.6$, $\mu = 10^3$, $F = \pm 10^{-50}$ (a-b) and $F = \pm 20$ (c-d), average over 10^4 samples.

networks, we show here that bending-dominated networks are actually *more* sensitive to buckling. We thus find that the effects of rectification, amplification and isotropization apply to these networks; in addition, the transmission of such non-linear forces in depleted networks is more reliable than that of infinitesimal forces, as we now show.

Randomization at linear order. We have seen in Section 4.4 that the linear response of such networks, while obeying dipole conservation on average, exhibits large fluctuations. The very low signal-to-noise ratio in force transmission results in a "randomization" of the far-field response to active local forces. We recast this result by plotting the distribution of linear amplifications of a two-point force dipole (Figures 5.26 *a-b*). For instance, a significant fraction (37%) of all network geometries yield negative amplification, *i.e.*, an effective extensility in response to a contractile dipole (inset of Figures 5.26). Due to linearity, contractility in response to an extensile dipole is just as likely. Overall, the far-field response in the linear regime is only loosely correlated to the applied force dipole.

Buckling and rectification. The situation is dramatically different in the large force regime ($F_0 \gg F_b$), where fibers buckle and induce nonlinear network response. This is illustrated by the distributions of dipole amplifications in two opposite cases: a large contractile and a large extensile force dipole (Figures 5.26 *c-d*). While the detailed shape of these curves are model-dependent, three robust features emerge: First,

locally extensile dipoles predominantly undergo negative amplification, and are rectified into far-field contractility irrespective of the sign of $\mathcal{D}_{\text{loc}}$ (as in, *e.g.*, the inset of Figure 5.26 *d*). Second, the randomization observed in the linear regime is strongly attenuated, and the sign of the amplification is very reproducible (positive for 98% of the contractile dipoles and negative for 86% of the extensile ones). Third, the magnitude of the average amplification is significantly larger than one (in Figure 5.26 *c-d* $\langle \mathcal{D}_{\text{far}}/\mathcal{D}_{\text{loc}} \rangle = 6.9$ and -3.2 for contractile and extensile dipoles, respectively).

The effects of rectification and amplification of the dipole observed in the case of a regular network are thus preserved and statistically robust in the case of depleted, bending-dominated random networks.

Isotropization in bending-dominated networks. The far-field stress distributions are typically quite anisotropic for an individual sample of a random network, as evident in the networks shown in the insets of Figure 5.26. Indeed, the average anisotropy of the far-field stress persists at large forces, as shown in Figure 5.28 (red curve). However, these anisotropies are randomly oriented, and it is more relevant to consider the anisotropy of the average far-field stress (blue curve). Dipole conservation at linear order imposes that this quantity equals the anisotropy of applied forces at linear order (0.5 for a uniaxial force dipole in a 2D system). At large force, similarly to the regular stretching-dominated case, we observe that the average far-field stress becomes close to isotropic: the information about the orientation of the local active forces is lost through non-linear force transmission.

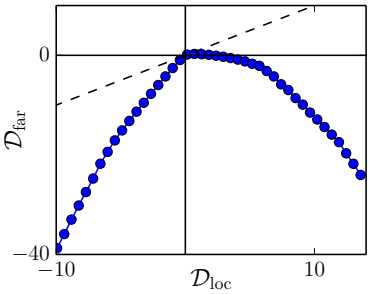

Figure 5.27: Far-field dipole as a function of the local dipole in a 2D bending-dominated network, showing amplification and rectification in the nonlinear regime. The dashed line indicates the linear prediction $\mathcal{D}_{\text{far}} = \mathcal{D}_{\text{loc}}$. Parameters: $p = 0.6$, $\mu = 2.10^3$, $R = 7$, average over 10^4 samples.

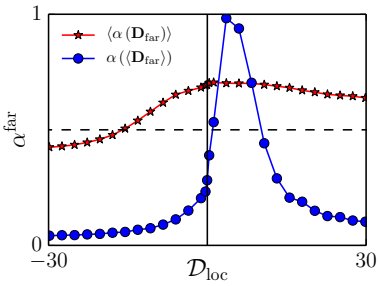

Figure 5.28: Far-field stress anisotropy as a function of the local force dipole in a 2D bending-dominated network. Parameters: $p = 0.6$, $\mu = 2.10^3$, $R = 21$, average over 10^3 samples.

5.2.3 Generality of stress rectification and amplification

On the examples of two-point force dipoles in regular stretching-dominated and random bending-dominated 2D networks, we have thus shown that buckling results in a rectification and amplification of large local forces into isotropic contraction in the far-field, regardless of their local geometry. These effects are generic properties of force transmission in elastic fiber networks, as we illustrate here. For instance, in contrast with plucking, rectification due to buckling can be observed regular bending-dominated networks (Figure 5.29).

We have systematically investigated these effects of rectification, amplification and isotropization of the stress in both bending- and stretching-dominated depleted networks, and in two and three dimensions, as shown in Figure 5.30. The far-field dipole and anisotropy dependence on the applied forces is, in each case, qualitatively similar to the 2D networks already discussed. Note that the very small threshold for non-linear effects is also observed in three-dimensional,

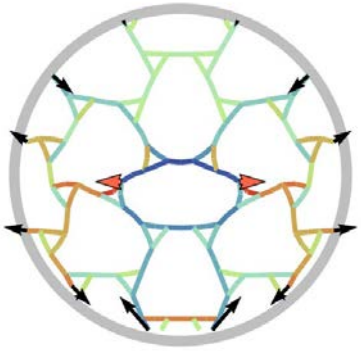

Figure 5.29: Rectification of an extensile force dipole due to buckling, in a regular bending-dominated network. The dipole amplification is $A = -0.3$. Parameters: $F = 3$, $\mu = 10^3$.

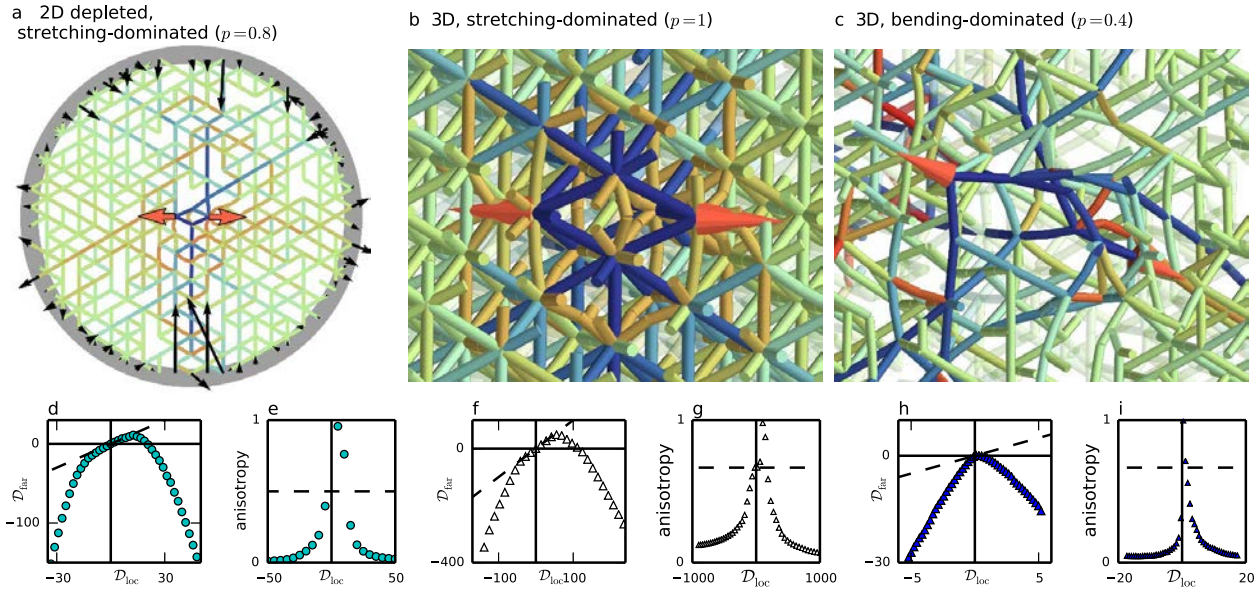

Figure 5.30: Rectification, amplification and isotropization effects are generic features of force transmission in fiber networks. **a-c:** Illustration of the rectification effect in response to an extensile force dipole in various networks. Because compressed segments buckle (red bonds), only tensile stresses (blue bonds) are propagated to the far-field. **d, f, h:** The far-field dipole becomes large and contractile for large local force dipoles of either sign. **e, g, i:** The anisotropy of the far-field stress vanishes for large local force dipoles.

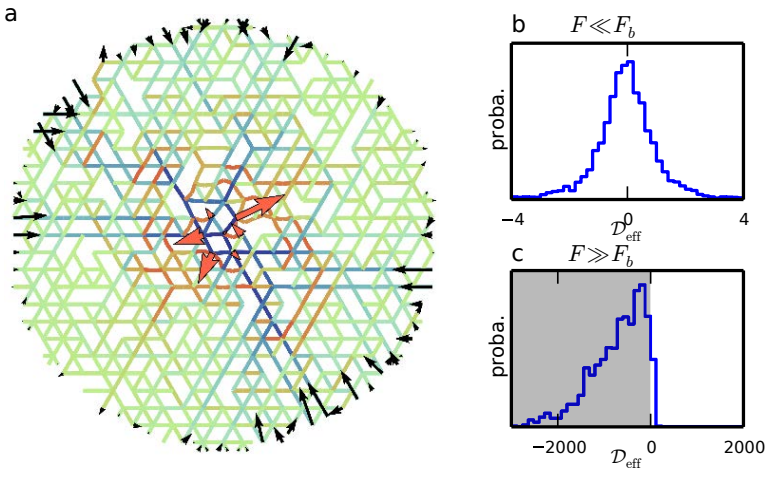

Figure 5.31: Rectification of arbitrary local force distributions into far-field contractility. We consider systems where random forces are applied in a small area of 7 lattice vertices, with the constraint that the total force and torque vanish. By symmetry, the resulting average local force dipole is equal to zero. **a:** Typical configuration, showing rectification at large forces. **b:** The distribution of the effective dipole measured at the boundary in the linear limit ($F \ll F_b$). As expected, the distribution is centered around zero, and the average effective dipole thus vanishes. **c:** In the large force limit, effective dipoles are overwhelmingly contractile (95% of cases), demonstrating the generality of the rectification effect. Here $p = 0.8$.

randomly depleted networks in the bending-dominated regime (Figure 5.30 *h-i*).

Complicated local force distributions. Finally, the precise geometry of the applied forces does not influence much the rectification effect, as illustrated by Figure 5.31 where we consider the response of a depleted network to a localized set of random forces. Again, for local forces the far-field response is overwhelmingly contractile.

5.2.4 Buckling and contraction: local asymmetry, global consequences

We have thus shown in this Section that beyond the immediate neighborhood of the active force-generating unit, strong isotropic contractile stresses emerge in the system from a generic local force distribution, due to the nonlinear force propagation properties of the fiber network. The crucial role of fiber buckling in this emergence of contraction can be further supported by the following "numerical experiment". We consider a similar lattice-based model, but replacing all segments of a regular triangular lattice by the unit pictured on the inset of Figure 5.32. This unit was designed so as to "anti-buckle": it yields under tension larger than a threshold force F_b, while it resists under compression.

Measuring in Figure 5.32 the far-field force dipole in response to local forces in this network, we observe the same effects of rectification and amplification of the stress – except that this time, extensile forces dominate. Contractile force dipoles are reversed at large forces, and extensility emerges in response to arbitrary local forces. This simulation demonstrates the central role of buckling in the emergence of contraction in fiber networks: reversing asymmetry in the force-extension of individual filaments results in a inversion of the rectification effect.

The asymmetry of the force-extension relation of the individual bonds constituting a fiber network thus results in the dominance of far-field contractile stresses. We note here that other physical systems, such as granular materials, exhibit force-extension relations for individual bonds that are essentially reversed, and closer to the anti-buckling units presented here. Hard spheres can be seen as an extreme case of this scenario: they can, by definition, sustain any amount of compressive stress, but will yield under any tensile stress. The consequences of this phenomenon are well-known in materials science: for instance, concrete needs to be reinforced so as not to crack under tension. Our simulations thus show that in response to large localized forces, such materials will tend to expand, regardless of the geometry of the applied forces. While this result may seem appealing[4], it may not be particularly useful. Indeed, the transmission of forces from the microscopic to the

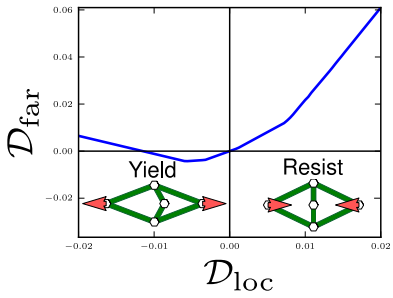

Figure 5.32: Far-field force dipole in response to local forces, in an "antibuckling network", *i.e.* a regular triangular lattice where all bonds are replaced by the local unit in inset. We designed this local unit so that it yields under tensile stress and resists to compressive stress.

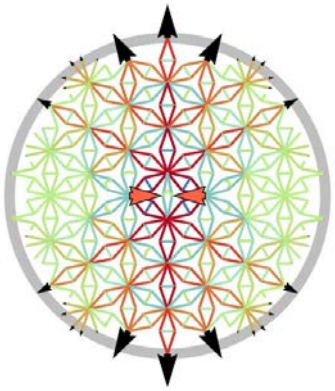

Figure 5.33: Reversal of contractile forces into far-field extension in an "anti-buckling network". Parameters: $\mu = 10^4$, $F = 400$.

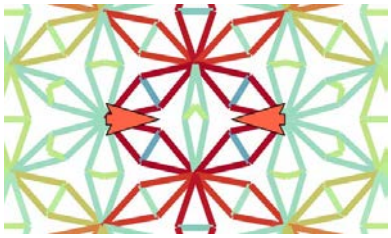

Figure 5.34: Close-up on Figure 5.33.

[4] To the author, at least.

macroscopic scale is, to this day, mostly interesting in the context of biological systems – where fibrous materials are prominent – in which local forces are exerted actively. In contrast, granular materials are typically passive, and their response to localized bulk forces does not have obvious applications.

5.3 The emergence of contractile stresses

We have discussed in this Chapter two kinds of local nonlinearities in the response of elastic fiber networks to local forces: plucking in response to normal forces, and buckling in response to compressive forces. In spite of their apparent similarity, the nature of these two effects is very different. Buckling is a *constitutive* nonlinearity: it is a property of the force-extension relation of individual semiflexible fibers[5]. It originates from their stiff, one-dimensional nature, and is intrinsically nonlinear, as it occurs only above a threshold force. In contrast, plucking is a purely *geometrical* nonlinearity, which sets in at infinitesimal force. It arises from the geometry of the exerted forces, while the precise nature of the force-extension relation of the filaments is irrelevant.

[5] Note that from the point of view of a single fiber made of atoms, buckling is also a geometric nonlinearity, as it arises due to the elongated geometry of the fiber rather than of the inter-atomic interactions; however, at the coarse grained scale of the fiber network, it is an intrinsic "constitutive" property of the individual fibers.

The consequences and importance of these two effects are also very different. Plucking leads to a force amplification, due to a geometrical projection effect: the tension in the filament can be much larger than the applied force. This results in dramatic effects, as this plucking tension – which is always tensile – can completely dominate the response, and for instance result in a reversal of extensile dipoles. However, it is a completely local effect: it either occurs at the point where the force is applied (if it is part of a soft mode), or not at all. Buckling, on the other hand, does not result in any *local* force amplification, but changes force transmission: it induces a better propagation of tensile stresses. This is not confined to the force application point, but can also strongly affect force transmission on large scales, as we will see in the next Chapter. Finally, buckling is a more generic property of fiber networks than plucking: while the latter occurs only in some specific configurations and in stiff networks, the former is essentially impossible to avoid, as soon as the applied forces are larger than the buckling force. In particular, most biologically relevant fiber networks are considered to be bending-dominated in physiological conditions. We have shown here that in such networks, plucking is essentially nonexistent, while buckling is easy and starts to be relevant at small forces.

Both of these phenomena result in far-field contraction, irrespective of the contractility of the source – provided that the local forces are strong enough. For this reason, we qualify this contractile nature of fiber networks as *emergent*. This emergence of contraction is accompanied by

a loss of information about the geometry of the source through force transmission. While linear materials preserve the sign and anisotropy of the source, we have shown here that in the presence of buckling, an *isotropization* of the stress occurs. A consequence of this combination of rectification and isotropization of the stress towards uniform contraction is that the local geometry of applied forces is of little relevance to the far-field response.

6
Buckling and force transmission

> I think there is only one way to do science – or to do philosophy for that matter; to meet a problem, to see its beauty and fall in love with it; to get married to it, and to live with it happily, till death do ye part – unless you should meet another and even more fascinating problem, or unless indeed you should obtain a solution. But even if you do obtain a solution you may then discover to your delight, the existence of a whole family of enchanting though perhaps difficult problem children for whose welfare you may work, with a purpose to the end of your days.
>
> — Karl Popper, *Realism and the Aim of Science.*

When compressed above a certain threshold force, a semiflexible fiber will yield and buckle. In the previous Chapter, we have seen how buckling modifies force distributions locally, and rectifies all forces towards isotropic contraction. It truncates compressive stresses above the buckling threshold, leading to a dominance of tensile stresses in the neighbourhood of a strong active unit. These tensile stresses may largely exceed the buckling force, and can thus lead to further filament buckling as they propagate towards larger scales. In this Chapter, we investigate the consequences of buckling at mesoscopic scales, beyond the immediate vicinity of the active unit:

What is the role of buckling in large-scale force transmission?

We will show that buckling modifies the scaling of stress decay away from an active unit, leading to long-ranged transmission of tensile forces. The distance at which an active unit is able to buckle fibers defines a new length scale R^*, which characterizes the range of non-linear effects that an active unit induces in the network. In Section 6.1, we start this Chapter by theoretical, continuum considerations about the

role of buckling in force transmission. We then present in Section 6.2 the adapted numerical model and in Section 6.3 the methods by which we study this force transmission problem in fiber networks. We finally discuss our numerical results in Section 6.4, and present open problems regarding soft disordered networks.

6.1 Linear and rope-like force transmission

We now study theoretically force propagation beyond the immediate vicinity of a strong active unit. We identify two asymptotic regimes for this propagation: in the far-field (Section 6.1.1), forces are too weak to result in buckling (or any other kind of nonlinear response), and linear elasticity theory applies. In the near-field, buckling results in a modification of the equations for force transmission (Section 6.1.2). The crossover between these two regions defines a new length scale, the "buckling radius" R^* (Section 6.1.3) which characterizes the far-field amplification of the stress (Section 6.1.4).

6.1.1 Linear force transmission

We consider a single active unit, localized at $r = 0$, embedded in an infinite d-dimensional fiber network. Let us start by considering the far-field response of the network. In this regime, stresses are small, and thus linear elasticity prevails. In the continuum limit, mechanical equilibrium in the absence of external forces yields $\nabla \cdot \sigma = 0$. Assuming spherical symmetry, we can rewrite this equation in spherical coordinates as:

$$\frac{1}{r^{d-1}} \frac{\mathrm{d}}{\mathrm{d}r} \left(r^{d-1} \sigma_{rr} \right) - \frac{d-1}{r} \sigma_{\theta\theta} = 0 \tag{6.1}$$

where $\sigma_{rr}(r)$ is the radial stress and $\sigma_{\theta\theta}(r)$ the angular stress (where θ denotes any of the $d-1$ angular directions). In an isotropic linear elastic material, the stress tensor is linear in the strain tensor:

$$\hat{\sigma} = 2G\hat{\gamma} + \lambda(\mathrm{Tr}\hat{\gamma})\hat{I}_d \tag{6.2}$$

where G and λ are Lamé's parameters for the material. In a spherically symmetric material, the strain components are:

$$\gamma_{rr} = \frac{\mathrm{d}u}{\mathrm{d}r}(r) \quad ; \quad \gamma_{\theta\theta} = \frac{u(r)}{r} \quad ; \quad \gamma_{r\theta} = 0 \tag{6.6}$$

where $u(r)$ is the radial displacement of the material. The stress components are therefore:

$$\sigma_{rr} = (2G + \lambda) \tfrac{\mathrm{d}u}{\mathrm{d}r}(r) + (d-1)\lambda \tfrac{u(r)}{r} \tag{6.7}$$

$$\sigma_{\theta\theta} = \lambda \tfrac{\mathrm{d}u}{\mathrm{d}r}(r) + (2G + (d-1)\lambda) \tfrac{u(r)}{r} \tag{6.8}$$

Lamé's parameters are convenient, as they yield very simple, dimensionality-independent stress-strain and strain-energy relations. The strain-energy relation is:

$$E(\hat{\gamma}) = \frac{\lambda}{2}(\mathrm{Tr}\hat{\gamma})^2 + G\mathrm{Tr}\hat{\gamma}^2 \tag{6.3}$$

The shear modulus is simply equal to G, while the bulk modulus, for instance, is given by

$$K = \lambda + \frac{2}{d}G \tag{6.4}$$

The Poisson ratio is:

$$\nu = \frac{\lambda}{2G + (d-1)\lambda} \tag{6.5}$$

Equation 6.1 thus yields:

$$(2G+\lambda)\left(\frac{\mathrm{d}^2u}{\mathrm{d}r^2}+\frac{d-1}{r}\frac{\mathrm{d}u}{\mathrm{d}r}-\frac{d-1}{r^2}u\right)=0 \tag{6.9}$$

which can be rewritten as

$$\frac{\mathrm{d}}{\mathrm{d}r}\left[r^{1-d}\frac{\mathrm{d}}{\mathrm{d}r}\left(r^{d-1}u\right)\right]=0 \tag{6.10}$$

Here we are interested in the deformations in response to a localized active unit in an infinite system, which should therefore vanish in the $r\to\infty$ limit. Solving Equation 6.10 yields $u(r)\propto r^{-(d-1)}$, which from Equations 6.2 and 6.6 implies:

$$\sigma_{rr}(r)\propto r^{-d} \tag{6.11}$$

The radial stress thus decays as r^{-d} with distance to an active unit in a linear elastic material.

It is interesting to note that the spherically symmetric deformation of a linear elastic material does not depend on its elastic moduli – and in particular on its Poisson ratio. The generic solution with arbitrary boundary conditions reads:

$$u(r)=Ar^{-(d-1)}+Br.$$

6.1.2 Rope-like networks

Let us now consider the transmission of large forces in a fiber network. The tensile strength of fibers allows the material to sustain any tensile stress, while compressive stresses above the buckling threshold are truncated. In the large force limit, we can therefore neglect all compressive stresses. We describe such a material as a *rope network*[1]. Indeed, in the limit of large stresses, the bending rigidity of semiflexible fibers becomes negligible, and they behave as flexible, almost inextensible ropes, which can sustain arbitrarily large tension, but no compression.

[1] The expression "cable network" can also be found in the literature, for instance in (Schwarz and Safran, 2013), with a slightly different meaning.

In a radial geometry, where an active unit exerts contractile forces at $r=R_0$, we can again write the spherically symmetric force balance equation (Equation 6.1):

$$\frac{1}{r^{d-1}}\frac{\mathrm{d}}{\mathrm{d}r}\left(r^{d-1}\sigma_{rr}\right)-\frac{d-1}{r}\sigma_{\theta\theta}=0$$

Here the radial stress is tensile, while the angular components are compressive, and can therefore be neglected due to buckling, which yields:

$$\frac{1}{r^{d-1}}\frac{\mathrm{d}}{\mathrm{d}r}\left(r^{d-1}\sigma_{rr}\right)=0 \tag{6.12}$$

The solution of this equation is straightforward, and reads:

$$\sigma_{rr}(r)\propto r^{-(d-1)} \tag{6.13}$$

Tensile forces thus decay as $r^{-(d-1)}$ in rope networks, and are therefore longer-ranged than in linear elastic materials. Physically, this longer range for forces comes from the fact that in a linear material,

radial tensile stresses are partially balanced by angular compression (Equation 6.1), while no such compensation occurs in a rope network (Equation 6.12). This long-range force transmission properties of elastic media with buckling was independently proposed by (Notbohm et al., 2014)[2], although using a peculiar linear-by-parts force-extension relation which results in different force transmission exponents and a singular absence of linear response at small force.

[2] Notbohm, J., Lesman, A., Rosakis, P., Tirrell, D. A., and Ravichandran, G. (2014). Microbuckling in fibrin networks enables long-range cell mechanosensing. *arXiv*, page 1407.3510
Rosakis, P., Notbohm, J., and Ravichandran, G. (2015). A model for compression-weakening materials and the elastic fields due to contractile cells. *Journal of the Mechanics and Physics of Solids*, 85:16–32

6.1.3 The buckling radius R^*

Consider an active unit of size R_0, exerting a contractile stress F at $r = R_0$. When this active stress is sufficient to induce buckling in the surrounding network, the stress decay corresponds to the rope-like regime (Equation 6.13), and thus:

$$\sigma_{rr}(r) \approx F \left(\frac{R_0}{r}\right)^{d-1} \qquad (R \ll R^*) \tag{6.14}$$

This equation remains valid as long as force-transmission is rope-like. However, at large distance the stress decays and eventually becomes smaller than the buckling force. At this point, compressive stresses become important, and force transmission crosses over to linear elasticity. Denoting by R^* this crossover length, we thus have in the far-field:

$$\sigma_{rr}(r) \approx F \left(\frac{R_0}{R^*}\right)^{d-1} \left(\frac{R^*}{r}\right)^{d} \qquad (R \gg R^*) \tag{6.15}$$

We can expect that this crossover between rope-like and linear force transmission occurs when radial stresses are comparable to the buckling stress, which implies that the crossover length depends on the active force as

$$R^* \approx R_0 \left(\frac{F}{F_b}\right)^{1/(d-1)}. \tag{6.16}$$

In two- and three-dimensional networks, this crossover length thus grows as F (resp. $\sqrt{F}$), and can therefore be very large for strong active units. Such a crossover length between near-field, long-range force transmission and the far-field linear regime was independently discussed in continuum theoretical models by (Xu and Safran, 2015)[3], although with different scaling exponents due to a different modeling of buckling, which allows the material to sustain large compressive stress.

[3] Xu, X. and Safran, S. A. (2015). Nonlinearities of biopolymer gels increase the range of force transmission. *Phys. Rev. E*, 92(3):032728

6.1.4 Stress amplification

Equation 6.15 describes the far-field effect of a strong active unit which induces buckling in a region of radius R^* around it. We can compare it

to the far-field stress $\sigma_{rr}^{(\mathrm{lin})}(r)$ it would induce in a linear elastic medium, in the absence of buckling:

$$\sigma_{rr}^{(\mathrm{lin})}(r) \approx F \left(\frac{R_0}{r} \right)^d \tag{6.17}$$

The far-field stress in the presence of buckling is thus amplified with respect to the linear stress field, as:

$$\frac{\sigma_{rr}(r)}{\sigma_{rr}^{(\mathrm{lin})}(r)} \approx \frac{R^*}{R_0} \qquad (R \gg R^*) \tag{6.18}$$

Since the "buckling radius" R^* grows with F and can be arbitrarily large, we conclude that buckling can lead to very large amplification of the far-field effects of an active unit. We now validate numerically the theoretical picture drawn in this Section.

6.2 A model for active units as "isotropic pullers"

In order to study transmission of large, tensile stresses in fiber networks, we first have to adapt our model for active units. Indeed, two-point force dipoles – as employed in the previous Chapter – are ill-fitted for this task, as the force they can exert is limited by a "pinching" effect: above a certain threshold, the points on which the force is applied collapse to a point, and they cannot exert any more force on the surrounding network. This effect is particularly notable in bending-dominated networks, where the network undergoes large deformations at forces just above the buckling force, as illustrated in Figure 6.1.

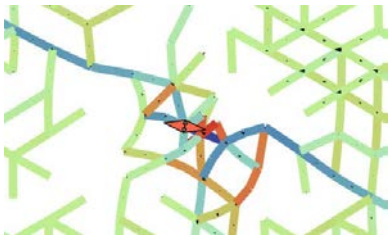

Figure 6.1: "Pinching" of a contractile two-points force dipole in a depleted network, where the two points of force exertion have collapsed to a point. The "dust" (small black arrowheads) in the rest of the network indicates non-converged residual forces, an algorithmic consequence of the singular nature of the force dipole Hamiltonian at a pinching point. Parameters: $p = 0.55$, $F = 3$.

This effect does not reflect a physical reality: biological active units, such as molecular motors and contractile cells, will continuously pull fibers in without collapsing. To study the response of fiber networks to large active forces, we thus need to adapt our model for active units. The model we propose is a localized, quadratic-by-parts potential well which processively "sucks in" nearby nodes of the network, and is therefore capable of exerting arbitrarily large forces without changing its size. This potential well is isotropic, which simplifies the study of radial stress propagation. This choice is furthermore justified by our study of the "isotropization" phenomenon in Chapter 5, where we have shown that local anisotropies are physically irrelevant in the large force case we consider here.

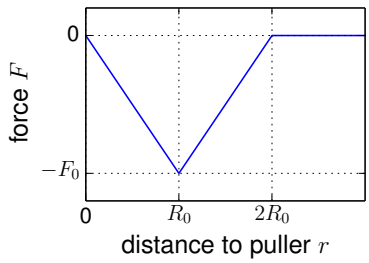

Figure 6.2: Force exerted by our "isotropic puller" model for active units, as in Equation 6.19.

More precisely, our model active unit is centered on a vertex i of the network, and pulls on every node j within a distance $2R_0$ with a radial force

$$\mathbf{F}_{ij} = \begin{cases} -F_0 \frac{r_{ij}}{R_0} \hat{\mathbf{r}}_{ij} & \text{if } r_{ij} < R_0 \\ -F_0 (2 - \frac{r_{ij}}{R_0}) \hat{\mathbf{r}}_{ij} & \text{if } R_0 \leqslant r_{ij} < 2R_0 \end{cases} \tag{6.19}$$

where F_0 is the maximum force exerted by the unit on a vertex, r_{ij} is the distance between i and j and $\hat{\mathbf{r}}_{ij}$ is the associated unit vector. The vertex j exerts in return a radial force $-\mathbf{F}_{ij}$ on the active unit node i, such that force and torque balance are ensured. In order to avoid the "plucking" effects described in Section 5.1, only lattice vertices are affected by the potential well, not mid-segment nodes. In practice, we choose $R_0 = 1.95$ throughout this Thesis (*i.e.*, the force is maximal at a distance of one lattice mesh size – or two mid-edge segments).

At infinitesimal force, such an active unit behaves exactly as a superposition of two-point force dipoles. At larger forces, and in particular at $F_0 > F_b$ in bending-dominated networks, the deformation around the active unit is large (Figure 6.3). The continuous "pulling in" of the unit results in an accumulation of fiber segments as a "clump" at the bottom of the potential well. This accumulation is an artifact of our model, the important part being the forces that are transmitted to the rest of the network by the filaments spanning the potential well's boundary, indicated as red arrows in Figure 6.3.

A strong active unit in a soft network may thus exert forces on large number of vertices, exerting a force $\approx F_0$ on each of them. Adding the contributions of all these fibers results in a large local dipole, the magnitude of which is not well reflected by the value of F_0. Furthermore, in soft networks, a large part of these exerted forces is directly compensated by the presence of compressive stresses inside the clump: segments that fall inside the potential well are compressed, since both of their endpoints are attracted towards the bottom of the well. Such stresses are irrelevant to the physics of the problem. To account for these effects, we employ the mean-stress theorem that we derived in Section 4.1.2. We remind the reader that at mechanical equilibrium, this theorem relates the force dipole $\mathcal{D}^{\text{loc}}$ exerted locally by active units to the far-field resulting force dipole at a fixed boundary $\mathcal{D}^{\text{far}}$ through the integrated stress Σ, which is the sum of stresses inside the elastic medium:

$$\mathcal{D}^{\text{far}} = \mathcal{D}^{\text{loc}} - \Sigma \tag{6.20}$$

We can rewrite this equation in the case of an isotropic puller i:

$$\mathcal{D}^{\text{far}} = \underbrace{\sum_{j|r_{ij}<2R_0} F_{ij} r_{ij}}_{\mathcal{D}^{\text{loc}}} - \sum_{\text{edges } e} \sigma_e \tag{6.21}$$

Here $\mathcal{D}^{\text{loc}}$ is the *internal* force dipole that the active unit exerts directly on filaments within its interaction range $2R_0$. We can now decompose

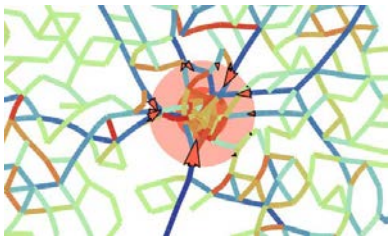

Figure 6.3: An isotropic puller embedded in a bending-dominated network. The light and dark red disks respectively indicate radius of $2R_0$ (where the active force vanishes) and R_0 (where it is maximal). Note the presence of a "clump" of fibers at the bottom of the well. The red arrows indicate tensions of the filaments that span the outer boundary of the motor.

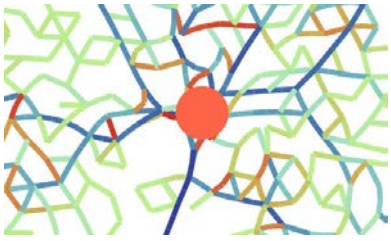

Figure 6.4: The same active unit, represented by a single disk of radius R_0, as in the remainder of this Thesis.

this equation into components outside and inside the active unit:

$$\mathcal{D}^{\text{far}} = \underbrace{\left(\sum_{j|r_{ij}<2R_0} F_{ij} r_{ij} - \sum_{e \text{ inside clump}} \sigma_e \right)}_{\mathcal{D}^{\text{unit}}} - \sum_{e \text{ outside clump}} \sigma_e \qquad (6.22)$$

This effectively results in separating the system into two subsystems, namely the inner and outer parts of the unit. The effective dipole that the active unit exerts on the rest of the network is $\mathcal{D}^{\text{unit}}$. Each of the subsystems obeys a separate mean-stress theorem:

$$\mathcal{D}^{\text{unit}} = \mathcal{D}^{\text{loc}} - \Sigma^{\text{clump}} \qquad \text{(inside)} \qquad (6.23)$$

$$\mathcal{D}^{\text{far}} = \mathcal{D}^{\text{unit}} - \Sigma^{\text{out}} \qquad \text{(outside)} \qquad (6.24)$$

Here Σ^{clump} and Σ^{out} are respectively the integrated stress for the portion of the network at a distance $r < 2R_0$ and $r > 2R_0$. The network edges that span the outer boundary of the active unit contribute to both terms, in proportions corresponding to the overlap with each region. Equation 6.23 describes the internal state of the active unit, which is uninteresting and quite unphysical. On the other hand, Equation 6.24 involves precisely the quantities of interest: it describes how the forces resulting from the action of the motor at the local scale propagate through the network to result in far-field stresses. Note that $\mathcal{D}^{\text{unit}}$ can equivalently be computed by measuring the dipolar moment of the forces at a virtual "cut" of the system at a radius $2R_0$ of the active unit[4], as indicated in Figure 6.3.

[4] And quite reassuringly these two methods give the same result numerically.

Note that in the linear case, we have $\mathcal{D}^{\text{loc}} = \mathcal{D}^{\text{far}}$ (on average in disordered systems), while nothing constrains the value of $\mathcal{D}^{\text{unit}}$: indeed, we have proved in Chapter 4 that $\Sigma^{\text{out}} + \Sigma^{\text{clump}}$ vanishes in the linear regime, but generically each of these two terms is different from zero. For this reason, $A = \mathcal{D}^{\text{far}}/\mathcal{D}^{\text{loc}}$ remains a useful quantity to measure stress amplification, as its average equals unity in the small-force limit where the network responds linearly.

To express the resulting dipole in terms of a typical force exerted by the active unit on the surrounding network, we divide it by its size and the area of the boundary of active unit[5]:

$$F = \frac{|\mathcal{D}^{\text{unit}}|}{(2R_0)^d \Gamma_d} \qquad (6.25)$$

[5] Strictly speaking, F as defined here would be a stress. However, the author feels that enough quantities are called "stress" in this manuscript already, and since the segment length is normalized this is also the typical force that the active unit exerts on a filament.

where Γ_d is the measure of the surface of the d-dimensional sphere (*i.e.*, $\Gamma_2 = 2\pi$ and $\Gamma_3 = 4\pi$). When an active unit pulls on many fibers, its force is thus better represented by the typical force F than by the force exerted on each vertex, which is of order F_0.

The isotropically pulling units defined in this Section are thus suited to the study of arbitrarily large active forces, and we use them in the remainder of this Thesis.

6.3 Numerical simulations of stress decay

The theoretical predictions we introduced in Section 6.1 for the decay of the radial stress σ_{rr} around a single active unit are continuum equations valid for an infinite system. In this Section, we introduce the tools needed to test them in our numerical simulations of a discrete, finite systems. In Section 6.3.1, we discuss our numerical setup. In Section 6.3.2, we describe the way we measure radial stresses. We can then infer the infinite-system radial stress by compensating the effects of boundary conditions, as we show in Section 6.3.3. This allows us to estimate the buckling radius R^* introduced in the previous Section, as explained in Section 6.3.4.

6.3.1 Boundary conditions

We consider a large, circular (or spherical in 3D) system of radius R_1 centered around an active unit. We choose here to use fixed boundary conditions, *i.e.* the lattice nodes at $r > R_1$ are frozen with zero displacement. This choice of boundary conditions is motivated by simplicity and efficiency: we are interested in the stress profile resulting from the forces exerted by a single active unit. Periodic boundary conditions would lead to a pollution of the stress by that generated by the virtual copies of the active unit, and thus would not be radially symmetric. Free boundary conditions would be acceptable, but lead to much slower numerical convergence of our numerical energy minimization algorithms than fixed boundary conditions.

6.3.2 Measuring radial stresses

We have introduced in Section 4.2.2 a discrete definition for the stress carried by a lattice bond, which includes stretching and bending components. We measure the radially averaged stress $\sigma_{rr}(r)$ by performing a virtual "cut" of the system in a circular (or spherical in three dimensions) shell, and averaging the radial components of the stress (including the bending tension) of all fibers that cross this shell.

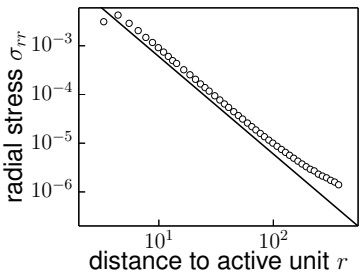

Figure 6.5: Radial stress decay away from an isotropic puller exerting a weak force, *i.e.* in the linear regime, in a large circular piece of regular 2D network. Parameters: $F_0 = 0.1$, $\mu = 10^3$, $R = 400$.

6.3.3 Compensating boundary effects

The decay of the radial stress in the linear regime in a 2D system is shown in Figure 6.5. Note that because the system is finite, boundary effects are visible: the stress is not a pure power law $\sigma_{rr} \propto r^{-d}$ as in an infinite system. This complicates our analysis of these stress profiles, and in particular the estimation of the buckling radius R^*.

We palliate this problem by compensating these boundary effects, using the finite size analytic solution in a linear homogeneous elastic

medium. For an isotropic elastic continuum with spherical symmetry, the generic solution to the linear elastic equations for the radial displacement $u_r(r)$ is:

$$u_r(r) = Ar^{-(d-1)} + Br \tag{6.26}$$

where d is the space dimension, and the constants A and B are set by the boundary conditions. The radial stress thus reads

$$\sigma_{rr}(r) = -2dGAr^{-d} + 2G\frac{1+\nu}{1-(d-1)\nu}B \tag{6.27}$$

where G is the shear modulus and ν is the Poisson ratio of the material. In the case of an infinite system, $B = 0$ and the linear regime is a pure scaling regime $\sigma_{rr} \propto r^{-d}$. However, in a finite system, any choice of boundary conditions will lead to a finite value for B, thus perturbing the scaling regime (raw value of $\sigma_{rr}(r)$ in Fig.6.6).

For the fixed boundary conditions used in this Chapter, we have $B = -A/R^d$, where R is the radius of the system. We have seen in Section 3.3.1 that the Poisson ratio of lattice fiber networks is independent of the precise geometry and connectivity of the network: in $d = 2$, $\nu \approx 3/5$, and in $d = 3$, $\nu \approx 2/7$ (note that these values do not correspond to actual experimental Poisson ratios, but only to idealized fiber networks, and are exact for regular networks). We can thus extrapolate the infinite-system value of the radial stress by subtracting the part due to the fixed boundaries. To avoid issues associated with bonds that intersect the system's boundary, we measure the radial stress at a radius R_1 slightly smaller than R, and compute the corrected "infinite system" stress as a function of our finite-size "raw" measurement using the formula:

$$\sigma_{rr}^{(\text{infinite})}(r) = \sigma_{rr}^{(\text{raw})}(r) - \frac{R_1^d}{R_1^d + gR^d}\sigma_{rr}^{(\text{raw})}(R_1) \tag{6.28}$$

where $g = d - d^2\nu/(1+\nu)$. The corrected stress exhibits a clear scaling regime in the far-field, as demonstrated in Figure 6.6 in 2D and Figure 6.7 in 3D.

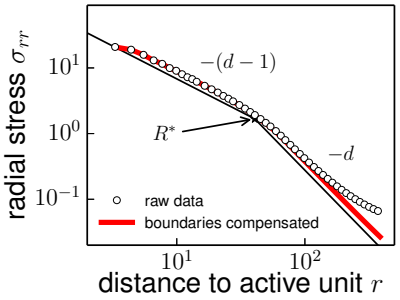

Figure 6.6: Compensation of the effect of the fixed boundaries of the system on the spatial distribution of radial stresses, for large active forces inducing extended buckling. The raw data (white circles) do not easily reveal the crossover between scaling regimes. Compensating the boundary effects (red line) reveals the crossover between scaling regimes and allows for a power-law by parts fit (black lines). Parameters: $F_0 = 80$, $\mu = 10^3$, $R = 400$.

6.3.4 Estimating R^*

We finally use the boundary-corrected radial stress to estimate the buckling radius, using a power-law by parts function:

$$\sigma_{rr}^{(\text{fit})}(r) = \begin{cases} \sigma^*(R^*/r)^{d-1} & \text{if } r < R^* \\ \sigma^*(R^*/r)^d & \text{if } r > R^* \end{cases} \tag{6.29}$$

This fit has only two parameters, the buckling radius R^* and the radial stress at this distance σ^* (which is expected to be comparable to the buckling stress, *i.e.* one), thus allowing for a robust estimate of R^*, as illustrated in Figure 6.6 in 2D and Figure 6.7 in 3D.

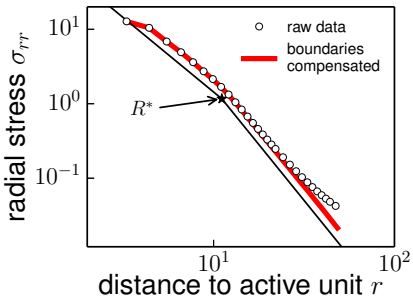

Figure 6.7: Similar treatment for a regular 3D network. Parameters: $F_0 = 120$, $\mu = 10^3$, $R = 50$.

6.4 Force transmission in soft and stiff networks

We now make use of the tools introduced in Sections 6.2 and 6.3 to test the scenario that we proposed theoretically in Section 6.1: in response to active units exerting forces F much larger than the buckling force, stress propagation crosses over from a near-field, rope-like regime to a far-field, linear regime. We find that the result depends on the elastic regime of the network: we show that in stretching-dominated networks (Section 6.4.1), the our theoretical predictions match fully with our results. In contrast, in bending-dominated networks (Section 6.4.2), we observe anomalous deviations to this scenario, and speculate about their origin.

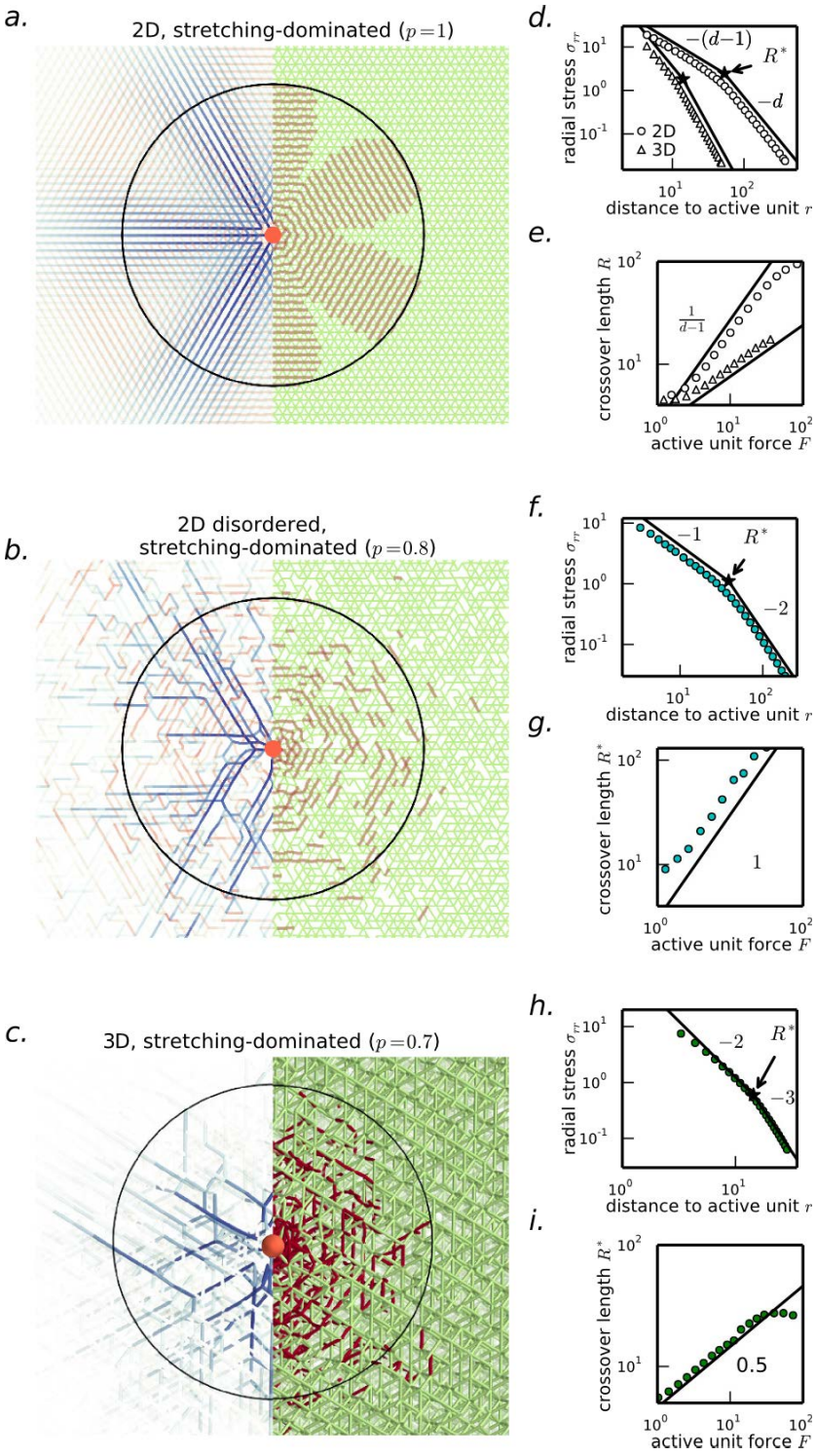

Figure 6.8: Non-linear force transmission in stretching-dominated networks coincides with the theoretical scenario presented in Section 6.1. **a-c:** A localized, isotropically pulling active unit (red circle of radius $R_0 = 1.95$) induces stress lines (left side of each panel, blue=tension and red=compression) and buckling (right side of each panel, in red; non-buckled bonds are green) in the surrounding fiber network. Black circle: radius R^* of the rope-like region. Panel **c** shows a slice of a 3D system. **d, f** and **h:** Decay of the average radial stress in the network (corrected for boundary effects) as a function of the distance to the active unit. Fitting the curve with the power laws of Equations 6.11-6.13 yields a measure of the crossover radius R^*. **e, g** and **i.** This buckling radius shows a power-law dependence on F as predicted by Equation 6.16. Parameters: 2D circular (3D spherical) network of radius 200 (33) with fixed boundaries and averaged over 100 samples for disordered networks.

6.4.1 Stretching-dominated networks

In the case of stretching-dominated networks – either regular or disordered, and two- or three dimensional – our numerical results coincide well with the scenario we have established, as we show in Figure 6.8. Rope-like radial stresses and bond buckling are predominant in the vicinity of the active unit, with radial stress decay as $\sigma_{rr} \propto r^{-(d-1)}$. The crossover to far-field linear elasticity occurs at

$$R^* \approx R_0 \left(\frac{F}{F_b} \right)^{1/(d-1)}$$

as predicted by our theory (Equation 6.16). Visually, this crossover length R^* coincides with the outer boundary of the radially tensed, buckling-rich region (Figure 6.8 *a-c*, thin black circles).

In such stretching-dominated networks, we conclude that the theoretical arguments developed in Section 6.1 are valid: radial stresses larger than the buckling stress propagate in a rope-like fashion, while those smaller than the buckling force transmit linearly. Buckling therefore results in an amplification of far-field stresses.

6.4.2 Anomalous force transmission in soft networks

In contrast, two- and three-dimensional bending-dominated networks display a more complex behavior, as shown in Figure 6.10. While the system still exhibits a transition from rope-like to linear force transmission, the crossover region is much broader than in the stretching-dominated case, as visible in Figures 6.10 *d,f,h*. Furthermore, the crossover length R^* at a given force F is much larger in the bending-dominated case, as shown in Figure 6.9: rope-like force transmission extends to larger distances in bending- than in stretching-dominated networks. Contrarily to the latter, the prediction of Equation 6.16 that $R^* \approx R_0 F^{1/(d-1)}$ is not verified. Instead, we find that we can reasonably well fit R^* by a power-law:

$$R^* \approx A F^{\alpha} \tag{6.30}$$

This phenomenological fit yields anomalous exponents $\alpha \approx 0.4$ in 2D (Figure 6.9) and $\alpha \approx 0.25$ in 3D (Figure 6.10 *i*). These exponents appear to be insensitive to the exact value of the depletion parameter p within the bending-dominated regime (Figure 6.10 *e,g,i*).

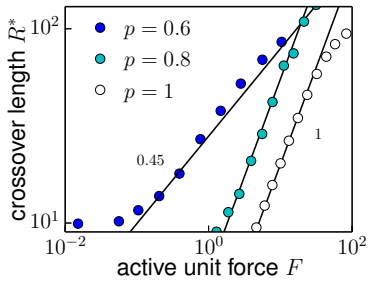

Figure 6.9: Crossover radius as a function of the active force, for 2D triangular lattices with variable depletion parameter. The black lines indicate power-law fits. Stretching-dominated networks ($p > pc \approx 0.65$), either depleted or regular, are well described by Equation 6.16. On the other hand, bending-dominated networks exhibit a clearly different behaviour, with smaller exponent. Parameters: $R = 200$, $\mu = 10^3$, average over 100 systems in disordered case.

Are there force chains? We speculate that this extended range for nonlinear force transmission is mediated by the strong concentration of tensile stresses along force chains[6] observed in Figure 6.10 *a-c*. Indeed, such force chains are visually much more pronounced in bending-dominated than in stretching-dominated networks (Figures 6.8 and

[6] Heussinger, C. and Frey, E. (2007). Force distributions and force chains in random stiff fiber networks. *Eur. Phys. J. E*, 24(1):47–53
Dasanayake, N. L., Michalski, P. J., and Carlsson, A. E. (2011). General Mechanism of Actomyosin Contractility. *Phys. Rev. Lett.*, 107(11):118101

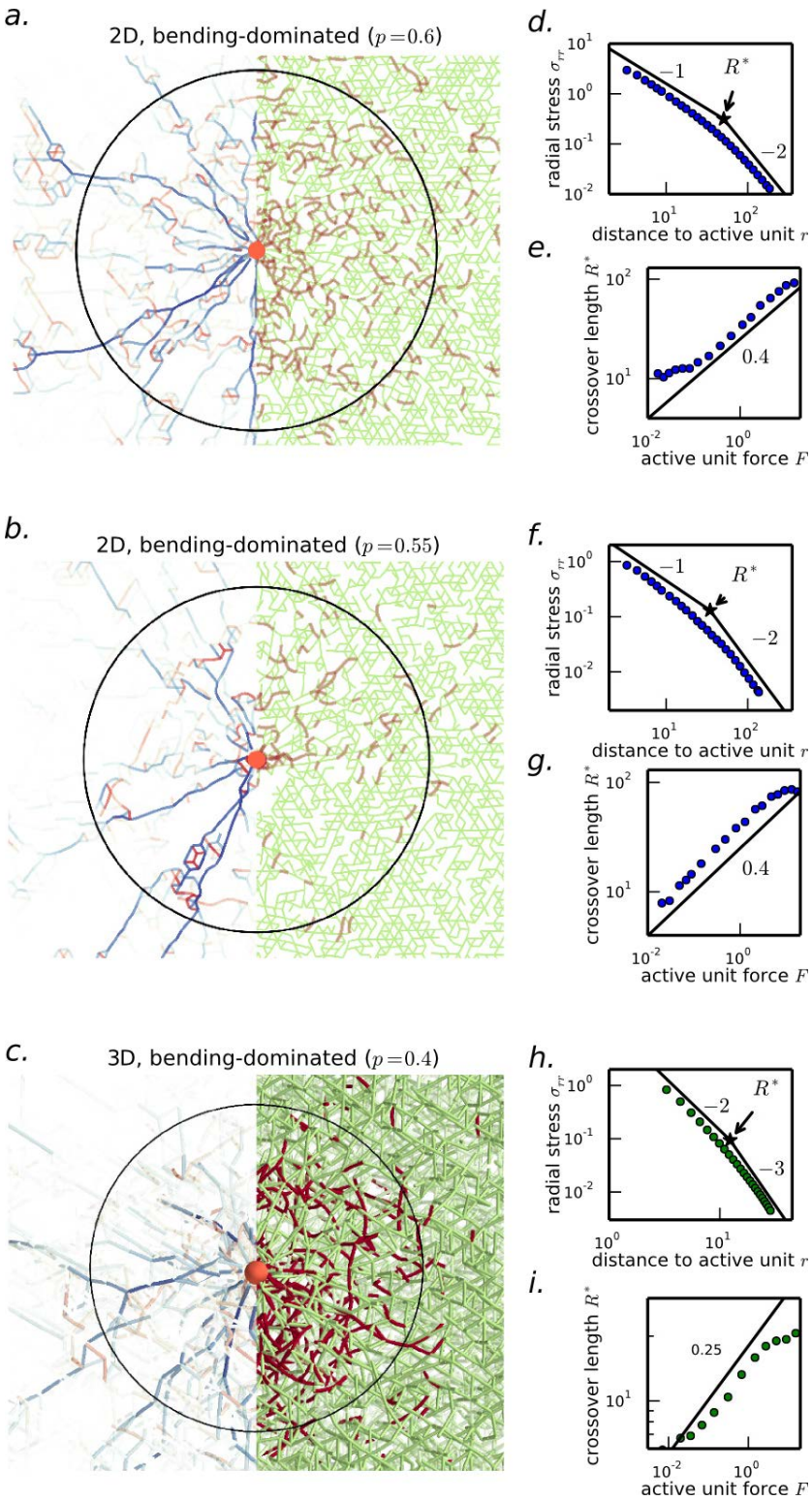

Figure 6.10: Non-linear force transmission in 2- and 3-dimensional bending-dominated networks. Parameters and notations as in Figure 6.8.

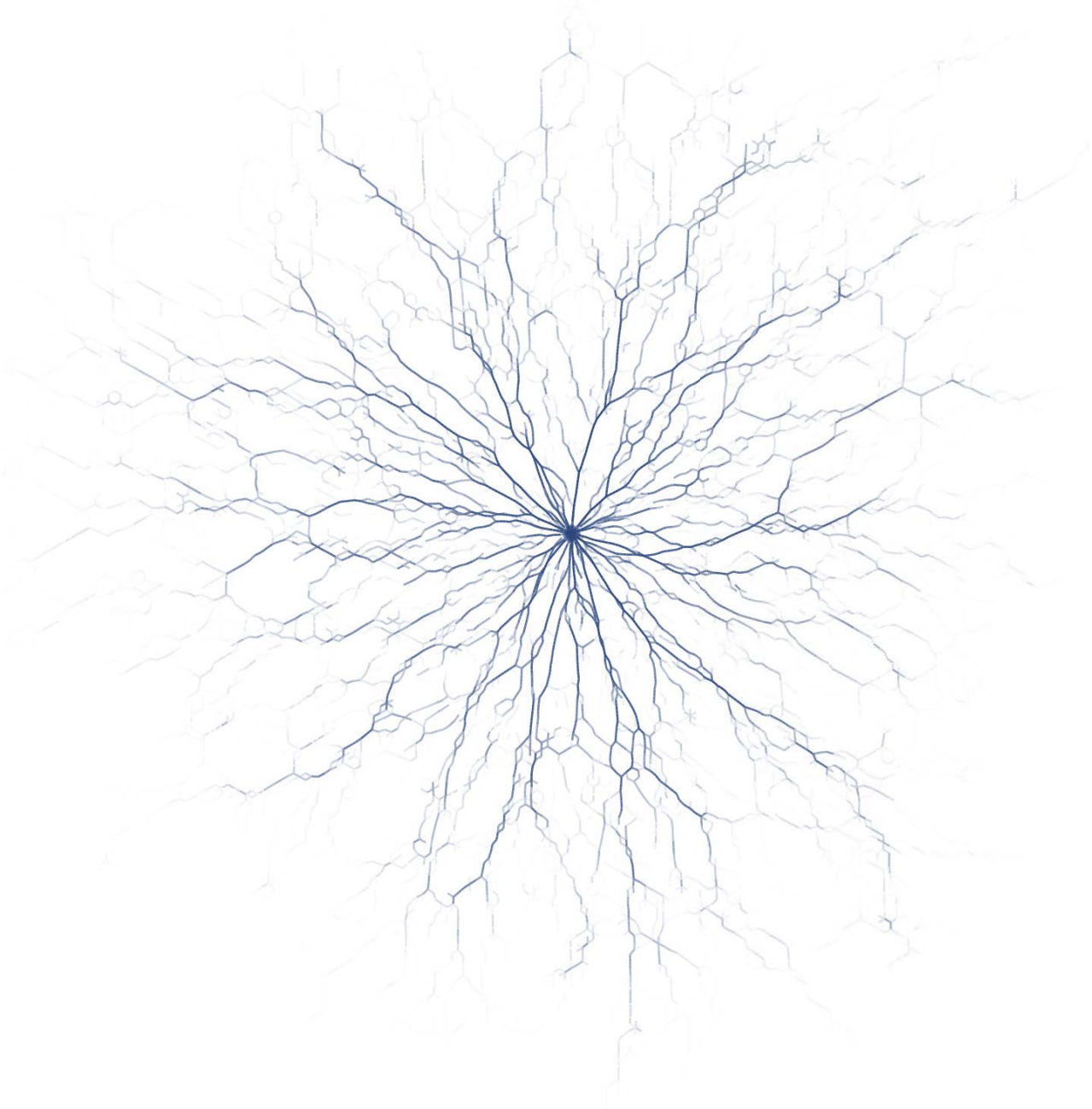

Figure 6.11: Force chains around a strong active unit in a bending-dominated network, in a very large system. Only tensed fibers are shown. Parameters: $p = 0.58$, $F_0 = 10$, $\mu = 10^3$, $R = 500$.

6.10). Because of these large stress heterogeneities, our continuum picture presented in Section 6.1 – which assumes spherically symmetric stresses – might break down. However, no theoretical framework describing the influence of these heterogeneities on force transmission has been developed yet.

We illustrate these force chains in Figure 6.11, which shows the distribution of tensile stresses in a large, depleted network. Note the branching pattern of radial, tensed fibers which becomes sparse in the far-field. The active unit leads to large displacements in the network, with and emerging star-shaped structure around the active unit. It is not obvious that a regular lattice underlies the network in Figure 6.11.

The difference between stretching- and bending-dominated exponents thus suggests that elastic heterogeneities qualitatively affect force transmission in such soft networks.

Regular bending-dominated networks. In order to elucidate the origin of the anomalous dependence of R^* on F in depleted, bending-dominated network, we consider in Figure 6.12 the response of a regular (non-depleted), bending-dominated network as introduced in Section 3.A. We recover the rope-like-to-linear crossover phenomenology. We plot in Figure 6.13 the F-dependence of crossover length R^*, which supports a normal dependence with exponent $1/(d-1)$, in contrast with depleted bending-dominated networks.

These results support the idea that it is the strongly disordered nature of these networks, rather than the fact that their elastic properties are bending-dominated, which is responsible for the anomalous force-dependence of the buckling radius. We note that similarly, regular bending-dominated networks have moderate bulk non-linear susceptibility, while it can be very large in depleted networks, as we have shown in Section 3.3.3. A possible way to explore further this question, which we have not carried out here, would be to consider depleted or randomized versions of the regular bending-dominated network.

Are there other length scales? The apparent power-law dependence of $R^*(F)$ in depleted, bending-dominated networks is characterized by an exponent α which is smaller than the stretching-dominated case. Combined with a large prefactor A in Equation 6.30, this allows for long-ranged nonlinear force transmission at relatively small forces compared to the buckling force. However, extrapolating to large forces, the consequences of such a power-law dependence are intriguing: indeed, we would thus conclude that nonlinear effects have a *shorter* range in these depleted networks than in stretching-dominated ones, which is quite counter-intuitive given the high nonlinear susceptibility of soft networks.

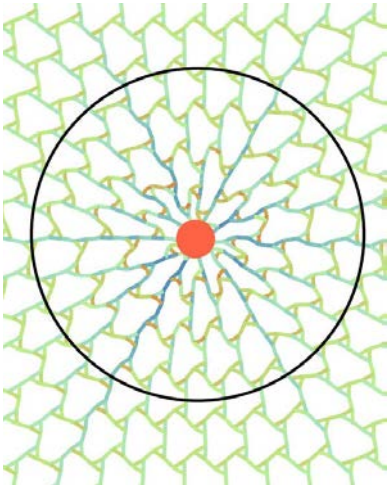

Figure 6.12: The response of a regular, bending-dominated "MAN" network to a strong active unit induces rope-like force transmission in a region of size R^* (black circle).

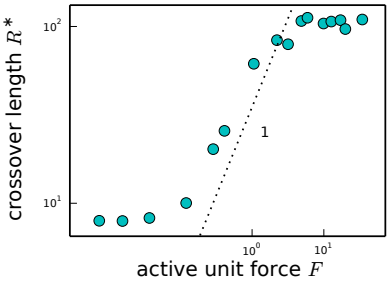

Figure 6.13: The force dependence of R^* in the regular bending-dominated network is compatible with Equation 6.16. At small F, there is no buckling, while at large F the crossover radius R^* is comparable to the system size: in both cases it is difficult to evaluate R^*. The sparsity of data in the intermediate regime comes from the multistability of our active units in such nonlinear cases. The low- and high force plateaus originate from the interference of our fit with the active unit size and system size, respectively.

Furthermore, combining Equation 6.30 with rope-like force transmission (Equation 6.13) in the near-field implies that at the crossover distance, the radial stress $\sigma^* = \sigma_{rr}(R^*)$ depends on the force:

$$\sigma^* \approx F \left(\frac{R_0}{R^*} \right)^{d-1} \approx B F^{1-\alpha(d-1)} \tag{6.31}$$

Since $\alpha < 1/(d-1)$, we conclude that the crossover radial stress increases with F, as confirmed by Figure 6.14.

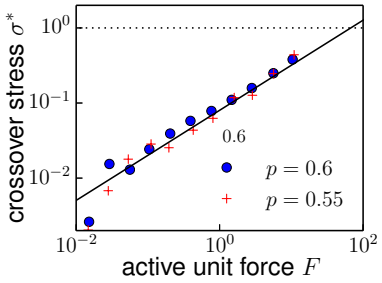

Figure 6.14: The force-dependence of the crossover stress in depleted, bending dominated networks, is well described by a power-law.

This leaves us with a paradox: extrapolating to forces $F \geq 100$, we would thus predict that σ^* can become larger than unity – *i.e.*, that the crossover towards linear elasticity can occur at stresses larger than the buckling stress. This appears impossible from the far-field linear side: indeed, linear force transmission implies that angular compressive stresses partially compensate radial tension, and fiber networks cannot withstand compressive stresses larger than the buckling threshold. We are lead to conclude that a change of regime of some sort should happen at large force, and that $R^*(F)$ departs from the power-law with exponent α, for instance towards the stretching-dominated scaling regime.

This would define another length scale, at which force transmission in depleted networks crosses over from anomalous to normal nonlinear response. Unfortunately, this regime is not accessible numerically, as it would occur at a value $R^* \approx 200$ of the nonlinear radius. Computations on systems of comparable size are possible, but spoiled by boundary effects which make R^* impossible to estimate – and it is not currently possible to study much larger systems.[7]

We thus speculate that the buckling radius at a given force is always larger in depleted bending-dominated networks than in stretching-dominated networks: *disorder enhances the range of force transmission*. While apparent power-laws suggest that this statement might not hold at large force, this is verified in all our numerical simulations.

[7] To obtain the curves in Figure 6.10 *e,g,i*, our simulations ran for about 5 cpu.year, and approximately 200GB of data were produced and analyzed. Improving the system size by an order of magnitude would require at the very least a hundredfold increase of these numbers.

Conclusion

In this Chapter, we have studied the influence of buckling on the force transmission properties of elastic fiber networks. We have shown that contractile forces large enough to induce buckling benefit from an enhanced range of transmission. Indeed, the absence of compressive stresses allows for a slower decay of tensile forces away from an active unit – a behaviour we qualify as *rope-like* force transmission, in contrast with linear elasticity. Our work parallels recent studies establishing long-range force transmission in fiber networks due to buckling[8] and strain stiffening[9].

This long-ranged nature of tensile forces results in an amplified

[8] Notbohm, J., Lesman, A., Rosakis, P., Tirrell, D. A., and Ravichandran, G. (2014). Microbuckling in fibrin networks enables long-range cell mechanosensing. *arXiv*, page 1407.3510
Rosakis, P., Notbohm, J., and Ravichandran, G. (2015). A model for compression-weakening materials and the elastic fields due to contractile cells. *Journal of the Mechanics and Physics of Solids*, 85:16–32

[9] Xu, X. and Safran, S. A. (2015). Nonlinearities of biopolymer gels increase the range of force transmission. *Phys. Rev. E*, 92(3):032728

far-field response to local contraction. We have already discussed local dipole amplification due to buckling in Chapter 5. Here we have shown that at large contractile forces, this nonlinear effect is characterized by the mesoscopic radius of the rope-like region R^*. This new length scale characterizes the range of nonlinear effects resulting from the action of an active unit. It grows with the applied contractile force, and can become much larger than the microscopic lengths characterizing the network. Importantly, this length scale characterizes the far-field amplification of the response to a strong active unit with respect to linear force transmission.

7
A phase diagram for stress production

Et dès lors, je me suis baigné dans le Poème
De la Mer, infusé d'astres, et lactescent,
Dévorant les azurs verts ; où, flottaison blême
Et ravie, un noyé pensif parfois descend ;

Où, teignant tout à coup les bleuités, délires
Et rythmes lents sous les rutilements du jour,
Plus fortes que l'alcool, plus vastes que nos lyres,
Fermentent les rousseurs amères de l'amour !

— Arthur Rimbaud, *Le bateau ivre.*

Over large length scales, active stresses in biological systems are generated by multiple active units. In this last Chapter, we consider the macroscopic response of fiber networks to many force-exerting objects:

What is the stress produced by a finite density of active units in an elastic fiber network?

We have already addressed this question in Chapter 4 in the context of the linear response of the network, when forces are weak. This linear prediction provides a reference stress, from which we can compute the stress amplification ratio in more complicated cases. We show in Section 7.1 that in the presence of nonlinear effects, this stress amplification depends on the active unit force F and density ρ in a simple and generic way, involving the interplay of three length scales: the active unit size R_0, the range for nonlinear effects R^*, and the average distance between units $R_{\text{a.u.}}$. We will draw a phase diagram for this stress generation problem. We then discuss the experimental validation of these theoretical results in Section 7.2.

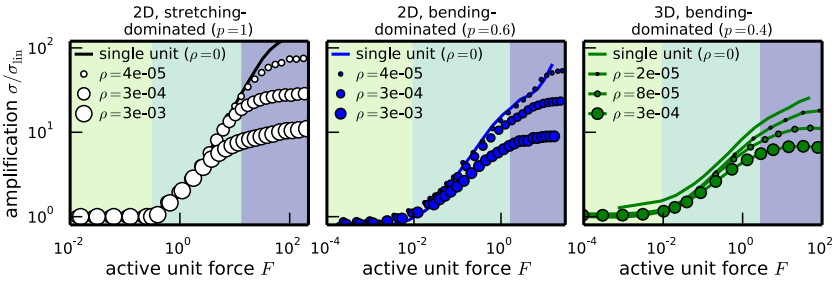

Figure 7.1: The amplification ratio for the stress with respect to the linear prediction of Equation 7.1, for fiber networks in different dimensions and elastic regimes. In all cases, three regimes appear as a function of active unit density ρ and force F, as suggested by the colored background.

7.1 Three regimes, three length scales

We start by considering the stress amplification ratio $\sigma/\sigma^{(\mathrm{lin})}$ in the presence of a finite density of randomly positioned active units in 2D and 3D for various densities ρ and depletion parameters p (Figure 7.1). In all cases we observe three stress amplification regimes as a function of the unit force F: a low-force plateau without amplification, an intermediate regime of increasing amplification and a saturation of the amplification at a level that depends on ρ. We now examine in turns these three regimes (Sections 7.1.1-7.1.3). In Section 7.1.4 we present a phase diagram summarizing these results.

7.1.1 Linear stress production

In the low-force regime, linear force transmission prevails. We have shown in Chapter 4 that in linear elastic materials, the active stress for a density ρ of active units, each exerting a local force dipole $\mathcal{D}^{\mathrm{loc}}$, is:

$$\sigma = \sigma^{(\mathrm{lin})} = -\rho\mathcal{D}^{\mathrm{loc}} \tag{7.1}$$

Considering locally contractile active units, we can write their local force dipole as $\mathcal{D}^{\mathrm{loc}} = -FR_0$, where F is their typical force and R_0 their typical size, as schematized in Figure 7.2. The large-scale linear reference for stress production is thus:

$$\sigma^{(\mathrm{lin})} = \rho F R_0 \tag{7.2}$$

We have proved in Chapter 4 that this relation is exact, including in disordered systems: indeed, while the response to an individual active unit is random, these fluctuations average out in the macroscopic response to a finite density of active units. Dipole conservation thus implies that Equation 7.2 is correct, as verified in the low-force regime of Figure 7.1, where the amplification ratio with respect to the linear theory is equal to unity on average. This regime of linear stress production is illustrated in Figure 7.3.

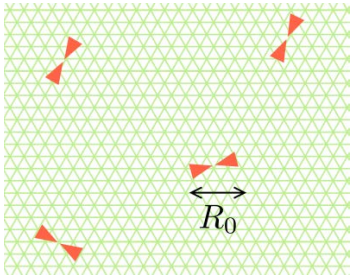

Figure 7.2: Schematic linear response of a fiber network to active units. The relevant length scale for stress production is the active unit size R_0.

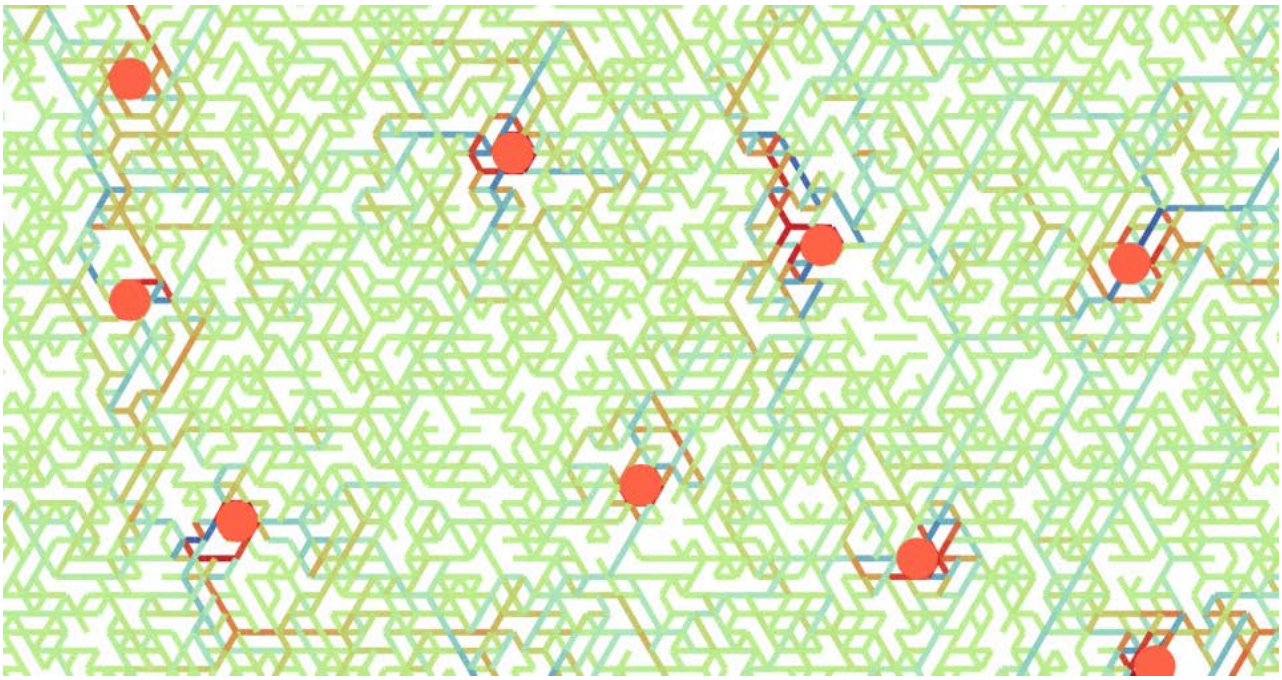

Figure 7.3: A bending-dominated network with finite density of active units, in the linear regime. Parameters: system size 100^2, $N = 21$ active units, force $F = 0.05$, $\mu = 10^3$, $p = 0.6$.

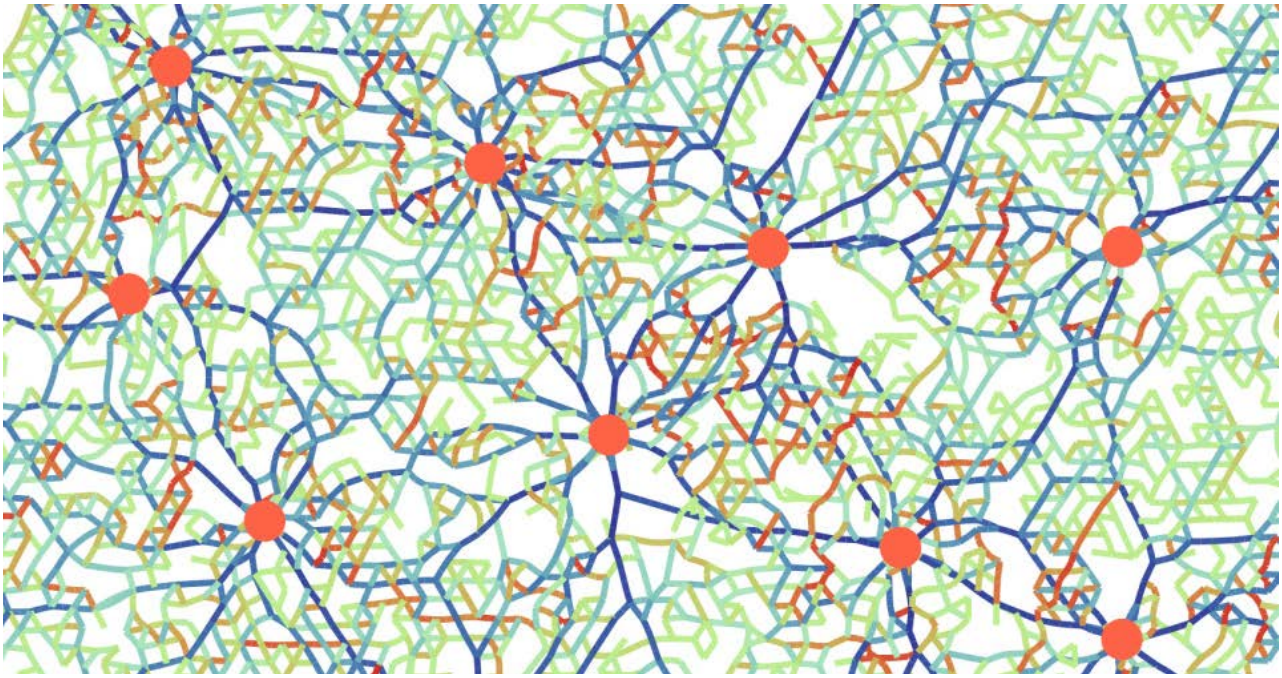

Figure 7.4: The same network as in Figure 7.3, in the force-controlled regime ($F = 4.5$). Each active unit is surrounded by a rope-like region in which force amplification takes place, and these regions do not overlap.

7.1.2 Amplification in rope-like regions

For moderate forces, we have seen in Chapter 6 that the fibers in the network buckle in the vicinity of each active unit, up to a distance R^*. Individual units are thus typically surrounded by *nonoverlapping* nonlinear regions of size R^*, as illustrated in Figures 7.4 and 7.5. Recalling Equation 6.18, the far-field stress is therefore amplified with respect to the linear prediction for radial tensions:

$$\frac{\sigma_{rr}(r)}{\sigma_{rr}^{(\mathrm{lin})}(r)} \approx \frac{R^*}{R_0} \qquad (R \gg R^*) \tag{7.3}$$

Equivalently, we can model each nonlinear region as an *effective active unit* of size R^* and force dipole $\mathcal{D}_{\mathrm{eff}} \approx -FR^*$, using Equation 6.13 to describe force propagation within the nonlinear region. As the effective units are themselves embedded in a linear medium, linear force transmission outside of these units implies

$$\sigma \approx -\rho \mathcal{D}_{\mathrm{eff}} \approx \rho F R^* \tag{7.4}$$

We thus predict that stress amplification in this regime scales as $\sigma/\sigma_{\mathrm{lin}} \approx R^*/R_0$. We confirm this prediction in Figure 7.6. Since R^* increases with the active unit force in this regime, the large-scale stress amplification $\sigma/\sigma_{\mathrm{lin}}$ increases with F as previously observed in Figure 7.1.

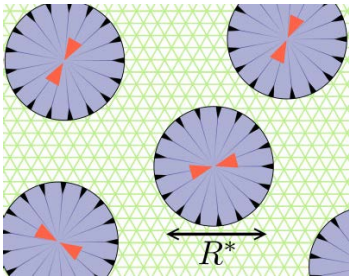

Figure 7.5: When active forces are strong enough to induce buckling, the relevant length scale for stress production is the nonlinear length R^*.

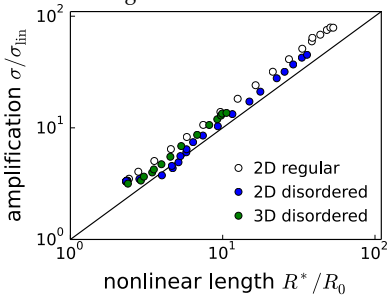

Figure 7.6: In the intermediate force regime, the stress amplification ratio is equal to the ratio R^*/R_0 as predicted by Equation 7.4.

7.1.3 Stress saturation at large forces

For large forces, the radius of the rope-like regions becomes so large as to exceed the typical distance between adjacent active units $R_{\mathrm{a.u.}} = \rho^{-1/d}$. This causes the nonlinear regions associated to neighboring active units to overlap. Once these rope-like regions percolate and start overlapping, the forces they exert on each other balance, and the whole network becomes mechanically equivalent to a collection of tensed, inextensible ropes whose geometry does not change significantly upon further increase of the force (Figure 7.9). To estimate the resulting network stress, we approximate the system as a mosaic of effective active units of size $R_{\mathrm{a.u.}}$ each with a force dipole $\mathcal{D}_{\mathrm{eff}} \approx -FR_{\mathrm{a.u.}}$, as illustrated in Figure 7.7. This yields

$$\sigma \approx -\rho \mathcal{D}_{\mathrm{eff}} \approx \rho F R_{\mathrm{a.u.}} = \rho^{1-1/d} F \tag{7.5}$$

The resulting prediction for the stress amplification, $\sigma/\sigma_{\mathrm{lin}} \approx R_{\mathrm{a.u.}}/R_0$, is remarkably well confirmed in Figure 7.8. Strikingly, the stress generated in this large-force regime has a nonlinear dependence on ρ, again consistent with Figure 7.1. Indeed, the addition or removal of active units leads to large rearrangements of the rope network, resulting in significant local modifications of force transmission.

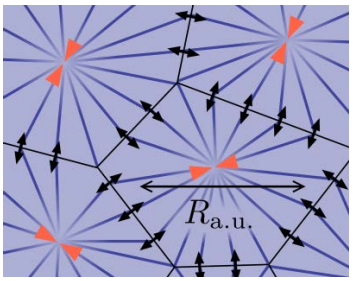

Figure 7.7: At large active forces, the whole system behaves as a network of tensed ropes connecting active units, and the relevant length scale is the average distance $R_{\mathrm{a.u.}}$ between these units.

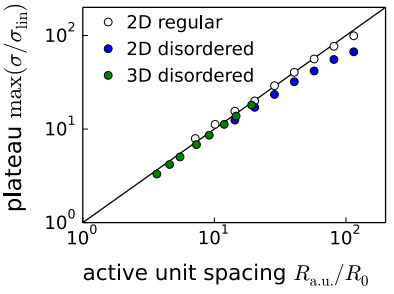

Figure 7.8: In the large-force regime, the stress amplification ratio is equal to the ratio $R_{\mathrm{a.u.}}/R_0$ as predicted by Eq. (7.5).

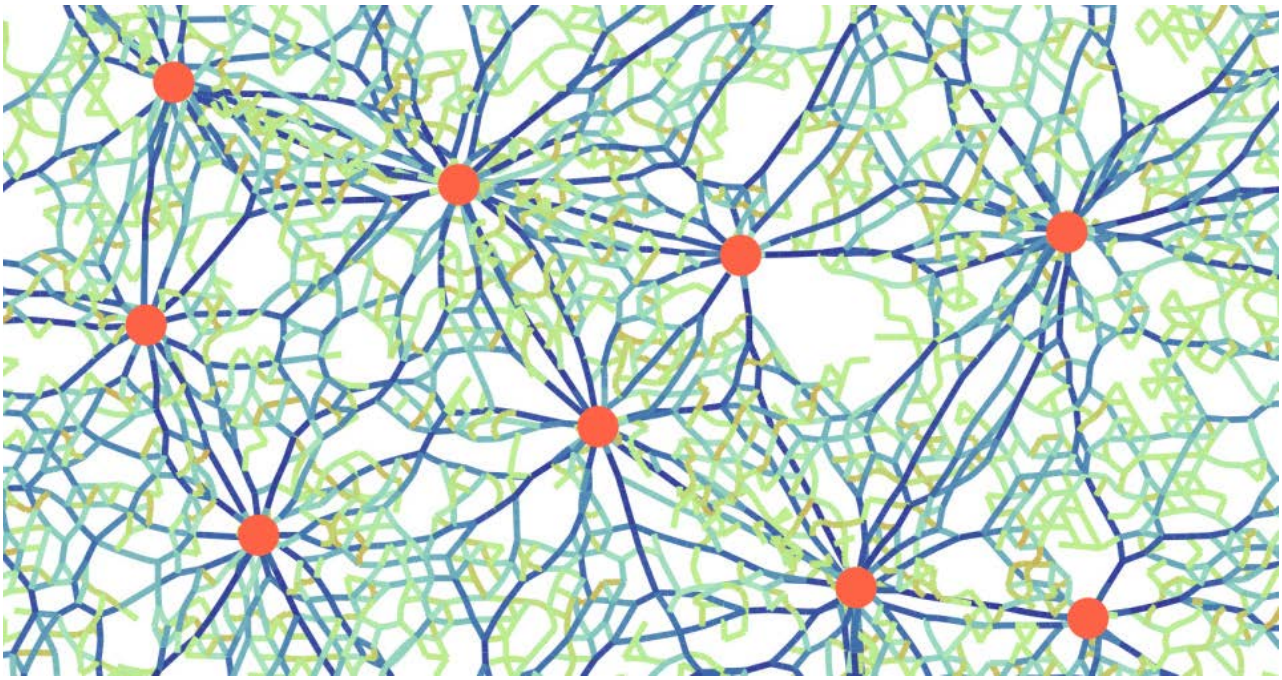

Figure 7.9: The same network as in Figure 7.3, in the density-controlled regime ($F = 15$). The rope-like regions percolate, and filament buckling extends to the whole network, while stress is transmitted by tensed fibers.

7.1.4 Phase diagram

We summarize the physics of collective stress-generation by many active units in a generic phase diagram in Figure 7.10. In each regime, the magnitude of an active unit's effective force dipole is directly proportional to one of the three length scales R_0, R^* and $R_{\text{a.u.}}$ [Eqs. (7.2-7.5)]. The background images show typical configurations of the network in the associated regimes.

While we have shown that R^* depends on the dimensionality and connectivity of the network, the other two length scales – active unit size R_0 and spacing $R_{\text{a.u.}}$ – are purely geometrical, and depend only on the active units. An important consequence of these findings is that the active stress generated in the associated regimes is essentially independent of the detailed properties of the fiber network: in both the $F \ll F_b$ and $F \gg F_b$ regimes, the network's mechanical properties are irrelevant to the amount of active stress generated by the network.

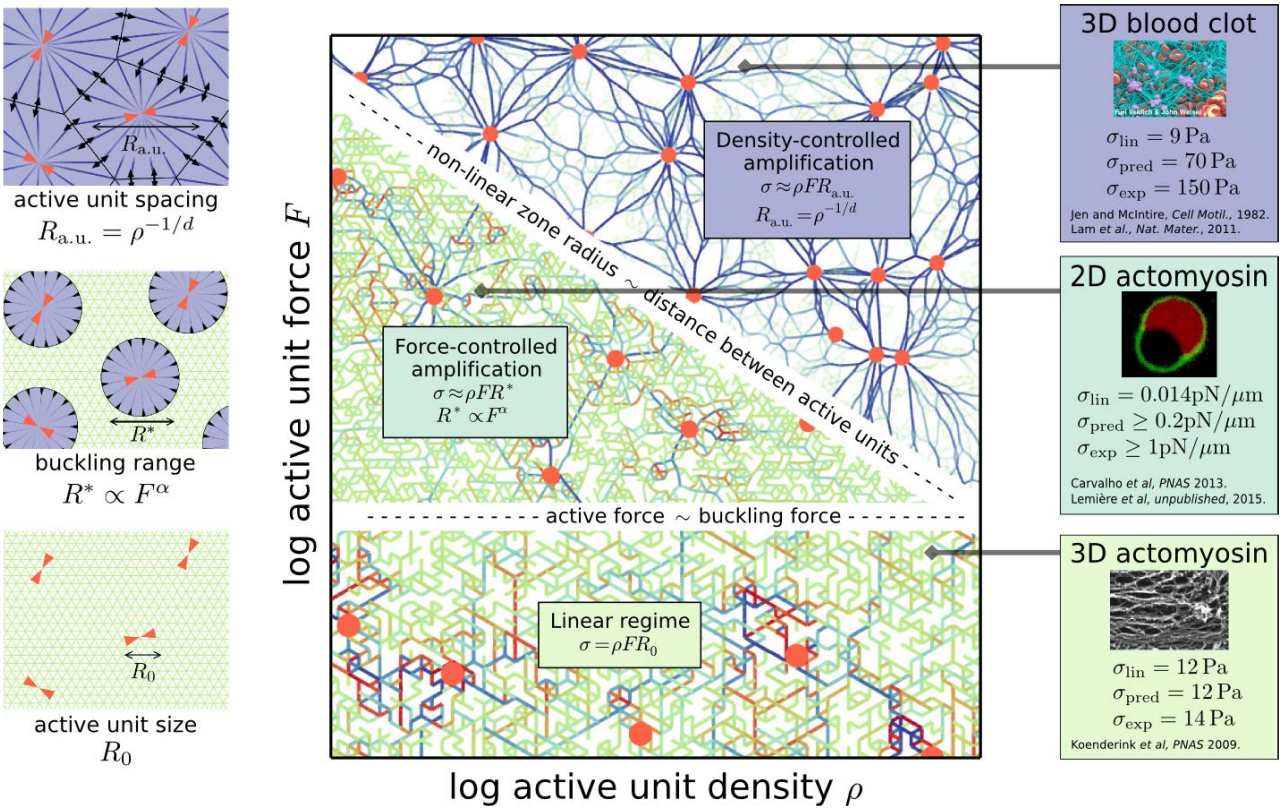

Figure 7.10: Force transmission in the presence of a finite density ρ of active units. Left: schematics of the network structure in each regime. The low-force linear regime (bottom) transitions to a regime of nonoverlapping nonlinear regions (center) as soon as F is sufficient to induce buckling. These nonlinear regions grow with increasing F, and amplification saturates as they start overlapping, which turns the whole network into a rope network (top). Center: Schematic phase diagram indicating the domain of applicability of the three stress amplification regimes, with representative snapshots of corresponding systems in a 2D depleted network in the background. Right: Comparison of our predictions with experimental measurements of the active stress in *in vitro* systems, as detailed in Section 7.2.

7.2 Biological relevance

Our generic phase diagram (Figure 7.10) recapitulates our quantitative understanding of stress generation by a collection of active units based on the interplay between three length scales: active unit size R_0, rope-like length R^*, and typical distance between units $R_{\text{a.u.}}$. To validate these predictions, we compare them with existing measurements on a broad range of *in vitro* systems, in $d = 2$ and $d = 3$ in reconstituted cytoskeletal as well as extracellular networks. For visual comparison with our theory, we schematically place these systems in the phase diagram of Figure 7.10, and compare our predictions to the experimentally measured active stress.

7.2.1 Three-dimensional actomyosin

We first consider a dense three-dimensional actin network illustrating the linear regime in three-dimensional actomyosin ("3D actomyosin" system in Figure 7.10). In Reference (Koenderink et al., 2009)[1], a crosslinked actin network with mesh size $\xi = 200\,\text{nm}$ is populated by myosin thick filaments of size $R_0 = 1\,\mu\text{m}$ each comprising $\simeq 300$ myosin heads. Each head actively exerts a $f = 4\,\text{pN}$ force 2% of the time[2]. Of these 300 heads, half pull in each direction. Furthermore, we use the simplifying assumption that the myosin thick filament is uniformly decorated with motor heads, and thus the average span of the force dipole is $R_0/2$. This results in a local force dipole $\mathcal{D}_{\text{loc}} = -150 \times R_0/2 \times f \times 2\%$ and each thick filament as a whole exerts a typical force $F = \mathcal{D}_{\text{loc}}/R_0 \simeq 6\,\text{pN}$ on the network. Actin filaments have a persistence length $\ell_p \simeq 10\,\mu\text{m}$, implying a buckling force $F_b \approx \pi^2 k_B T \ell_p/\xi^2 = 10\,\text{pN}$ for a single network bond. As a result, the active unit force is too small to induce filament buckling, and we thus expect linear force transmission in this experiment. Hence $\sigma_{\text{th}} = -\rho\mathcal{D}_{\text{loc}} = \rho F R_0 \simeq 12\,\text{Pa}$, where we used $\rho = 1\,\mu\text{m}^{-3}$. This number is in very good agreement with the estimation $\sigma_{\text{exp}} \simeq 14\,\text{Pa}$ of the macroscopic stress in (Koenderink et al., 2009).

[1] Koenderink, G. H., Dogic, Z., Nakamura, F., Bendix, P. M., MacKintosh, F. C., Hartwig, J. H., Stossel, T. P., and Weitz, D. A. (2009). An active biopolymer network controlled by molecular motors. *Proc. Natl. Acad. Sci. U.S.A.*, 106(36):15192–7

[2] Rosenfeld, S. S., Xing, J., Chen, L.-Q., and Sweeney, H. L. (2003). Myosin IIB Is Unconventionally Conventional. *J. Biol. Chem.*, 278(30):27449–27455
Lenz, M., Thoresen, T., Gardel, M. L., and Dinner, A. R. (2012b). Contractile Units in Disordered Actomyosin Bundles Arise from F-Actin Buckling. *Phys. Rev. Lett.*, 108(23):238107

7.2.2 Two-dimensional actomyosin on a vesicle

We next consider a two-dimensional actin network bound to the outer surface of a lipid vesicle illustrating force-controlled amplification in two-dimensional actomyosin networks ("2D actomyosin" system in Figure 7.10). Reference (Lemière et al., 2015)[3] reports measurements based on doublets of giant unilamellar lipid vesicle where the active stresses generated by a membrane-supported two-dimensional actomyosin sheet competes with the tension of a bare lipid membrane to

[3] Lemière, J., Bussonnier, M., Betz, T., Sykes, C., and Carvalho, K. (2015). Cell-sized liposome doublets reveal active cortical tension build up. communicated by C. Sykes

set the angle at which the sheet and the bare membrane meet. This novel measurement technique reveals that the active stresses generated by thick filaments ($F \simeq 6\,\mathrm{pN}$ as above) in a two-dimensional actin network ($\xi = R_0 = 1\,\mu\mathrm{m}$) covering a giant unilamellar vesicle of radius $r \simeq 10\,\mu\mathrm{m}$ are of the same order as the tension of the membrane $\sigma_{\mathrm{exp}} \approx \sigma_{\mathrm{membrane}} \approx 10^{-6} - 10^{-4}\,\mathrm{N\,m^{-1}}$ (the vesicles are electroformed and contain a mixture of egg-phosphatidylcholine (EPC) and biotin-PEG lipids). The range of tensions given here are typical values for such vesicles as no direct tension measurement are available in these experiments. The experiments involve an average of three myosin thick filaments per vesicle, implying $\rho = 3/(4\pi r^2) \simeq 2 \times 10^{-3}\,\mu\mathrm{m}^{-2}$. Computing the buckling force as $F_b \approx \pi^2 k_B T \ell_p / \xi^2 = 0.4\,\mathrm{pN}$ and assuming a stretching-dominated network, we predict a buckling radius $R^* = R_0 F / F_b = 15\,\mu\mathrm{m}$ that is both larger than the mesh size and smaller than the inter-motor spacing $R_{\mathrm{a.u.}} = \rho^{-1/2} \simeq 20\,\mu\mathrm{m}$, placing this system in the force-controlled amplification regime. This yields an amplification factor $\sigma_{\mathrm{th}}/\sigma_{\mathrm{lin}} = R^*/R_0 \simeq 15$, and an overall two-dimensional active stress $\sigma_{\mathrm{th}} = \rho F R^* \simeq 2 \times 10^{-7}\,\mathrm{N\,m^{-1}}$.

7.2.3 Reconstituted blood clot

Finally, we consider a clot comprised of fibrin filaments and contractile platelets as active units, which addresses the density-controlled amplification regime ("3D blood clot" system in Figure 7.10). We consider stress generation in a reconstituted clot comprised of a fibrin network rendered contractile by a concentration $\rho = 3 \times 10^8\,\mathrm{cells \cdot mL^{-1}}$ of blood platelets[4]. Atomic force microscopy measurements on individual platelets[5] show that each platelet of size $R_0 = 2\,\mu\mathrm{m}$ exerts a pulling force $F = 15\,\mathrm{nN}$, thus yielding a force dipole $\mathcal{D}_{\mathrm{loc}} = -Fd = -3 \times 10^{-14}\,\mathrm{N\,m}$. The linear prediction for the active stress is thus $\sigma_{\mathrm{lin}} = -\rho \mathcal{D}_{\mathrm{loc}} \approx 9\,\mathrm{Pa}$. Comparing this to the experimentally measured active contractile stress $\sigma_{\mathrm{exp}} = 150\,\mathrm{Pa}$ generated by a blood clot, we thus find a stress amplification factor $\sigma_{\mathrm{exp}}/\sigma_{\mathrm{lin}} = 17$: the measured stress is much larger than the linear prediction.

To account for this amplification, we evaluate the scaling regime in which this system lies. As the microstructure of the fibrin network was not investigated in (Jen and McIntire, 1982), we assume that the network essentially consists of single fibrin filaments or of small-diameter fibrin bundles and thus estimate a persistence length $\ell_p = 0.5\,\mu\mathrm{m}$ and a mesh size[6] larger than two hundred nanometers ($\xi \geqslant 200\,\mathrm{nm}$). To assess the validity of these estimates, we note that they imply[7] a network shear modulus $G' \approx 6 k_B T \ell_p^2 / \xi^5 \simeq 20\,\mathrm{Pa}$, consistent with the value $G' = 70\,\mathrm{Pa}$ reported in (Jen and McIntire, 1982). They moreover imply a rope-like region size $R^* = \xi (F/F_b)^{1/2} \geqslant 350\,\mu\mathrm{m}$ (with $F_b \approx \pi^2 k_B T \ell_p / \xi^2$), much

[4] Jen, C. J. and McIntire, L. V. (1982). The structural properties and contractile force of a clot. *Cell Motil.*, 2(5):445–455

[5] Lam, W. A., Chaudhuri, O., Crow, A., Webster, K. D., Li, T.-D., Kita, A., Huang, J., and Fletcher, D. A. (2011). Mechanics and contraction dynamics of single platelets and implications for clot stiffening. *Nat. Mater.*, 10:61–66

[6] Storm, C., Pastore, J. J., MacKintosh, F. C., Lubensky, T. C., and Janmey, P. A. (2005). Nonlinear elasticity in biological gels. *Nature*, 435(7039):191–4

[7] Broedersz, C. P. and MacKintosh, F. C. (2014). Modeling semiflexible polymer networks. *Rev. Mod. Phys.*, 86:995

larger than the inter-cell distance $R_{\text{a.u.}} = \rho^{-1/3} \simeq 15\,\mu\text{m}$. The rope-like regions of neighboring cells thus interpenetrate, implying density-controlled amplification. In this regime, we predict a contractile stress $\sigma_{\text{th}} \simeq 70\,\text{Pa}$ and a stress amplification factor $\sigma_{\text{th}}/\sigma_{\text{lin}} = R_{\text{a.u.}}/R_0 \simeq 8$, in order of magnitude agreement with the experimental result. Note that as this system lies deep in the density-controlled regime, this prediction is insensitive to our precise estimates of ℓ_p and ξ.

7.2.4 Further validation of the theory

These three examples demonstrate our theory's ability to quantitatively account for stress amplification, and recent progress in the micromechanical characterization of active fiber networks opens promising perspectives for further exploring active stress amplification[8].

[8] Murrell, M. and Gardel, M. L. (2012). F-actin Buckling Coordinates Contractility and Severing in a Biomimetic Actomyosin Cortex. *Proc. Natl. Acad. Sci. U.S.A.*, 109(51):20820–20825

Particularly striking are our predictions for the linear and density-controlled regimes. Indeed, Equations 7.2 and 7.5 contain no adjustable, network-dependent parameter: they should therefore be relatively easy to test. For instance, we have shown in Section 7.2.3 that contractile blood clots in physiological conditions lie far in density-controlled regime. We therefore expect from Equation 7.5 that

$$\sigma \approx F\rho^{2/3}$$

While varying the force exerted by platelets may not be easy, their density is a straightforward experimental parameter. The power-law with exponent $2/3$ in the density-dependence of the active stress should thus be testable by varying the density of platelets. The observation of this sublinear scaling of the stress with the density of platelets would be a strong validation of our novel theory for the nonlinear, strongly interacting density-controlled regime.

8
Discussion

Run, rabbit, run
Dig that hole, forget the sun,
And when at last the work is done
Don't sit down, it's time to dig another one

— Pink Floyd, *Breathe.*

Summary

In living organisms, microscopic units exert active forces that are transmitted by fibrous networks to generate large-scale stresses. In this Thesis, we propose a theoretical description of this force transmission problem, and find surprisingly simple and robust behaviors. When active forces are weak and linear force transmission avails, we uncover a new conservation law, whereby the force dipole is an invariant of linear elasticity. However, biological active forces are often strong enough to result in filament buckling, which complicates our analysis. In this case, we show that in response to any distribution of active forces, dramatically amplified contractile stresses emerge in the network on large scales. This remarkable property hinges only on the local asymmetry in elastic response between tensed and compressed fibers, and is enhanced by network disorder. Our simple, yet realistic description of individual fibers yields a universal scenario for force transmission: long-ranged, rope-like propagation near a strong active unit, and linear transmission in the far-field. Our theory provides quantitative predictions for the macroscopic active stress, which are, in both the small-force and large-force limits, independent of the network's properties. These predictions are in good agreement with experimental measures of the active stress in *in vitro* active fiber networks.

In the last few pages of this Thesis, we suggest open directions for future research, and discuss the biological implications of our findings.

Open directions

We have already discussed in Chapter 6 the anomalous force transmission behaviour of disordered, bending-dominated, which remains to be elucidated. Here we propose a few other directions for future work.

Non-linear active elastic equations. Our theory provides explicit formulas for the active stress in fiber networks, thus giving a microscopic foundations to this term in so-called *active gel theories*, which aim at describing the macroscopic properties of such systems[1]. We have shown in Chapter 4 that in linear active elastic materials, the macroscopic stress is simply the sum of the active stress predicted by our theory and a standard elastic stress. In Chapter 7, we have extended our theory to include buckling, and proposed simple equations for the active stress, in the absence of macroscopic strain. In this non-linear regime however, elastic and active stresses may not add up, and a full equation of state relating stress, strain and active unit density remains to be established. Given the simplicity of the large-force, density-controlled regime – in which the active stress depends only on the active unit force and density – we can hope to establish a similarly simple, comprehensive description of the mechanical equilibrium states of these systems at the macroscopic scale. Stability analysis of such equations could, for instance, help elucidate our qualitative observation that at large forces, active units tend to self-organize into spatially heterogeneous states, with intriguing alignments of active units.

[1] Prost, J., Julicher, F., and Joanny, J.-F. (2015). Active gel physics. *Nat Phys*, 11(2):111–117

Active stress in floppy networks. We have also shortly discussed in Chapter 3 the properties of floppy networks, which are connected, although too loosely to exhibit a macroscopic rigidity. Clearly, at linear order such networks are unable to transmit forces; however, strong active units could rigidify them, just as they stiffen under large dilation. Stiffening of soft, bending-dominated networks by active units was reported in the past[2]. Could we extend our theory to include floppy networks stiffened by active units, and what form would the active stress take in such systems?

[2] Broedersz, C. P. and MacKintosh, F. C. (2011). Molecular motors stiffen non-affine semiflexible polymer networks. *Soft Matter*, 7:3186–3191
Sheinman, M., Broedersz, C. P., and MacKintosh, F. C. (2012). Actively Stressed Marginal Networks. *Phys. Rev. Lett.*, 109(23):238101

Pre-stressed networks. We have assumed in this Thesis that the network is unstressed in the absence of active forces and macroscopic strain. However, active units are not the only local source of stress in fiber networks, and such an unstressed state does not exist in general, as filament entanglement and cross-links can result in *frustrated* states, with residual stress in any configuration. Similarly to active stress, such *pre-stress* may stiffen the network, and alter its mechanical properties; for instance, it is not clear whether bending-dominated networks would

remain so soft in the presence of pre-stress. How would it affect force transmission and stress production?

Network dynamics. Biological fiber networks are highly dynamic, and their elastic response concerns only a limited range of time scales. At short time scales $t \leq 1\,\mathrm{s}$, they relax in a viscoelastic manner; at large time scales $t \geq 100\,\mathrm{s}$ to $1000\,\mathrm{s}$, crosslinker detachment and cytoskeletal remodeling induce flow in the fibrous matrix. How do these phenomena affect stress production? Can we adapt our static phase diagram to include such dynamical effects?

Non-equilibrium properties. In the static problem treated in this Thesis, the active nature of the local forces is not intrinsically different from passive external forces. On the other hand, the dynamical coupling of the internal out-of-equilibrium properties of the active units and the network's response could result in novel and interesting non-equilibrium phenomena, which started to focus attention recently[3].

[3] Battle, C., Broedersz, C. P., Fakhri, N., Geyer, V. F., Howard, J., Schmidt, C. F., and MacKintosh, F. C. (2016). Broken detailed balance at mesoscopic scales in active biological systems. *Science*, 352(6285):604–607
Gladrow, J., Fakhri, N., MacKintosh, F. C., Schmidt, C. F., and Broedersz, C. P. (2016). Broken detailed balance reveals stress heterogeneity in active matter. *arXiv:1603.04783 [cond-mat, physics:physics]*. arXiv: 1603.04783

Large-scale structures of the network. In this Thesis, we have considered only spatially homogeneous (although possibly disordered) networks. However, real biological networks self-assemble, and can exhibit correlations in their structural heterogeneities. It would be of interest to check to what extent such correlations affect the quantitative results of this Thesis.

Biological implications.

Active unit clustering increases stress amplification Our results suggest a novel design principle for active fiber networks geared to maximize stress generation. In a linear medium, the stress generated does not depend on the spatial distribution of active units. In contrast, we predict that in fiber networks, larger stresses can be obtained by clustering the active units. Indeed, for a fixed density of active units, regrouping them results in fewer, larger and stronger "effective active units":

- depending on the system, their size may be larger, resulting in an enhanced R_0 value[4];
- clustered active units exert larger forces than isolated units, which results in an enhanced range R^* for nonlinear effects;
- clustering active units increases the average density $R_{\mathrm{a.u.}}$ between them.

[4] This is a bit subtle: for clustering to actually enhance stress in the linear regime, the force dipole FR_0 should increase, which is not the case by simple linear superposition. It may however be the case for myosin thick filaments.

All these effects result in an increase of the effective dipole size, whatever the stress production regime. Therefore, clustering active units is

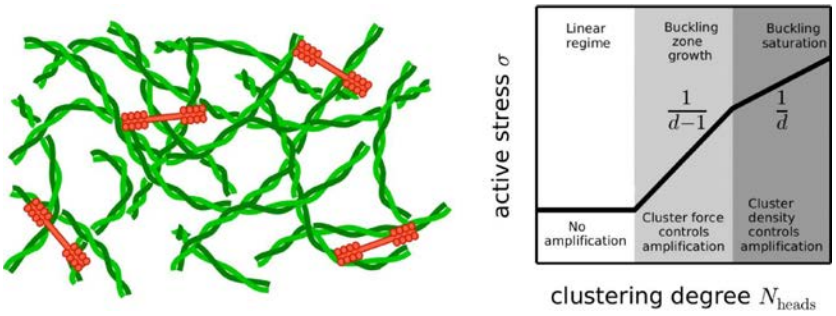

Figure 8.1: Clustering active units increase the macroscopic stress. Left: myosin thick filaments are composed of a large, variable number N_{heads} of myosin heads. Right: the active stress varies with N_{heads}, with different power laws depending on the active stress production regime.

a way for biological systems to increase the amount of stress they can generate, using the same components, as schematized in Figure 8.1.

Such regrouping of a set number of force generators to enhance stress amplification could play a role in smooth muscle, where the number of myosins in individual thick filament is regulated dynamically[5]. Similarly, at the tissue level, clustering of contractile cells occurs during wound repair[6].

There are potential counterparts for this improvement of the macroscopic stress by clustering of the active units. For instance, going to amplified stress regimes requires larger deformation of the network, in order to rearrange it into the tensed rope networks in the buckled area around active units. These larger deformations require that the active units perform a larger amount of work before reaching force balance: amplified contraction may thus be more energetically costly. Furthermore, due to these large local deformations, the mechanical response of the network may be slower, *i.e.* the time scale for stress production is increased.

Emergent contractility in actomyosin. Far from merely transmitting active forces, we show that fiber networks dramatically alter force propagation as contractility emerges from arbitrary spatial distributions of local active forces. This could imply that living organisms do not have to fine-tune the detailed geometry of their active units, since any local force distribution yields essentially the same effects on large length scales. This emergence of contractility sheds a new light on the long-standing debate in cytoskeletal mechanics regarding the emergence of macroscopic contraction in non-muscle actomyosin despite the absence of an intrinsic contractility of individual myosin motors[7]. Indeed, while these motors exert equal amounts of local pushing and pulling forces[8] (Figure 8.2), our result suggests that the surrounding network rectifies pushing contributions into uniform contraction. This rectification effect in two and three dimensions contrasts with the behavior of previously studied one-dimensional actomyosin systems, where extensile dipoles

[5] Seow, C. Y. (2005). Myosin filament assembly in an ever-changing myofilament lattice of smooth muscle. *Am. J. Physiol.-Cell Physiol.*, 289(6):C1363–C1368

[6] Rocha-Azevedo, B. d. and Grinnell, F. (2013). Fibroblast morphogenesis on 3d collagen matrices: The balance between cell clustering and cell migration. *Exp. Cell Res.*, 319(16):2440–2446

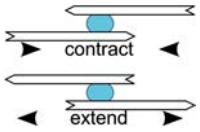

Figure 8.2: Myosin motors (blue) exert forces on actin filament by moving processively towards their barbed end. Depending on the local geometry, this can result in either local contractility or extensility. Source: (Lenz, 2014).

[7] Dasanayake, N. L., Michalski, P. J., and Carlsson, A. E. (2011). General Mechanism of Actomyosin Contractility. *Phys. Rev. Lett.*, 107(11):118101
Mizuno, D., Tardin, C., Schmidt, C. F., and Mackintosh, F. C. (2007). Nonequilibrium mechanics of active cytoskeletal networks. *Science*, 315(5810):370–373
Murrell, M., Oakes, P. W., Lenz, M., and Gardel, M. L. (2015). Forcing cells into shape: the mechanics of actomyosin contractility. *Nature Reviews Molecular Cell Biology*, 16(8):486–498

[8] Lenz, M. (2014). Geometrical Origins of Contractility in Disordered Actomyosin Networks. *Phys. Rev. X*, 4(4):041002
Lenz, M., Gardel, M. L., and Dinner, A. R. (2012a). Requirements for contractility in disordered cytoskeletal bundles. *New J. Phys.*, 14:033037

are attenuated but not reversed[9].

More broadly, we suggest that this strong propensity for the emergence of contraction in fibrous materials can explain the overwhelming dominance of contractile stresses in active biological materials up to the tissue level. Clearly, this does not mean that it is impossible to generate large-scale expansion in living organisms as required for limb abduction and extension or for lung inflation. Nevertheless, in each of these examples the expansion actually results from the clever harnessing of muscle contraction through lever structures involving our skeleton.

[9] Lenz, M., Thoresen, T., Gardel, M. L., and Dinner, A. R. (2012b). Contractile Units in Disordered Actomyosin Bundles Arise from F-Actin Buckling. *Phys. Rev. Lett.*, 108(23):238107

Bibliography

Alberts, B., Johnson, A., Lewis, J., Raff, M., Roberts, K., and Walter, P. (2002). *Molecular Biology of the Cell*. Garland Science, 4th edition.

Alvarado, J., Sheinman, M., Sharma, A., MacKintosh, F. C., and Koenderink, G. H. (2013). Molecular motors robustly drive active gels to a critically connected state. *Nat. Phys.*, 9:591.

Battle, C., Broedersz, C. P., Fakhri, N., Geyer, V. F., Howard, J., Schmidt, C. F., and MacKintosh, F. C. (2016). Broken detailed balance at mesoscopic scales in active biological systems. *Science*, 352(6285):604–607.

Blanchoin, L., Boujemaa-Paterski, R., Sykes, C., and Plastino, J. (2014). Actin Dynamics, Architecture, and Mechanics in Cell Motility. *Physiol. Rev.*, 94:235–263.

Broedersz, C. P. and MacKintosh, F. C. (2011). Molecular motors stiffen non-affine semiflexible polymer networks. *Soft Matter*, 7:3186–3191.

Broedersz, C. P. and MacKintosh, F. C. (2014). Modeling semiflexible polymer networks. *Rev. Mod. Phys.*, 86:995.

Broedersz, C. P., Mao, X., Lubensky, T. C., and MacKintosh, F. C. (2011). Criticality and isostaticity in fibre networks. *Nat Phys*, 7(12):983–988.

Broedersz, C. P., Sheinman, M., and MacKintosh, F. C. (2012). Filament-Length-Controlled Elasticity in 3d Fiber Networks. *Phys. Rev. Lett.*, 108(7):078102.

Calladine, C. R. (1978). Buckminster Fuller's "Tensegrity" structures and Clerk Maxwell's rules for the construction of stiff frames. *International Journal of Solids and Structures*, 14(2):161–172.

Carlsson, A. E. (2006). Contractile stress generation by actomyosin gels. *Phys. Rev. E*, 74(5 Pt 1):051912.

Dasanayake, N. L., Michalski, P. J., and Carlsson, A. E. (2011). General Mechanism of Actomyosin Contractility. *Phys. Rev. Lett.*, 107(11):118101.

DiDonna, B. A. and Lubensky, T. C. (2005). Nonaffine correlations in random elastic media. *Phys. Rev. E*, 72(6):066619.

Egami, T. (2011). Atomic level stresses. *Progress in Materials Science*, 56(6):637–653.

Ehrlich, H. P. (1988). Wound closure: evidence of cooperation between fibroblasts and collagen matrix. *Eye*, 2:149–157.

Eshelby, J. D. (1956). The Continuum Theory of Lattice Defects. *Solid State Phys.*, 3:79–144.

Feng, S., Thorpe, M. F., and Garboczi, E. (1985). Effective-medium theory of percolation on central-force elastic networks. *Phys. Rev. B*, 31(1):276–280.

Gladrow, J., Fakhri, N., MacKintosh, F. C., Schmidt, C. F., and Broedersz, C. P. (2016). Broken detailed balance reveals stress heterogeneity in active matter. *arXiv:1603.04783 [cond-mat, physics:physics]*. arXiv: 1603.04783.

Gurtin, M. E. (1973). The Linear Theory of Elasticity. In Truesdell, P. D. C., editor, *Linear Theories of Elasticity and Thermoelasticity*, pages 1–295. Springer Berlin Heidelberg. DOI: 10.1007/978-3-662-39776-3_1.

Head, D. A., Levine, A. J., and MacKintosh, F. C. (2005). Mechanical response of semiflexible networks to localized perturbations. *Phys. Rev. E*, 72(6 Pt 1):061914.

Hentschel, H. G. E., Karmakar, S., Lerner, E., and Procaccia, I. (2011). Do athermal amorphous solids exist? *Phys. Rev. E*, 83(6):061101.

Heussinger, C. and Frey, E. (2007). Force distributions and force chains in random stiff fiber networks. *Eur. Phys. J. E*, 24(1):47–53.

Huang, Y., Men, Y., and Yin, G. (1999). Calculation of Thin Plates on Statistical Non—Uniform Foundations. In *Computational Mechanics in Structural Engineering*, pages 245–258. Elsevier Science Ltd, Oxford.

Hunter, J. D. (2007). Matplotlib: A 2d graphics environment. *Comput. Sci. Eng.*, 9(3):90–95.

Jen, C. J. and McIntire, L. V. (1982). The structural properties and contractile force of a clot. *Cell Motil.*, 2(5):445–455.

Joanny, J.-F. and Prost, J. (2009). Active gels as a description of the actin-myosin cytoskeleton. *HFSP J.*, 3(2):94–104.

Jülicher, F., Kruse, K., Prost, J., and Joanny, J.-F. (2007). Active behavior of the Cytoskeleton. *Phys. Rep.-Rev. Sec. Phys. Lett.*, 449(1–3):3–28.

Kane, C. L. and Lubensky, T. C. (2014). Topological boundary modes in isostatic lattices. *Nat Phys*, 10(1):39–45.

Kasza, K. E., Koenderink, G. H., Lin, Y. C., Broedersz, C. P., Messner, W., Nakamura, F., Stossel, T. P., MacKintosh, F. C., and Weitz, D. A. (2009). Nonlinear elasticity of stiff biopolymers connected by flexible linkers. *Phys. Rev. E*, 79(4):041928.

Koenderink, G. H., Dogic, Z., Nakamura, F., Bendix, P. M., MacKintosh, F. C., Hartwig, J. H., Stossel, T. P., and Weitz, D. A. (2009). An active biopolymer network controlled by molecular motors. *Proc. Natl. Acad. Sci. U.S.A.*, 106(36):15192–7.

Lam, W. A., Chaudhuri, O., Crow, A., Webster, K. D., Li, T.-D., Kita, A., Huang, J., and Fletcher, D. A. (2011). Mechanics and contraction dynamics of single platelets and implications for clot stiffening. *Nat. Mater.*, 10:61–66.

Lemière, J., Bussonnier, M., Betz, T., Sykes, C., and Carvalho, K. (2015). Cell-sized liposome doublets reveal active cortical tension build up. communicated by C. Sykes.

Lenz, M. (2014). Geometrical Origins of Contractility in Disordered Actomyosin Networks. *Phys. Rev. X*, 4(4):041002.

Lenz, M., Gardel, M. L., and Dinner, A. R. (2012a). Requirements for contractility in disordered cytoskeletal bundles. *New J. Phys.*, 14:033037.

Lenz, M., Thoresen, T., Gardel, M. L., and Dinner, A. R. (2012b). Contractile Units in Disordered Actomyosin Bundles Arise from F-Actin Buckling. *Phys. Rev. Lett.*, 108(23):238107.

LIGO Scientific Collaboration and Virgo Collaboration (2016). Observation of Gravitational Waves from a Binary Black Hole Merger. *Phys. Rev. Lett.*, 116(6):061102.

Liu, B. and Qiu, X. (2009). How to Compute the Atomic Stress Objectively? *Journal of Computational and Theoretical Nanoscience*, 6(5):1081–1089.

Marchetti, M. C., Joanny, J. F., Ramaswamy, S., Liverpool, T. B., Prost, J., Rao, M., and Simha, R. A. (2013). Hydrodynamics of soft active matter. *Rev. Mod. Phys.*, 85:1143.

Maxwell, J. C. (1864). On the calculation of the equilibrium and stiffness of frames. *Philosophical Magazine Series 4*, 27(182):294–299.

Mizuno, D., Tardin, C., Schmidt, C. F., and Mackintosh, F. C. (2007). Nonequilibrium mechanics of active cytoskeletal networks. *Science*, 315(5810):370–373.

Murrell, M. and Gardel, M. L. (2012). F-actin Buckling Coordinates Contractility and Severing in a Biomimetic Actomyosin Cortex. *Proc. Natl. Acad. Sci. U.S.A.*, 109(51):20820–20825.

Murrell, M., Oakes, P. W., Lenz, M., and Gardel, M. L. (2015). Forcing cells into shape: the mechanics of actomyosin contractility. *Nature Reviews Molecular Cell Biology*, 16(8):486–498.

Notbohm, J., Lesman, A., Rosakis, P., Tirrell, D. A., and Ravichandran, G. (2014). Microbuckling in fibrin networks enables long-range cell mechanosensing. *arXiv*, page 1407.3510.

Oliphant, T. E. (2007). Python for Scientific Computing. *Computing in Science & Engineering*, 9(3):10–20.

Perez, F. and Granger, B. E. (2007). IPython: A System for Interactive Scientific Computing. *Computing in Science & Engineering*, 9(3):21–29.

Prost, J., Julicher, F., and Joanny, J.-F. (2015). Active gel physics. *Nat Phys*, 11(2):111–117.

Ramachandran, P. and Varoquaux, G. (2011). Mayavi: 3d Visualization of Scientific Data. *Computing in Science Engineering*, 13(2):40–51.

Rocha-Azevedo, B. d. and Grinnell, F. (2013). Fibroblast morphogenesis on 3d collagen matrices: The balance between cell clustering and cell migration. *Exp. Cell Res.*, 319(16):2440–2446.

Ronceray, P., Broedersz, C. P., and Lenz, M. (2016). Fiber networks amplify active stress. *Proc. Natl. Acad. Sci. U.S.A.*, 113(11):2827–2832.

Ronceray, P. and Harrowell, P. (2011). The variety of ordering transitions in liquids characterized by a locally favoured structure. *EPL (Europhysics Letters)*, 96(3):36005.

Ronceray, P. and Harrowell, P. (2012). Geometry and the entropic cost of locally favoured structures in a liquid. *The Journal of chemical physics*, 136(13):134504.

Ronceray, P. and Harrowell, P. (2013). Influence of liquid structure on the thermodynamics of freezing. *Physical Review E*, 87(5):052313.

Ronceray, P. and Harrowell, P. (2014). Multiple ordering transitions in a liquid stabilized by low symmetry structures. *Physical review letters*, 112(1):017801.

Ronceray, P. and Harrowell, P. (2015a). Favoured local structures in liquids and solids: a 3d lattice model. *Soft matter*, 11(17):3322–3331.

Ronceray, P. and Harrowell, P. (2015b). The free energy of a liquid when viewed as a population of overlapping clusters. *accepted for publication in Mol. Simul.*, (arXiv:1510.03073).

Ronceray, P. and Harrowell, P. (2016a). From Liquid Structure to Configurational Entropy: Introducing Structural Covariance. *submitted to the Journal of Statistical Mechanics: Theory and Experiment*.

Ronceray, P. and Harrowell, P. (2016b). Suppression of crystalline order by competing liquid structures. *in preparation*.

Ronceray, P. and Lenz, M. (2015). Connecting local active forces to macroscopic stress in elastic media. *Soft Matter*, 11(8):1597–1605.

Rosakis, P., Notbohm, J., and Ravichandran, G. (2015). A model for compression-weakening materials and the elastic fields due to contractile cells. *Journal of the Mechanics and Physics of Solids*, 85:16–32.

Rosenfeld, S. S., Xing, J., Chen, L.-Q., and Sweeney, H. L. (2003). Myosin IIB Is Unconventionally Conventional. *J. Biol. Chem.*, 278(30):27449–27455.

Schwarz, U. S. and Safran, S. A. (2013). Physics of adherent cells. *Rev. Mod. Phys.*, 85(3):1327.

Seow, C. Y. (2005). Myosin filament assembly in an ever-changing myofilament lattice of smooth muscle. *Am. J. Physiol.-Cell Physiol.*, 289(6):C1363–C1368.

Sheinman, M., Broedersz, C. P., and MacKintosh, F. C. (2012). Actively Stressed Marginal Networks. *Phys. Rev. Lett.*, 109(23):238101.

Storm, C., Pastore, J. J., MacKintosh, F. C., Lubensky, T. C., and Janmey, P. A. (2005). Nonlinear elasticity in biological gels. *Nature*, 435(7039):191–4.

Sykes, M. F. and Essam, J. W. (1964). Exact Critical Percolation Probabilities for Site and Bond Problems in Two Dimensions. *Journal of Mathematical Physics*, 5(8):1117–1127.

The ATLAS collaboration (2012). Observation of a new particle in the search for the Standard Model Higgs boson with the ATLAS detector at the LHC. *Physics Letters B*, 716(1):1–29.

Tsai, D. H. (1979). The virial theorem and stress calculation in molecular dynamics. *The Journal of Chemical Physics*, 70(3):1375–1382.

Xu, X. and Safran, S. A. (2015). Nonlinearities of biopolymer gels increase the range of force transmission. *Phys. Rev. E*, 92(3):032728.

Zimmerman, J. A., WebbIII, E. B., Hoyt, J. J., Jones, R. E., Klein, P. A., and Bammann, D. J. (2004). Calculation of stress in atomistic simulation. *Modelling Simul. Mater. Sci. Eng.*, 12(4):S319.

Gallery

Ô Mort, vieux capitaine, il est temps! levons l'ancre!
Ce pays nous ennuie, ô Mort! Appareillons!
Si le ciel et la mer sont noirs comme de l'encre,
Nos coeurs que tu connais sont remplis de rayons!

Verse-nous ton poison pour qu'il nous réconforte!
Nous voulons, tant ce feu nous brûle le cerveau,
Plonger au fond du gouffre, Enfer ou Ciel, qu'importe?
Au fond de l'Inconnu pour trouver du nouveau!

— Charles Baudelaire, *Le voyage.*

The lattice fiber network model I have studied in this Thesis is not only scientifically interesting – it can also be beautiful. As anyone who has read through to this point will probably have already guessed, I like showing figures. More than that: when I choose a new scientific project, the expectation of nice graphics comes into account. I had this in mind when I started my PhD, but still, I have often been agreeably surprised by the visual potential of my simulation results. In these last few pages, I present a few attempts to render it, for their aesthetic value only.

Legend:

1. A bending-dominated network stiffened by an isotropic dilation. Only tension lines are shown.
2. A dilated floppy network; at intermediate strain its response is bending-dominated.
3. At large strain, the response is stretching dominated.
4. Force chains around a strong active unit in a bending-dominated network.
5. Stress patterns around strong active units in a rope-like network. This image was selected for the cover of PNAS when our article

(Ronceray et al., 2016) was published.

6. Color study for the PNAS cover.

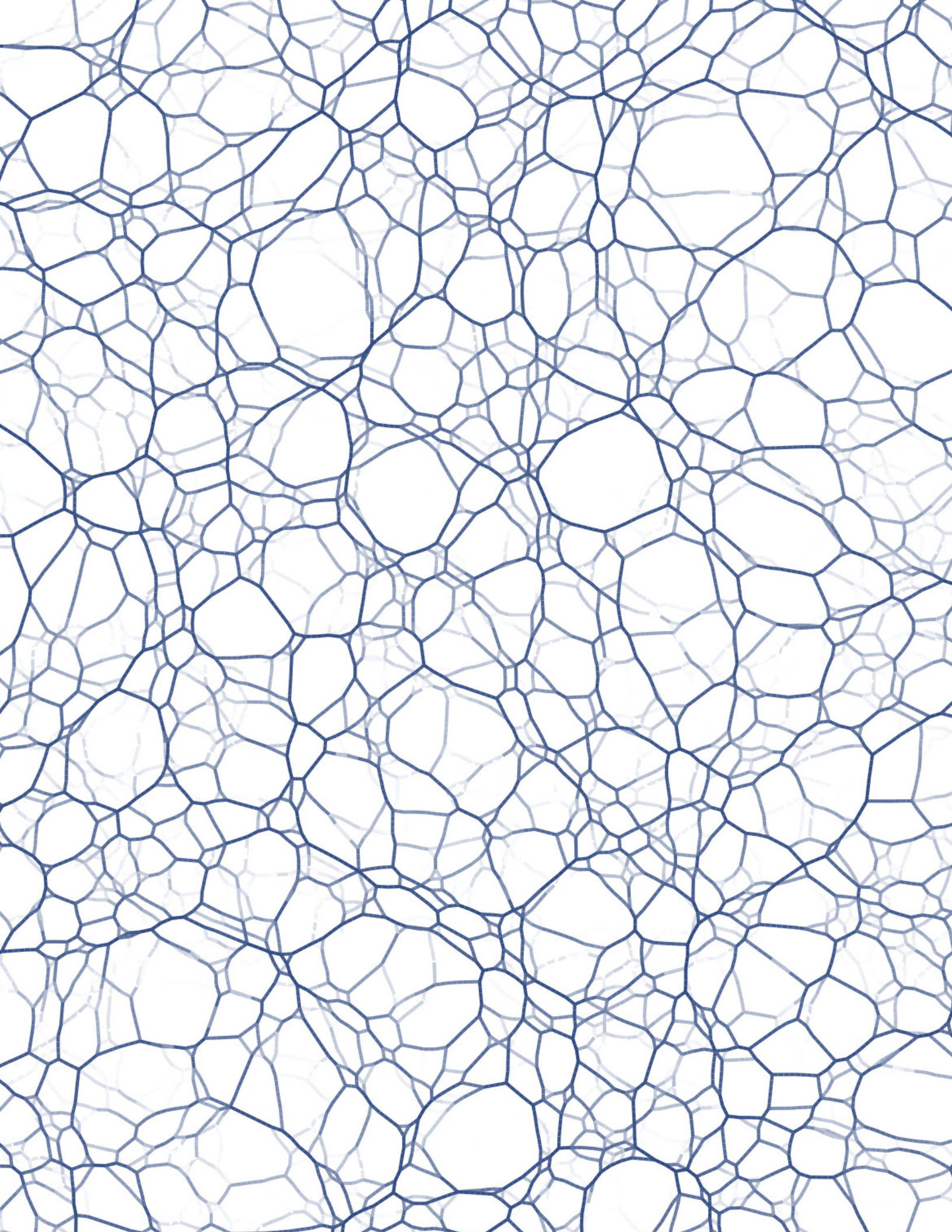

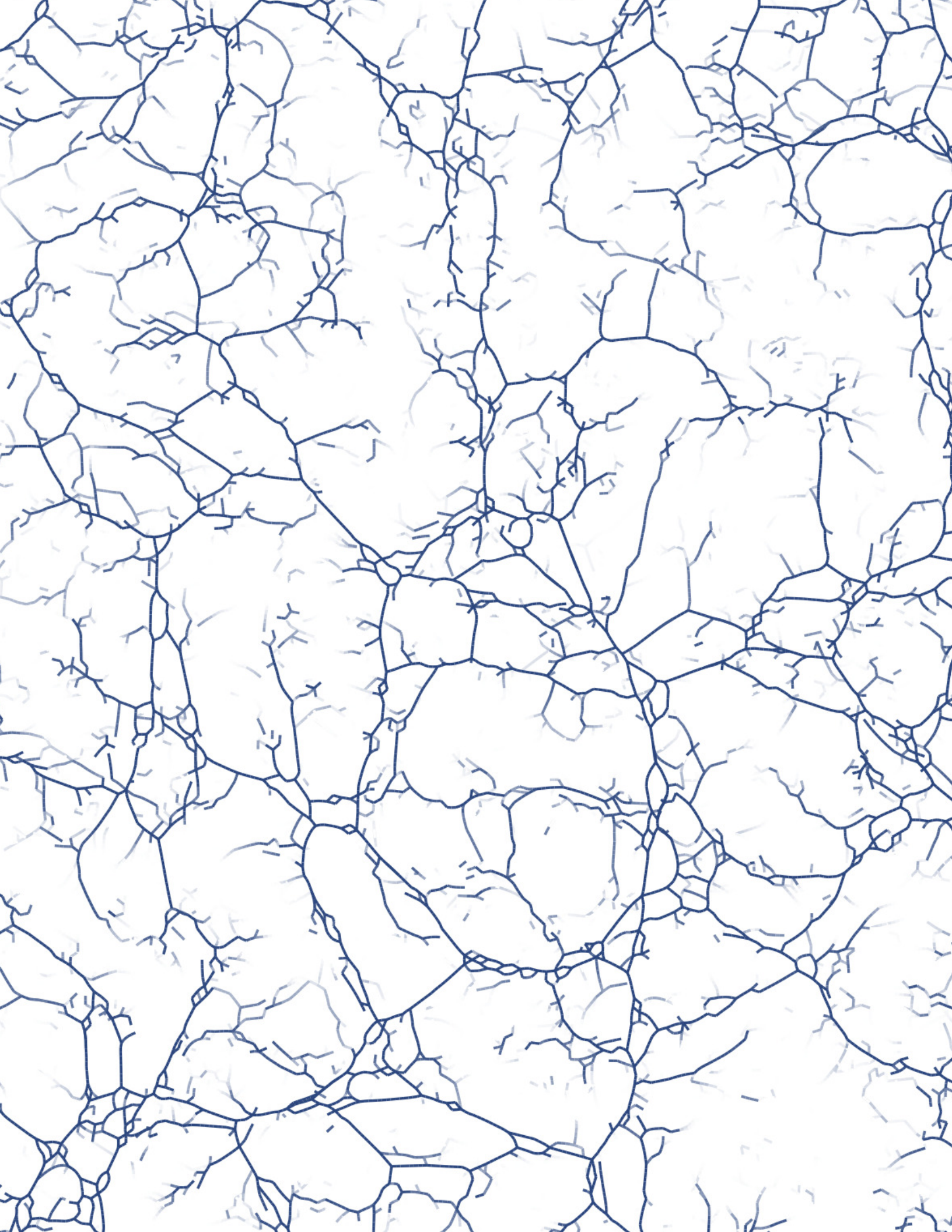

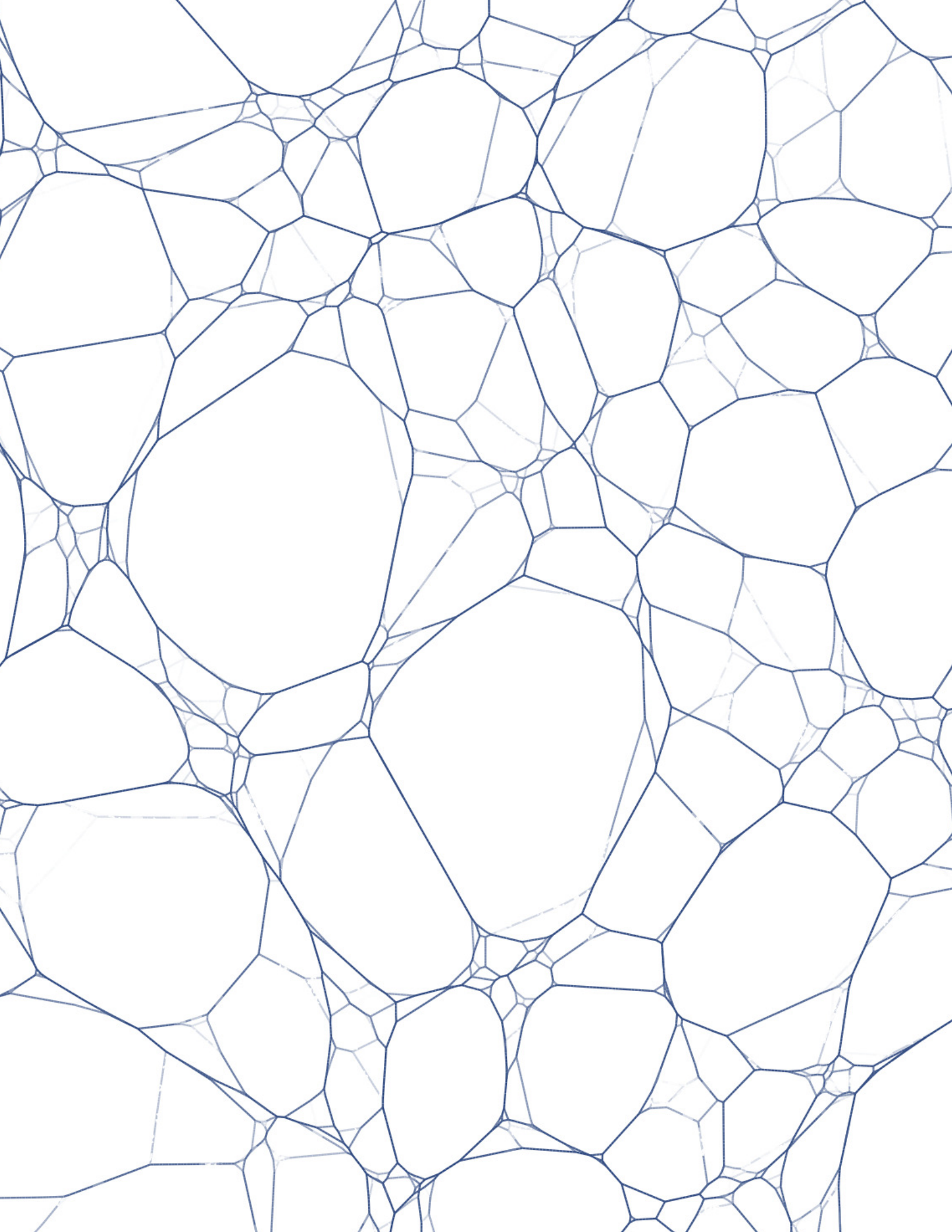

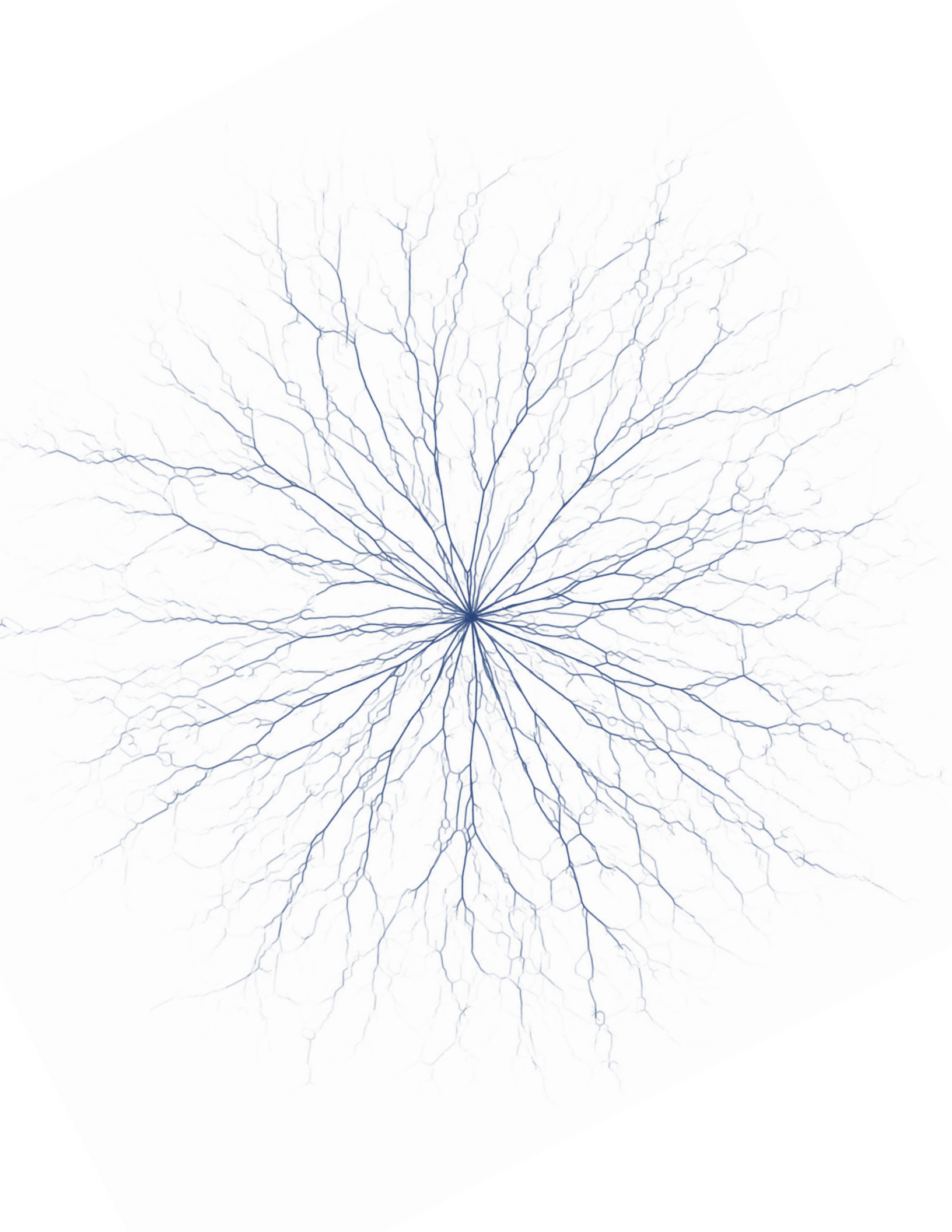

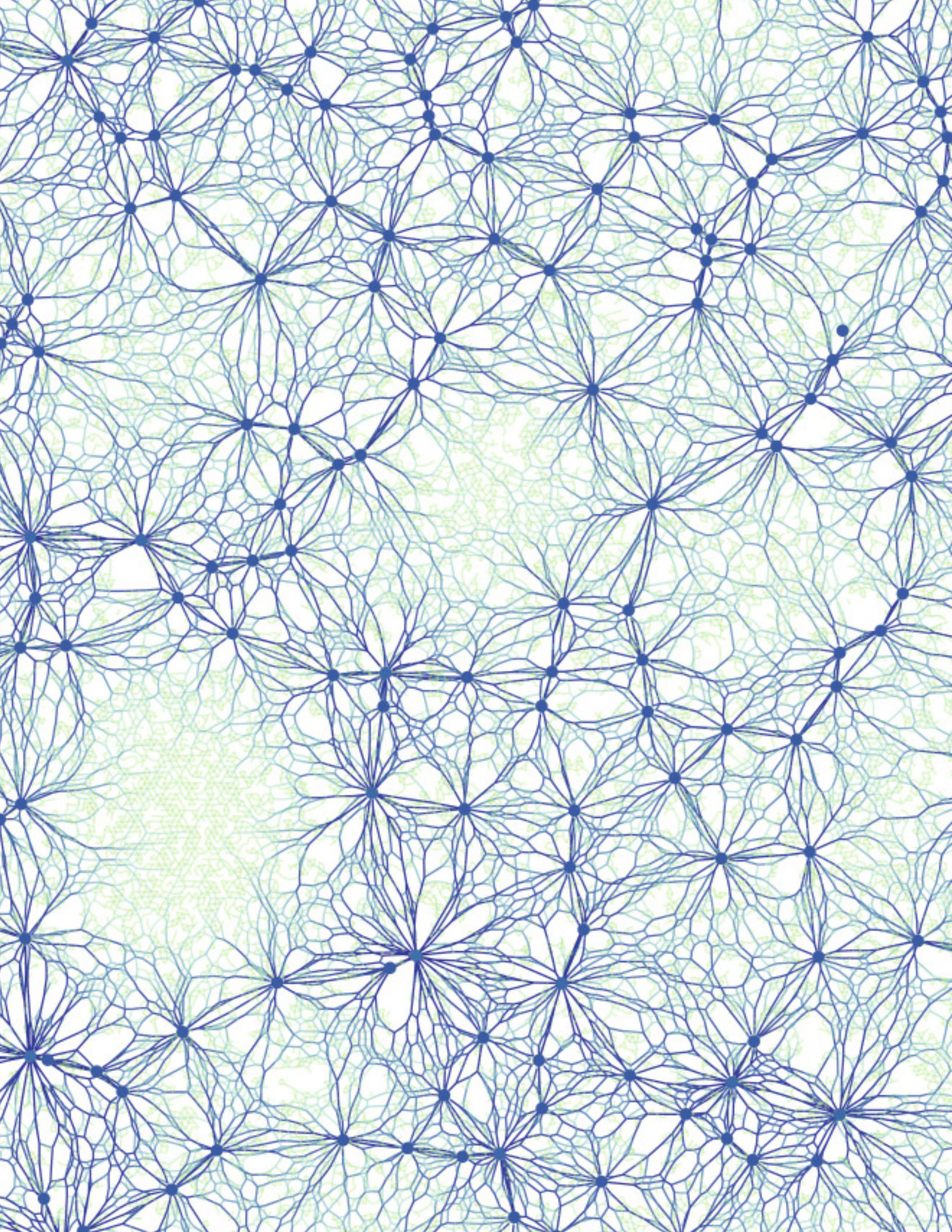

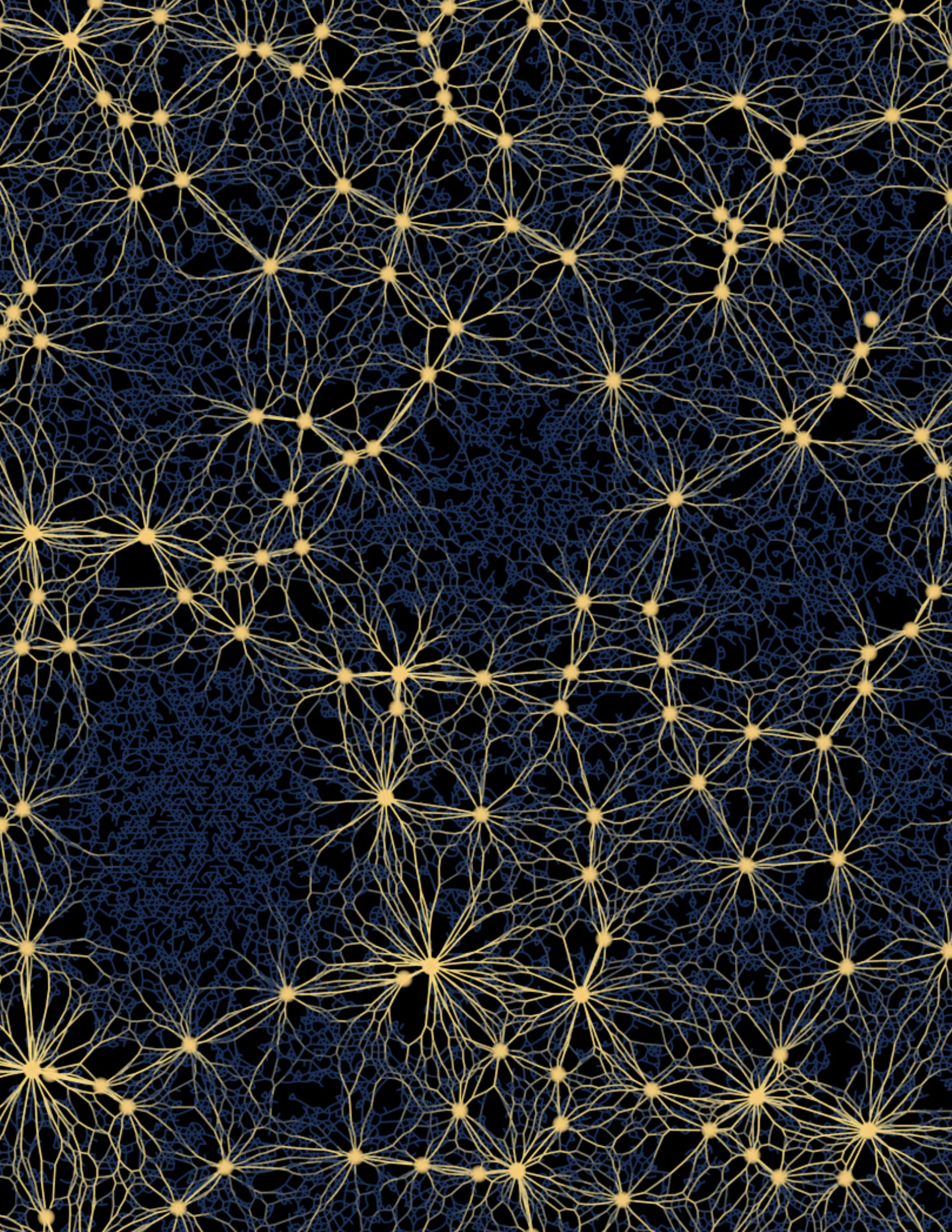

Pierre Ronceray *Thèse de doctorat* 31 mai 2016

Active contraction in biological fiber networks

Living organisms generate forces to move, change shape and maintain their internal functions. These forces are typically produced by molecular motors embedded in networks of fibers. While these motors are traditionally regarded as the defining elements of biological force generation, here we show that the surrounding network also plays a central role in this process. Indeed, rather than merely propagating forces like a simple elastic medium, fiber networks produce emergent, dramatically amplified stresses, and can go so far as reversing small-scale extensile forces into large-scale contraction. Our theory quantitatively accounts for experimental measurements of contraction, and suggests mechanisms for the physiological regulation of biological active stresses.

Cover image: *computer-generated representation of an actively contracting biological fiber networks. The star-shaped stress patterns of tensile stress (dark blue) are responsible for a dramatic amplification of the local pulling forces exerted by molecular motors (spheres).*

université PARIS-SACLAY
ÉCOLE DOCTORALE Physique en île-de-France (EDPIF)
UNIVERSITÉ PARIS SUD
Comprendre le monde, construire l'avenir
LPTMS
Laboratoire de Physique Théorique et Modèles Statistiques

université PARIS-SACLAY
ÉCOLE DOCTORALE
Physique en Île-de-France (EDPIF)

Titre : Contraction active de réseaux de fibres biologiques

Mots clés : matière active, cytosquelette, élasticité

Résumé : Le fonctionnement des organismes vivants requiert la production de forces à grande échelle, pour des processus biologiques aussi divers que la motilité cellulaire, le développement embryonnaire, la cicatrisation ou encore la contraction musculaire. Dans de tels systèmes, les forces générées à l'échelle moléculaire par des moteurs protéiques sont transmises par des réseaux de fibres désordonnés, menant à des tensions actives à grande échelle. Les propriétés macroscopiques passives de ces réseaux de fibres sont bien caractérisées. En revanche, ce problème de production de stress par des unités actives microscopiques n'est pas résolu. Cette Thèse présente une étude approfondie, par des méthodes théoriques et numériques, de la transmission de forces dans les réseaux élastiques de biopolymères. Je montre que la réponse linéaire, à faible force, des réseaux est remarquablement simple : elle est déterminée par la seule la géométrie des unités actives exerçant les forces. Au contraire, lorsque les forces actives sont suffisamment importantes pour provoquer le flambage non-linéaire des fibres, ces forces sont rectifiées par le réseau, et deviennent isotropiquement contractiles. La contraction émergente qui en résulte est amplifiée par la transmission de forces non-linéaire à travers le réseau. Cette amplification du stress macroscopique est renforcée par le caractère désordonnée du réseau, mais sature lorsque la densité d'unités actives est grande. Nos prédictions sont en accord quantitatifs avec des résultats expérimentaux sur des tissus reconstitués et des réseaux d'actomyosine in vitro, et apportent un éclairage nouveau sur l'influence de l'architecture microscopique des réseaux sur structure des stress à l'échelle de la cellule et du tissu.

Title : Active contraction in biological fiber networks

Keywords : active matter, cytoskeleton, elasticity

Abstract : Large-scale force generation is essential for biological functions such as cell motility, embryonic development, wound healing and muscle contraction. In these processes, forces generated at the molecular level by motor proteins are transmitted by disordered fiber networks, resulting in large-scale active stresses. While fiber networks are well characterized macroscopically, this stress generation by microscopic active units is not well understood. In this Thesis, I present a comprehensive theoretical and numerical study of force transmission in elastic fiber networks. I show that the linear, small-force response of the networks is remarkably simple, as the macroscopic active stress depends only on the geometry of the force-exerting unit. In contrast, as non-linear buckling occurs around these units, local active forces are rectified towards isotropic contraction, making the local geometry of force exertion irrelevant. This emergent contractility is amplified by non-linear force transmission through the network. This stress amplification is reinforced by the networks' disordered nature, but saturates for high densities of active units. Our predictions are quantitatively consistent with experiments on reconstituted tissues and actomyosin networks, and that they shed light on the role of the network microstructure in shaping active stresses in cells and tissue.

Université Paris-Saclay
Espace Technologique / Immeuble Discovery
Route de l'Orme aux Merisiers RD 128 / 91190 Saint-Aubin, France